A High-Resolution Reconstruction of Southern California Hydroclimate During the Holocene: Interannual Precipitation Variability Response to Climate Forcing

by

Xiaojing Du

A dissertation submitted in partial fulfillment
of the requirements for the degree of
Doctor of Philosophy
(Earth and Environmental Sciences)
in the University of Michigan
2020

Doctoral Committee:

Professor Ingrid L. Hendy, Chair
Professor Julia E. Cole
Associate Professor Xianglei Huang
Associate Professor Naomi E. Levin
Assistant Professor Ashley E. Payne
Professor Christopher J. Poulsen

Xiaojing Du
xjdu@umich.edu
ORCID iD: 0000-0001-8228-5086

Dedication

This dissertation is dedicated to my parents and my husband.

Acknowledgements

First and foremost, I would like to express my sincere gratitude to my advisor, Ingrid Hendy, for the continuous support of my study and research, for her patience, motivation, and wisdom, and for her encouragement. Her guidance helps me learn how to do scientific research and how to develop my own ideas. I would like to thank my committee for their helpful discussion and suggestions. I especially need to thank Julia Cole, who provided inside into paleoENSO study, to Chris Poulsen, who provided perspective on climate modeling, and Xianglei Huang, who gave me valuable suggestions on climate data analysis.

My collaborators have been essential to my research and career development. Linda Hinnov, thank you for teaching me time series analysis and suggestions on other statistic methods. Your constant encouragement, enthusiasm, and patience are essential to me. Arndt Schimmelmann, Erik Brown, and Dorothy Pak, thank you for your edits on my manuscripts and encouragement in the process of publication. Jiang Zhu, thank you for thoughtful discussions of data-model comparison. Linda Heusser, thank you for pollen analysis and helpful discussion of pollen data. It has been a joy to work with all of you.

Thank you to my labmates, Allie, Tiffany, Yi, Madelyn, Mark. You have all been so supportive. Thanks for reading rough manuscripts and watching my presentations, and helping me to improve them, for exciting discussions of science, advice, and encouragement. Thank you to my wonderful family and friends, both here in Michigan and China. Your constant support has been essential for me to get to this point. My fellow grad students, thanks for being so supportive and helpful. Mom, thanks for your constant encouragement and support, and for believing in me. Dad, your spirit is always together with me and encourage me to overcome any difficulties. I wouldn’t have gotten where I am without you. I would like to give my special thanks to my husband, Mingda. Thank you for being a loving husband, for being so supportive, and for experiencing every joyful moment and difficult time together with me. You have been critical to me getting to the finish line.

Acknowledgement is made to the National Science Foundation, the University of Michigan Rackham Graduate School, and the University of Michigan Earth and Environmental Sciences Department for supporting this work.

Table of Contents

List of Tables

List of Figures

List of Appendices

Abstract

Southern California has a Mediterranean climate characterized by wet winters and dry summers. With both significant seasonal precipitation variability and unusually large interannual variance relative to the rest of the US, Southern California presents a huge challenge to water resource management as state water demands continue to grow. In this dissertation, I use multiple lines of evidence, including precipitation reconstructions, climate model outputs, and reconstructed vegetation, to explore the causes of hydroclimate change in this region. This understanding is critical for regional climate projections, water resource management, and forest ecosystems sustainability.

A robust 9000-year high-resolution Bayesian age model was generated using 89 accelerator mass spectrometric ^{14}C dates for laminated marine sediments from central Santa Barbara Basin (SBB), California. Multiple flood (extreme precipitation events with an average return interval of ~100 years) and turbidite (earthquake induced slope failures with an average return interval of ~500 years) layers were identified. A master stratigraphy for the Holocene was created using these layers and correlated multiple marine sediment cores from SBB to place all published SBB proxy paleoclimate records into the new chronology. A sub-annually resolved Southern California precipitation record was reconstructed using ITRAX scanning X-ray fluorescence titanium counts from the same laminated sediment sequence in SBB. Instrumental precipitation data from the 20th and 21st centuries was analyzed to demonstrate that Southern California precipitation is significantly correlated with El Niño Southern Oscillation (ENSO) on interannual timescales via an ENSO teleconnection between the tropical Pacific and North America. The Ti-based precipitation reconstruction over the Common Era demonstrates the ENSO teleconnection is modulated by both tropical forcing and mid-latitude atmospheric pressure systems (the Aleutian Low). Strong interannual precipitation variability occurred when greater ENSO variance was observed in the tropical Pacific and when the Aleutian Low deepens in the northeast Pacific (e.g. 1370-

1540 CE). Interannual precipitation was weak when either ENSO variance is reduced (700-900 CE) or the ENSO teleconnection was muted by a weakening of the AL (1540-1680 CE).

The sub-annual SBB precipitation reconstruction was extended back through the Holocene (9,000 years) to demonstrate that interannual precipitation variability increased significantly during late Holocene (after 4,500 years ago) when the Intertropical Convergence Zone (ITCZ) migrated southward and the Aleutian Low strengthened. The influence of ITCZ and Aleutian Low position was examined using model simulation outputs: a southward shifted ITCZ weakens across-equatorial trade wind, potentially enhancing tropical Pacific ENSO variability and strengthening the Aleutian Low in the North Pacific. Such atmospheric circulation changes lead to a stronger ENSO teleconnection with Southern California and thus greater interannual precipitation variability in the region. A new multidecadal-resolution pollen record in SBB was compared to regional precipitation reconstructions to explore the vegetation response to different aspects of hydroclimate change including interannual precipitation variability. The drought-adapted endemic vegetation appears insensitive to both interannual precipitation variability and extreme precipitation events, displaying only a subtle long-term response to orbital-forced seasonal insolation variance over the Holocene. However, prolonged or severe droughts may have a minor impact on the distribution of the coastal mosaic oak woodland/ chaparral/ sage scrub communities in this region on multidecadal to centennial timescales.

Chapter 1

Introduction

Southern California has a Mediterranean climate, characterized by cool, wet winters and hot, dry summers, and highly variable total annual precipitation (Dettinger et al., 2011). Southern California has experienced a long-term drying trend, together with extreme events such as floods and severe droughts over the past few decades (Seager & Hoerling, 2014; Seager & Vecchi, 2010), which creates challenges for regional water resource management. The subsequent negative impact on society and the economy is further aggravated by the complex regional geography of the region and a rapidly growing population in Southern California. As water managers rely heavily on interannual climate variability (El Niño) to fill reservoirs, a more complete understanding of the climate forcing driven natural interannual precipitation changes is critical for better future hydroclimate prediction and water resource management in this region.

The highly seasonal precipitation changes of Southern California are due to the latitudinal changes in northeast Pacific large-scale atmospheric pressure fields between winter and summer. In winter, the North Pacific High pressure system (NPH) is relatively weak and moves to a southward position over the North Pacific (Haston and Michaelsen, 1997; Kenyon, 1999; Nezlin and Stein, 2005). During this season, an enhanced Aleutian Low pressure system (AL) migrates southward and steers storm tracks toward Southern California, contributing to winter precipitation. The North Pacific High strengthens and moves northward in spring and summer, deflecting storm fronts to the north, resulting in little to no summer precipitation (Haston and Michaelsen, 1997).

Between different years (on interannual timescales), the El Niño Southern Oscillation (ENSO) impacts winter precipitation in Southern California via an atmospheric teleconnection between the central tropical Pacific and the west coast of North America (Fig. 1.1) (Dettinger et al., 1998; Jong et al., 2016; Kim et al., 2017;

Trenberth et al., 1998). ENSO is a periodic variation in sea surface temperature (SST) and air pressure across the tropical Pacific that oscillates between El Niño (warm phase) and La Niña (cold phase) with a period of 2–7 years. ENSO originates in the ocean-atmosphere interactions in the tropical Pacific Ocean (Bjerknes, 1969; Wang and Fiedler, 2006): The easterly trade winds normally move warm surface water across the equatorial Pacific to the western tropical Pacific (WTP), forming the Western Pacific Warm Pool (SST is above 28°C); In contrast, colder subsurface water

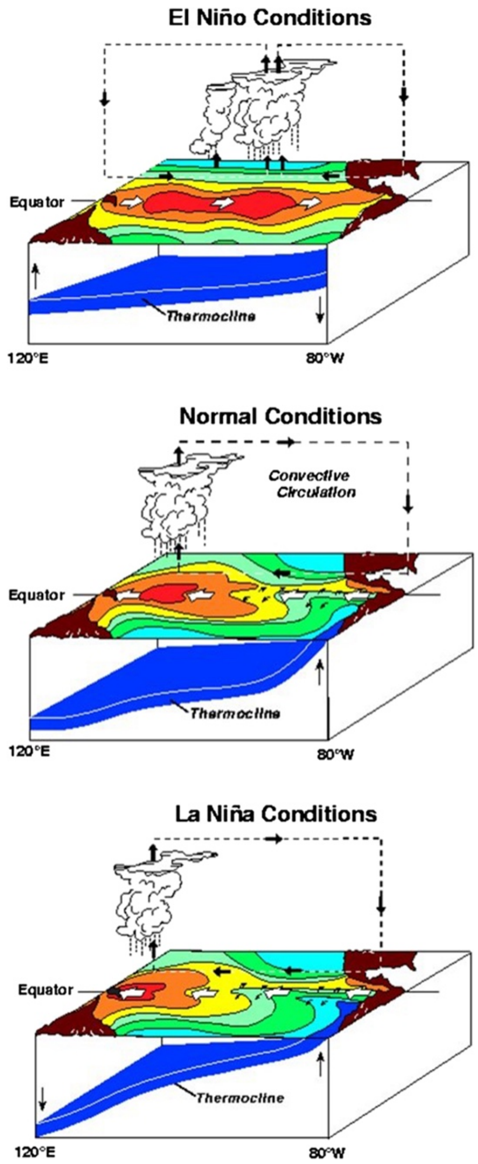
El Niño Conditions

Normal Conditions

La Niña Conditions

Figure 0-1 Schematic diagrams of the atmospheric and oceanic conditions across the equator during El Niño and La Niña phases. Figure courtesy of National Oceanic and Atmospheric Administration Pacific Marine Environmental Laboratory.

upwells to the surface in the eastern tropical Pacific (ETP), contributing to the ETP cold tongue (5–10 ˚C cooler SST than the warm pool) (Fig. 1.1). These conditions are exaggerated during La Niña events when the trade winds are enhanced: SST is warmer than normal in the WTP, while the ETP is cooler than normal because of intensified upwelling. The consequent westward shift of low pressure systems in the WTP contribute to drier hydroclimates in ETP, such as Ecuador and Peru; and wetter hydroclimates in the southeastern Asia and Australia. During El Niño years, the east-west SST gradient is reduced due to diminished trade wind strength. The Western Pacific Warm Pool and the low-pressure systems in the WTP spread eastward, enhancing convection in the central ETP, which leads to increased precipitation and flood events in the ETP and severe drought in the WTP.

ENSO also drives global-scale interannual temperature and precipitation variability via atmospheric and oceanic teleconnections (Ropelewski and Halpert, 1987; Vecchi and Wittenberg, 2010; Yeh et al., 2018). A teleconnection refers to the linkage between weather and climate changes occurring in widely separated regions of the globe (Stan et al., 2017). Liu and Alexander (2007) proposed that *"teleconnections enable the atmosphere to act like a "bridge" between different parts of the ocean and enable the ocean to act like a "tunnel" linking different atmospheric regions*". ENSO teleconnections influence weather and climate conditions, including extreme events, around the globe (Alexander et al., 2002; Lau and Nath, 1996; Trenberth et al., 1998): changes in SST and deep convection due to ENSO leads to changes in low-level convergence and upper-level divergence in the equatorial Pacific (Hoskins and Karoly, 1981). The anomalous horizontal component of upper-level atmospheric vorticity drives large-scale Rossby waves (giant meanders in high-altitude winds associated with pressure systems and the jet stream) propagating poleward out of the tropics. Rossby waves lead to large-scale changes in atmospheric wave and jet stream patterns in extratropics, and therefore influence temperature, precipitation, and storm tracks in both Northern and Southern Hemispheres (Horel and Wallace, 1981; Hoskins and Karoly, 1981; Karoly, 1989; Trenberth et al., 1998).

Southern California winter precipitation is closely related to ENSO on multidecadal timescales. During El Niño events, anomalously warm SSTs and enhanced deep convection occur in the ETP, producing Rossby wave propagation from the equator to the eastern North Pacific (Trenberth et al., 1998). This enhanced deep convection strengthens the AL and intensifies the North Pacific Jet – upper atmosphere winds that flow around pressure systems - shifting the jet southeastward to steer storm tracks toward Southern California. This atmospheric circulation change that results from the ENSO teleconnection brings intensified precipitation to Southern California (Jong et al., 2016; Seager et al., 2010) (Fig. 1.2A). During La Niña years, suppressed convection in the central Pacific due to lower SSTs produces a stronger and northward shifted of North Pacific High that blocks storm tracks from the North Pacific and steers moisture away from Southern California, leading to drier conditions in the region.

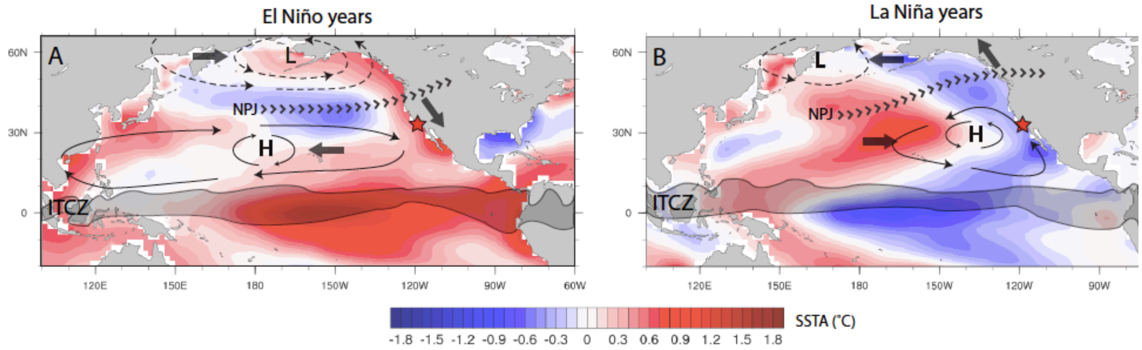

Figure 0-2 Schematic map of average SSTA (sea surface temperature anomalies), the position of atmospheric pressure systems and the North Pacific Jet (NPJ) in (A) El Niño years and (B) La Niña years. Movement direction of atmospheric circulation is indicated by arrows. The location of Santa Barbara Basin is indicated by a red star. Adapted from Du et al. (under review)

The relationship between ENSO and interannual precipitation in Southern California has been observed in historical record (Fig. 1.2B). For example, the brief, severe drought in 1976-1977 started with a strong La Niña event in the winter of 1975-1976 and ended when an extremely wet El Niño event occurred in 1978, produced the 4th wettest year in the history of California since 1895. Another example was the 1976-1977 drought lead a reduction in the California's major reservoirs of 37% –57%. The 1987-1992 drought was an extended dry period lasting 6 years. It was intensified by a strong La Niña year at 1988, and ended when a strong El Niño event occurred during the winter of 1991-1992. All 6 years were dry, and 4 of the years rank in the top ten percent in terms of least statewide runoff. The statewide reservoir storage was reduced to 40% of the average and did not return to average levels until 1994. The severe drought conditions also were associated with major wild fire damage, such as the 1991 Oakland Hills fire (PEMA, 1991). On the other hand, extreme precipitation events are closely related to El Niño years: the precipitation in the Santa Barbara county during the 1997-1998 El Niño winter was 259% of the average regional precipitation. Reservoirs in the region filled and spilled, and the consequent floods and mud slides lead to dramatic damage to agriculture and property (Santa Barbara County Flood Control and Water Conservation District). Similarly, during the 1982-1983 El Niño, large parts of Southern California received over 200% of normal rainfall and were subjected to severe flooding.

The instrumental record is both impacted by anthropogenic warming and is of insufficient duration (less than 200 years) to reveal natural interannual precipitation variability on longer timescales (e.g., multidecadal to centennial timescales), making prediction difficult. Paleoprecipitation proxy records (e.g., tree rings, marine and lake sediments) allow for us to characterize precipitation changes in Southern California prior to instrumental records. Tree ring records provide annually-resolved precipitation reconstructions, but are mostly limited to the past 2000 years or the Common Era (Cook et al., 2010; Cook et al., 2004). Long-duration and continuous lacustrine sediments from multiple lakes across Southern California have also been studied to reconstruct hydroclimate changes (Dingemans et al., 2014; Hiner et al., 2016; Kirby et al., 2015; Kirby et al., 2007; Kirby et al., 2010; Kirby et al., 2005; Kirby et al., 2019), but their sedimentation rates are insufficient to resolve interannual precipitation changes. Here, I reconstruct a high-resolution precipitation history over the last 9,000 years, using marine sediments from Santa Barbara Basin, California, to study the cause and effect of Southern California interannual precipitation variability.

Santa Barbara Basin (SBB) is located in the Southern California Bight (Fig. 1.3). The continuous, annual-scale marine sediment records preserved in SBB provide valuable material for precipitation reconstructions. During spring and summer, the northward displacement of North Pacific High leads to strong coastal upwelling, producing a greater biogenic sediment flux to SBB sediments (Thunell, 1998; Thunell et al., 1995; Warrick and Farnsworth, 2009; Warrick et al., 2008). During winter, precipitation events generate episodic sediment-laden discharge from the Santa Clara, Ventura and Santa Ynez Rivers, such that plumes of terrigenous detrital siliciclastic sediments are delivered to SBB sediments (Fig 1.3) (Nezlin et al., 2005; Warrick et al., 2007; Warrick and Farnsworth, 2009; Warrick et al., 2008). Due to the high tectonic uplift rates of Santa Ynez Mountains (>5 mm/yr) (Duvall et al., 2004; Thunell, 1998; Warrick and Mertes, 2009), sedimentation rates in SBB are unusually high (>120 cm/kyr) in SBB. Additionally, the seasonal deposition of biogenic and terrigenous detrital sediments are preserved in SBB as annual laminae (varves) because bioturbation by macrofauna is prevented by suboxic bottom water in the central basin. The continuous laminated sediment sequences spanning warm climate intervals of the late Quaternary (Behl, 1995; Schimmelmann et al., 2006) provide ideal materials for high-resolution paleoclimate reconstruction.

The terrigenous detrital siliciclastic sediment flux into SBB is mainly controlled by the amount of precipitation that falls in the catchments draining into the basin (Soutar and Crill, 1977; Warrick and Farnsworth, 2009b). Therefore, precipitation events in Southern California can be identified by high concentrations of siliciclastic elements in SBB sediments. As an immobile terrestrial element during chemical weather, Titanium is commonly used as an indicator of terrigenous detrital input in sediment (Haug et al., 2001; Wei et al., 2003). A significant correlation between regional precipitation and Ti concentration has been demonstrated using transfer function modeling (Napier and

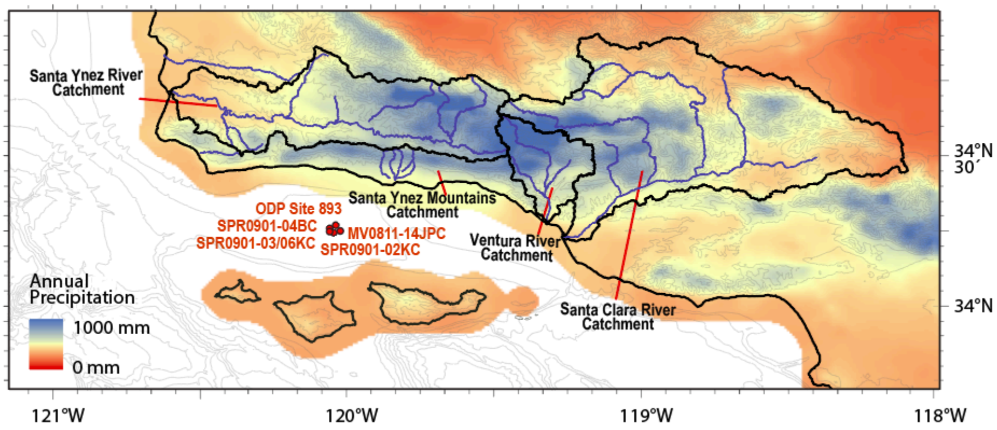

Figure 0-3 The 30-year (1981-2010) annual precipitation distribution in the coastal region of Southern California. The locations of core MV0811-14JC, core SPR0901-02KC, and ODP Site 893 in the Santa Barbara Basin (SBB) are shown. The river catchments draining into SBB are outlined by solid black lines. Elevation is shown at 200 m intervals. Precipitation data are from PRISM Climate Group, Oregon State University. Adapted from Du et al. (in preparation).

Hendy, 2016; Napier et al., 2020). Thus I use Ti concentrations determined by Scanning XRF counts as a proxy for precipitation/river runoff reconstructions in this study.

Scanning XRF is a non-destructive, semi-quantitative analysis technique that provides high-resolution elemental profiles of sediment cores (Croudace et al., 2006). The XRF analysis of major and trace elements is based on the behavior of atoms after interaction with radiation. When materials are excited with X-ray radiation, their component atoms are ionized. The X-ray radiation expels electrons from the inner orbitals of the atom, and electrons from the higher orbitals then fall into the inner orbital to fill the vacancy left behind. While the electrons are falling into the inner orbitals, energy is released as an X-ray photon - fluorescence. As the energy of the emitted photon is characteristic of a transition between specific election orbitals in a particular element, the resulting fluorescence can be used to detect the abundance of that element in the material. In contrast to traditional XRF methods which are time-consuming and acquiring gram quantities of material, the rapid and non-destructive scanning XRF method is useful for obtaining elemental information of sediment cores at high resolution (>200μm). In this study, the Ti concentration from multiple sediment cores (Table 1, Fig. 1.3) from SBB were estimated using scanning XRF counts to reconstruct the hydroclimate changes in Southern California over the Holocene.

Table 0-1 Sediment cores from Santa Barbara Basin used in this dissertation.

Core ID	Latitude/Longitude	Water depth (m)	Year collected
SPR0901-04BC	34˚ 16.90’ N, 120˚ 02.49’ W	588	2009
SPR0901-02KC	34˚16.80’ N, 120˚02.30’W	588	2009
SPR0901-03KC	34°16.91’N, 120°02.42’W	591	2009
SPR0901-06KC	34˚16.91’N, 120˚02.42’W	591	2009
MV0811-14JC	34°16.91’N, 120°02.16’W	580	2008
ODP Hole 893A	34°17.25’N, 120˚02.2′W	588	1992

This dissertation is divided into four data chapters (Chapter 2–5), and one appendix that contains information that supplements the data chapters, as well as data tables.

Chapter 2 presents an improved high-resolution radiocarbon chronology for the sediments in SBB over the last 9000 yrs. This work provides the foundation of the precipitation reconstructions used in my thesis, as accurate chronology is necessary for sediment-based paleoclimate records and enables comparisons with regional and global data time-series of similar quality. The improved chronology is based on 89 accelerator mass spectrometric (AMS) ^{14}C dates of mixed planktonic foraminiferal carbonate from three sediment cores collected in SBB (MV0811-14JC, SPR0901-06KC and ODP Hole 893A). I conducted core-to-core correlation using prominent gray flood and olive turbidite layers identified in multiple cores from SBB. The stratigraphy correlation allows for direct comparison of proxy records from multiple cores in SBB. The age of these stratigraphic markers has been estimated using the revised chronology and therefore provides a readily available robust chronology for future SBB coring efforts. A relationship between gray flood layers and mass accumulation rates was found, suggesting sediment accumulation in SBB is mainly controlled by sediment delivery via river runoff following precipitation events. Additionally, sediment slump and small olive turbidite layers identified and dated in SBB were found to be temporally linked with large earthquakes within the region and can therefore potentially used to reconstruct earthquake history in Southern California.

Chapter 3 investigates the cause of interannual precipitation variability in Southern California over the Common Era, using sub-annually resolved scanning XRF Ti counts from SBB. I analyzed the instrumental winter Pacific SST and precipitation in Southern California from 1900-2013 to demonstrate the significant correlation between Southern California precipitation and ENSO on interannual timescales via the ENSO teleconnection between the tropical Pacific and North America. I applied time series analysis to analyze the interannual precipitation variability of the reconstructed precipitation record and compared that with paleoENSO records from the tropical Pacific and reconstructions of Aleutian Low and ITCZ. The result suggests that interannual precipitation variability in Southern California is driven by changes in tropical Pacific ENSO variability and/or the strength of the ENSO teleconnection modulated by extratropical pressure systems. When the ITCZ migrated southward (1370–1540 CE) and the Aleutian Low strengthened, a robust ENSO teleconnection was produced increasing interannual precipitation variance, which was associated with longer periodicities (5–7 years). Weak interannual precipitation variance with shorter periodicity (2–3 years) was observed when the ITCZ shifted northward (700-900 CE) and/or the Aleutian Low was weak (1540-1680 CE).

Chapter 4 extends the sub-annually resolved scanning XRF Ti record over the past 9000 years, allowing me to investigate how tropical and extratropical forcing drives the interannual precipitation changes in Southern California over the Holocene. Wavelet analysis of the SBB Ti record demonstrates interannual (2–7 years) precipitation variance was relatively weak and associated with shorter intervals (2–3 years) between events prior to 4.4 ka. Interannual precipitation variance in Southern California increased after 4.4 ka, accompanied by the appearance of longer period variability (5–7 years) within the ENSO-band. The synthesis of this record and previously published proxy records suggests that a southward shift of the ITCZ in the late Holocene have amplified the interannual precipitation variance by weakening the zonal SST gradient and southeasterly trade winds across the equatorial Pacific. Meanwhile, the amplified interannual precipitation variance after 4.4 ka may due to a deeper, westward-shifted Aleutian Low which strengthened the ENSO teleconnection between the tropical Pacific and Southern California. I analyzed model simulation results (coupled ocean, atmosphere, sea ice and land surface simulations from the Community Earth System Model) to further investigate the tropical and extratropical of Southern California interannual precipitation variability. I found that compared to the early to mid-Holocene (6ka and 9ka), ENSO variability increased during the late Holocene (Pre Industrial and 3ka), along with a southward shift of ITCZ and enhanced Aleutian Low, supporting the interannual precipitation variability. These results are generally consistent with paleoproxy records.

Chapter 5 focuses on the effect of different aspects of hydroclimate change on vegetation composition and distribution in Southern California during the Holocene. A new multidecadal- to centennial-scale pollen record from SBB sediments for the last 9,000 years is compared with previously published multiproxy hydroclimate reconstructions in Southern California including SBB. Using a compilation of records, I investigate the vegetation response in the SBB catchment to different aspects of hydroclimate change (e.g., interannual precipitation variability, the frequency/amplitude of megadroughts and floods) over the Holocene. Additionally, this SBB proxy compilation is compared to terrestrial hydroclimate and pollen records across the Southern California, to identify the vegetation response to hydroclimate changes in a broader region. I found oak woodland/ chaparral/ sage scrub communities in coastal

Southern California are insensitive to interannual precipitation variability related to ENSO. On the other hand, coincident reduced mesic pollen abundance and megadrought events were observed, suggesting mortality or contraction of oak woodlands on multidecadal to centennial timescales could occur following prolonged or severe droughts.

In Chapter 6, I summarize the major findings of the dissertation, and discuss the applicability of this work and future research directions.

References

Alexander, M.A., Blade, I., Newman, M., Lanzante, J.R., Lau, N.C., Scott, J.D., 2002. The atmospheric bridge: The influence of ENSO teleconnections on air-sea interaction over the global oceans. Journal of Climate 15, 2205-2231.

Behl, R.J., 1995. 22. Sedimentary facies and sedimentology of the late Quaternary Santa Barbara Basin, Site 893. Proceedings of the Ocean Drilling Program, Scientific Results 146 (Pt. 2), 295-308.

Bjerknes, J., 1969. Atmospheric teleconnections from the equatorial Pacific. Mon Weather Rev 97, 163-172.

Cook, E.R., Seager, R., Heim, R.R., Vose, R.S., Herweijer, C., Woodhouse, C., 2010. Megadroughts in North America: placing IPCC projections of hydroclimatic change in a long-term palaeoclimate context. Journal of Quaternary Science 25, 48-61.

Cook, E.R., Woodhouse, C.A., Eakin, C.M., Meko, D.H., Stahle, D.W., 2004. Long-term aridity changes in the western United States. Science 306, 1015-1018.

Dettinger, M.D., Cayan, D.R., Diaz, H.F., Meko, D.M., 1998. North-south precipitation patterns in western North America on interannual-to-decadal timescales. Journal of Climate 11, 3095-3111.

Dettinger, M.D., Ralph, F.M., Das, T., Neiman, P.J., Cayan, D.R., 2011. Atmospheric Rivers, Floods and the Water Resources of California. Water 3, 445-478.

Dingemans, T., Mensing, S.A., Feakins, S.J., Kirby, M.E., Zimmerman, S.R.H., 2014. 3000 years of environmental change at Zaca Lake, California, USA. Frontiers in Ecology and Evolution 2.

Duvall, A., Kirby, E., Burbank, D., 2004. Tectonic and lithologic controls on bedrock channel profiles and processes in coastal California. J Geophys Res-Earth 109.

Haston, L., Michaelsen, J., 1997. Spatial and temporal variability of southern California precipitation over the last 400 yr and relationships to atmospheric circulation patterns. Journal of Climate 10, 1836-1852.

Haug, G.H., Hughen, K.A., Sigman, D.M., Peterson, L.C., Rohl, U., 2001. Southward migration of the intertropical convergence zone through the Holocene. Science 293, 1304-1308.

Hiner, C.A., Kirby, M.E., Bonuso, N., Patterson, W.P., Palermo, J., Silveira, E., 2016. Late Holocene hydroclimatic variability linked to Pacific forcing: evidence from Abbott Lake, coastal central California. Journal of Paleolimnology 56, 299-313.

Horel, J.D., Wallace, J.M., 1981. Planetary-Scale Atmospheric Phenomena Associated with the Southern Oscillation. Mon Weather Rev 109, 813-829.

Hoskins, B.J., Karoly, D.J., 1981. The Steady Linear Response of a Spherical Atmosphere to Thermal and Orographic Forcing. J Atmos Sci 38, 1179-1196.

Jong, B.T., Ting, M.F., Seager, R., 2016. El Nino's impact on California precipitation: seasonality, regionality, and El Nino intensity. Environmental Research Letters 11.

Karoly, D.J., 1989. Southern-Hemisphere Circulation Features Associated with Elnino - Southern Oscillation Events. Journal of Climate 2, 1239-1252.

Kenyon, K.E., 1999. North Pacific High: an hypothesis. Atmos Res 51, 15-34.

Kim, H.-M., Zhou, Y., Alexander, M.A., 2017. Changes in atmospheric rivers and moisture transport over the Northeast Pacific and western North America in response to ENSO diversity. Climate Dynamics.

Kirby, M.E., Knell, E.J., Anderson, W.T., Lachniet, M.S., Palermo, J., Eeg, H., Lucero, R., Murrieta, R., Arevalo, A., Silveira, E., Hiner, C.A., 2015. Evidence for insolation and Pacific forcing of late glacial through Holocene climate in the Central Mojave Desert (Silver Lake, CA). Quaternary Research 84, 174-186.

Kirby, M.E., Lund, S.P., Anderson, M.A., Bird, B.W., 2007. Insolation forcing of Holocene climate change in Southern California: A sediment study from Lake Elsinore. Journal of Paleolimnology 38, 395-417.

Kirby, M.E., Lund, S.P., Patterson, W.P., Anderson, M.A., Bird, B.W., Ivanovici, L., Monarrez, P., Nielsen, S., 2010. A Holocene record of Pacific Decadal Oscillation (PDO)-related hydrologic variability in Southern California (Lake Elsinore, CA). Journal of Paleolimnology 44, 819-839.

Kirby, M.E., Lund, S.P., Poulsen, C.J., 2005. Hydrologic variability and the onset of modern El Niño-Southern Oscillation: A 19 250-year record from Lake Elsinore, southern California. Journal of Quaternary Science 20, 239-254.

Kirby, M.E.C., Patterson, W.P., Lachniet, M., Noblet, J.A., Anderson, M.A., Nichols, K., Avila, J., 2019. Pacific Southwest United States Holocene Droughts and Pluvials Inferred From Sediment delta O-18((calcite)) and Grain Size Data (Lake Elsinore, California). Front Earth Sc-Switz 7.

Lau, N.C., Nath, M.J., 1996. The role of the "atmospheric bridge" in linking tropical Pacific ENSO events to extratropical SST anomalies. Journal of Climate 9, 2036-2057.

Liu, Z.Y., Alexander, M., 2007. Atmospheric bridge, oceanic tunnel, and global climatic teleconnections. Reviews of Geophysics 45.

Napier, T.J., Hendy, I.L., 2016. The impact of hydroclimate and dam construction on terrigenous detrital sediment composition in a 250-year Santa Barbara Basin record off southern California. Quaternary International.

Napier, T.J., Hendy, I.L., Fahnestock, M.F., Bryce, J.G., 2020. Provenance of detrital sediments in Santa Barbara Basin, California, USA: Changes in source contributions between the Last Glacial Maximum and Holocene. Geol Soc Am Bull 132, 65-84.

Nezlin, N.P., DiGiacomo, P.M., Stein, E.D., Ackerman, D., 2005. Stormwater runoff plumes observed by SeaWiFS radiometer in the Southern California Bight. Remote Sensing of Environment 98, 494-510.

Nezlin, N.P., Stein, E.D., 2005. Spatial and temporal patterns of remotely-sensed and field-measured rainfall in southern California. Remote Sensing of Environment 96, 228-245.

Ropelewski, C.F., Halpert, M.S., 1987. Global and Regional Scale Precipitation Patterns Associated with the El-Nino Southern Oscillation. Mon Weather Rev 115, 1606-1626.

Schimmelmann, A., Lange, C.B., Roark, E.B., Ingram, B.L., 2006. Resources for paleoceanographic and paleoclimatic analysis: A 6,700-year stratigraphy and regional radiocarbon reservoir-age (ΔR) record based on varve counting and 14C-AMS dating for the Santa Barbara Basin, offshore California, U.S.A. Journal of Sedimentary Research 76, 74-80.

Seager, R., Naik, N., Ting, M., Cane, M.A., Harnik, N., Kushnir, Y., 2010. Adjustment of the atmospheric circulation to tropical Pacific SST anomalies: Variability of transient eddy propagation in the Pacific-North America sector. Q J Roy Meteor Soc 136, 277-296.

Stan, C., Straus, D.M., Frederiksen, J.S., Lin, H., Maloney, E.D., Schumacher, C., 2017. Review of Tropical-Extratropical Teleconnections on Intraseasonal Time Scales. Reviews of Geophysics 55, 902-937.

Thunell, R.C., 1998. Particle fluxes in a coastal upwelling zone: Sediment trap results from Santa Barbara Basin, California. Deep-Sea Research Part II: Topical Studies in Oceanography 45, 1863-1884.

Thunell, R.C., Tappa, E., Anderson, D.M., 1995. Sediment Fluxes and Varve Formation in Santa-Barbara Basin, Offshore California. Geology 23, 1083-1086.

Trenberth, K.E., Branstator, G.W., Karoly, D., Kumar, A., Lau, N.C., Ropelewski, C., 1998. Progress during TOGA in understanding and modeling global teleconnections associated with tropical sea surface temperatures. J Geophys Res-Oceans 103, 14291-14324.

Vecchi, G.A., Wittenberg, A.T., 2010. El Nino and our future climate: where do we stand? Wires Clim Change 1, 260-270.

Wang, C.Z., Fiedler, P.C., 2006. ENSO variability and the eastern tropical Pacific: A review. Prog Oceanogr 69, 239-266.

Warrick, J.A., DiGiacomo, P.M., Weisberg, S.B., Nezlin, N.P., Mengel, M., Jones, B.H., Ohlmann, J.C., Washburn, L., Terrill, E.J., Farnsworth, K.L., 2007. River plume patterns and dynamics within the Southern California Bight. Cont Shelf Res 27, 2427-2448.

Warrick, J.A., Farnsworth, K.L., 2009. Dispersal of river sediment in the Southern California Bight. Geol Soc Am Spec Pap 454, 53-67.

Warrick, J.A., Mertes, L.A.K., 2009. Sediment yield from the tectonically active semiarid Western Transverse Ranges of California. Geol Soc Am Bull 121, 1054-1070.

Warrick, J.A., Xu, J.P., Noble, M.A., Lee, H.J., 2008. Rapid formation of hyperpycnal sediment gravity currents offshore of a semiarid California river. Cont Shelf Res 28, 991-1009.

Wei, G.J., Liu, Y., Li, X.H., Shao, L., Liang, X.R., 2003. Climatic impact on Al, K, Sc and Ti in marine sediments: Evidence from ODP Site 1144, South China Sea. Geochem J 37, 593-602.

Yeh, S.W., Cai, W.J., Min, S.K., McPhaden, M.J., Dommenget, D., Dewitte, B., Collins, M., Ashok, K., An, S.I., Yim, B.Y., Kug, J.S., 2018. ENSO Atmospheric Teleconnections and Their Response to Greenhouse Gas Forcing. Reviews of Geophysics 56, 185-206.

Chapter 2

A 9000-Year Flood History for Southern California: A Revised Stratigraphy of Varved Sediments in Santa Barbara Basin

Abstract

The center of Santa Barbara Basin (SBB) preserves annual laminations through most of the Holocene providing an important locality for high-resolution late Quaternary paleoclimate and paleoceanography reconstructions. An accurate chronology is necessary for these sediment-based records and enables comparisons with more distal data time-series of similar quality. Here we present an improved high-resolution radiocarbon chronology for the last 9000 yrs based on 89 accelerator mass spectrometric (AMS) ^{14}C dates of mixed planktonic foraminiferal carbonate from three sediment cores collected in SBB (MV0811-14JC, SPR0901-06KC and ODP Hole 893A). Accurate core-to-core correlation is demonstrated using prominent gray flood and olive turbidite layers identified in SBB and dated in multiple cores. Gray layer deposits were found more frequently in wetter intervals as determined by multi-proxy hydroclimate records in Southern California (e.g., lake deposits and tree rings). Mass accumulation rates (MARs) calculated for the SBB depocenter using the improved radiocarbon age model indicate high MARs are associated with these gray layers that have been associated with floods. Thus sediment accumulation in SBB is largely controlled by sediment delivery *via* river runoff following precipitation events although MARs may also be influenced by other factors that enhance erosion in river catchments. Folded sediment is observed within the basal core section of MV0811-14JC which stratigraphically correlates with ^{14}C age reversals in ODP Hole 893A. We associate this sediment slump feature with the large Goleta submarine slide complex in Santa Barbara Channel and estimate the submarine slide event occurred at ~ 9000 ± 200 yrs BP. Furthermore, small olive turbidite layers identified and dated in SBB can be temporally linked with large earthquakes along San

Andreas Fault and can therefore potentially reconstruct earthquake history in Southern California.

2.1 Introduction

The study of Holocene paleoclimate is crucial for understanding climate variability from millennial to interannual time scales (Mayewski et al., 2004; Wanner et al., 2008). The sediment record at the depocenter of Santa Barbara Basin (SBB) offshore of Southern California has been the basis of several paleoclimate and paleoceanography reconstructions (e.g. Lange et al., 1987; Kennett and Venz, 1995; Heusser, 1998; Schimmelmann et al., 2006). The predominantly annually laminated sediment record in SBB during the Holocene has the potential to resolve decadal and even interannual-to-annual paleoenvironmental and paleoceanographic changes (Weinheimer and Cayan, 1997; Hendy et al., 2015). However, an accurate chronology is needed to provide a time scale for SBB sediments and is essential for detailed comparisons with other paleoclimatic and paleoceanographic records.

Numerous investigations of SBB sediments chronology have taken place over the past 40 yrs. Soutar and Crill (1977) developed a chronology for 19th and 20th century SBB sediment based on annual layer/lamination or varve counting and ^{210}Pb dating. The establishment of a precise varve chronology and core-to-core correlation for the 19th century was followed by a detailed description of the ODP Hole 893A (34˚17.25'N 120˚02.2'W) varve stratigraphy (Lange and Schimmelmann, 1995). Additionally a number of AMS ^{14}C dates have been produced using mixed planktonic foraminiferal carbonate from ODP Hole 893A samples with 31 dates from the Holocene (Ingram and Kennett, 1995; Roark et al., 2003). Schimmelmann et al. (2006) expanded the chronology of partially varved sediment to the past 6700 yrs using piston core 6P based on varve counting and ^{14}C-AMS dating. However, disagreements were found when comparing the traditional varve-count-based chronology to independent ^{14}C dates of planktonic foraminifera in multiple cores (Schimmelmann et al., 2006; Fisler and Hendy, 2008).

The discrepancy between SBB varve and ^{14}C chronologies may be explained by variations in the radiocarbon reservoir age of the regional surface ocean water and/or undercounting of annual layers in the varve chronology. Loss of varves (under-counting of absolute years) could be caused by erosion of varves and/or laminations being not consistently produced during drought intervals (Schimmelmann et al., 2006; Hendy et al., 2013; Schimmelmann et al., 2013). To resolve these issues a new high-resolution ~2000-yr chronology was developed using a combination of organic carbon ^{14}C dates from terrestrial floral macrofossils such as seeds, leaves, charcoal, and twigs and closely sampled planktonic foraminiferal carbonate ^{14}C dates (Hendy et al., 2013). Age differences between the ^{14}C planktonic foraminiferal carbonate and terrestrial organic carbon chronologies revealed variable reservoir ages (ΔR) while increasing offset between the ^{14}C and varve chronologies indicated a cumulative varve count error through the last 2000 yrs. Hendy et al. (2013) produced an improved chronology for SBB sediments with a variable ΔR applied to 49 mixed planktonic foraminiferal carbonate ^{14}C dates, however the chronology does not extend through the remainder of the Holocene.

Here we extend the high-resolution 2000-yr ^{14}C SBB chronology (Hendy et al., 2013) to 9000 yrs BP (Before Present or before 1950 AD). Fifty new mixed planktonic foraminiferal carbonate ^{14}C dates were produced from jumbo piston core MV0811-14JC. In addition, we created a stratigraphy of 'instantaneous' gray flood and olive turbidite layers in SBB based on highly resolved imaging of core MV0811-14JC. We then employed this stratigraphy to correlate MV0811-14JC with ODP Site 893 and SPR0901-06KC such that the planktonic foraminiferal carbonate ^{14}C dates from these cores could be incorporated into a new master chronology for SBB sediments. Our new chronology is applied to the dated stratigraphic pattern of gray and olive layers and therefore can be applied to any future newly acquired SBB sediment cores to provide an easily accessible chronology for forthcoming paleoclimate studies. Finally we relate the gray flood and olive turbidite layers to regional paleoclimate reconstructions and tectonic activity.

2.2 Regional setting of SBB

Located off the southern coast of California, SBB is a tectonic depression representing the submerged southwestern part of the Transverse Ranges Province (Fig. 2.1). Late Quaternary sediments deposited in SBB are mostly composed of laminae couplets including biogenic (e.g., diatoms, radiolaria, planktonic and benthic foraminifera) and terrigenous sediments (Fleischer, 1972; Kolpack and Drake, 1984; Kennett and Venz, 1995; Rack and Merrill, 1995). Terrigenous sediments are delivered to SBB by rivers and streams (the Santa Clara and Ventura rivers and the Santa Ynez

Mountains). The rivers and streams drain the tectonically active Western Transverse Ranges that are uplifting at rate of <5 mm/yr (Duvall et al., 2004) producing an unusually high sedimentation rate (Thunell, 1998; Romans et al., 2009; Warrick and Mertes, 2009).

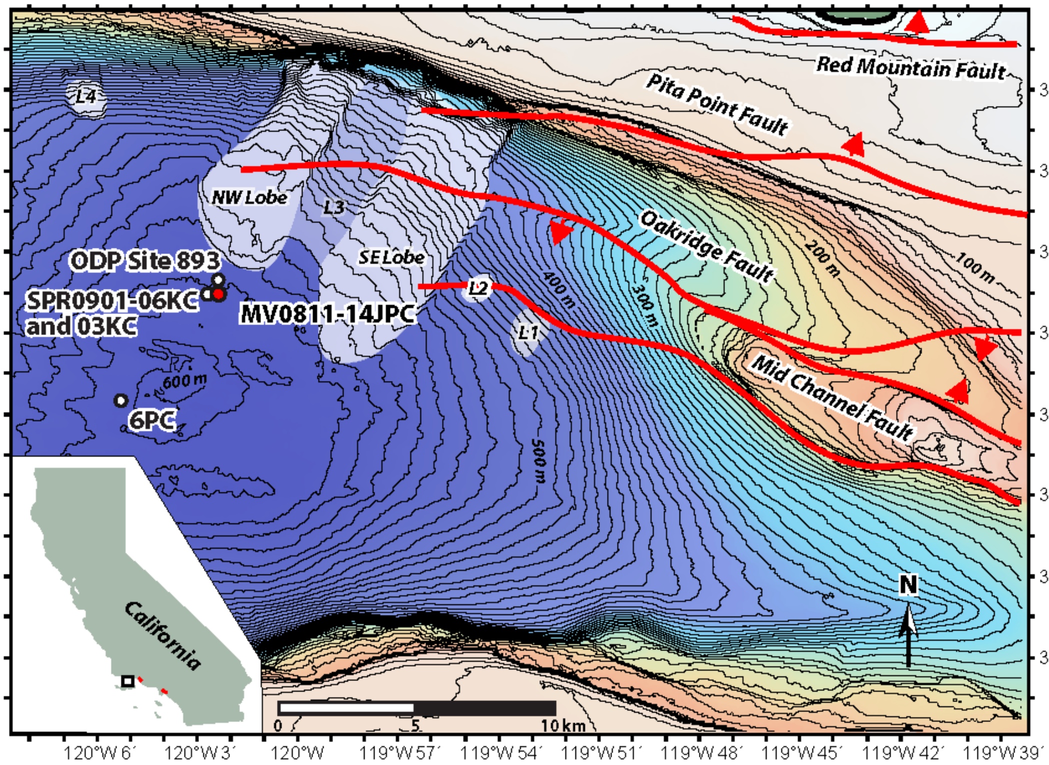

Figure 0-1 Map of Santa Barbara Basin displaying the location of cores MV0811-14JC (filled red circle) ODP site 893 SPR0901-06KC 03KC and 6PC. Gray shading indicates the location of underwater slides denoted by the lettered numbers L1-4: L3 is the Goleta landslide complex and L4 is the Gaviota mudslide. The Goleta landslide complex includes two main surficial lobes: the northwest (NW) lobe and the southeast (SE) lobe (Fisher et al. 2005). Red lines show fault lines with arrows indicating direction of movement (adapted from Heck 1998; Marshall 2017). Bathymetric lines are 10 m apart with 100 m intervals marked by thick lines. paleoseismological record locations are shown as red dots on the inset figure (from north to south: Pitas Point, Ventura, Los Angeles Basin and Seal Beach salt marsh).

Southern California has a semiarid Mediterranean climate with cool winters and hot dry summers. Terrigenous material is delivered to SBB during winter precipitation events resulting in detrital siliciclastic sedimentation (dark laminae in X-radiographs) (Warrick et al., 2007) while biogenic sedimentation (light laminae in X-radiographs) occurs during the highly productive spring and summer seasons (Hülsemann and Emery, 1961). The northward migration of the North Pacific High Pressure System during the spring season positions strong northerly winds over the California coast and causes intense coastal upwelling (Lynn and Simpson, 1987). This imports nutrients into the photic zone and drives high regional biological productivity and the deposition of biogenic laminae. Suboxic bottom water in the deep center of the SBB renders the seafloor inhospitable to benthic macrofauna and prevents bioturbation allowing the seasonal variations in sedimentation to be preserved as annual laminae couplets (Behl, 1995; Schimmelmann et al., 2016). Thus the production and preservation of annual laminations provide the scientific basis for a varve chronology in SBB.

2.3 Methods

2.3.1 Radiocarbon dating

Samples two cm in thickness were collected at ~20 cm intervals over a total length of 980 cm from jumbo piston core MV0811-14JC (34˚ 16.906'N 120˚ 02.162'W; 580 m water depth; Fig. 2.1). Sediment samples were oven-dried, washed and wet sieved to retain the >63 µm size fraction. Mixed planktonic foraminifera primarily consisting of *Globigerina bulloides* and *Neogloboquadrina incompta* were picked from the >150 µm size fraction in each sediment sample to generate 50 carbonate ^{14}C dates (Table 1). Following standard methods, approximately 11 mg of foraminiferal shells were first leached in dilute HCl, then rinsed using Milli-Q water, dried and hydrolyzed using 85 % phosphoric acid to produce CO_2 (Beverly et al., 2010). The resulting CO_2 was extracted, purified and graphitized using vacuum lines with H_2 gas and iron catalyst powder. Both pre-treatment and high-precision accelerator mass spectrometry (AMS) dating were performed at the Keck Carbon Cycle Accelerator Mass Spectrometer at the University of California Irvine.

2.3.2 Age-depth model

Gray and massive olive layers were logged in cores MV0811-14JC, SPR0901-06KC (34°16.914N 120°02.419W; 591 m water depth) and ODP Hole 893A (34˚17.25'N 120˚02.2'W; 588 m water depth) to create a master stratigraphy. Since flood layers and turbidites represent 'instantaneous' sedimentary events (Hendy et al., 2013; Schimmelmann et al., 2013) the thicknesses of the gray and olive layers were subtracted from the original core to create a corrected depth scale that incorporates only regular background sedimentation (typically laminated) (Table 1). The gray and olive layers were then used as stratigraphic tie points to correlate SPR0901-06KC and ODP Hole 893A depths to the MV0811-14JC depth scale (Table 2). A new composite corrected depth scale was generated so that the 49 ^{14}C dates from SPR0901-06KC (Hendy et al., 2013) and the 10 ^{14}C dates from core ODP Hole 893A (Roark et al., 2003) could be combined with the 50 MV0811-14JC ^{14}C dates.

An age-depth model from 46 to 9066 yrs BP was generated using the software BACON2.2 (Blaauw and Christen, 2011). BACON uses Bayesian statistics to reconstruct

Table 2.0-1 Raw radiocarbon dates (yrs BP) for planktonic foraminifera samples (with age uncertainties), uncorrected depth in core, depth corrected for instantaneous event thickness, calibrated ages (Cal yrs. BP) and 1 sigma range of calibrated ages (Cal yrs. BP). The calibrated age and 1 sigma range are calculated using CALIB 7.1 radiocarbon calibration program.

Sample name (Core, section, interval/cm)	Uncorrected depth (cm below core top)	Corrected depth (cm below core top)	Raw 14C age (yrs)	Error (± yrs)	Calibrated age (Cal years)
MV0811-14JC-					
Sec1, 33-34*	33.0	23.2	2500	30	1979
Sec1, 49-50.5	49.0	35.9	2645	15	2161
Sec1, 58-60	58.0	40.8	2680	15	2200
Sec1, 68-70	68.0	48.9	2745	15	2271
Sec1, 80-81	80.0	57.9	2915	30	2507
Sec2, 15-16	100.0	70.6	2990	35	2585
Sec2, 114-116	114.0	84.4	3135	15	2768
Sec2, 58-59	143.0	98.6	3325	30	2977
Sec2, 154-156	154.0	102.2	3415	15	3093
Sec2, 174-176	174.0	116.2	3460	15	3154
Sec2, 182.5-185.5	182.5	122.0	3590	15	3313
Sec2, 204-205	204.0	136.6	3780	15	3535
Sec2, 124*	209.0	141.6	3515	30	3225
Sec2, 214-216	214.0	146.6	3915	15	3706
Sec3, 13-14*	241.0	166.9	4115	30	3969
Sec3, 242-244	242.0	167.9	4085	15	3928
Sec3, 282-284	282.0	188.9	4225	20	4119
Sec3, 65-66	293.0	199.8	4315	30	4245
Sec3, 304-306	304.0	208.3	4365	15	4310
Sec3, 332-334	332.0	222.3	4475	15	4463
Sec3, 362-364	362.0	244.8	4670	15	4712
Sec3, 135	363.0	245.8	4670	35	4710
Sec3, 382-384	382.0	264.8	4810	15	4901
Sec4, 12-14	391.0	276.8	4995	15	5141
Sec4, 32-34	411.0	294.4	5170	20	5379
Sec4, 72-74	451.0	312.5	5230	15	5440
Sec4, 91-93	470.0	328.4	5400	15	5618

Sec4, 112-114	491.0	349.2	5585	20	5806
Sec4, 132-134	511.0	369.2	5760	20	6017
Sec5, 12-14	509.5	382.3	5965	15	6235
Sec6, 14-16	539.3	397.6	6195	15	6470
Sec6, 36-38	561.3	415.7	6415	15	6723
Sec6, 45-47	570.3	424.3	6450	15	6764
Sec6, 55-57	580.3	430.6	6515	20	6839
Sec6, 74-76	599.3	438.6	6570	20	6908
Sec6, 93-95	618.3	455.9	6710	20	7076
Sec6, 104-106	629.3	466.9	6815	20	7196
Sec6, 135-137*	660.3	479.2	7055	20	7418
Sec7, 4-6*	676.5	492.9	6955	20	7331
Sec7, 4-6*	676.5	492.9	6750	15	7121
Sec7, 24-26	696.5	512.9	7155	20	7502
Sec7, 44-46	716.5	525.5	7420	15	7738
Sec7, 64-66	736.5	541.7	7590	15	7901
Sec7, 86-88	758.5	562.3	7750	15	8064
Sec7, 106-108	778.5	582.3	7995	20	8310
Sec7, 126-128	798.5	600.7	8105	20	8422
Sec7, 146-148	818.5	616.5	8260	20	8586
Sec8, 8-10	830.5	625.7	8260	15	8586
Sec8, 26-28	848.5	641.2	8445	15	8843
Sec8, 47-49	869.5	656.7	8555	20	9009
146-893A-					
2H-05, 146-148	NA	NA	8860	50	9373
2H-06, 48-51	NA	NA	8950	100	9465
2H-06, 55-57	NA	NA	8680	80	9168
2H-06, 55-57B	NA	NA	9040	160	9599
2H-06, 73-75	NA	NA	8880	60	9392
2H-06, 76-79	NA	NA	9610	70	10325
2H-06, 93-95	NA	NA	8600	60	9071

* Dates not included in the age model.

coherent accumulation histories for deposits by combining radiocarbon dates with known sedimentary information (Blaauw and Christen, 2011) (Fig. 2.2). In this age model ^{14}C dates from cores SPR0901-06KC (Hendy et al., 2013) MV0811-14JC and ODP Hole 893A (Roark et al., 2003) were converted to calendar ages using the Marine13 calibration curves (Reimer et al., 2013). A variable reservoir age was applied to ages younger than 2000 yrs BP where constraints were available (Hendy et al., 2013). Beyond 2000 yrs BP a constant ΔR of 147 ± 70 yrs was applied based on an estimate from the last constrained surface ocean reservoir age (Hendy et al., 2013). Eleven out of 49 ^{14}C ages from

SPR0901-06KC, 6 out of 50 MV0811-14JC ^{14}C dates, and 3 out of 10 from core ODP Hole 893A (indicated as open symbols in Fig. 2.3) fell outside the age-depth line and were not used in this age model.

The ^{14}C plateaus during the last 300 yrs preclude good calendar year calibration

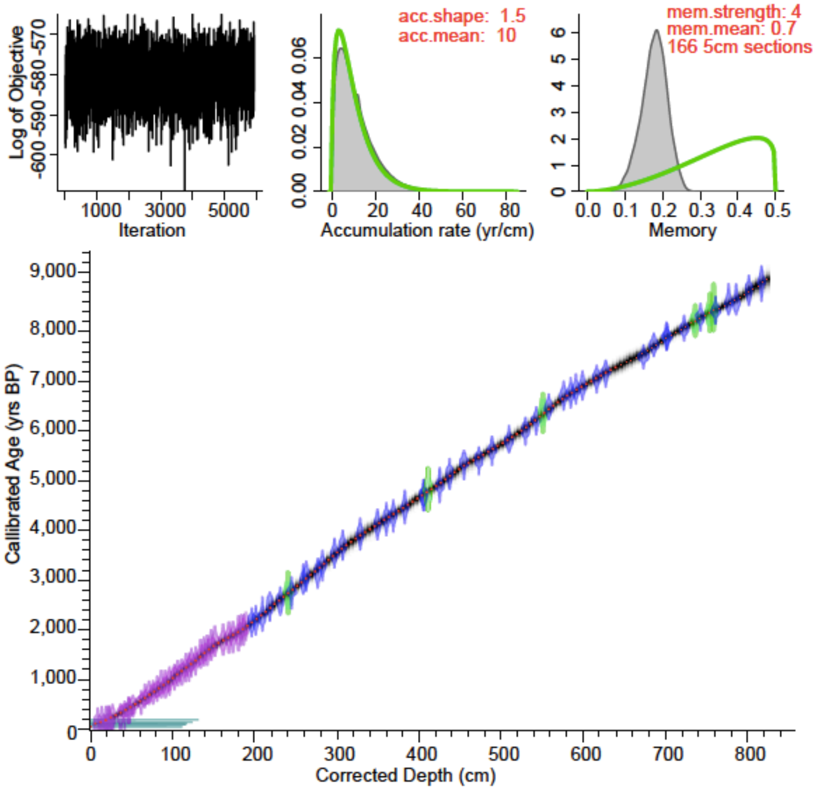

Figure 0-2 BACON 2.2 output graph showing calibrated ^{14}C dates from MV0811-14JC (blue envelopes) SPR0901-06KC (purple) and ODP Hole 893A (green) and the age-depth model (gray shading indicates probability within the 95 % confidence interval with darkness indicating greater probability; red curve shows single 'best' model based on the weighted mean age for each depth).

of ^{14}C dates in the youngest sediment sequence. Instead, previously published varve chronology data were employed after correlating stratigraphic marker layers between cores. These marker layers were previously identified in other box and kasten core studies (Schimmelmann et al., 1992; Hendy et al., 2013) and include: the coretop (AD 1905), a gray layer at AD 1861-62, the *Macoma* layer at AD 1841, a turbidite at AD 1811 and a gray layer at AD 1761. Radiocarbon

dates were employed downcore of the AD 1761 gray layer (Table 3). Radiocarbon dates were not incorporated in the age model if they were associated with gray or olive layers or if they demonstrated stratigraphic inversion. Thus 89 ^{14}C total dates from the three sediment cores and five calendar ages were used in the Bayesian statistics of BACON 2.2 (Blaauw and Christen, 2011) to generate a new age model spanning the Holocene in SBB (Fig. 2.2). Sedimentation rates (SR in mm yr^{-1}) were calculated every 5 cm from the BACON 2.2 generated age model. Bulk mass accumulation rates (MAR in g cm^{-2} ka^{-1}) were calculated as the product of SR and dry bulk density (DBD in g cm^{-3}). Dry bulk density was generated using:

$$DBD = (1 - P/100) \times \rho$$

where P is porosity and ρ is density.

2.3.3 Bulk elemental analysis

Core MV0811-14JC was sampled at a variable spacing of 2-10 cm to generate 10 cm^3 bulk samples for elemental analyses. Samples were freeze dried, powdered and digested with hydrofluoric, nitric, perchloric and hydrochloric acids. Inductively coupled plasma-mass spectrometry (ICP-MS) and inductively coupled plasma-atomic emission spectroscopy (ICP-AES) were used to determine the elemental concentrations of major minor and trace element at ALS Laboratories in Vancouver Canada. The standard errors (1 st. err.) of measurements of lab standards GBM908-10 and MRGeo08 are ±0.06 and ±0.03 % for calcium (Ca) and are ±0.01 % and ±0.01 % for titanium (Ti).

2.4. Results

2.4.1 Radiocarbon chronology

In Figure 4 the mixed planktonic foraminiferal ^{14}C dates of core MV0811-14JC (Table 2.1) are plotted against a depth scale that has not been corrected for instantaneous sedimentation events in SBB. Dates generally exhibit increasing age with depth except those associated with instantaneous sedimentary structures. The trend of increasing age with depth weakens when dates straddle gray or olive layers. For example the section of MV0811-14JC between ~410 and 450 cmbct (cm below core top) contains three gray layers and two olive layers and the ^{14}C dates indicate that 40 cm of sediment was deposited in ~60 yrs (sedimentation rate is ~ 1.5 yr cm^{-1}).

However, for segments without instantaneous sedimentary events such as between ~490 and 510 cmbct the sedimentation rate is ~8.7 yr cm^{-1}.

Table 0-2 BACON 2.2 input used in the age model construction

Lab ID	Age	Error	Depth	Mean reservoir age (yrs)	1 standard deviation error
Varve_1.01	45	0	0.1	0	0
Varve_4.01	89	0	3.8	0	0
Varve_7.99	109	0	5.8	0	0
Varve_7.100	139	0	12.6	0	0
Varve_21.44	189	0	19.8	0	0
SPR09-06KC 10	790	45	8.8	304	70
SPR09-06KC 15	860	30	13.8	319	70
SPR09-06KC 20	890	30	18.8	343	70
SPR09-06KC 25	885	30	21.8	346	70
SPR09-06KC 31	885	30	22.8	347	70
SPR09-06KC 35	955	30	26.8	347	70
SPR09-06KC 45	985	30	36.8	347	70
SPR09-06KC 50	1075	30	41.8	347	70
SPR09-06KC 55	1110	30	46.8	336	70
SPR09-06KC 59	1100	30	46.8	336	70
SPR09-06KC 65	1175	30	51.8	323	70
SPR09-06KC 75	1250	30	61.8	297	70
SPR09-06KC 80	1345	30	66.3	285	70
SPR09-06KC 85	1425	30	71.3	272	70
SPR09-06KC 95	1425	30	76.3	259	70
SPR09-06KC 100	1505	30	81.3	246	70
SPR09-06KC 105	1570	30	86.3	233	70
SPR09-06KC 115	1555	30	91.3	219	70
SPR09-06KC 120	1620	30	96.3	206	70
SPR09-06KC 126	1705	30	102.3	191	70
SPR09-06KC 130	1755	35	106.3	180	70
SPR09-06KC 135	1765	30	111.3	167	70
SPR09-06KC 140	1845	30	116.1	154	70
SPR09-06KC 145	1850	30	120.1	144	70
SPR09-06KC 155	1925	35	123.1	136	70
SPR09-06KC 160	1930	30	128.1	123	70
SPR09-06KC 166	2030	35	134.1	107	70
SPR09-06KC 170	2080	30	138.1	97	70
SPR09-06KC 175	2100	30	142.1	86	70
SPR09-06KC 180	2195	30	147.1	73	70
SPR09-06KC 185	2245	30	151.6	74	70
SPR09-06KC 199	2280	30	161.6	89	70
SPR09-06KC 206	2345	30	168.6	99	70
SPR09-06KC 211	2365	30	173.6	107	70
SPR09-06KC 240	2410	35	180.24	118	70

SPR09-06KC 245	2475	30	183.46	125	70
SPR09-06KC 250	2495	30	186.7	133	70
SPR09-06KC 254	2580	30	189.28	139	70
MV0811-14JC-1 49	2645	15	196.44	147	70
MV0811-14JC-1 58	2680	15	201.34	147	70
MV0811-14JC-1 68	2745	15	209.44	147	70
MV0811-14JC-1 80	2915	30	218.5	147	70
MV0811-14JC-2 15	2990	35	231.2	147	70
893A-1H-04 30	3130	80	240.794	147	70
MV0811-14JC-2 114	3135	15	244.98	147	70
MV0811-14JC-2 58	3325	30	259.18	147	70
MV0811-14JC-2 154	3415	15	262.78	147	70
MV0811-14JC-2 174	3460	15	276.74	147	70
MV0811-14JC-2 182.5	3590	15	282.56	147	70
MV0811-14JC-2 204	3780	15	297.22	147	70
MV0811-14JC-2 214	3915	15	307.22	147	70
MV0811-14JC-3 242	4085	15	328.48	147	70
MV0811-14JC-3 282	4225	20	349.48	147	70
MV0811-14JC-3 65	4315	30	360.42	147	70
MV0811-14JC-3 304	4365	15	368.86	147	70
MV0811-14JC-3 332	4475	15	382.84	147	70
MV0811-14JC-3 362	4670	15	405.34	147	70
MV0811-14JC-3 135	4670	35	406.34	147	70
893A-2H-01 55B	4740	70	411.095	147	70
MV0811-14JC-3 382	4810	15	425.34	147	70
MV0811-14JC-4 12	4995	15	437.38	147	70
MV0811-14JC-4 32	5170	20	454.94	147	70
MV0811-14JC-4 72	5230	15	473.1	147	70
MV0811-14JC-4 91	5400	15	489	147	70
MV0811-14JC-4 112	5585	20	509.74	147	70
MV0811-14JC-4 132	5760	20	529.74	147	70
MV0811-14JC-5 12	5965	15	542.9	147	70
893A-2H-02 71	6100	90	550.926	147	70
MV0811-14JC-6 14	6195	15	558.14	147	70
MV0811-14JC-6 36	6415	15	576.32	147	70
MV0811-14JC-6 45	6450	15	584.92	147	70
MV0811-14JC-6 55	6515	20	591.18	147	70
MV0811-14JC-6 74	6570	20	599.22	147	70
MV0811-14JC-6 93	6710	20	616.5	147	70
MV0811-14JC-6 104	6815	20	627.5	147	70
MV0811-14JC-7 24	7155	20	673.48	147	70
MV0811-14JC-7 44	7420	15	686.06	147	70
893A-2H-04 18	7600	50	701.42	147	70

MV0811-14JC-7 64	7590	15	702.32	147	70
MV0811-14JC-7 86	7750	15	722.92	147	70
893A-2H-04 68	7910	70	736.495	147	70
MV0811-14JC-7 106	7995	20	742.92	147	70
893A-2H-04 93	8060	80	754.232	147	70
893A-2H-04 105B	8120	110	758.859	147	70
MV0811-14JC-7 126	8105	20	761.26	147	70
MV0811-14JC-7 146	8260	20	777.1	147	70
MV0811-14JC-8 8	8260	15	786.32	147	70
MV0811-14JC-8 26	8445	15	801.82	147	70
MV0811-14JC-8 47	8555	20	817.24	147	70

Radiocarbon dating in MV0811-14JC was not undertaken beyond 870 cmbct (~60 cm depth in MV0811-14JC-sec 8) due to evidence of core disturbance (e.g., observed folds in laminations). This segment of MV0811-14JC corresponds to ~145 to 150 cmbct in

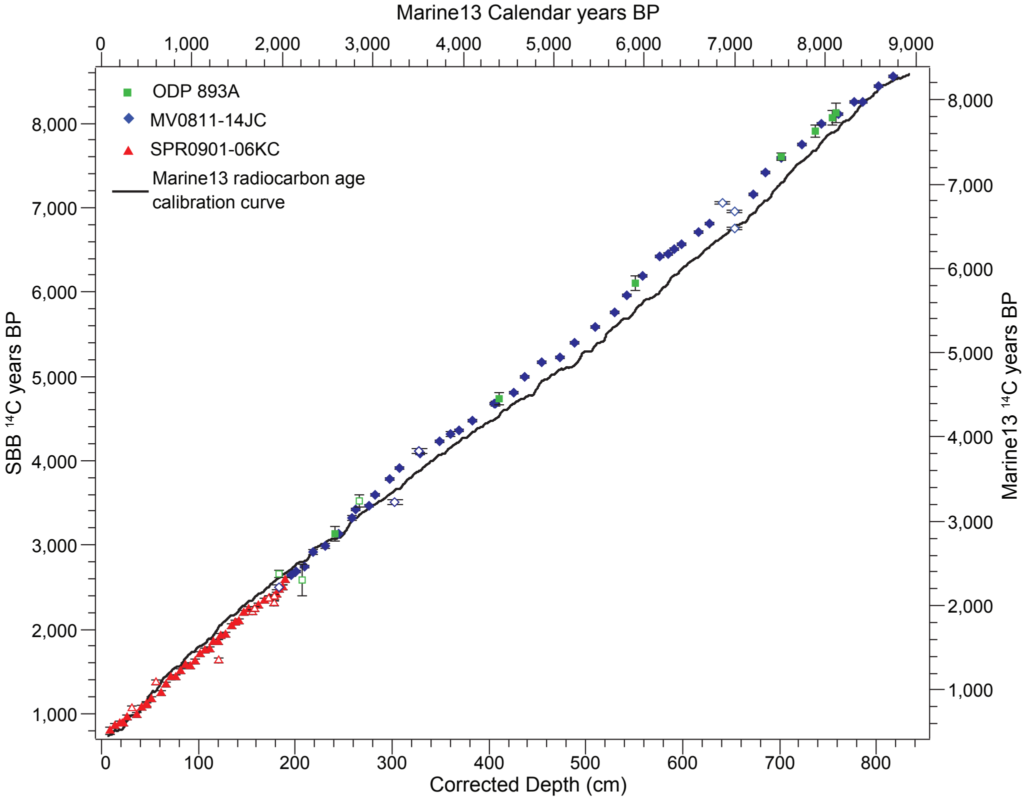

Figure 0-3 Comparison of Santa Barbara Basin (SBB) dates and Marine13 calibration curve. Planktonic foraminiferal carbonate ^{14}C dates (reservoir age-corrected) from core SPR0901-06KC (solid red triangles), core MV0811-14JC (solid blue diamonds) and ODP Hole 893A (solid green squares) are plotted against depth corrected for instantaneous event thickness. Radiocarbon yrs are plotted against calendar years on the Marine13 calibration curve (black line). Rejected dates are indicated by open symbols.

ODP Hole 893A section 2H-05 and 0 to ~90 cmbct in section 2H-06 where ^{14}C age reversals are observed (Table 2.1). These radiocarbon age reversals in ODP Hole 893A occur between 8600 and 9610 ^{14}C yrs and are calibrated to 9070 – 10325 yrs BP.

2.4.2 Gray and olive layer stratigraphy

Gray and olive layers were identified in multiple cores (core MV0811-14JC and ODP Site 893) through visual examination based on color and sedimentary structure as well as elemental composition when available (i.e. MV0811-14JC). Gray layers range in thickness from 1 mm to >15 cm and are typically fine-grained, sharp-based and contain high Ti concentrations (average Ti wt. % ~ 0.45 ±0.02) and low Ca/Ti elemental ratios (average Ca/Ti ~ 4.10 ±0.68) compared to laminated sections (average Ti wt. % ~ 0.37 ±0.02 average Ca/Ti ~ 12.50 ±1.34) (Table S1 in Supplemental materials). Most gray

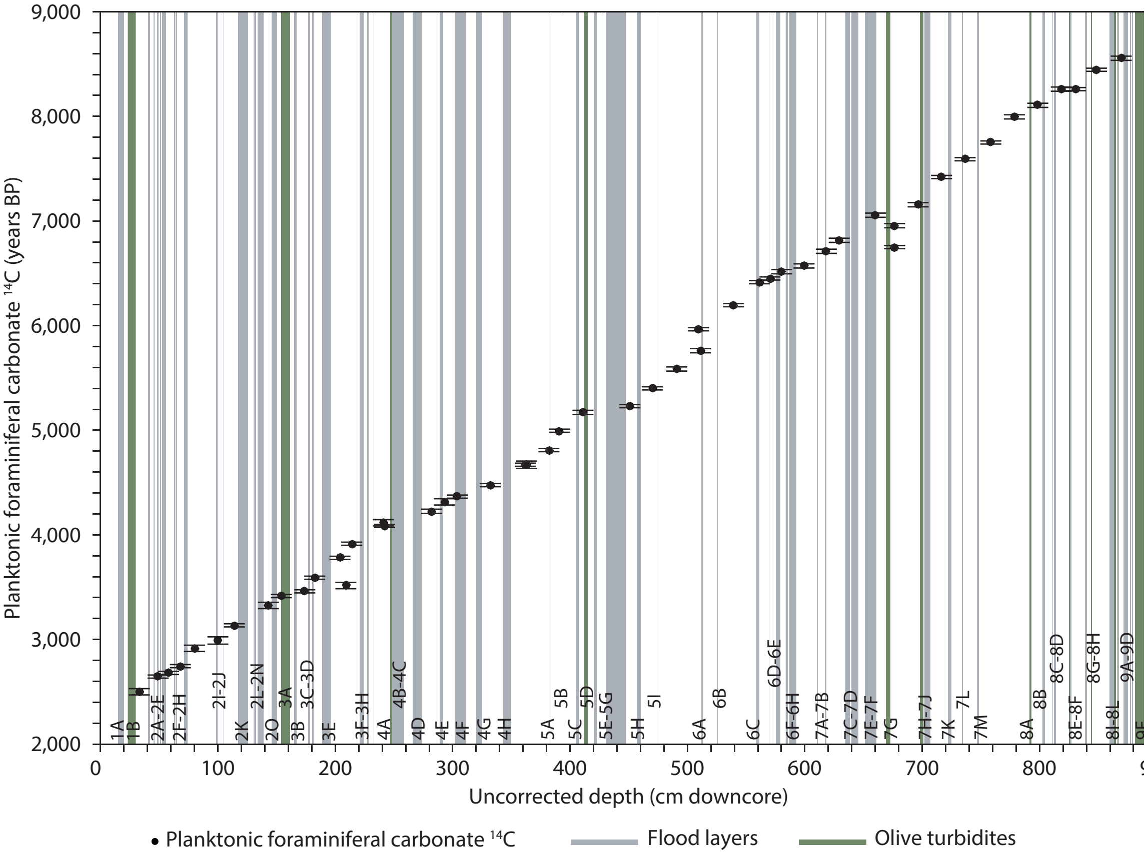

Figure 0-4 Uncalibrated radiocarbon dates (solid circles) from core MV0811-14JC with 1σ analytical error (bars) plotted against uncorrected core depth. Stratigraphic markers including gray layers (light gray bars) and olive layers (dark green bars) are indicated and labeled using the notation from Table 2.3.

layers are homogenous but some (notably the thicker gray layers) are not and are instead composed of multiple closely-spaced thin layers that are distinguished by changes in color and sedimentary structure (Fig. 2.5).

Olive layers are not laminated and range in thickness from 1 mm to ~10 cm and have sharp bases. Compared to gray layers, olive layers contain lower Ti concentrations (average Ti wt. % ~ 0.38 ±0.01) and higher Ca/Ti elemental ratios (average Ca/Ti ~ 10.66 ±0.91) (Table S1 in Supplemental materials). Benthic foraminiferal sands are observed at the base of some olive layers such as 1B and 3A (Fig. S1 in Supplemental materials).

Table 0-3 Stratigraphy and chronology of gray and olive layers in core MV0811-14JC with layer notations. Ages are estimated using the age model derived from BACON 2.2.

Type of layer	Layer identification notation	Uncorrected depth of top (cm)	Uncorrected depth of bottom (cm)	Layer thickness (cm)	Corrected depth in core (cm)	Dates of events (Cal BP)	95% confidence ranges
Gray layer	1A	15.04	20.04	5.00	15.02	1912	1822-2006
Olive layer	1B	23.22	30.02	6.80	19.02	1950	1858-2046
Gray layer	2A	40.38	42.00	1.62	29.36	2065	1967-2165
Gray layer	2B	45.22	45.72	0.50	32.56	2105	2006-2205
Gray layer	2C	48.18	49.22	1.04	35	2134	2031-2246
Gray layer	2D	50.92	51.72	0.80	36.68	2155	2055-2260
Gray layer	2E	52.56	55.92	3.36	37.5	2165	2063-2269
Gray layer	2F	62.50	63.26	0.76	44.06	2250	2136-2364
Gray layer	2G	64.06	65.16	1.10	44.84	2259	2147-2377
Gray layer	2H	71.22	74.14	2.92	50.86	2336	2223-2461
Gray layer	2I	98.44	99.62	1.18	67.26	2564	2431-2689
Gray layer	2J	104.94	105.14	0.20	72.56	2636	2499-2751
Gray layer	2K	117.32	125.82	8.50	84.72	2794	2680-2915
Gray layer	2L	130.54	131.34	0.80	89.42	2860	2737-2999
Gray layer	2M	131.72	132.32	0.60	89.78	2865	2745-3001
Gray layer	2N	133.92	138.68	4.76	91.36	2887	2768-3017
Gray layer	2O	145.94	150.28	4.34	98.6	2986	2859-3116
Olive layer	3A	153.90	161.22	7.32	102.2	3038	2912-3162
Gray layer	3B	165.06	166.84	1.78	106.02	3090	2960-3217
Gray layer	3C	177.06	178.68	1.62	116.22	3219	3088-3340
Gray layer	3D	180.48	181.50	1.02	118	3242	3109-3360
Gray layer	3E	189.12	195.94	6.82	125.6	3353	3222-3476
Gray layer	3F	220.84	223.84	3.00	150.48	3698	3555-3837
Gray layer	3G	227.20	228.30	1.10	153.82	3737	3586-3881
Gray layer	3H	232.94	233.12	0.18	164.04	3855	3702-4001

Olive layer	4A	246.86	248.32	1.46	177.76	4005	3860-4149
Gray layer	4B	248.34	254.64	6.30	177.76	4005	3860-4149
Gray layer	4C	254.82	258.68	3.86	177.92	4007	3861-4151
Gray layer	4D	266.10	273.40	7.30	185.32	4084	3943-4221
Gray layer	4E	289.12	291.66	2.54	200.96	4252	4125-4373
Gray layer	4F	301.88	310.98	9.10	211.16	4358	4231-4476
Gray layer	4G	320.02	324.90	4.88	220.18	4454	4324-4579
Gray layer	4H	343.42	349.50	6.08	238.68	4658	4521-4780
Gray layer	5A	383.76	384.12	0.36	269.94	5008	4878-5147
Gray layer	5B	392.82	393.10	0.28	278.62	5119	4975-5257
Gray layer	5C	405.26	407.38	2.12	290.76	5263	5107-5392
Olive layer	5D	412.00	414.96	2.96	295.36	5317	5159-5441
Gray layer	5E	420.88	422.76	1.88	301.26	5376	5224-5495
Gray layer	5F	427.16	427.42	0.26	305.64	5416	5268-5536
Gray layer	5G	430.54	447.22	16.68	308.74	5444	5299-5561
Gray layer	5H	457.16	460.22	3.06	318.68	5537	5401-5651
Gray layer	5I	473.94	474.18	0.24	332.36	5673	5548-5791
Gray layer	6A	512.08	512.96	0.88	370.22	6079	5942-6204
Gray layer	6B	525.56	525.68	0.12	386	6286	6169-6403
Gray layer	6C	558.94	561.34	2.40	415.26	6664	6537-6781
Gray layer	6D	569.48	569.86	0.38	423.38	6754	6641-6859
Gray layer	6E	575.60	579.30	3.70	429.08	6811	6704-6916
Gray layer	6F	583.30	583.54	0.24	433.06	6851	6751-6953
Gray layer	6G	583.96	585.26	1.30	433.46	6855	6753-6958
Gray layer	6H	587.24	592.80	5.56	435.42	6875	6772-6980
Gray layer	7A	610.32	610.94	0.62	449.12	7008	6888-7125
Gray layer	7B	617.00	618.06	1.06	455.16	7068	6949-7185
Gray layer	7C	634.56	638.12	3.56	471.62	7222	7091-7336
Gray layer	7D	639.94	645.64	5.70	473.4	7238	7104-7356
Gray layer	7E	651.30	659.34	8.04	479.04	7286	7147-7421
Gray layer	7F	659.36	660.70	1.34	479.06	7287	7147-7421
Olive layer	7G	669.30	672.74	3.44	487.6	7361	7216-7501
Olive layer	7H	697.98	699.48	1.50	513.84	7587	7460-7719
Olive layer	7I	699.88	700.92	1.04	514.22	7590	7462-7723
Gray layer	7J	701.94	706.76	4.82	515.22	7600	7478-7730
Gray layer	7K	721.80	724.68	2.88	530.24	7770	7662-7880
Gray layer	7L	733.84	734.66	0.82	539.38	7867	7747-7977
Gray layer	7M	746.62	748.00	1.38	551.32	7988	7881-8092
Olive layer	8A	791.44	792.86	1.42	594.5	8397	8291-8499
Gray layer	8B	802.74	804.50	1.76	603.78	8475	8384-8577
Gray layer	8C	811.14	811.28	0.14	610.4	8533	8432-8643
Gray layer	8D	812.14	813.74	1.60	611.24	8540	8440-8649
Olive layer	8E	824.92	825.64	0.72	622.98	8644	8532-8765

Gray layer	8F	825.66	827.26	1.60	622.98	8644	8532-8765
Gray layer	8G	838.90	840.60	1.70	634.6	8753	8618-8898
Olive layer	8H	843.98	844.74	0.76	637.96	8790	8651-8935
Gray layer	8I	859.84	863.46	3.62	652.96	8950	8785-9108
Olive layer	8J	863.48	864.88	1.40	652.96	8950	8785-9108
Olive layer	8K	865.90	866.16	0.26	653.96	8961	8791-9122
Olive layer	8L	867.48	867.62	0.14	655.26	8974	8804-9136
Gray layer	9A	871.58	874.42	2.84	659.2	9014	8835-9183
Gray layer	9B	874.82	875.32	0.50	659.72	9019	8839-9189
Gray layer	9C	877.10	877.88	0.78	661.44	9037	8854-9211
Gray layer	9D	878.90	879.42	0.52	662.44	9048	8861-9224
Olive layer	9E	881.12	893.00	11.88	664.14	9065	8873-9251

Gray and olive layers serve as stratigraphic tie points to correlate core MV0811-14JC to ODP Site 893 (Fig. 2.6). Some sedimentary segments are missing in ODP Site 893 between core sections which has been previously addressed by splicing ODP Hole 893A with Hole 893B. In contrast, MV0811-14JC was retrieved using a continuous coring technique resulting in a more complete record of gray and olive layers. Gray layers in core MV0811-14JC are comparable with gray layers in ODP site 893 except in the missing segments (i.e. ~6.8 – 7.9 m in ODP Hole 893A; ~11.1 – 11.4 m and ~11.7 – 13.7 m in ODP Hole 893B) (Fig. 2.6). There are offsets between cores in the depths and thicknesses of layers that are likely due to both coring differences (stratigraphic compression upon water loss and missing segments) between the cores and variations in the deposition of flood layers throughout the basin (Fig. 2.6). Olive layers are generally too obscure in the poorly resolved ODP core photos because of cracks or oxidization on the core surface but are clearly visible in scanned images of MV0811-14JC and SPR0901-03KC (Fig. 2.5). Rapid imaging after core splitting appears necessary to capture olive layers in SBB as oxidation of the sediments conceals the features of these layers. The dates of prominent gray and olive layers were estimated based on the improved age model presented here (Table 3).

2.4.3 Mass accumulation rates and sedimentation rates

The mass accumulation rate (MAR) of sediments closely follows the sedimentation rate (SR) during the last 9000 yrs (Fig. 2.7d). The MAR of sediments decreases gradually from 200 to 90 g cm^{-2} kyr^{-1} between 9000 to 2500 yrs BP. A sharp decrease (from 200 to 75 g cm^{-2} kyr^{-1}) occurred at ~6500 yrs BP. The MAR rapidly increased to ~165 g cm^{-2} kyr^{-1} from 2300 to 1800 yr BP before decreasing again to ~90 g cm^{-2} ka^{-1} for 500 yrs. During the last 1400 yrs the MAR increased dramatically from ~90 to ~280 g cm^{-2} kyr^{-1}.

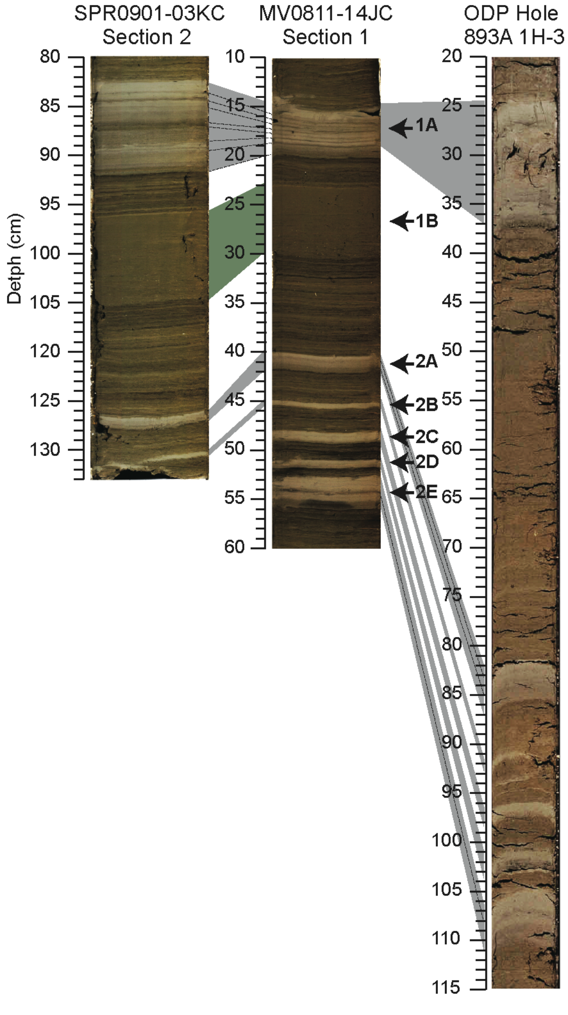

Figure 0-5 Core image example of a typical segment of the correlation between cores MV0811-14JC, SPR0901-03KC and ODP Hole 893A. Gray and dark green shadings indicate the position and correlation of gray and olive layers, respectively. Core images were brightened to enhance the display of diagnostic color differences.

2.5 Discussion

2.5.1 Chronology

The strong linear relationship between the ^{14}C dates from multiple cores and corrected depth ($R^2 = 0.9956$ in linear regression; Fig. 2.3) indicates that sedimentation in SBB is consistent through time. Additionally the linear relationship demonstrates the SBB stratigraphic record of grey layers can be used to correlate cores within the basin. Combining the cores (SPR0901-06KC, MV0811-14JC and core ODP Hole 893A) to generate an age-depth model using BACON 2.2 produces an average 95 % confidence interval range of 236 yrs through the record with a minimum of 144 yrs at ~47 cm and a maximum of 372 yrs at 825 cm (Fig. 2.2). Using this high-precision chronology, the well-dated stratigraphic pattern of gray and olive layers can now be applied to any SBB sediment cores to provide a readily available chronology.

However the age-depth relationship of the SBB sedimentary ^{14}C dates is not perfectly linear (Fig. 2.3). A consistent one-to-one relationship between the corrected age-depth relationship in SBB sediments and Marine13 calendar ages should exist if we assume an invariable reservoir age, a constant sedimentation rate and negligible differences in sediment compaction (i.e. *via* water loss) across the studied sections. Although the two curves are consistent prior to ~2500 yrs BP, the SBB ^{14}C dates are generally ~200 yrs older than the Marine13 calibration curve between 2500 and 8000 yrs BP. Multiple reservoir ages probably caused the strong covariation of the two age-depth curves prior to ~2500 yrs BP. However, between 8000 and 2500 yrs BP SBB either experienced greater surface ocean reservoir ages (>550 years) or a decreased SR. Neither possibilities can be excluded as the SBB SR does show a general decrease between 9000 to 2500 yrs BP (Fig. 2.7d) and the surface ocean reservoir age varied by ~350 yrs during the last 2000 yrs. This result suggests further refinement of the SBB chronology is needed using independent dating methods such as terrestrial organic carbon ^{14}C dates matched to marine carbonate ^{14}C dates to determine reservoir age variability beyond the last 2000 yrs.

2.5.2 Flood events and mass accumulation rate

The stratigraphic record of SBB contains 75 gray layers deposited during the last 9000 yrs. Gray layers are characterized by high detrital elemental concentrations and

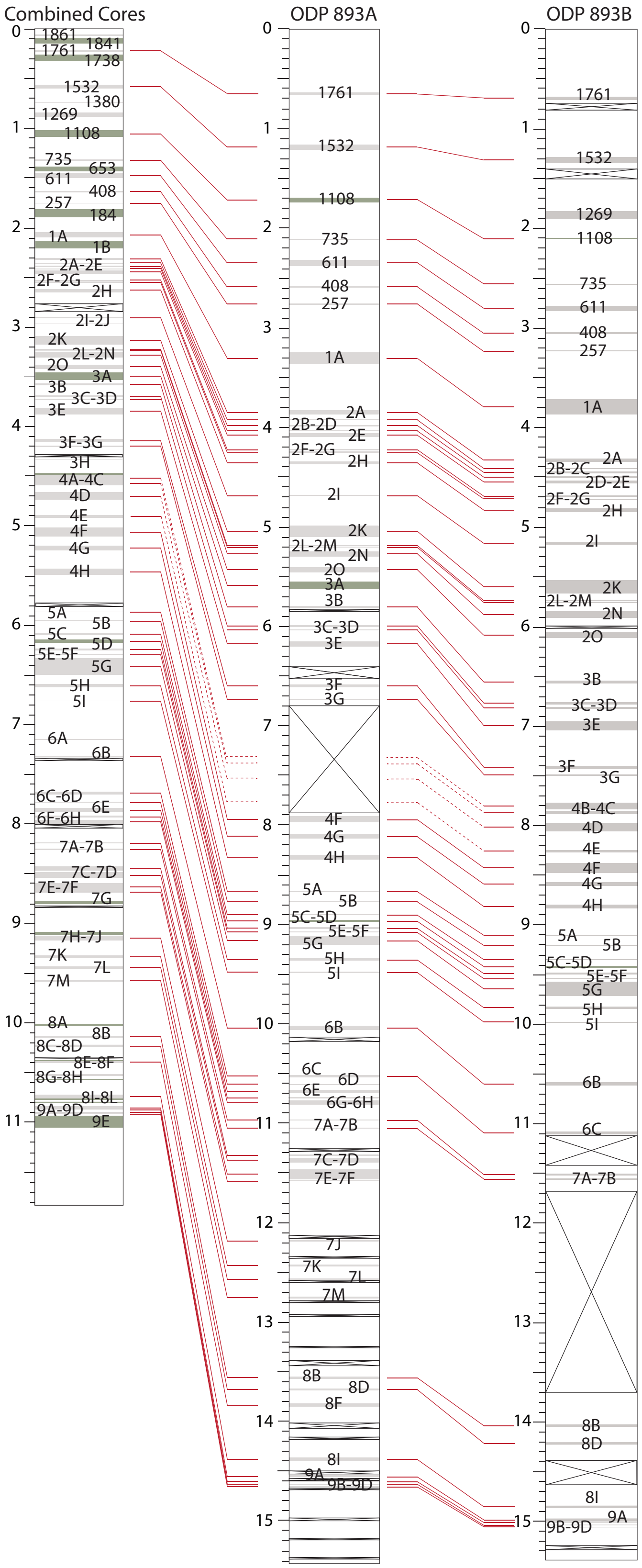

Figure 0-6 Schematic stratigraphic correlation between combined cores SPR09-03KC and

MV0811-14JC and ODP Holes 893A and 893B. The gray and dark green layers represent gray and olive layers respectively. Crossed boxes denote missing core material. Stratigraphic correlation between cores is indicated by red lines. Red dashed lines indicate where gray and olive layers are absent alongside missing core material.

significant increases in clay mineral abundance (Schimmelmann et al., 1998; Schimmelmann et al., 2003; Napier and Hendy, 2016), clayey silt or silty clay grain size without normal grading, high siliciclastic element concentrations (high Ti and low Ca/Ti) (Hendy et al., 2015), elevated terrestrial organic carbon abundance (lower $\delta^{13}C$) (Schimmelmann and Kastner, 1993), a presence of fresh water diatoms (such as

Aulacoseira) (Barron et al., 2015) and an absence of marine microfossils such as foraminifera (Schimmelmann et al., 2003). As these characteristics are typical of flood suspensates, the gray layers likely derived from suspended silt-size particles in large freshwater flood plumes that rapidly delivered siliciclastic sediments across the shelf to the center of the SBB (Thornton, 1984; Schimmelmann et al., 1998). Gray layers are therefore interpreted to be instantaneous events generated by extreme precipitation events in Southern California generating anomalous river runoff (Inman and Jenkins, 1999; Warrick et al., 2007; Romans et al., 2009; Covault et al., 2011).

Using the new age model, the number and thickness of gray layers per century was calculated to highlight changes in flood frequency and magnitude (Fig. 2.7b and c). The frequency and magnitude of floods generally increase during most of the high precipitation/run-off intervals indicated by multiple lacustrine records from Southern California between ~400-800, 3000-5500, 6600-7300 and 8500-9000 yrs BP (Fig. 2.7a-c) (Kirby et al., 2010; Kirby et al., 2012; Kirby et al., 2014; Kirby et al., 2015; Hiner et al., 2016). The Holocene length records of increased C/N ratios from Lower Bear Lake (Kirby et al., 2012) and sand deposits in Lake Elsinore (Kirby et al., 2010) indicate high lake levels are consistent with intervals of greater flood frequency and magnitude in SBB at ~400, 3000, 6,500 and 8,500 yrs BP (Figure 7a-c). Additionally, elevated aridity between 650 to 1050 yrs BP identified from tree-ring records of the western United States (Cook et al., 2004) occurred during the absence of gray layers. The concurrence of frequent (infrequent) gray layers and wetter (drier) climate indicates that flood events are likely to occur during wetter climate intervals suggesting the frequency of SBB gray layers might be utilized in paleoclimate reconstructions.

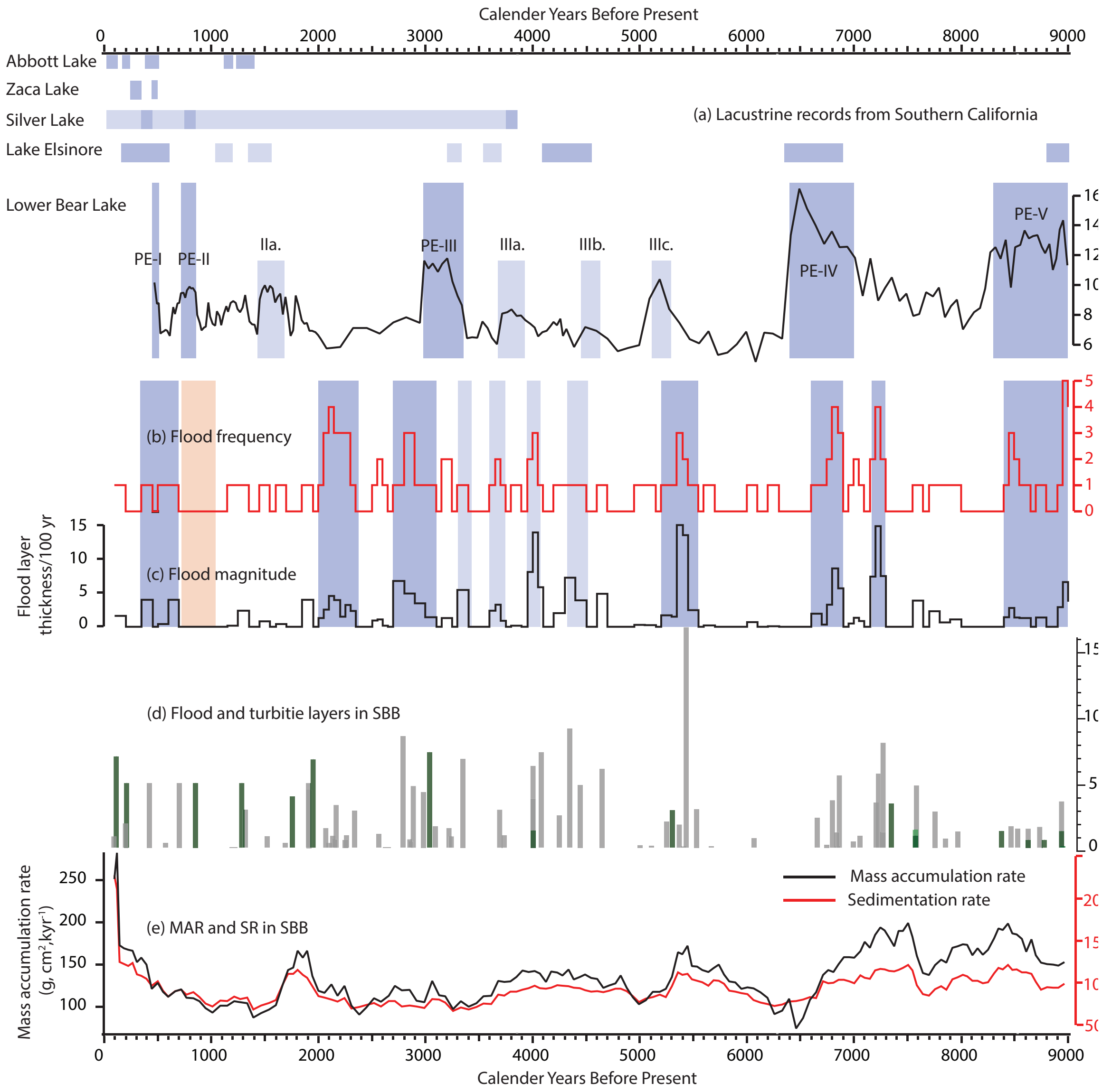

Figure 0-7 Gray layer frequency and magnitude, SR and MAR in core MV0811-14JC and pluvial interval recorded from lakes in Southern California through the Holocene. (a) Lacustrine records from Abbott Lake (Hiner et al., 2016) , Zaca Lake (Kirby et al., 2014), Silver Lake (Kirby et al., 2015) and Lake Elsinore (Kirby et al., 2010) in Southern California. Dark gray blocks refer to major, and light gray to minor pluvial episodes. Lower Bear Lake molar CN ratios are shown with pluvial episodes (PE) labeled (Kirby et al., 2012). (b) Flood frequency curve (flood events per century) and (c) Flood magnitude (flood layer thickness per century) in core MV0811-14JC. (d) Sedimentation rate (SR; red line) and mass accumulation rate (MAR; blue line) calculated using the new chronology for Santa Barbara Basin. The dark gray bar shows wet intervals indicated by higher frequency and larger magnitude of flood events recorded in core MV0811-14JC. The light red bar shows an interval with elevated aridity found in tree-ring networks in the western United States (Cook et al., 2004).

Although MAR and SR fluctuated during the last 9,000 years, they both increase when the frequency and magnitude of flood layers increase (Fig 7c and d). A statistically significant correlation (r = 0.18, p=0.016<0.05) was found between MAR and sediment flux of floods (thickness of gray layers per century), confirming that a principal process driving sediment accumulation in SBB during the Holocene was precipitation (Warrick and Milliman, 2003). Approximately 85 % of the central SBB sediment mass is composed of terrigenous sediments (Schwalbach and Gorsline, 1985) delivered by rivers. Precipitation plays a key role in weathering, erosion and transport of terrigenous sediments to depositional basins which contribute to changes in SR (Inman and Jenkins, 1999; Warrick et al., 2007; Romans et al., 2009; Covault et al., 2011; Gray et al., 2014;).

Precipitation allows soil clay minerals to sorb water and disintegrate aggregates resulting in more mobile and erodible clay particles, which are available for run-off transport and are eventually deposited in the SBB (Bryan, 2000; Robert, 2004; Napier and Hendy, 2016). During extreme precipitation events and frequent winter storms, erosion is more intense, increasing the fluvial sediment load and terrigenous sediment delivery by the Santa Clara River, Ventura River and Santa Ynez Mountain streams to the SBB (Inman and Jenkins, 1999; Warrick et al., 2007; Romans et al., 2009; Covault et al., 2011). However, flood events are infrequent when extreme precipitation does not occur and river discharge is lower. Consequently, less terrestrial sediments are delivered to the SBB leading to decreased SR and MAR. However, although the relationship between MAR and flood events was statistically significant, the correlation was only weak to moderate. Thus other factors must play a role in the delivery and accumulation of terrestrial sediments in SSB.

In addition to precipitation, vegetation cover also influences erosion in river catchments of Southern California because the rooting habit and density of vegetation are closely associated with hillside slope stability (Rice, 1969). The pollen record indicates that chaparral and coastal sage scrub community gradually increased during the Holocene, particularly since ~2300 yrs BP and then decreased after AD 1300 before being replaced by grasses in the late 1700s (Heusser, 1978, 1998; Keeley, 2002; Ejarque et al., 2015; Heusser et al., 2015). Chaparral vegetation has stronger and deeper roots compared to grasses and can reduce erosion by enhancing slope stability (Hellmers et al., 1955; Gabet and Dunne, 2002) thus increased chaparral cover relative to grass could decrease the SR and MAR in SBB. Additionally, erosion can also be affected by the frequency of wildfires as the downslope movement rate of soil can be significantly increased when vegetation and litter are removed by fire (Florsheim et al., 1991; Kean et al., 2011; Kirby et al., 2014). However, no significant correlation was found in Zaca Lake between charcoal and runoff, indicating fire is not the dominant erosional process in the region (Kirby et al., 2014). Finally, earthquakes in tectonically active Southern California could increase SR and MAR in central SBB sediment by triggering easily erodible landslides in catchments or inducing considerable downslope displacement of marine sediments from the margin of the basin (Keefer, 1994; Wieczorek and Jager, 1996; Thunell et al., 1999).

2.5.3 Submarine downslope sediment processes and slumping

Nineteen massive olive layers were found in SBB laminated sediments during the last 9000 yrs from core MV0811-14JC and SPR0901-03KC (olive layers in ODP Site 893 are no longer visible in the highly oxidized cores.). In contrast to gray layers, which are generated by flood events, the olive layers contain high Ca/Ti which is related to higher concentration of calcareous organisms – mainly foraminifera. This indicates that the olive layers contain marine-derived material (Hülsemann and Emery, 1961) and this observation is further supported by the appearance of benthic foraminiferal sands at the base of several of these layers (e.g., 1B and 3A). We interpret the olive layers as turbidites produced by fine-grained turbidity currents that originate from mass failure (e.g., debris-flows and submarine slides) on the upper slopes of SBB (Thornton, 1984; Rack and Merrill, 1995; Fisher et al., 2005). Sedimentary studies of Cariaco Basin found similar olive layers derived from turbidity flows (Peterson et al., 1991; Hughen et al., 1996). A seismically induced turbidity flow was observed in Cariaco Basin ~90 km from the rupture zone following a 6.8 earthquake in 1997. This downslope event was captured by transmissometer profiles, sediment traps and an associated box core and resulted in the downslope displacement of $>10^5$ tons of sediments (Thunell et al., 1999).

Slope failure and subsequent turbidity currents have been associated with massive earthquakes on the North American Pacific Margin (Goldfinger et al., 2007) and more specifically in the tectonically active SBB (Fisher et al., 2005). The SBB lies within the San Andreas transform fault zone which contains many active faults (Toppozada et al., 2002) that could trigger slope failure within SBB and generate turbidity currents. One of the major earthquakes in California occurred around Santa Barbara in AD 1811-1812 (Mission Quake) is reported to have produced a tsunami and probably generated submarine slope failure (Keefer, 1984; Borrero et al., 2001). The Mission Quake has been associated with turbidites of similar age in SBB and Santa Monica Basin (Schimmelmann et al., 1992; Gorsline, 1996). Furthermore, seismically induced slope failures and subsequent turbidity flows have been directly observed in association with several recent offshore earthquakes (Thunell et al., 1999; McHugh et al., 2011; Ashi et al., 2014) and marine turbidite stratigraphy has been widely used to record the history of significant offshore earthquakes in various regions (Gorsline, 1996; Goldfinger et al., 2007; McHugh et al., 2011).

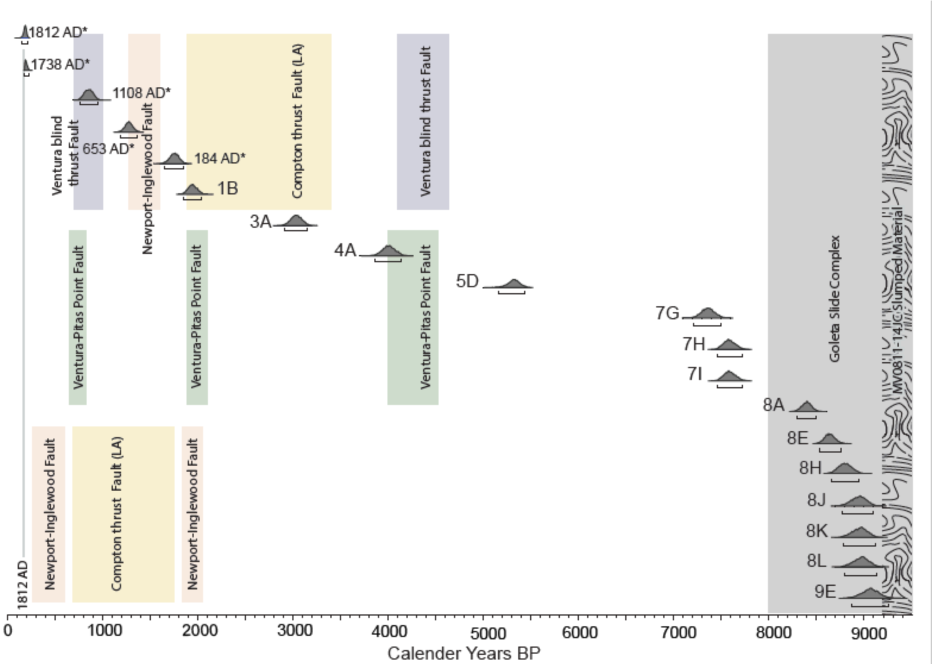

Figure 0-8 Probability density functions (PDFs) for the 19 turbidites (olive layers) in core MV0811-14JC and core SPR090106KC in Santa Barbara Basin generated from Bacon 2.2. Brackets show 95% confidence intervals. Estimate emergence times of the Newport-Inglewood Fault (Leeper et al., 2017) in pink, Ventura-Pitas Point Fault (Rockwell et al., 2016) in green, Ventura blind thrust fault (McAuliffe et al., 2015) in purple, Compton Thrust Fault (Leon et al., 2009) in yellow and the Goleta Slide Complex (Fisher et al., 2005)in grey. Age of slumped material in 14JC is indicated by wavy texture.

Turbidites (olive layers) identified in core MV0811-14JC can be temporally linked to large earthquakes along the San Andreas Fault especially in the Transverse Ranges (listed in Table 4; Figure 8). Four large Holocene coseismic uplift events resulted from slip on the Ventura – Pitas Point fault system, along the coast between Ventura and Carpinteria (Rockwell et al., 2016) . Three of these emergence times, estimated at AD 955-1195, 1850-2090 yrs BP and 4150-4640 yrs BP, can be related to turbidites generated at AD 1108, 1950 yrs BP (1B), and 4005 yrs BP (4A) (Figure 8). Two of these uplift events are also co-incident with large-magnitude earthquakes (after AD 1210 ± 75 and at 4000-4600 year BP) on the Ventura blind thrust fault (McAuliffe et al., 2015).The, large earthquakes on the Compton thrust fault, Los Angeles have less well resolved emergence times; those being 200-1250 years AD, 700-3400 years BP, 1900-3400 years BP, 5600-7200 years BP, 5400-8400 years BP (Leon et al., 2009), and therefore could be associated with a number of SBB turbidites (the olive layer at 184 AD, and layers 1B, 3A, 5D, 7G, and 7H; Figure 8). Two late Holocene coseismic subsidence events (at AD 347-648 and 2085-1910 yrs BP) resulting from large-magnitude earthquakes along the Newport-Inglewood fault could be related to turbidites at AD 653 and AD 1950 yrs BP, respectively. Thus, marine turbidites in SBB can potentially be used to reconstruct the earthquake history in Southern California.

Additionally, evidence for the emplacement of a large slide is found at the base of core MV0811-14JC (sections 8-9) where laminated sediments are clearly not *in situ* as high-resolution core images show folding (section 9, Fig. S1 in Supplemental material). This segment is related to a series of age reversals (9070 – 10325 yrs BP) observed in section 2H-06 from ODP Hole 893A previously ascribed to slumped material (Nederbragt and Thurow, 2005). The stratigraphic disturbances could be the result of massive slope failure associated with submarine slides at the northern flank of SBB. The cores discussed here are located within ~1 km of the toe of the Goleta submarine slide complex western lobe whose offshore stratigraphy and geologic structure have been identified by multibeam bathymetric mapping and seismic-reflection data (Fig. 2.1) (Fisher et al., 2005; Greene et al., 2006; Lee et al., 2009). Composed of slump blocks and mudflows, the submarine slide (14 km long and 11 km wide) originates from along the North Channel – Pitas Point – Red Mountain fault system and extends southwestward to a water depth of 570 m (Fisher et al., 2005; Greene et al., 2006).

Fisher et al. (2005) estimated the age of the central and western segments of the Goleta slide complex as ~ 8000 to 10000 yrs BP based on the chronostratigraphy and oxygen-isotope record of ODP 893 core (Ingram and Kennett, 1995; Kennett, 1995) coupled with high resolution seismic-reflection data. The corresponding depth of the slide in ODP Hole 893A is ~15 mbct (m below core top) similar to the depth of the observed ^{14}C age reversals. Thus we constrain the slide's age to ~9000 yrs BP ±200 yrs using the ^{14}C dates of laminated sediment sitting directly above the disturbed sediment in cores MV0811-14JC and ODP Hole 893A. Frequent turbidites are deposited in the millennia following the slump (Figure 8) suggesting either slope stability was not quickly achieved after the slide or repeated triggering earthquakes occurred in the early Holocene.

Although regional earthquakes are the most obvious triggers for slope failure and turbidity currents, other processes could enhance the frequency of such events, especially rapid sediment accumulation (Gorsline, 1996; Fisher et al., 2005; Greene et al., 2006; Lee et al., 2009). During a major flood event, the discharge of Santa Clara River (accounting for the ~80 % of sediment flux to the SBB) can approach 10^7 to 10^8 m^3 resulting in a total sediment discharge of 10^2 to 10^3 kt (Warrick et al., 2004). Flood sediment initially deposited on the shelf can subsequently be resuspended and transported to the central SBB by waves and currents, or can be temporarily loaded on slopes that will ultimately fail and generate turbidity currents (Gorsline, 1996). Evidence for these processes can be found in MV0811-14JC. Olive layer 8E directly overlays a thick gray layer (8F) suggesting a turbidity current derived from slope failure subsequent to a significant flood event (Fig. S1). Other processes such as high fluid pressures and oversteepening may also impact sediment on shelf slopes and contribute to slope failure. Further investigation of massive olive layers in laminated SBB sediments is necessary to determine whether the slope failure is triggered by tectonic activity and/or rapid sediment delivery.

2.6 Conclusion

High-resolution radiocarbon measurements of mixed planktonic foraminifera from core MV0811-14JC in combination with ^{14}C dates from SPR0901-06KC and ODP Hole 893A provide a revised chronology for the SBB sedimentary record over last 9000 yrs. Prominent gray and olive layers identified in multiple cores allowed for stratigraphic correlation between cores. The age of these stratigraphic markers has been estimated using the revised chronology providing a readily available chronology for future SBB coring efforts. Gray layers are interpreted to be the product of floods associated with extreme precipitation events. The frequency of flood layers was calculated and frequent (infrequent) floods were found during generally wetter (drier) intervals identified by Southern California hydroclimate reconstructions. Both mass accumulation rate and sedimentation rate increase when floods are frequent indicating that Holocene sedimentation accumulation in SBB is influenced by precipitation.

A second type of massive sedimentary event was identified in the SBB stratigraphic sequence. Olive layers are interpreted as turbidities derived from downslope displacement of sediments. Although not all downslope events are associated with seismic activity, the newly identified olive layers are well dated and can potentially be used to reconstruct the earthquake history in Southern California. A slump related to the Goleta submarine slide complex was identified at the base of MV0811-14JC by folded sediments in high-resolution core images. Core-to-core correlation with ODP Hole 893A places these disturbed sediments within ^{14}C age reversals in ODP Hole 893A which serve as evidence for sediment displacement around 9000 ±200 yrs. Our improved radiocarbon chronology for the past 9000 yrs of sedimentation in SBB together with the identified gray and olive layers provide a valuable well constrained and easily accessible stratigraphy for future high-resolution core-to-core correlations and thus enhance the value of SBB sediment for paleoceanographic and paleoclimatic studies.

2.7 References

Ashi, J., Sawada, R., Omura, A., Ikehara, K., 2014. Accumulation of an earthquake-induced extremely turbid layer in a terminal basin of the Nankai accretionary prism. Earth, Planets and Space 66:51.

Barron, J.A., Bukry, D., Hendy, I.L., 2015. High-resolution paleoclimatology of the Santa Barbara Basin during the Medieval Climate Anomaly and early Little Ice Age based on diatom and silicoflagellate assemblages in Kasten core SPR0901-02KC. Quaternary International 387, 13-22.

Behl, R.J., 1995. 22. Sedimentary facies and sedimentology of the late Quaternary Santa Barbara Basin, Site 893. Proceedings of the Ocean Drilling Program, Scientific Results 146 (Pt. 2), 295-308.

Beverly, R.K., Beaumont, W., Tauz, D., Ormsby, K.M., von Reden, K.F., Santos, G.M., Southon, J.R., 2010. The Keck Carbon Cycle AMS Laboratory, University of California, Irvine: Status Report. Radiocarbon 52, 301-309.

Blaauw, M., Christen, J.A., 2011. Flexible paleoclimate age-depth models using an autoregressive gamma process. Bayesian Analysis 6, 457-474.

Borrero, J.C., Dolan, J.F., Synolakis, C.E., 2001. Tsunamis within the eastern Santa Barbara Channel. Geophysical Research Letters 28, 643-646.

Bryan, R.B., 2000. Soil erodibility and processes of water erosion on hillslope. Geomorphology 32, 385-415.

Cook, E.R., Woodhouse, C.A., Eakin, C.M., Meko, D.H., Stahle, D.W., 2004. Long-term aridity changes in the western United States. Science 306, 1015-1018.

Covault, J.A., Romans, B.W., Graham, S.A., Fildani, A., Hilley, G.E., 2011. Terrestrial source to deep-sea sink sediment budgets at high and low sea levels: Insights from tectonically active Southern California. Geology 39, 619-622.

Duvall, A., Kirby, E., Burbank, D., 2004. Tectonic and lithologic controls on bedrock channel profiles and processes in coastal California. Journal of Geophysical Research-Earth Surface 109.

Ejarque, A., Anderson, R.S., Simms, A.R., Gentry, B.J., 2015. Prehistoric fires and the shaping of colonial transported landscapes in southern California: A paleoenvironmental study at Dune Pond, Santa Barbara County. Quaternary Science Reviews 112, 181-196.

Fisher, M.A., Normark, W.R., Greene, H.G., Lee, H.J., Sliter, R.W., 2005. Geology and tsunamigenic potential of submarine landslides in Santa Barbara Channel, Southern California. Marine Geology 224, 1-22.

Fisler, J., Hendy, I.L., 2008. California Current System response to late Holocene climate cooling in southern California. Geophysical Research Letters 35, L09702.

Fleischer, P., 1972. Mineralogy and Sedimentation History, Santa Barbara Basin, California. Journal of Sedimentary Petrology 42, 49-58.

Florsheim, J.L., Keller, E.A., Best, D.W., 1991. Fluvial Sediment Transport in Response to Moderate Storm Flows Following Chaparral Wildfire, Ventura County, Southern California. Geological Society of America Bulletin 103, 504-511.

Gabet, E.J., Dunne, T., 2002. Landslides on coastal sage-scrub and grassland hillslopes in a severe El Nino winter: The effects of vegetation conversion on sediment delivery. Geological Society of America Bulletin 114, 983-990.

Goldfinger, C., Morey, A.E., Nelson, C.H., Gutiérrez-Pastor, J., Johnson, J.E., Karabanov, E., Chaytor, J., Eriksson, A., Party, S.S., 2007. Rupture lengths and temporal history of significant earthquakes on the offshore and north coast segments of the Northern San Andreas Fault based on turbidite stratigraphy. Earth and Planetary Science Letters 254, 9-27.

Gorsline, D.S., 1996. Depositional events in Santa Monica Basin, California Borderland, over the past five centuries. Sedimentary Geology 104, 73-88.

Gray, A.B., Warrick, J.A., Pasternack, G.B., Watson, E.B., Goni, M.A., 2014. Suspended sediment behavior in a coastal dry-summer subtropical catchment: Effects of hydrologic preconditions. Geomorphology 214, 485-501.

Greene, H.G., Murai, L.Y., Watts, P., Maher, N.A., Fisher, M.A., Paull, C.E., Eichhubl, P., 2006. Submarine landslides in the Santa Barbara Channel as potential tsunami sources. Natural Hazards and Earth System Sciences 6, 63-88.

Hellmers, H., Horton, J.S., Juhren, G., O'keefe, J., 1955. Root Systems of Some Chaparral Plants in Southern California. Ecology 36, 667-678.

Hendy, I.L., Dunn, L., Schimmelmann, A., Pak, D.K., 2013. Resolving varve and radiocarbon chronology differences during the last 2000 years in the Santa Barbara Basin sedimentary record, California. Quaternary International 310, 155-168.

Hendy, I.L., Napier, T.J., Schimmelmann, A., 2015. From extreme rainfall to drought: 250 years of annually resolved sediment deposition in Santa Barbara Basin, California. Quaternary International 387, 3-12.

Heusser, L., 1978. Pollen in Santa Barbara Basin, California: A 12,000-yr record Geological Society of America Bulletin 89, 673-678.

Heusser, L., 1998. Direct correlation of millennial-scale changes in western North American vegetation and climate with changes in the California current system over the past similar to 60 kyr. Paleoceanography 13, 252-262.

Heusser, L.E., Hendy, I.L., Barron, J.A., 2015. Vegetation response to southern California drought during the Medieval Climate Anomaly and early Little Ice Age (AD 800-1600). Quaternary International 387, 23-35.

Hiner, C.A., Kirby, M.E., Bonuso, N., Patterson, W.P., Palermo, J., Silveira, E., 2016. Late Holocene hydroclimatic variability linked to Pacific forcing: evidence from Abbott Lake, coastal central California. Journal of Paleolimnology 56, 299-313.

Hughen, K.A., Overpeck, J.T., Peterson, L.C., Anderson, R.F., 1996. The nature of varved sedimentation in the Cariaco Basin, Venezuela, and its palaeoclimatic significance. Geological Society, London, Special Publications, 116(1), 171-183.

Hülsemann, J., Emery, K.O., 1961. Stratification in Recent Sediments of Santa-Barbara Basin as Controlled by Organisms and Water Character. The Journal of Geology 69, 279-290.

Ingram, B.L., Kennett, D.J., 1995. Radiocarbon chronology and planktonic–benthic foraminifera 14C age differences in Santa Barbara Basin sediments, Hole 893A. Proceedings of the Ocean Drilling Program, Scientific Results 146 (Pt. 2), 19-27.

Inman, D.L., Jenkins, S.A., 1999. Climate change and the episodicity of sediment flux of small California rivers. Journal of Geology 107, 251-270.

Kean, J.W., Staley, D.M., Cannon, S.H., 2011. In situ measurements of post-fire debris flows in southern California: Comparisons of the timing and magnitude of 24 debris-flow events with rainfall and soil moisture conditions. Journal of Geophysical Research: Earth Surface 116(F4).

Keefer, D.K., 1984. Landslides Caused by Earthquakes. Geological Society of America Bulletin 95, 406-421.

Keefer, D.K., 1994. The Importance of Earthquake-Induced Landslides to Long-Term Slope Erosion and Slope-Failure Hazards in Seismically Active Regions. Geomorphology 10, 265-284.

Keeley, J.E., 2002. Native American impacts on fire regimes of the California coastal ranges. Journal of Biogeography 29, 303-320.

Kennett, J.P., Venz, K., 1995. 21. Late Quaternary climatically related planktonic foraminiferal assemblage changes: hole 893A, Santa Barbara Basin, California.

Proceedings of the Ocean Drilling Program, Scientific Results 146 (Pt. 2), 281-294.

Kennett, P.J., 1995. 1. Latest Quaternary benthic oxygen and carbon isotope stratigraphy: hole 893A, Santa Barbara Basin, California. Proceedings of the Ocean Drilling Program, Scientific Results 146 (Pt. 2), 3-18.

Kirby, M.E., Feakins, S.J., Hiner, C.A., Fantozzi, J., Zimmerman, S.R.H., Dingemans, T., Mensing, S.A., 2014. Tropical Pacific forcing of Late-Holocene hydrologic variability in the coastal southwest United States. Quaternary Science Reviews 102, 27-38.

Kirby, M.E., Knell, E.J., Anderson, W.T., Lachniet, M.S., Palermo, J., Eeg, H., Lucero, R., Murrieta, R., Arevalo, A., Silveira, E., Hiner, C.A., 2015. Evidence for insolation and Pacific forcing of late glacial through Holocene climate in the Central Mojave Desert (Silver Lake, CA). Quaternary Research 84, 174-186.

Kirby, M.E., Lund, S.P., Patterson, W.P., Anderson, M.A., Bird, B.W., Ivanovici, L., Monarrez, P., Nielsen, S., 2010. A Holocene record of Pacific Decadal Oscillation (PDO)-related hydrologic variability in Southern California (Lake Elsinore, CA). Journal of Paleolimnology 44, 819-839.

Kirby, M.E., Zimmerman, S.R.H., Patterson, W.P., Rivera, J.J., 2012. A 9170-year record of decadal-to-multi-centennial scale pluvial episodes from the coastal Southwest United States: a role for atmospheric rivers? Quaternary Science Reviews 46, 57-65.

Kolpack, R.L., Drake, D.E., 1984. Transport of Clays in the Eastern Part of Santa-Barbara Channel, California. Geo-Marine Letters 4, 191-196.

Lange, C.B., Berger, W.H., Burke, S.K., Casey, R.E., Schimmelmann, A., Soutar, A., Weinheimer, A.L., 1987. El Niño in Santa Barbara Basin: Diatom, radiolarian and foraminiferan responses to the "1983 El Niño" event. Marine Geology 78, 153-160.

Lange, C.B., Schimmelmann, A., 1995. 26. Data report: x-radiography of selected, predominantly varved intervals at Hole 893A. Proceedings of the Ocean Drilling Program, Scientific Results 146 (Pt. 2), 333-346.

Lee, H.J., Greene, H.G., Edwards, B.D., Fisher, M.A., Normark, W.R., 2009. Submarine landslides of the Southern California Borderland. Earth Science in the Urban Ocean: The Southern California Continental Borderland: Geological Society of America Special Paper 454, 251-269.

Leeper, R., Rhodes, B., Kirby, M., Scharer, K., Carlin, J., Hemphill-Haley, E., Avnaim-Katav, S., MacDonald, G., Starratt, S., Aranda, A., 2017. Evidence for coseismic subsidence events in a southern California coastal saltmarsh. Scientific Reports 7, 44615.

Leon, L.A., Dolan, J.F., Shaw, J.H., Pratt, T.L., 2009. Evidence for large holocene earthquakes on the compton thrust fault, Los Angeles, California. Journal of Geophysical Research: Solid Earth 114.

Lynn, R.J., Simpson, J.J., 1987. The California Current System - the Seasonal Variability of Its Physical Characteristics. Journal of Geophysical Research: Oceans 92, 12947-12966.

Mayewski, P.A., Rohling, E.E., Stager, J.C., Karlen, W., Maasch, K.A., Meeker, L.D., Meyerson, E.A., Gasse, F., van Kreveld, S., Holmgren, K., Lee-Thorp, J., Rosqvist, G., Rack, F., Staubwasser, M., Schneider, R.R., Steig, E.J., 2004. Holocene climate variability. Quaternary Research 62, 243-255.

McAuliffe, L.J., Dolan, J.F., Rhodes, E.J., Hubbard, J., Shaw, J.H., Pratt, T.L., 2015. Paleoseismologic evidence for large-magnitude (MW 7.5-8.0) earthquakes on the Ventura blind thrust fault: Implications for multifault ruptures in the Transverse Ranges of southern California. Geosphere 11, 1629-1650.

McHugh, C.M., Seeber, L., Braudy, N., Cormier, M.H., Davis, M.B., Diebold, J.B., Dieudonne, N., Douilly, R., Gulick, S.P.S., Hornbach, M.J., Johnson, H.E., Mishkin, K.R., Sorlien, C.C., Steckler, M.S., Symithe, S.J., Templeton, J., 2011. Offshore sedimentary effects of the 12 January 2010 Haiti earthquake. Geology 39, 723-726.

McHugh, C.M.G., Seeber, L., Cormier, M.H., Hornbach, M., 2014. Submarine Paleoseismology Along Populated Transform Boundaries: The Enriquillo-Plantain-Garden Fault, Canal du Sud, Haiti, and the North Anatolian Fault, Marmara Sea, Turkey. Oceanography 27, 118-131.

Napier, T.J., Hendy, I.L., 2016. The impact of hydroclimate and dam construction on terrigenous detrital sediment composition in a 250-year Santa Barbara Basin record off southern California. Quaternary International.

Nederbragt, A.J., Thurow, J., 2005. Geographic coherence of millennial-scale climate cycles during the Holocene. Palaeogeography Palaeoclimatology Palaeoecology 221, 313-324.

Peterson, L.C., Overpeck, J.T., Kipp, N.G., Imbrie, J., 1991. A High-Resolution Late Quaternary Upwelling Record from the Anoxic Cariaco Basin, Venezuela. Paleoceanography 6, 99-119.

Rack, F.R., Merrill, R.B., 1995. 12. Santa Barbara Basin: Construction of a 16,000-year composite record using magnetic susceptibility and digital color imaging data. Proceedings of the Ocean Drilling Program, Scientific Results 146 (Pt. 2), 169-192.

Reimer, P.J., Bard, E., Bayliss, A., Beck, J.W., Blackwell, P.G., Ramsey, C.B., Buck, C.E., Cheng, H., Edwards, R.L., Friedrich, M., Grootes, P.M., Guilderson, T.P., Haflidason, H., Hajdas, I., Hatte, C., Heaton, T.J., Hoffmann, D.L., Hogg, A.G., Hughen, K.A., Kaiser, K.F., Kromer, B., Manning, S.W., Niu, M., Reimer, R.W., Richards, D.A., Scott, E.M., Southon, J.R., Staff, R.A., Turney, C.S.M., van der Plicht, J., 2013. IntCal13 and Marine13 radiocarbon age calibration curves 0–50,000 years cal BP. Radiocarbon 55, 1869-1887.

Rice, R.M., 1969. Soil slips related to vegetation, topography, and soil in southern California. Water Resources Research 5, 647-659.

Roark, E.B., Ingram, B.L., Southon, J., Kennett, J.P., 2003. Holocene foraminiferal radiocarbon record of paleocirculation in the Santa Barbara Basin. Geology 31, 379-382.

Robert, C., 2004. Late quaternary variability of precipitation in Southern California and climatic implications: clay mineral evidence from the Santa Barbara Basin, ODP site 893. Quaternary Science Reviews 23, 1029-1040.

Rockwell, T.K., Clark, K., Gamble, L., Oskin, M.E., Haaker, E.C., Kennedy, G.L., 2016. Large transverse range earthquakes cause coastal upheaval near ventura, Southern California. Bulletin of the Seismological Society of America 106, 2706-2720.

Romans, B.W., Normark, W.R., McGann, M.M., Covault, J.A., Graham, S.A., 2009. Coarse-grained sediment delivery and distribution in the Holocene Santa Monica Basin, California: Implications for evaluating source-to-sink flux at millennial time scales. Geological Society of America Bulletin 121, 1394-1408.

Schimmelmann, A., Hendy, I.L., Dunn, L., Pak, D.K., Lange, C.B., 2013. Revised ~2000-year chronostratigraphy of partially varved marine sediment in Santa Barbara Basin, California. Geologiska Föreningen i Stockholm Förhandlingar (GFF) 135, 258-264.

Schimmelmann, A., Kastner, M., 1993. Evolutionary changes over the last 1000 years of reduced sulfur phases and organic carbon in varved sediments of the Santa Barbara Basin, California. Geochimica et Cosmochimica Acta 57, 67-78.

Schimmelmann, A., Lange, C.B., Berger, W.H., Simon, A., Burke, S.K., Dunbar, R.B., 1992. Extreme climatic conditions recorded in Santa Barbara Basin laminated sediments: the 1835-1840 Macoma event. Marine Geology 106, 279-299.

Schimmelmann, A., Lange, C.B., Meggers, B.J., 2003. Palaeoclimatic and archaeological evidence for a similar to 200-yr recurrence of floods and droughts linking California, Mesoamerica and South America over the past 2000 years. Holocene 13, 763-778.

Schimmelmann, A., Lange, C.B., Roark, E.B., Ingram, B.L., 2006. Resources for paleoceanographic and paleoclimatic analysis: A 6,700-year stratigraphy and regional radiocarbon reservoir-age (ΔR) record based on varve counting and 14C-AMS dating for the Santa Barbara Basin, offshore California, U.S.A. Journal of Sedimentary Research 76, 74-80.

Schimmelmann, A., Lange, C.B., Schieber, J., Francus, P., Ojala, A.E.K., Zolitschka, B., 2016. Varves in marine sediments: A review. Earth-Science Reviews 159, 215-246.

Schimmelmann, A., Zhao, M., Harvey, C.C., Lange, C.B., 1998. A large California flood and correlative global climatic events 400 years ago. Quaternary Research 49, 51-61.

Schwalbach, J.R., Gorsline, D.S., 1985. Holocene Sediment Budgets for the Basins of the California Continental Borderland. Journal of Sedimentary Petrology 55, 829-842.

Soutar, A., Crill, P.A., 1977. Sedimentation and climatic patterns in the Santa Barbara Basin during the 19th and 20th centuries Geological Society of America Bulletin 88, 1161-1172.

Thornton, S.E., 1984. Basin model for hemipelagic sedimentation in a tectonically active continental margin: Santa Barbara Basin, California Continental Borderland, Geological Society Special Publication, pp. 377-394.

Thunell, R., Tappa, E., Varela, R., Llano, M., Astor, Y., Muller-Karger, F., Bohrer, R., 1999. Increased marine sediment suspension and fluxes following an earthquake. Nature 398, 233-236.

Thunell, R.C., 1998. Particle fluxes in a coastal upwelling zone: Sediment trap results from Santa Barbara Basin, California. Deep-Sea Research Part II: Topical Studies in Oceanography 45, 1863-1884.

Toppozada, T.R., Branum, D.M., Reichle, M.S., Hallstrom, C.L., 2002. San Andreas fault zone, California: M >= 5.5 earthquake history. Bulletin of the Seismological Society of America 92, 2555-2601.

Wanner, H., Beer, J., Butikofer, J., Crowley, T.J., Cubasch, U., Fluckiger, J., Goosse, H., Grosjean, M., Joos, F., Kaplan, J.O., Kuttel, M., Muller, S.A., Prentice, I.C., Solomina, O., Stocker, T.F., Tarasov, P., Wagner, M., Widmann, M., 2008. Mid- to Late Holocene climate change: an overview. Quaternary Science Reviews 27, 1791-1828.

Warrick, J.A., DiGiacomo, P.M., Weisberg, S.B., Nezlin, N.P., Mengel, M., Jones, B.H., Ohlmann, J.C., Washburn, L., Terrill, E.J., Farnsworth, K.L., 2007. River plume patterns and dynamics within the Southern California Bight. Continental Shelf Research 27, 2427-2448.

Warrick, J.A., Mertes, L.A.K., 2009. Sediment yield from the tectonically active semiarid Western Transverse Ranges of California. Geological Society of America Bulletin 121, 1054-1070.

Warrick, J.A., Mertes, L.A.K., Washburn, L., Siegel, D.A., 2004. A conceptual model for river water and sediment dispersal in the Santa Barbara Channel, California. Continental Shelf Research 24, 2029-2043.

Warrick, J.A., Milliman, J.D., 2003. Hyperpycnal sediment discharge from semiarid southern California rivers: Implications for coastal sediment budgets. Geology 31, 781-784.

Weinheimer, A.L., Cayan, D.R., 1997. Radiolarian assemblages from Santa Barbara Basin sediments: Recent interdecadal variability. Paleoceanography 12, 658-670.

Wieczorek, G.F., Jager, S., 1996. Triggering mechanisms and depositional rates of postglacial slope-movement processes in the Yosemite valley, California. Geomorphology 15, 17-31.

Chapter 3

Interannual Southern California Precipitation Variability During the Common Era and the ENSO Teleconnection

Abstract

Southern California's Mediterranean-type hydroclimate is highly variable on interannual time scales due to teleconnected climate forcings such as the El Niño-Southern Oscillation (ENSO). Here we present sub-annually resolved scanning XRF Ti counts from deep-sea cores in Santa Barbara Basin (SBB), California recording 2,000 years of hydroclimate variability. The reconstructed Southern California precipitation record contains interannual variability in the 2-7 year band that could be driven by changes in tropical Pacific ENSO variability and/or the strength of the ENSO teleconnection modulated by extratropical pressure systems. Observed interannual precipitation variance increased and was associated with longer periodicities (5–7 years) when the Intertropical Convergence Zone (ITCZ) migrated southward (1370–1540 CE) and the Aleutian Low (AL) strengthened creating a robust ENSO teleconnection. Weak interannual precipitation variance with shorter periodicity (2–3 years) was observed when ITCZ shifted northward (700-900 CE) and/or the AL was weak (1540-1680 CE).

3.1 Introduction

The El Niño-Southern Oscillation (ENSO) drives a significant portion of interannual temperature and precipitation variability around the globe through 'teleconnections'. The origin of El Niño and its opposite phase - La Niña - is attributed to internal atmosphere-ocean interactions [*Cane and Zebiak*, 1985], however, short-term radiative forcing from volcanic and solar variability has also been implicated [*Emile-Geay et al.*, 2008; *Mann et al.*, 2005]. An ENSO teleconnection is a statistically significant climate response in a region distal to the ENSO forcing region in the equatorial Pacific. Understanding both ENSO variability and its global teleconnections requires long-duration annual reconstructions during different background climates. Yet, continuous multi-millennial sediment records often lack the annual resolution required for resolving ENSO frequencies [*Conroy et al.*, 2008] and/or suffer from poor age control [*Moy et al.*, 2002]. Fossil coral sequences provide well dated high temporal resolution (monthly to seasonal) records [*Cobb et al.*, 2003] but lack the duration to reconstruct continuous multi-centennial to millennial-scale records. In spite of these spatial and temporal limitations, paleoclimate reconstructions indicate considerable natural ENSO variability during the last millennium [*Cobb et al.*, 2003; *Emile-Geay et al.*, 2013; *Rustic et al.*, 2015].

The Mediterranean-type hydroclimate of Southern California results in limited water resources. Precipitation in southern California is highly variable, increasing the difficulty of managing the region's limited water resources. The tropics impact Southern California precipitation through an ENSO teleconnection; increased tropical mean zonal SSTs enhances tropical convection during El Niño events, producing stronger upper tropospheric tropical divergence and subtropical convergence that shifts the mid-latitude jet southward to bring more moisture to Southern California [*Seager et al.*, 2010; *Trenberth et al.*, 1998]. Simultaneously, an eastward shift of a deepened Aleutian Low (AL) advects warm, moist air onto North America, enhancing precipitation events in Southern California [*Trenberth et al.*, 1998]

Here we present a subannually resolved precipitation record from Southern California for the last 2000 years and explore tropical and extratropical forcing of the interannual variability in the record. The precipitation reconstruction is generated by ITRAX scanning X-ray fluorescence (XRF) Ti counts at 0.2 mm sampling intervals or 4–7 data points per year from box core SPR0901-04BC (588 m water depth; 34°16.895' N, 120°02.489' W) and kasten core SPR0901-03KC (591 m water depth; 34°16.914' N, 120°02.419' W) collected in Santa Barbara Basin (SBB), CA. Titanium is relatively immobile during chemical weathering, making the element an indicator of terrigenous detrital input to sediments [*Haug et al.*, 2001]. Annual precipitation variability is captured when terrestrial siliciclastic sediment is transported into SBB by river runoff, which only occurs when precipitation events exceed 0.25 cm [*Nezlin et al.*, 2005]. Thus, Ti in SBB sediments is significantly correlated with regional observed precipitation, including events associated with 20th century El Niño, and can be used to reconstruct Southern California hydroclimate [*Hendy et al.*, 2015; *Napier and Hendy*, 2016]. A ^{14}C-based chronology was generated employing Bacon 2.2 [*Blaauw and Christen*, 2011] with a variable reservoir ages and the Marine13 calibration curve [*Du et al.*, 2018; *Hendy et al.*, 2013] (Fig. B1 and Table B1). Ti peaks associated with winter siliciclastic laminae deposits were counted to produce an annually tuned chronology that is used to identify ENSO band periodicity. During droughts, winter siliciclastic laminae are not deposited in SBB, resulting in missing years in this annual tuned chronology. For this reason, the ^{14}C chronology is employed to determine absolute ages with annual tuning providing dating error estimates of <30 years.

3.2 Correlation between Southern Californian interannual precipitation and ENSO variability

Historical observations and models have related interannual winter precipitation variability in Southern California to ENSO [*Jong et al.*, 2016; *Seager et al.*, 2010; *Trenberth et al.*, 1998]. A field correlation between extended winter (November – April) Pacific sea surface temperature (SST) from 100° E–100° W and 26° S–66° N, and instrumental precipitation in Southern California (122°–114° W, 32°–36° N) from 1900 to 2013 further supports this relationship (Fig. 3.1; SST data are from NOAA ERSS Data Version 4 [*Huang et al.*, 2015]; precipitation data are from GPCC Full Data Reanalysis Version 6 [*Schneider et al.*, 2014]). Winter precipitation in Southern California is positively correlated ($p<0.013$; dashed line in Fig. 3.1a) to SSTs in both the central and eastern tropical Pacific, and the eastern North Pacific, while negatively correlated with SSTs in central North Pacific Ocean. When a 2–7-year bandpass filter was applied to examine the correlation coefficient on an interannual scale, the significantly correlated ($p<0.013$) regions in the North Pacific shrink (Fig. 3.1b). Consequently, the central and eastern tropical Pacific (the core region of the ENSO SST anomalies and ENSO index regions including Niño 3.4, 3 and 4), dominate the correlation between SSTs and precipitation on interannual time scales. Thus, Southern California winter precipitation increases when the central and eastern tropical Pacific Ocean warms, and the western tropical Pacific cools, similar to the El Niño SST pattern (Fig 3.1b).

We further explored whether the relationship with Southern California precipitation and ENSO persisted in the sedimentary archive of river runoff by comparing

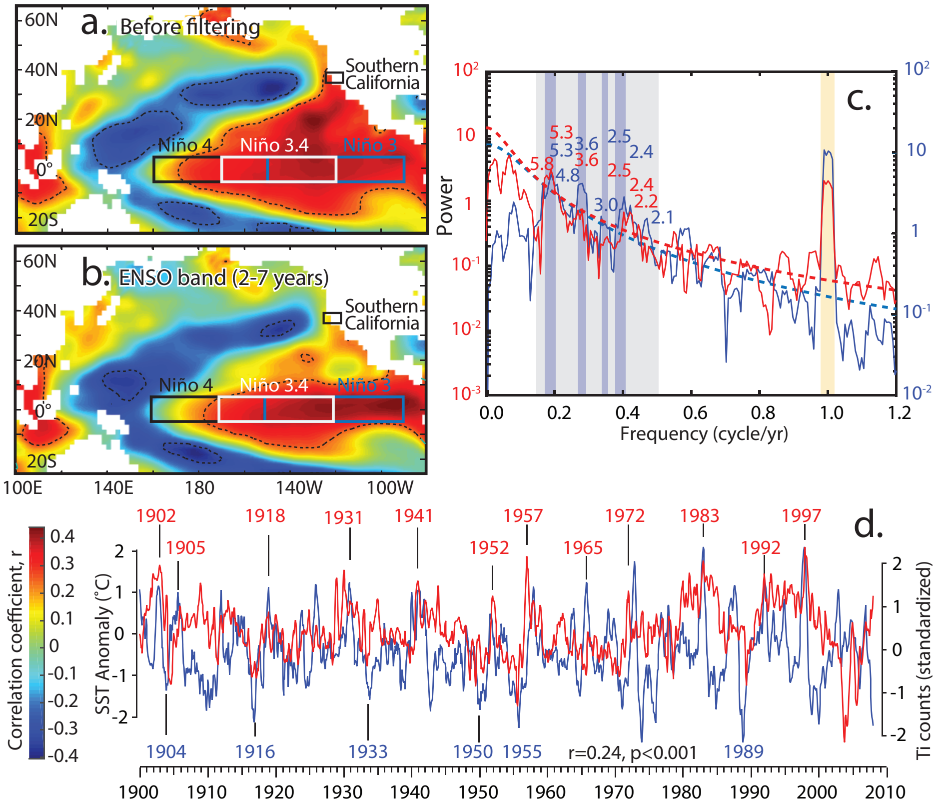

Figure 0-1 Field correlation of extended winter (Nov-April) SST in tropical and northern Pacific with (a) average, and (b) ENSO band (2–7 years) filtered extended winter (November–April) precipitation in Southern California from 1900–2013. The black dashed contour encloses regions significantly correlated (P<0.013) with Southern California precipitation. Monthly SST data (2˚ spatial resolution, 26˚ S to 66˚ N, 100˚ E to 100˚ W) are from the version 4 of NOAA Extended Reconstructed Sea Surface Temperature [*Huang et al.*, 2015] (NOAA_ERSST_V4 data from http://www.esrl.noaa.gov/psd/). Average monthly southern California precipitation data (0.5˚ spatial resolution, 32˚ N to 36˚ N, 122˚ W to 114˚ W, white dashed box) are taken from the GPCC Full Data Reanalysis Version 6.0 [*Schneider et al.*, 2014]. Santa Barbara Basin (SBB; red star), Niño 1+2 (white box: 0–10˚ S, 80˚W–90˚ W) Niño 3 (blue box: 5˚ N–5˚ S, 150˚ W–90˚ W), Niño 3.4 (black box: 5˚ N–5˚ S, 170˚ W–120˚ W), and Niño 4 (white box: 5˚ N–5˚ S, 160˚ E–150˚ W) [*Trenberth and Stepaniak*, 2001] are displayed. (c) Comparison of Ti time series from SPR0901-04BC (red line) and Niño 3.4 SST (blue line) from 1900 to 2008. (d) 2π prolate multitaper power spectrum of the annually tuned SPR0901-04BC Ti time series compared to the Niño 3.4 SST monthly time series from 1900 to 2008 [Rayner et al., 2003] (data source: http://www.esrl.noaa.gov/psd/gcos_wgsp/Timeseries/Nino34/). Periods exceeding 95 % confidence level of classical red noise modeling are labeled. Orange shading represents a π/4 phase lead/lag and the dashed line indicates no phase difference. All the significant signals (≥95% confidence level) produced by multitaper power spectrum (Fig. B4a), with coherency above 95% confidence level (Fig. B4b) and phase lag (Fig. B4c) within π/4 (equals 1.5 year for annual cycle) are marked with purple bars. The annual signal is indicated by a yellow bar. Niño

3.4 SST data (5° S-5° N and 170°-120° W average area) were calculated from the HadISST1 (Hadley Centre Sea Ice and Sea Surface Temperature data set).

20th century Ti counts from SBB sediments (SPR0901-04BC) with the Niño 3.4 SST anomalies (Fig. 3.1c-d, and B2). A statistically significant correlation coefficient (r=0.30, P <0.01) was found between the Niño 3.4 and the annually tuned 04BC Ti time series from 1900 to 2008 after a 2–7-year band pass filter was applied (Fig. B2). Multi-taper method (MTM) spectrum analysis (Fig. 3.1d) was then employed with the same data sets. The 04BC Ti time series contains significant (95 %) spectral peaks in the ENSO band (2–7 year) corresponding to 5.8, 5.3, 3.6, 2.5, 2.4 and 2.2 year periods consistent with Niño 3.4 SST, which contains significant (95 %) peaks at 5.3, 4.8, 3.6, 3.0, 2.5, 2.4 and 2.1 years (Fig. 3.1c). Cross-spectral analysis between the records reveals that all signals with coherency above the 95 % significance level and phase lag within π/4 (equals 1.5 years for an annual cycle) fall within ENSO band (at 5.3, 3.6 3.0 and 2.5 years, indicated by vertical purple bars) (Fig. B3b-c). Thus the relationship between interannual precipitation variability in Southern California and tropical ENSO forcing remains after river runoff sediments are deposited in SBB.

3.3 Interannual precipitation variability in Southern California during the Common Era

Southern Californian hydroclimate has varied significantly over the past 2000 years [*Cook et al.*, 2010; *Kirby et al.*, 2014]. High Ti counts in SBB (Fig. 3.2a), lake high stands [*C. A. Hiner et al.*, 2016; *Kirby et al.*, 2012; *Kirby et al.*, 2014; *Kirby et al.*, 2010] and the regional Palmer Drought Severity Index (PDSI) tree ring records [*Cook et al.*, 2010] indicate that Californian hydroclimate was wetter during the Little Ice Age (after 1300). Two megadroughts (~830–1075 and 1120–1300) during the Medieval Climate Anomaly associated with lake low stands [*Stine*, 1994], and identified in tree rings [*Cook et al.*, 2010] and low Ti in SBB, suggest a drier hydroclimate. Heavy rainfall in Southern California occurs during El Niño while La Niña results in less rain, so it has been assumed that a wetter Southern California hydroclimate implies a sustained El Niño-like ocean-atmosphere pattern while the megadroughts were associated with a cool La Niña-like state in the equatorial Pacific [*Cook et al.*, 2010; *Christine A Hiner*, 2016; *Kirby et al.*, 2014; *Li et al.*, 2011].

Employing MTM power spectrum analysis to explore 2000 years of interannual variability in the Ti time series, significant peaks (>95 % confidence level) are observed at 8.1, 6.3, 5.4, 4.6, 3.6, 3.3, 3.0, 2.3, and 2.1 year periods (Fig. B4). However, the power of these periodicity peaks changes within the 2–7-year ENSO band throughout the last 2000 years (Fig. B5). Wavelet spectrum analysis and an evolutionary FFT power spectrogram of the Ti time series shows significant (black contours in Fig. 3.2e) power in the 2–7-year ENSO band between 280–400, 650–680, 940–980, 1000–1140, 1270–1290,

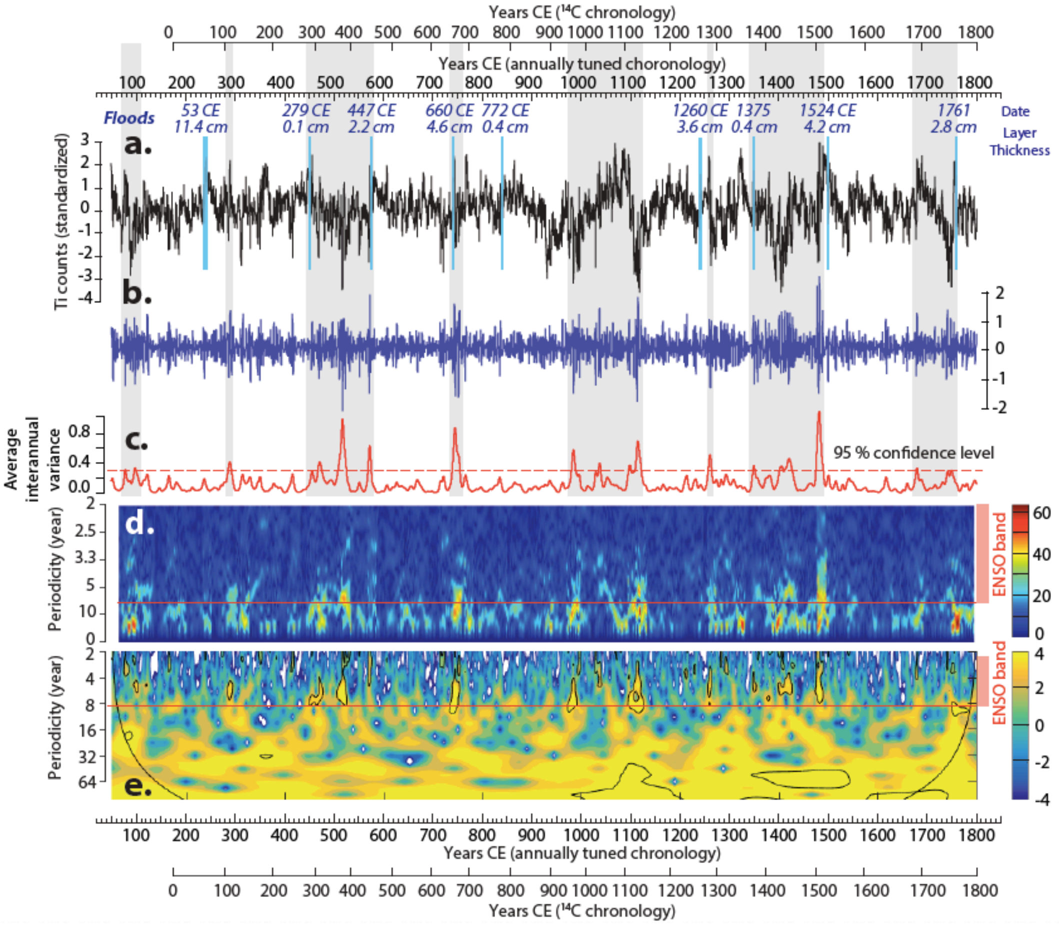

Figure 0-2 (a) The annually tuned SPR0901-03KC Ti time series (black line) after pre-whitening by subtracting the LOESS (locally estimated scatterplot smoothing) curve (with window equals to the length of the Ti time series) curve. Blue bars indicate flood layers. (b) Interannual precipitation variance of (a) isolated by applying a 2-to-7-year Taner bandpass filter. (c) Scale-average wavelet power spectrum over the 2–7 years for Ti time series (red line). Dashed red line is the 95 % confidence level. (d) Evolutionary FFT power spectrogram of the Ti time series with a 20-year sliding window. Power is not normalized per spectrum, with the highest power in dark red and the lowest in dark blue. (e) Wavelet analysis of the Ti time series. The thick contour encloses regions of > 95 % confidence for a red-noise process with a lag-1 coefficient. Gray shading represents intervals with strong interannual variability of the Ti time series.

1500-1520, 1750-1770 (based on ^{14}C chronology). Increased interannual variance based on the scale-averaged wavelet analysis of the Ti time series occurs between ~100–120, 280–460, 650–680, 950–1140, 1270–1290, 1370–1520 and 1680–1770, while decreased variance occurs between ~150–280, 500–600, 700–950, 1150–1270 and 1550–1680 (based on ^{14}C chronology) (Fig. 3.2c). The weak Ti interannual variance between 700–950 and 1150–1270 (Fig. 3.2) generally overlaps with megadroughts (~830–1075 and 1120–1300) indicated by reconstructed PDSI [*Cook et al,* 2010]. Exceptions occurred at 950–980, 1020–1040, and 1110–1140 as multidecadal droughts terminated, and may be associated with extreme precipitation events that shifted the hydroclimate state from dry to wet. For example in 20th century, the six-year drought in Santa Barbara County from 1986 to 1991 ended with precipitation events associated with the 1991–1992 El Niño event. Interannual precipitation variance was not consistent during the Little Ice Age: high variance was observed between 1370–1520 and 1680–1770, while low variance dominated 1540–1680 (Fig. 3.2).

3.4 Interannual precipitation variability in Southern California and ENSO

In the eastern equatorial Pacific, long hydroclimate records from the well-dated, low resolution El Junco Lake in the Galápagos Islands [*Conroy et al.*, 2008] show intensified precipitation between ~200–450 and 600–750 (Fig. 3.3a), reflecting higher ENSO variance along with more ENSO events in 100-year overlapping windows. Greater interannual precipitation variance recorded in SBB between 280–460 and 650–680 (Fig. 3.3e) agrees within age model and resolution uncertainties. However, the relationship between SBB and the eastern equatorial Pacific breaks down during the last millennium: higher interannual precipitation variance was observed in SBB during 1370–1520 and 1680–1770, while ENSO variance recorded in Galápagos Islands was weak during these two intervals (Fig. 3.3). Such inconsistencies between records could be related to the distinct teleconnection patterns of Eastern Pacific and Central Pacific ENSOs. Eastern Pacific El Niños, characterized by SST anomalies in the Eastern Equatorial Pacific (EEP), more likely contribute to heavy precipitation in the EEP by intensifying convection locally, while central Pacific El Niños, characterized by warming in the Niño 3.4 and 4 regions, are more closely associated with a stronger, south-shifted jet stream [*Mo*, 2010; *Parsons and Coats*, 2019; *Weng et al.*, 2009; *Yu and Zou*, 2013] that brings tropical moisture to Southern California. Increased interannual variance in Southern California precipitation between 1370–1520 and 1680–1770 suggests greater ENSO variance or stronger ENSO teleconnection between the tropical Pacific and North

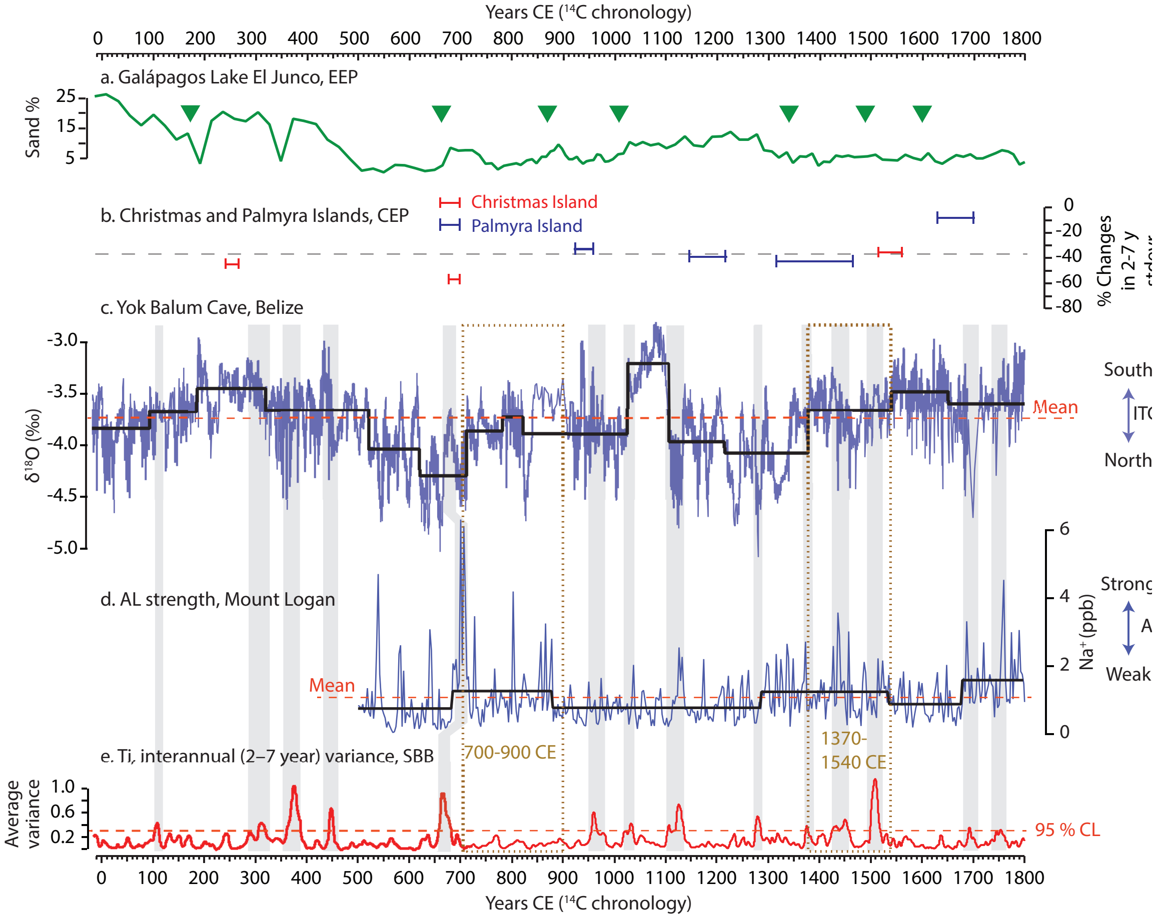

Figure 0-3 Southern California interannual precipitation compared to ITCZ migration, AL strength and ENSO variance strength in other ENSO reconstructions. (a) Sand abundance from lake El Junco [Conroy et al., 2008] Galápagos. (b) Relative ENSO variance (SD of the 2- to 7-year band, plotted as percent difference from 1968–1998) of fossil coral δ18O from Palmyra (blue) and Christmas (red) Islands, central Pacific Ocean [Cobb et al., 2003; Cobb et al., 2013]. (c) Yok Balum Cave δ18O speleothem, Belize [Kennett et al., 2012] indicating the ITCZ position. (d) Mount Logan annual Na+ concentration (pbb) indicating wintertime AL strength [Osterberg et al., 2014]. Mean values are shown with dashed red line. Regime shifts were detected using SRSD (black lines). (e) Scale-averaged interannual precipitation variance over 2–7-years of the standardized SPR0901-03KC Ti counts from this study. The 95 % confidence level is shown with red dashed lines. Intervals with strong ENSO variance are indicated by grey bars.

America. In the western Pacific tree-ring cellulose δ^{18}O from Taiwan (Fig. B6d) demonstrates higher central Pacific ENSO variance between ~1350-1600 [*Liu et al.*, 2017]. Tree-ring based North American Drought Atlas (NADA, Fig. B6d) also indicates increased ENSO variance between ~1400–1800 [*Li et al.*, 2011]. Well-dated decadal to centennial coral records with monthly resolution from Christmas and Palmyra Islands (Fig. 3.3b) in central tropical Pacific indicate higher ENSO variance during 1516–1561 and 1635–1703 [*Cobb et al.*, 2003; *Cobb et al.*, 2013]. $\delta^{18}O$ of individual *G. ruber* shells from Galápagos marine sediments (Fig. B6e) suggests increased ENSO activity after ~1500 [*Rustic et al.*, 2015].

Additionally, increased variability of reconstructed Niño 3.4 SST between ~1450–1550 was reported (Fig. B6f) [*Emile-Geay et al.*, 2013]. Taken together, the above high-resolution ENSO records from the tropical Pacific suggest increased ENSO variance since ~1350, while interannual precipitation variance recorded from SBB is weak during 1540–1680 (Fig 3.5). Thus SBB interannual precipitation variance is not only driven by ENSO variance in the tropical Pacific; the strength and position of midlatitude pressure systems in the north Pacific could be modulating the ENSO teleconnection between the tropical Pacific and North America.

3.5 The ENSO teleconnection in the northeastern Pacific

As the west coast of North America is not located in an ENSO SSTA core region, tropical climate influences precipitation in Southern California through an ENSO teleconnection. Although the teleconnection strength increases with the amplitude of tropical Pacific SST anomalies [*Diaz et al.*, 2001], the position and strength of extratropical pressure systems may complicate ENSO variance recorded in SBB. An intensified AL, associated with the southeastward shift of the low pressure center (AL) and North Pacific Jet Stream [*Rodionov et al.*, 2007], allows warm, moist air advection onto the West Coast, enhancing the tropical and mid-latitude Pacific climate coupling [*Osterberg et al.*, 2014]. The resulting intensified ENSO teleconnection increases Southern California's sensitivity to ENSO. When the AL is weak, the North Pacific High intensifies and shifts northward, creating a persistent high-pressure ridge and preventing moisture from reaching Southern California [*Rodionov et al.*, 2007; *Wang et al.*, 2014]. The resulting weak ENSO teleconnection consequently suppresses interannual precipitation variance recorded in SBB.

A comparison of AL strength and Southern Californian interannual precipitation variability records through Sequential Regime Shift Detection (SRSD) [*Rodionov*, 2004] supports the influence of shifting pressure system patterns on the ENSO teleconnection. A sea salt (Na^+) record from the Mount Logan ice core from Alaska [*Osterberg et al.*, 2014] records changes in AL strength in the eastern Pacific during the past 1200 years (Fig. 3.3d). A weak AL between 1540–1680 (Fig. 3.3d) is coincident with increased ENSO variance recorded by tropical Pacific proxies [*Cobb et al.*, 2003; *Cobb et al.*, 2013; *Liu et al.*, 2017; *Moy et al.*, 2002; *Rustic et al.*, 2015], when reduced interannual precipitation variance was observed in SBB (Fig. 3.3). This suggests a weak ENSO teleconnection may suppress the sensitivity of the Southern California hydroclimate to ENSO activity in tropical Pacific, leading to dampened interannual precipitation variance.

The migration of the ITCZ also potentially impacts ENSO variance in the tropical Pacific; a northward shift of the ITCZ strengthens the interhemispheric and equatorial Pacific zonal SST gradient, contributing to stronger cross-equatorial trade winds and reducing ENSO variance, while a southward shift of the ITCZ results in greater ENSO variance [*Chiang et al.*, 2008; *Rustic et al.*, 2015]. A high-resolution, well-dated speleothem $\delta^{18}O$ record from Yok Balum Cave (YBC), Belize [*Kennett et al.*, 2012] provides a subannually resolved precipitation archive mainly driven by the ITCZ displacement over the last two millennia (Fig. 3.3c). We compared this ITCZ-related precipitation reconstruction with intervals when the ENSO teleconnection in California was strong. Both 700-900 and 1370-1540 (^{14}C chronology; the duration of both intervals is 167 years within the annually tuned chronology) are characterized by a strong AL, minimizing the changing ENSO teleconnection influence on interannual precipitation in southern California. MTM spectrum analysis shows during 1370-1540, when ITCZ shifted southward, interannual precipitation variance was higher with longer periodicity (5–7 years, Fig. 3.4a, c); while when ITCZ moved northward in 700-900, the interannual precipitation variance was reduced with shorter periodicity (2–4 years, Fig. 3.4b, d). This result indicates that a southward shift of ITCZ contributes to stronger and longer-period ENSO events in Southern California's hydroclimate.

The correlation between ITCZ migration and the amplitude/frequency of ENSO has also been observed in modern observation and model simulation. A 20 % ENSO amplitude reduction over the last decade has been linked to a northward-displaced ITCZ and stronger cross-equatorial winds [*Hu and Fedorov*, 2018]. Relative to 1950-1970, the

ITCZ shifted southward in 1980-2000, causing the boreal spring to begin earlier and end later, and allowing more time for ENSO development, which could result in less frequent but stronger El Niño events [*Fang et al.*, 2008].

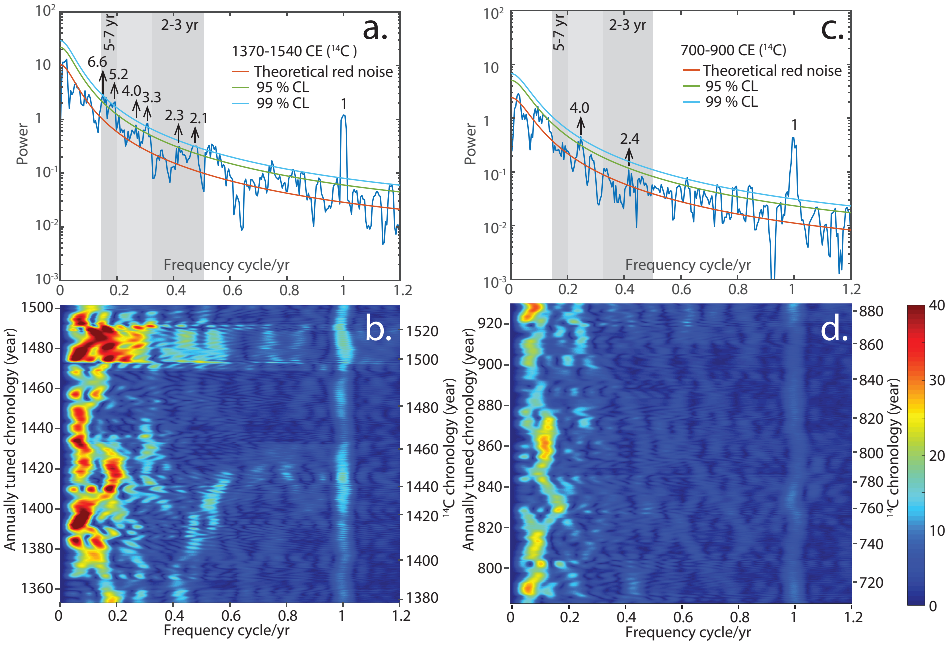

Figure 0-4 2π prolate multitaper power spectrum of two selected intervals from the SPR0901-03KC Ti time series from SBB: (a) 1370–1540 CE, (c) 700–900 CE. The two intervals are dated using the 14C chronology, while the duration of both intervals is 167 years according to the annually tuned chronology. Shaded areas represent the ENSO band (2–7 years). Confidence levels are shown with significant spectral peaks (⩾95% confidence level) labeled in years. Evolutionary FFT power spectrogram of Ti time series over (b) 1370–1540 CE and (d) 700–900 CE with a 20-year sliding window. Power is not normalized per spectrum for either series. The highest power is in dark red and the lowest is in dark blue.

From 0-500 CE, the ITCZ shifted southward, potentially leading to higher ENSO variance in the tropical Pacific, as indicated by the ENSO record from Galápagos Lake sediments (Fig. 3.3a). The Mount Logan AL record does not cover 0-500 CE, preventing evaluation of the impact of AL strength on interannual precipitation in Southern California. The northern position of the ITCZ and weak AL during 500–700 (Fig. 3.3c, d) led to persistent low interannual precipitation variance in Southern California (Fig. 3.3e). The isolated ENSO variance peak at 660-680 coincides with the extremely strong AL interval around 690–720. The ITCZ remained in a northerly position from 900–1370, except for a southward shift between 1020–1110 (Fig. 3.3c). A Kiritimati lake record in the central tropical Pacific supports a northward ITCZ position from ~900–1200, and a southward shift between ~1000–1050 [*Higley et al.*, 2018]. Additionally the AL was weak during 880-1280 (Fig. 3.3d). The generally low interannual Southern California precipitation variance between 700–950 and 1150–1280 is consistent with a weakened ENSO variance and/or ENSO teleconnection. Intervals of increased interannual precipitation variance during 950-1140 are related to the transition between dry and wet hydroclimate concurrent with the significant shift of ITCZ. The transient high ENSO variance at ~1280 might be associated with the 1257 Samalas volcanic eruption [*Gao et al.*, 2012] that impacted the winter of 1258, ahead of an extreme El Niño event [*Emile-Geay et al.*, 2008]. Thus, interannual precipitation in Southern California is driven by tropical ENSO variance, but is also modulated by extratropical pressure systems at multidecadal to centennial scales through ENSO teleconnections.

3.4 Conclusion

Interannual precipitation variability in Southern California is closely related to SST in tropical Pacific via an ENSO teleconnection. Subannually-resolved ITRAX scanning XRF Ti counts from SBB were used to reconstruct the Southern California hydroclimate during the past two millennia and indicate an interannual precipitation variability response to tropical and extratropical climate forcing. After ~1350, when the ITCZ shifted southward, interannual precipitation variance in Southern California was increased, except for a ~100 year interval (1550-1680) when the AL weakened. Thus extra-tropical pressure system activity modulates the ENSO teleconnection between tropical Pacific and North America. Two 200-year intervals associated with a robust ENSO teleconnection created by strong AL were selected to minimize the impact of mid-latitude pressure systems on precipitation and therefore explore the possible forcing of tropical Pacific ENSO variance on Southern California hydroclimate. Interannual precipitation variance in Southern California increased when the ITCZ migrated southward (1370–1540 CE), accompanied by longer periodicities (5–7 years). Weak interannual precipitation variance with shorter periodicity (2–3 years) was observed when ITCZ shifted northward (700-900 CE). Therefore, interannual precipitation in Southern California is driven by tropical ENSO variance via the ENSO teleconnection modulated by extratropical pressure systems.

3.5 References

Blaauw, M., and J. A. Christen (2011), Flexible paleoclimate age-depth models using an autoregressive gamma process, Bayesian Anal, 6(3), 457-474, doi: 10.1214/11-Ba618.

Cane, M. A., and S. E. Zebiak (1985), A Theory for El-Niño and the Southern Oscillation, Science, 228(4703), 1085-1087, doi: 10.1126/science.228.4703.1085.

Chiang, J. C. H., Y. Fang, and P. Chang (2008), Interhemispheric thermal gradient and tropical Pacific climate, Geophysical Research Letters, 35(14), doi: 10.1029/2008gl034166.

Cobb, K. M., C. D. Charles, H. Cheng, and R. L. Edwards (2003), El Niño/Southern Oscillation and tropical Pacific climate during the last millennium, Nature, 424(6946), 271-276, doi: 10.1038/nature01779.

Cobb, K. M., N. Westphal, H. R. Sayani, J. T. Watson, E. Di Lorenzo, H. Cheng, R. L. Edwards, and C. D. Charles (2013), Highly Variable El Nino-Southern Oscillation Throughout the Holocene, Science, 339(6115), 67-70, doi: 10.1126/science.1228246.

Conroy, J. L., J. T. Overpeck, J. E. Cole, T. M. Shanahan, and M. Steinitz-Kannan (2008), Holocene changes in eastern tropical Pacific climate inferred from a Galápagos lake sediment record, Quaternary Science Reviews, 27(11-12), 1166-1180, doi: 10.1016/j.quascirev.2008.02.015.

Cook, E. R., R. Seager, R. R. Heim, R. S. Vose, C. Herweijer, and C. Woodhouse (2010), Megadroughts in North America: placing IPCC projections of hydroclimatic change in a long-term palaeoclimate context, Journal of Quaternary Science, 25(1), 48-61, doi: 10.1002/jqs.1303.

Diaz, H. F., M. P. Hoerling, and J. K. Eischeid (2001), ENSO variability, teleconnections and climate change, International Journal of Climatology, 21(15), 1845-1862, doi: 10.1002/joc.631.abs.

Du, X., I. L. Hendy, and A. Schimmelmann (2018), A 9000-year flood history for Southern California: A revised stratigraphy of varved sediments in Santa Barbara Basin, Marine Geology, 397, 29-42.

Emile-Geay, J., K. M. Cobb, M. E. Mann, and A. T. Wittenberg (2013), Estimating central equatorial pacific SST variability over the past millennium. part II: Reconstructions and implications, Journal of Climate, 26(7), 2329-2352, doi: 10.1175/JCLI-D-11-00511.1.

Emile-Geay, J., R. Seager, M. A. Cane, E. R. Cook, and G. H. Haug (2008), Volcanoes and ENSO over the past millennium, Journal of Climate, 21(13), 3134-3148, doi: 10.1175/2007jcli1884.1.

Fang, Y., J. C. H. Chiang, and P. Chang (2008), Variation of mean sea surface temperature and modulation of El Nino-Southern Oscillation variance during the past 150 years, Geophysical Research Letters, 35(14), doi: 10.1029/2008gl033761.

Gao, C. C., A. Robock, and C. Ammann (2012), Volcanic forcing of climate over the past 1500 years: An improved ice core-based index for climate models, J Geophys Res-Atmos, 117, doi: 10.1029/2012jd018052.

Haug, G. H., K. A. Hughen, D. M. Sigman, L. C. Peterson, and U. Rohl (2001), Southward migration of the intertropical convergence zone through the Holocene, Science, 293(5533), 1304-1308, doi: 10.1126/science.1059725.

Hendy, I. L., T. J. Napier, and A. Schimmelmann (2015), From extreme rainfall to drought: 250 years of annually resolved sediment deposition in Santa Barbara Basin, California, Quaternary International, 387, 3-12, doi: 10.1016/j.quaint.2015.01.026.

Hendy, I. L., L. Dunn, A. Schimmelmann, and D. K. Pak (2013), Resolving varve and radiocarbon chronology differences during the last 2000 years in the Santa Barbara Basin sedimentary record, California, Quaternary International, 310, 155-168, doi: 10.1016/j.quaint.2012.09.006.

Higley, M. C., J. L. Conroy, and S. Schmitt (2018), Last Millennium Meridional Shifts in Hydroclimate in the Central Tropical Pacific, Paleoceanogr Paleocl, 33(4), 354-366, doi: 10.1002/2017pa003233.

Hiner, C. A. (2016), Late Holocene hydroclimatic variability linked to Pacific forcing: evidence from Abbott Lake, coastal central California.

Hiner, C. A., M. E. Kirby, N. Bonuso, W. P. Patterson, J. Palermo, and E. Silveira (2016), Late Holocene hydroclimatic variability linked to Pacific forcing: evidence from Abbott Lake, coastal central California, Journal of Paleolimnology, 56(4), 299-313, doi: 10.1007/s10933-016-9912-4.

Hu, S., and V. A. Fedorov (2018), Cross-equatorial winds control El Niño diversity and change, Nat Clim Change.

Huang, B. Y., V. F. Banzon, E. Freeman, J. Lawrimore, W. Liu, T. C. Peterson, T. M. Smith, P. W. Thorne, S. D. Woodruff, and H. M. Zhang (2015), Extended Reconstructed Sea Surface Temperature Version 4 (ERSST.v4). Part I: Upgrades and Intercomparisons, Journal of Climate, 28(3), 911-930, doi: 10.1175/Jcli-D-14-00006.1.

Jong, B. T., M. F. Ting, and R. Seager (2016), El Nino's impact on California precipitation: seasonality, regionality, and El Nino intensity, Environmental Research Letters, 11(5), doi: 10.1088/1748-9326/11/5/054021.

Kennett, D. J., et al. (2012), Development and Disintegration of Maya Political Systems in Response to Climate Change, Science, 338(6108), 788-791, doi: 10.1126/science.1226299.

Kirby, M. E., S. R. H. Zimmerman, W. P. Patterson, and J. J. Rivera (2012), A 9170-year record of decadal-to-multi-centennial scale pluvial episodes from the coastal Southwest United States: a role for atmospheric rivers?, Quaternary Science Reviews, 46, 57-65, doi: 10.1016/j.quascirev.2012.05.008.

Kirby, M. E., S. J. Feakins, C. A. Hiner, J. Fantozzi, S. R. H. Zimmerman, T. Dingemans, and S. A. Mensing (2014), Tropical Pacific forcing of Late-Holocene hydrologic variability in the coastal southwest United States, Quaternary Science Reviews, 102, 27-38, doi: 10.1016/j.quascirev.2014.08.005.

Kirby, M. E., S. P. Lund, W. P. Patterson, M. A. Anderson, B. W. Bird, L. Ivanovici, P. Monarrez, and S. Nielsen (2010), A Holocene record of Pacific Decadal Oscillation (PDO)-related hydrologic variability in Southern California (Lake Elsinore, CA), J Paleolimnol, 44(3), 819-839, doi: 10.1007/s10933-010-9454-0.

Kodama, K. P., and L. A. Hinnov (2015), Rock Magnetic Cyclostratigraphy, Rock Magnetic Cyclostratigraphy, 145-156.

Li, J. B., S. P. Xie, E. R. Cook, G. Huang, R. D'Arrigo, F. Liu, J. Ma, and X. T. Zheng (2011), Interdecadal modulation of El Nino amplitude during the past millennium, Nat Clim Change, 1(2), 114-118, doi: 10.1038/Nclimate1086.

Liu, Y., et al. (2017), Recent enhancement of central Pacific El Nino variability relative to last eight centuries, Nature Communications, 8, doi: 10.1038/ncomms15386.

Mann, M. E., M. A. Cane, S. E. Zebiak, and A. Clement (2005), Volcanic and solar forcing of the tropical Pacific over the past 1000 years, Journal of Climate, 18(3), 447-456, doi: 10.1175/Jcli-3276.1.

Mo, K. C. (2010), Interdecadal modulation of the impact of ENSO on precipitation and temperature over the United States, Journal of Climate, 23(13), 3639-3656, doi: 10.1175/2010JCLI3553.1.

Moy, C. M., G. O. Seltzer, D. T. Rodbell, and D. M. Anderson (2002), Variability of El Niño/Southern Oscillation activity at millennial timescales during the Holocene epoch, Nature, 420(6912), 162-165, doi: 10.1038/nature01194.

Napier, T. J., and I. L. Hendy (2016), The impact of hydroclimate and dam construction on terrigenous detrital sediment composition in a 250-year Santa Barbara Basin record off southern California, Quaternary International, doi: 10.1016/j.quaint.2016.07.045.

Nezlin, N. P., P. M. DiGiacomo, E. D. Stein, and D. Ackerman (2005), Stormwater runoff plumes observed by SeaWiFS radiometer in the Southern California Bight, Remote Sensing of Environment, 98(4), 494-510, doi: 10.1016/j.rse.2005.08.008.

Osterberg, E. C., P. A. Mayewski, D. A. Fisher, K. J. Kreutz, K. A. Maasch, S. B. Sneed, and E. Kelsey (2014), Mount Logan ice core record of tropical and solar influences on Aleutian Low variability: 500-1998 AD, J Geophys Res-Atmos, 119(19), 11189-11204, doi: 10.1002/2014jd021847.

Paillard, D., L. Labeyrie, and P. Yiou (1996), Macintosh Program performs time-series analysis, Eos, Trans. Am. Geophys. Union, 77(39), 379, doi: 10.1029/96EO00259.

Parsons, L. A., and S. Coats (2019), Ocean-Atmosphere Trajectories of Extended Drought in Southwestern North America, Journal of Geophysical Research: Atmospheres.

Rayner, N. A., D. E. Parker, E. B. Horton, C. K. Folland, L. V. Alexander, D. P. Rowell, E. C. Kent, and A. Kaplan (2003), Global analyses of sea surface temperature, sea ice, and night marine air temperature since the late nineteenth century, J Geophys Res-Atmos, 108(D14), doi: 10.1029/2002JD002670.

Reimer, P. J., et al. (2013), IntCal13 and Marine13 radiocarbon age calibration curves 0–50,000 years cal BP, Radiocarbon, 55(4), 1869-1887.

Rodionov, S. N. (2004), A sequential algorithm for testing climate regime shifts, Geophysical Research Letters, 31(9), doi: 10.1029/2004gl019448.

Rodionov, S. N., N. A. Bond, and J. E. Overland (2007), The Aleutian Low, storm tracks, and winter climate variability in the Bering Sea, Deep-Sea Res Pt Ii, 54(23-26), 2560-2577, doi: 10.1016/j.dsr2.2007.08.002.

Rustic, G. T., A. Koutavas, T. M. Marchitto, and B. K. Linsley (2015), Dynamical excitation of the tropical Pacific Ocean and ENSO variability by Little Ice Age cooling, Science, 350(6267), 1537-1541, doi: 10.1126/science.aac9937.

Schimmelmann, A., I. L. Hendy, L. Dunn, D. K. Pak, and C. B. Lange (2013), Revised ~2000-year chronostratigraphy of partially varved marine sediment in Santa Barbara Basin, California, Geologiska Föreningen i Stockholm Förhandlingar (GFF), 135(3-4), 258-264, doi: 10.1080/11035897.2013.773066.

Schimmelmann, A., C. B. Lange, W. H. Berger, A. Simon, S. K. Burke, and R. B. Dunbar (1992), Extreme climatic conditions recorded in Santa Barbara Basin laminated sediments: the 1835-1840 Macoma event, Marine Geology, 106(3-4), 279-299, doi: 10.1016/0025-3227(92)90134-4.

Schneider, U., A. Becker, P. Finger, A. Meyer-Christoffer, M. Ziese, and B. Rudolf (2014), GPCC's new land surface precipitation climatology based on quality-controlled in situ data and its role in quantifying the global water cycle, Theoretical and Applied Climatology, 115(1-2), 15-40, doi: 10.1007/s00704-013-0860-x.

Seager, R., N. Naik, M. Ting, M. A. Cane, N. Harnik, and Y. Kushnir (2010), Adjustment of the atmospheric circulation to tropical Pacific SST anomalies: Variability of transient eddy propagation in the Pacific-North America sector, Q J Roy Meteor Soc, 136(647), 277-296, doi: 10.1002/qj.588.

Stine, S. (1994), Extreme and persistent drought in California and Patagonia during medieval time, Nature, 369(6481), 546-549, doi: 10.1038/369546a0.

Thomson, D. J. (1982), Spectrum estimation and harmonic analysis: Proceedings of the IEEE, 70(9), 1055-1096.

Trenberth, K. E., and D. P. Stepaniak (2001), Indices of El Nino evolution, Journal of Climate, 14(8), 1697-1701, doi: 10.1175/1520-0442(2001)014<1697:Lioeno>2.0.Co;2.

Trenberth, K. E., G. W. Branstator, D. Karoly, A. Kumar, N. C. Lau, and C. Ropelewski (1998), Progress during TOGA in understanding and modeling global teleconnections associated with tropical sea surface temperatures, J Geophys Res-Oceans, 103(C7), 14291-14324, doi: 10.1029/97jc01444.

Wang, S. Y., L. Hipps, R. R. Gillies, and J. H. Yoon (2014), Probable causes of the abnormal ridge accompanying the 2013-2014 California drought: ENSO precursor and anthropogenic warming footprint, Geophysical Research Letters, 41(9), 3220-3226, doi: 10.1002/2014GL059748.

Weng, H. Y., S. K. Behera, and T. Yamagata (2009), Anomalous winter climate conditions in the Pacific rim during recent El Niño Modoki and El Niño events, Climate Dynamics, 32(5), 663-674, doi: 10.1007/s00382-008-0394-6.

Yu, J. Y., and Y. H. Zou (2013), The enhanced drying effect of Central-Pacific El Nino on US winter, Environmental Research Letters, 8(1), doi: Artn 014019 10.1088/1748-9326/8/1/014019.

Chapter 4

High-Resolution Interannual Precipitation Reconstruction of Southern California: Implications for Holocene ENSO Evolution

Abstract

The El Niño-Southern Oscillation (ENSO) is the leading driver of global interannual climate variability through ‘teleconnections’. ENSO variability on centennial to millennial time-scales is poorly understood due to the insufficient length, continuity, or resolution of existing paleoclimate records. Field correlation analysis of historical observational data demonstrates that interannual precipitation changes in Southern California are closely related to ENSO in the tropical Pacific through an atmospheric teleconnection. Here we present a sub-annually resolved scanning XRF Ti record from deep-sea cores collected from Santa Barbara Basin (SBB) to reveal interannual precipitation changes in Southern California for the past 9000 years. Wavelet analysis of the SBB Ti record demonstrates interannual (2–7 years) precipitation variance was relatively weak and associated with shorter intervals (2¬–3 years) between events prior to 4.4 ka. Interannual precipitation variance in Southern California increased after 4.4 ka, accompanied by the appearance of longer periods (5–7 years) within the ENSO-band.

By synthesizing our proxy record and previously published ones, we suggest that a southward shift of the Intertropical Convergence Zone (ITCZ) in the late Holocene may have weakened the zonal SST gradient and southeasterly trade winds across the equatorial Pacific and amplified ENSO variability. Meanwhile, a deeper, westward-shifted Aleutian Low after 4.4 ka may have strengthened the ENSO teleconnection between the tropical Pacific and Southern California and amplified interannual precipitation variance in the SBB record. The interpretation of our SBB precipitation record and the inferred dynamical linkage with processes in the tropical Pacific and extratropics are supported by simulations of the mid and late Holocene using the Community Earth System Model.

4.1. Introduction

The El Niño Southern Oscillation (ENSO) is the leading driver of global-scale interannual climate variability (Vecchi and Wittenberg, 2010). ENSO is a periodic variation in sea surface temperature (SST) and air pressure across the tropical Pacific that oscillates between El Niño (warm phase) and La Niña (cold phase) with a period of 2–7 years. ENSO impacts precipitation and temperature around the globe via atmospheric and oceanic teleconnections (Vecchi and Wittenberg, 2010). Instrumental observations indicate the phase and variability of ENSO have changed over the past few decades (Hu et al., 2017), but the length of these records (<150 years) is insufficient to determine whether these changes originate from internal variability or are forced by climate change. Paleo-ENSO reconstructions can extend the instrumental record, providing the opportunity to explore long-term ENSO variability under different mean climate states. ENSO variations on centennial to millennial timescales have been attributed to numerous mechanisms including internal climate variability (Cobb et al., 2013), as well as external forcing such as orbital-driven insolation changes (Clement et al., 2000), volcanic aerosols (Emile-Geay et al., 2008), and solar output variability (Mann et al., 2005). However, the response of ENSO and ENSO teleconnections to changes in mean climate states, notably global warming, remain uncertain.

A variety of proxies have been used to reconstruct ENSO variability during the Holocene, including fossil coral (Cobb et al., 2013), marine and lacustrine sediments (Conroy et al., 2008; Rein et al., 2005), tree rings (Liu et al., 2017), and speleothems (Chen et al., 2016). However, many paleo-ENSO records lack sufficient length and continuity, or resolution to fully document millennial-scale ENSO variability. For example, reconstructions based on fossil coral from equatorial Pacific provide direct record of ENSO-related SST changes with precise chronology and high temporal resolution (Cobb et al., 2013), but are limited in duration (< 50 years on average) and discontinuous (with gaps up to 900 years). Annual-resolution tree ring data from tropics and the mid-latitudes with strong ENSO signals are usually restricted to the last millennium (Liu et al., 2017). Subannual-resolved speleothem ENSO records are also limited by short duration and discontinuity (Chen et al., 2016). Sediments records can be long and continuous but often lack the temporal resolution required to resolve ENSO-band variability, and thus mainly reflect changes in mean climate state (Conroy et al., 2008). These restrictions in proxy systems prohibit the study of the frequency and amplitude of ENSO variability on centennial to millennial timescales.

Southern California has a Mediterranean climate, characterized by cool wet winters and hot dry summers, and highly variable total annual precipitation. In summer, the North Pacific High (NPH) strengthens and moves northward, deflecting storm fronts to the north and resulting in little summer precipitation. In winter, the NPH moves to a southward position during winter, causing storms to track over Southern California. Winter precipitation in Southern California is influenced by ENSO via a teleconnection between the tropical Pacific and North America (Fig. 4.1): during El Niño years, anomalously warm SST and enhanced deep convection in the tropical Pacific induce Rossby wave propagation from the equator to the extratropics over the North Pacific (Trenberth et al., 1998). As a result, the Aleutian Low (AL) deepens and the North Pacific Jet (NPJ) intensifies and moves southeastward, leading to a southward shift of the storm track over the North Pacific (Fig. 4.1A) and greater precipitation in Southern California (Seager et al., 2010). Therefore, annual precipitation reconstructions in Southern California should integrate information on ENSO variability in the tropical Pacific when the ENSO teleconnection is strong.

Santa Barbara Basin (SBB), located in the Southern California Bight, contains continuous, annual-scale marine sediment records that provide valuable material for precipitation reconstruction. The high tectonic uplift rates of Santa Ynez Mountains (>5 mm/yr) contribute to unusually high sedimentation rates in SBB (Thunell, 1998). In winter, precipitation events generate episodic sediment-laden discharge from Santa Clara, Ventura and Santa Ynez River, delivering terrigenous detrital siliciclastic sediments to SBB as plumes (Warrick and Farnsworth, 2009). The amount of precipitation and storm intensity controls sediment flux into the basin such that precipitation events can be identified by high concentrations of siliclastic sediment-associated elements such as Ti (Hendy et al., 2015). Titanium is relatively immobile during chemical weathering and therefore commonly used as an indicator of terrigenous detrital input in sediments (Haug et al., 2001). Transfer function modeling demonstrates that Ti concentration in SBB is significantly correlated with regional precipitation and therefore is suitable for precipitation and river runoff reconstructions (Napier and Hendy, 2016).

During spring and summer, strong coastal upwelling associated with the northward displacement of NPH produces a biogenic sediment flux in SBB (Thunell, 1998; Warrick and Farnsworth, 2009) that can be identified by high concentrations of biogenic sediment-associated elements (Hendy et al., 2015). Suboxic bottom water in the center of SBB prevents bioturbation such that the seasonal deposition of biogenic and terrigenous detrital sediments is preserved in SBB as annual laminae (varve), resulting in

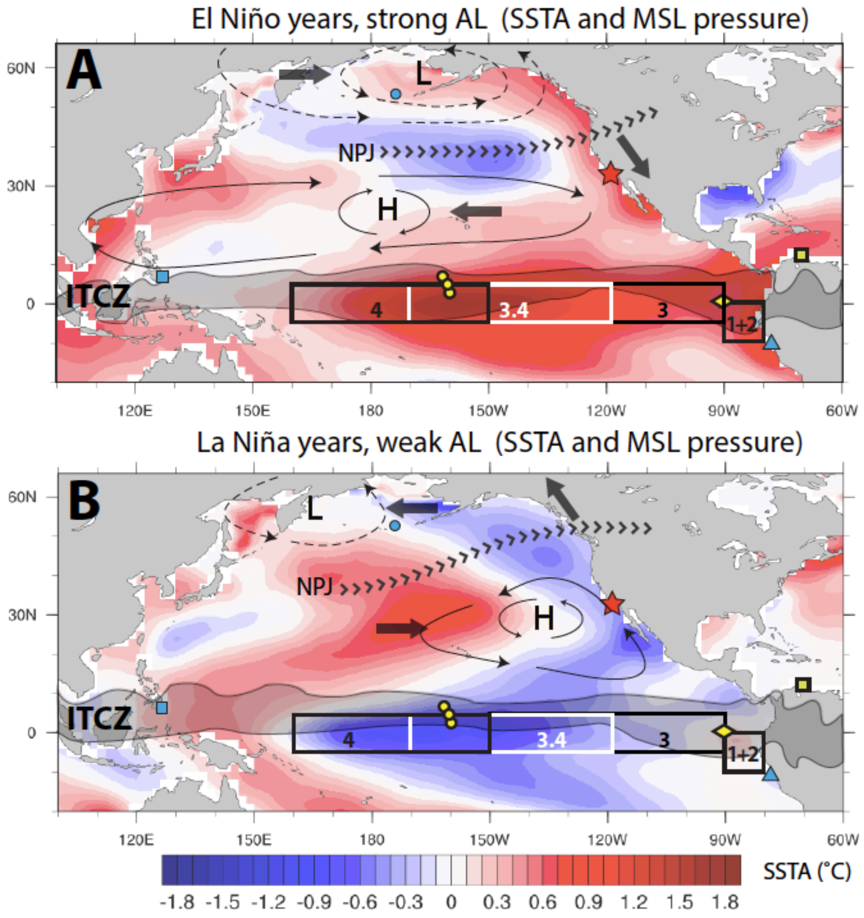

Figure 0-1 Schematic map showing average SSTA (sea surface temperature anomalies), the position of atmospheric pressure systems, and the North Pacific Jet (NPJ) in (A.) moderate to strong El Niño years and (B.) La Niña years. Arrows represent movement direction of atmospheric circulation. The locations of Santa Barbara Basin (red star), Cariaco Basin (yellow square), Heart Lake (blue circle), Northern Line Islands (yellow dots), core V21-30 (yellow diamond) and Lake El Junco (yellow diamond), core 106KL (blue triangle), and core MD98-2181 (blue square) are marked.

continuous laminated sediment sequences spanning warm climate intervals of the late Quaternary (Hendy et al., 2015; Schimmelmann et al., 1992).

Here we present a 9000-year subannually resolved Ti record from laminated sediments in SBB that reconstructs Holocene precipitation in Southern California. Time series analysis of this record is used to identify the amplitude and frequency of ENSO-related precipitation variability. We compare this Southern California precipitation reconstruction with other ENSO records in the Pacific Basin and climate simulations, using a state-of-the-art Earth system model, to explore the possible mechanisms driving ENSO-related interannual precipitation changes in Southern California, and the frequency and amplitude of ENSO variance during Holocene.

4.2 Material and methods

4.2.1 Sediment cores

The 9000-year precipitation reconstruction was produced from cores that targeted material from 2009 CE through the Holocene (Fig. 4.1A). The box core SPR0901-04BC (34° 16.895’ N, 120° 02.489’ W; 588 m water depth) spans the interval 1788 –2008 CE (Hendy et al, 2016). The kasten core SPR0901-03KC (34° 16.914’ N, 120° 02.419’ W; 591 m water depth; 03KC) spans the interval 46 –2089 years BP (Du et al., in press), the jumbo piston core MV0811-14JC (34° 16.906’ N, 120° 02.162’ W; 580 m water depth; 03KC) spans 1787 –9065 years BP, and ODP Hole 893A (34° 17.25’ N 120° 02.2’ W; 588 m water depth; 893A) includes the entire Holocene. Kasten core SPR0901-06KC (34° 16.914’ N, 120° 02.419’ W; 591 m water depth; 06KC) and 03KC are proximal cores with almost identical sedimentology. All cores are laminated and contain flood layers and turbidites. The “instantaneous” flood layers and turbidites are logged in all cores based on highly resolved imaging and then employed to correlate 14JC with 893A, 06KC, and 03KC. Core 14JC and 03KC were spliced together to create a master record at subannual resolution extending from 150 to 9000 years BP.

4.2.2 Bulk elemental analysis

4.2.2.1 Scanning X-ray fluorescence

Core 04BC, 03KC and 14JC were scanned using a second-generation ITRAX core XRF scanner at the University of Minnesota Duluth. A range of elements was analyzed; only Ti counts were used in this study. All cores were scanned at 0.2 mm intervals using a Cr tube with 8 seconds count time for core 04BC and 03KC, and 16 second count time for 14JC. Raw XRF data were reprocessed using Q-Spec 8.6.0 software to optimize peak fitting. The ITRAX scanner outputs results as counts per minute and these counts are considered semi-quantitative (Croudace et al., 2006).

4.2.2.2 Quantitative elemental analysis

Core 14JC was sampled at 2–10 cm to generate bulk sediment samples for additional elemental analysis. Samples were freeze-dried, powdered and digested with hydrofluoric, nitric, per- chloric and hydrochloric acids. Elemental concentration was determined using inductively coupled plasma-mass spectrometry (ICP-MS) and inductively coupled plasma-atomic emission spectroscopy (ICP-AES) at ALS Laboratories in Vancouver Canada. The standard errors of measurements of lab standards GBM908-10 and MRGeo08 are ± 0.01% for titanium (Ti). Titanium counts determined by scanning XRF are significantly linearly correlated with Ti concentration determined by ICP-MS measurement (R^2= 0.90 for section 1–3; R^2=0.81 for section 4–8). For core 03KC and 14JC, the high-resolution Ti series estimated ITRAX scanning XRF (in unit of counts per minute) was converted to Ti concentration (weight percent) using the described linear relationship, which were used in the time series analysis.

4.2.3 Age model

4.2.3.1 Radiocarbon chronology

A high-resolution radiocarbon chronology was generated for SBB sediment cores using mixed planktonic foraminifera dates from kasten core SPR0901-06KC (Hendy et al., 2013), piston core MV0811-14JC and core ODP Hole 893A. This chronology is described in detail in Du et al. (2018). The chronology was generated as follows: the thickness of instantaneous layers (flood layers and turbidites) was subtracted from the original cores to generate a corrected depth, which only incorporates background sedimentation. The ^{14}C dates from the ODP Hole 893A and SPR0901-06KC were translated to the corrected depth scale of MV0811-14JC to generate a master chronology for SBB sediments. To avoid the impact of ^{14}C plateaus during the last 300 years, five stratigraphic marker layers with dates generated from varve chronology (Schimmelmann et al., 1992) were used in the age model. These marker layers were identified in SPR0901-03KC and previous core studies from central SBB (Hendy et al., 2013; Hendy et al., 2015; Schimmelmann et al., 1992), including: the coretop (1905 CE), a gray layer at 1861–62 CE, the *Macoma* layer at 1841 CE, a turbidite at 1811 CE and a gray layer at 1761 CE.

An age-depth model from 46 to 9066 years BP was generated using the software Bacon 2.2 (Blaauw and Christen, 2011). Bacon uses Bayesian statistics to reconstruct coherent accumulation histories by combining radiocarbon dates with known sedimentary information (Blaauw and Christen, 2011). ^{14}C dates were converted to years BP using Marine 13 calibration curves (Reimer et al., 2013). Hendy et al. (2013) estimated variable reservoir ages for the last 2000 years, which were applied to this age model. A constant reservoir age (ΔR) of 147 ± 70 years was used beyond 2000 years based on the last constrained surface ocean reservoir age (Hendy et al., 2013). Thirty-eight ^{14}C dates from core SPR0901-06KC (Hendy et al., 2013), 44 ^{14}C dates from core MV0811-14JC, 7 dates from core ODP Hole 893A and 5 varve chronology dates of marker layers are used in this age model.

4.2.3.2 Annually tuned chronology

The maximum value of Ti is deposited in the sediments of SBB following winter rainfall (Hendy et al., 2015). Thus, we assume each Ti peak represents a single year. Ti maxima resolved by 4-7 data points were visually counted downcore to generate an annual tuned chronology. The Ti time series was assigned an annually tuned chronology in Matlab using the script *depthtotime.m.* Time series analyses in this study were based on our annually tuned chronology. Because missing years occur in the annually tuned chronology when winter siliciclastic laminae failed to deposit in SBB, we used radiocarbon chronology when comparing our SBB record to other paleoclimate records. The dating error estimated by comparing the annually tuned and radiocarbon chronology is <30 years.

4.2.4 Time series analysis

The multi-taper method (MTM) power spectrum (Thomson, 1982) of the annual-tuned SBB Ti time series was computed using Matlab's *pmtm.m*. The Ti time series was pre-whitened by removing a LOESS (locally estimated scatterplot smoothing) curve computed over the length of the time series using Matlab's *smooth.m*. The MTM power spectrum was computed and tested against an order 1 autoregressive red noise spectrum at 95% and 99% confidence levels using *classicredpad.m*; the 1-year cycle was removed prior to red noise estimation using *deharm.m*; and interannual (2–7 year) variability of the Ti time series was bandpass-filtered using *tanerfilter.m* (the three scripts are available at http://mason.gmu.edu/~lhinnov/cyclostratigraphytools.html). The interannual variance of Ti was calculated for 100-year windows along the time series. Cross-spectrum analysis was performed in the software package Analyseries (Paillard et al., 1996) using the Blackman-Turkey method with a Bartlett window and 50% of the time series.

Morlet wavelet analysis was computed using the software package *wavelets* (http://paos.colorado.edu/research/wavelets//) to reveal the localized variations of power within the annual-tuned Ti time series. Scaled-average ENSO variance is defined as the weighted sum of the wavelet power in the 2–7-year band, which was tested against lag-1 autoregressive red noise spectrum at the 95% confidence level.

4.2.5 Regime shift analysis

The Sequential Regime Shift Detection (SRSD) method was used to detect the regime shifts (Rodionov, 2004) in the interannual variance of Holocene Ti time series from SBB. Weighed means of the regimes were calculated using the Huber weight function (tuning constant =2). The length of the regimes is 2000 data points (~420 years). Target p-value equals 0.05. The SRSD was performed in *Excel* using the software package *Regime shift test-v6.2.xlsm (*https://sites.google.com/site/climatelogic/).

4.2.6 Field correlation analysis

The field correlation between extended winter (November– April) SST in the region within 100° E– 100° W, 26° S– 66° N and Southern California (defined as the region within 122° W– 114° W, 32° N– 36° N) extended winter precipitation from 1900/10 to 2013/04 was calculated to verify the relationship between Southern California precipitation and ENSO. Monthly SST data with 2°× 2° spatial solution are from NOAA Extended Reconstructed Sea Surface Temperatures version 4 (Huang et al., 2015). The monthly Southern California precipitation data at 0.5° are taken from the GPCC (Global Precipitation Climatology Centre) Full Data Reanalysis version 6.0 (Schneider et al., 2011). The mean extended winter precipitation in Southern California is calculated by averaging precipitation in each gridded cell. The linear trend of precipitation and SST are removed for the following analysis using Matlab's *detrend.m*. SST in the Niño 3.4 region

(120°W-170°W, 5°S-5°N; see also Fig. 4.1) is used as the ENSO index. (The Niño 3.4 SST index data are from https://www.esrl.noaa.gov/psd/gcos_wgsp/Timeseries/Nino34/ .)

4.2.7 Climate modeling

Four Holocene simulations, including pre-industrial (1850 AD), 3 ka, 6 ka and 9 ka timeslices, were performed using the Community Earth System Model version 1.2 (CESM1.2, Hurrell et al., 2013). CESM1.2 is comprised of coupled general circulation models of the atmosphere and ocean, as well as models of sea ice and land surface. CESM simulates realistic ENSO variability and teleconnections in present-day and past climates (Zhu et al., 2017). The Holocene experiments were forced by boundary conditions consistent with protocols from the Paleoclimate Modeling Intercomparison Project phase 4 (PMIP4), including altered greenhouse gas concentrations, orbital parameters, ice sheets and vegetation coverage (Otto-Bliesner et al., 2017). Following PMIP4 recommendations, evergreen shrub and savanna/steppe were prescribed over the Sahara and boreal forest at the Northern Hemisphere high latitudes in 6-ka and 9-ka experiments. Other boundary conditions including aerosol emission and solar constant were prescribed at their pre-industrial values. All the simulations were run for at least 900 model years at an atmosphere and land resolution of 1.9°×2.25° and an ocean and sea ice resolution of nominal ~1°. The upper ocean in Holocene simulations (3 ka, 6 ka and 9 ka) has reached quasi-equilibrium with a top-of-the-atmosphere radiation imbalance comparable with that of the pre-industrial simulation (<0.09 W m^{-2}). Monthly model output from the last 200 years of each simulation was analyzed. A 2–7-year bandpass filter was applied to extract interannual variability.

4.3 Results

4.3.1 20th century precipitation and ENSO

The field correlation demonstrates that winter precipitation in Southern California is positively correlated with SSTs of the central and eastern tropical Pacific, and eastern north Pacific, while negatively correlated with western tropical and western-central North Pacific SSTs (Fig. 4.2A) (Du et al., in press). A 2–7-year bandpass filter was applied to Southern California precipitation in order to separate the ENSO-related interannual oscillation from multi-decadal (30–60 year) climate variability and the correlation significance is tested using P values (shown as black dashed contour in Fig. 4.2). The correlation coefficient of Southern California precipitation and central and eastern tropical Pacific SST (in the eastern of Niño 3.4 region and Niño 3 region) increases after the 2–7-year bandpass filter is applied, while regions with significant correlation (P<0.013; indicated by black dashed contour in Fig. 4.2B) in the North Pacific shrink (Fig. 2B). After a multi-decadal (30–60-year) band-pass filter is applied, Southern California precipitation is significantly positively correlated (P<0.013) with eastern North Pacific SSTs and negatively correlated with the western-central North Pacific SSTs, while no significant correlation (P<0.013) is found with any Niño regions in the tropical Pacific (Fig. 4.2C).

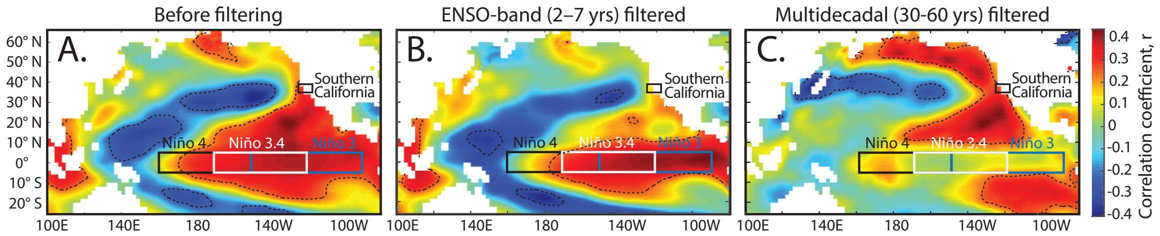

Figure 0-2 Fig. 2 Field correlation of extended winter (Nov-April) SST in tropical and Northern Pacific with (A) average, (B) ENSO band (2–7 years) filtered, and (C) Multidecadal (30–60 years) filtered extended winter (Nov–April) precipitation in Southern California from 1900–2013. The black dashed contour encloses regions significantly correlated (P<0.05) with Southern California precipitation. SST data are from NOAA ERSS Data Version 4; precipitation data are from GPCC Full Data Reanalysis Version 6. Boxes represent regions used to calculate SST anomalies are indicated for Niño 4 (black box), Niño 3.4 (white box) and Niño 3 (blue box). Adapted from Du et al. (2020).

We applied the MTM analysis to the annually tuned Ti time series of SPR0901-04BC and instrumental Niño 3.4 SST time series between the years 1870 to 2008, and then used cross-spectral analysis to test the coherence between these two records. The Ti time series show significant (>95% CL) spectral peaks within the ENSO band (2–7-year) at 5.9, 4.3 and 2.4 years (Fig. 4.3A), generally consistent with the significant ENSO signals at 5.5, 5.0, 3.6, 2.8, 2.5 and 2.1 years in the Niño 3.4 SST time series (Fig. 4.3B). Cross-spectral analysis demonstrates that all signals with significant coherency (>95% CL) and phase lag < π/4 (< 1.5 months for a 1-year cycle) fall within the 2–7-year ENSO band.

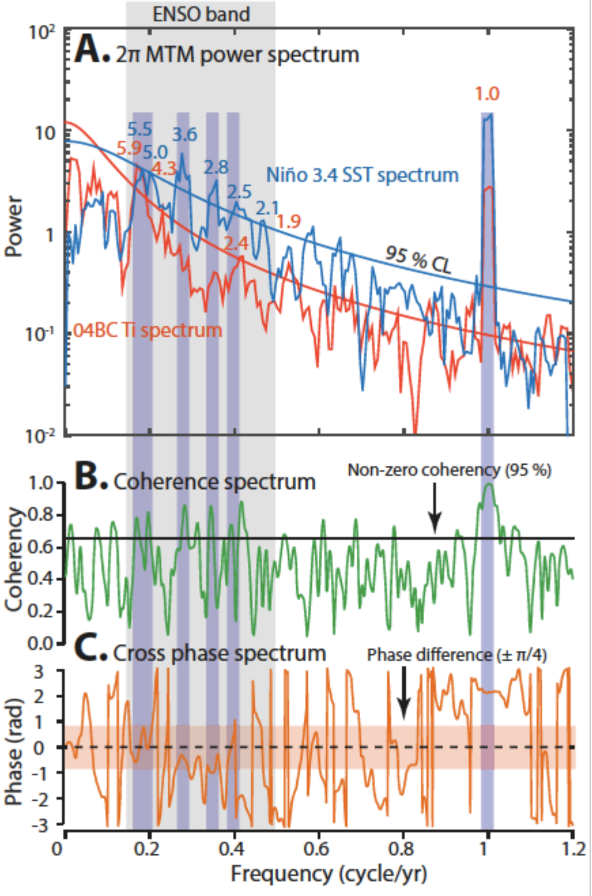

Figure 0-3 (A) 2π MTM power spectrum of the annually tuned SPR0901-04BC Ti time series (red line) compared to the Niño 3.4 SST monthly time series (blue line) from 1870 to 2008 (data source: http://www.esrl.noaa.gov/psd/gcos_wgsp/Timeseries/Nino34/). Peaks exceeding 95% confidence level of classical red noise modeled after removal of the 1-year cycle are labeled in years. (B) The coherence spectrum of the Niño 3.4 SST and Ti time series (green line), with the 95 % confidence level indicated and (C) cross-phase spectrum of the Niño 3.4 SST and Ti time series (orange line). Orange shading represents ±π/4 phase and the dashed line indicates no phase difference. Niño 3.4 SST data (5˚ S-5˚ N and 170˚-120˚ W average area) were calculated from the HadISST1 (Hadley Centre Sea Ice and Sea Surface Temperature data set). Cross-phase spectrum was calculated using AnalySeries 2.0.8.2. Grey shading represents frequencies in the 2–7 year ENSO-band, while blue shading indicates signal with coherency above the 95% significance level and phase lags within π/4 fall within the 2–7 year ENSO-band. Adapted from Du et al. (2020).

4.3.2 Ti time series over the past 9 ka

In order to explore the modulation of interannual precipitation changes on centennial to millennial time scales over the full 9000-year Ti record, the Holocene trend was removed using a LOESS curve with the window equal to the length of the Ti time series (dashed line in Fig. 4.4A). SRSD was used to detect the time and magnitude of shifts in 2–7-year band wavelet power. After 4.4 ka, the weighted mean of ENSO-band

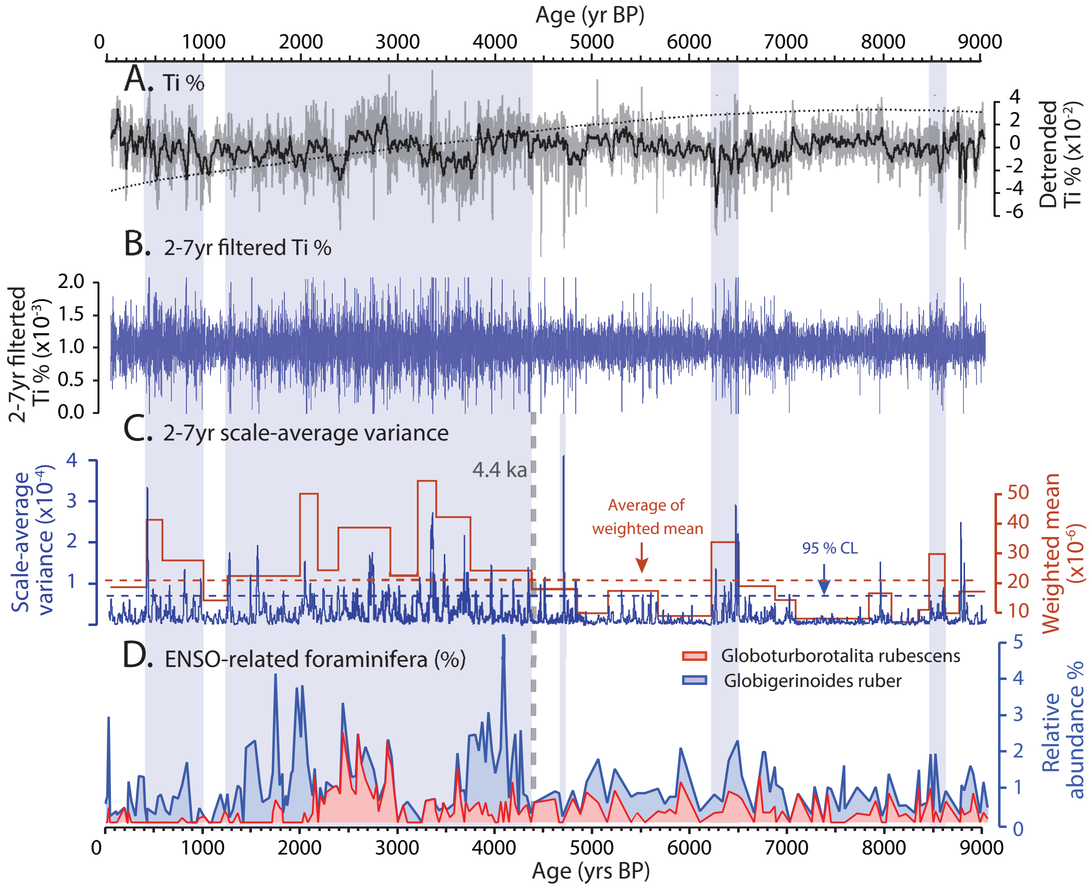

Figure 0-4 Comparison of Ti time series and warm planktonic foraminifera species in Santa Barbara Basin. (A) Standardized Ti concentration from SBB (gray line), smoothed using 100-point moving window (black solid line). The LOESS (locally estimated scatterplot smoothing) curve has been subtracted from the Ti time series to remove the long-term trend (black dashed line). The window of the LOESS curve equals to the length of the Ti time series. (B) 2- to 7-year bandpass filtered Ti time series. (C) The 2–7-year scale-average variance of the Ti time series (blue line) and 95% confidence level (blue dashed line), and the weighted mean (red line) produced by Sequential Regime Shift Detection (SRSD) and average of weighted mean (red dashed line). Shaded blue bars indicate intervals of high interannual precipitation variance identified by SRSD weighted means above average. (D) Relative abundance of warm planktonic foraminifera species Globigerinoides ruber (blue shading) and Globoturborotalita rubescens (red shading) from ODP Site 893 in SBB (Fisler and Hendy, 2008).

wavelet power (red solid line) is higher than average (red dashed line), excepting between 0-0.4 and 1-1.2 ka. Additionally, the 2–7-year scale-averaged wavelet power of the Ti time series continuously exceeds the 95% confidence level (Fig. 4.4C). A 2–7-year bandpass filter was applied to the Ti time series (Fig. 4.4B), and its variance in 100-year windows was found to decrease by 48.6% prior to 4.4 ka. Energetic 2–7-year band precipitation

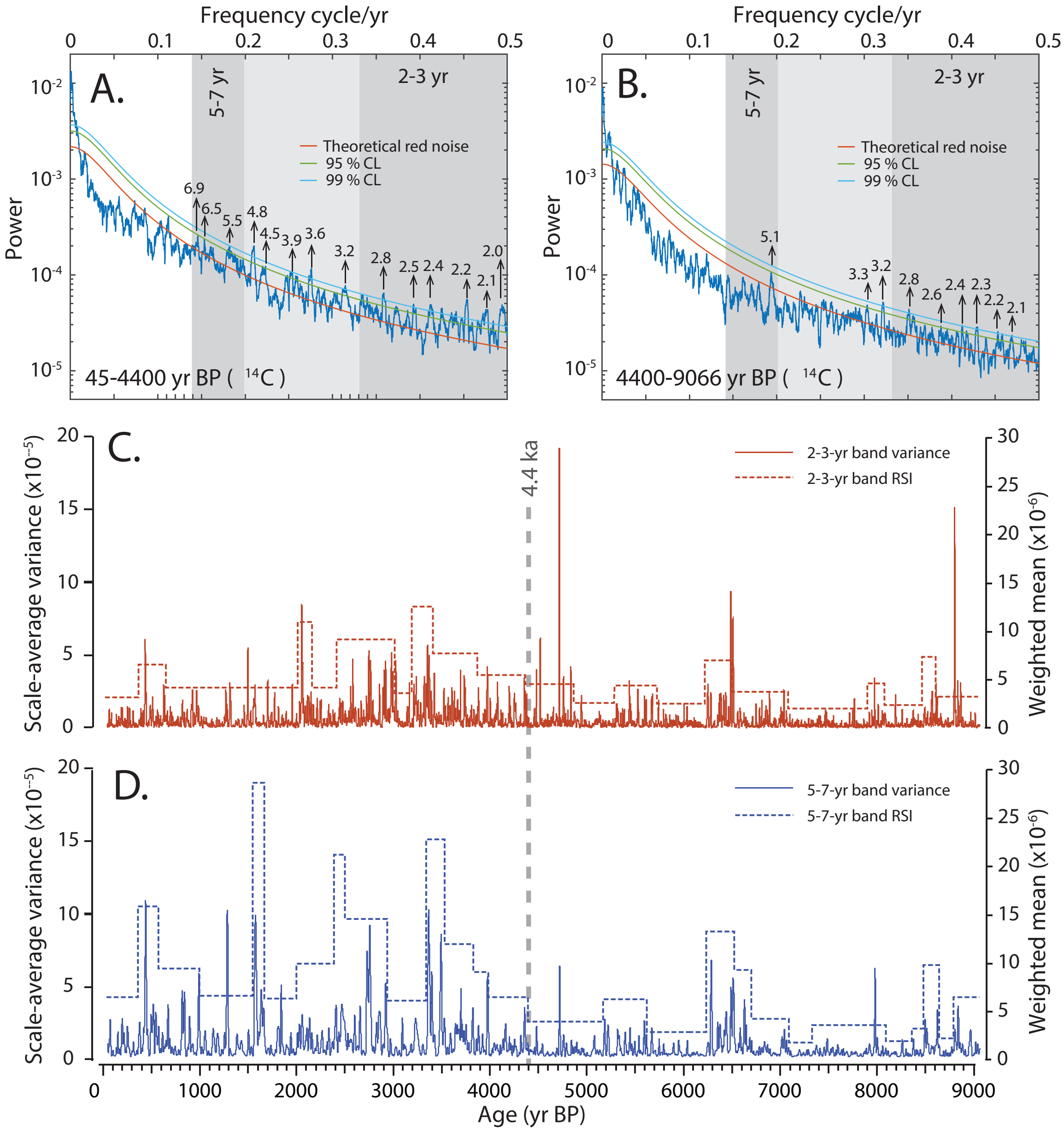

Figure 0-5 2π MTM power spectrum of the annually tuned Ti time series of (A) 45¬–4400 years BP, and (B) 4400–9066 years BP. Order 1 autoregressive red noise (red line) is shown with 95% (green line) and 99% (light-blue line) confidence levels. Significant spectral peaks (⩾95% confidence level) are labeled in years. ENSO-band frequencies are indicated by grey shading. (C) Scale-average 2–3-yr band variance of the Ti time series (red line) and Sequential Regime Shift Detection (SRSD) of shifts in the 2–3-yr variance (dashed red line). (D) Scale-average 5–7-yr band variance (blue line) of the Holocene Ti time series and SRSD of shifts in the 5–7-yr variance (dashed blue line).

variance (> 95% confidence level) was observed between 8.6–8.9, 6.3–7.0, 1.2–4.4 and 0.4–1.0 ka. Between 8.1–8.5, 7.1–7.9, 5.7–6.2, 4.9–5.2, 1.0–1.2 and 0–0.4 ka, ENSO related precipitation variance was relatively weak and below the 95% confidence level (Fig. 4.4C).

Power spectrum analysis displays changes in ENSO-band frequency and variance throughout the Holocene (Fig. 4.5A and 5B). Within the ENSO band, significant shorter-period cycles (with a periodicity of 2–3 years) are observed in the late to mid-Holocene. Longer-period ENSO-band cycles (periodicity at 5.5, 6.5 and 6.9 years) are significant during late Holocene, but are dramatically dampened during the mid-Holocene, with only one significant cycle at 5.1 years. Scale-averaged variance within the 2–3 yr and 5–7 yr bands was computed separately to reveal changes in ENSO variance at different frequencies. SRSD shows that 5–7 yr ENSO variance was stronger during the late Holocene (after ~4.4 ka) compared with the variance in the mid-Holocene (Fig. 4.5D). A moderate change was observed in ENSO variance at periodicities of 2–3 yr throughout the last 9 ka, with higher values between 2–3.5 ka (Fig. 4.5C).

4.3.3 Model simulations

Evolution of the ENSO variability and precipitation over Southern California in CESM simulations agree well with our reconstructions in the SBB. The interannual (2–7-year) variance of Niño 3.4 SST is 69% lower in the 6 ka and 9 ka simulations than in the late Holocene simulations (0 ka and 3 ka, Fig. 4.6A). The interannual variance of Southern California precipitation (122° W– 114° W, 32° N– 36° N) is reduced by 52% in the 6-ka and 9-ka time-slice experiments compared to late Holocene (0 ka and 3 ka), consistent with the 49% reduction in the interannual variance of Ti from SBB. The winter (DJF) precipitation, sea level pressure and wind speed at 850 hPa, relative to pre-industrial condition, was calculated for 3 ka and 6 ka to determine how precipitation and atmospheric pressure conditions changed between the late and mid Holocene (Fig. 4.7A and 7B). At ~10°N, winter precipitation at 6 ka was enhanced relative to the Pre-industrial, accompanied by stronger SE trade winds across the equator (Fig. 4.7B). Additionally, a weaker AL and westerly winds, and a reduction of precipitation at ~ 35°N on the North American margin were observed at 6 ka relative to the pre-industrial (Fig. 4.7B). Notably, averaged winter precipitation in Southern California is reduced by 30.5% compared to the pre-industrial simulation. The 3-ka experiment exhibits a generally similar atmospheric circulation and precipitation with that in the pre-industrial

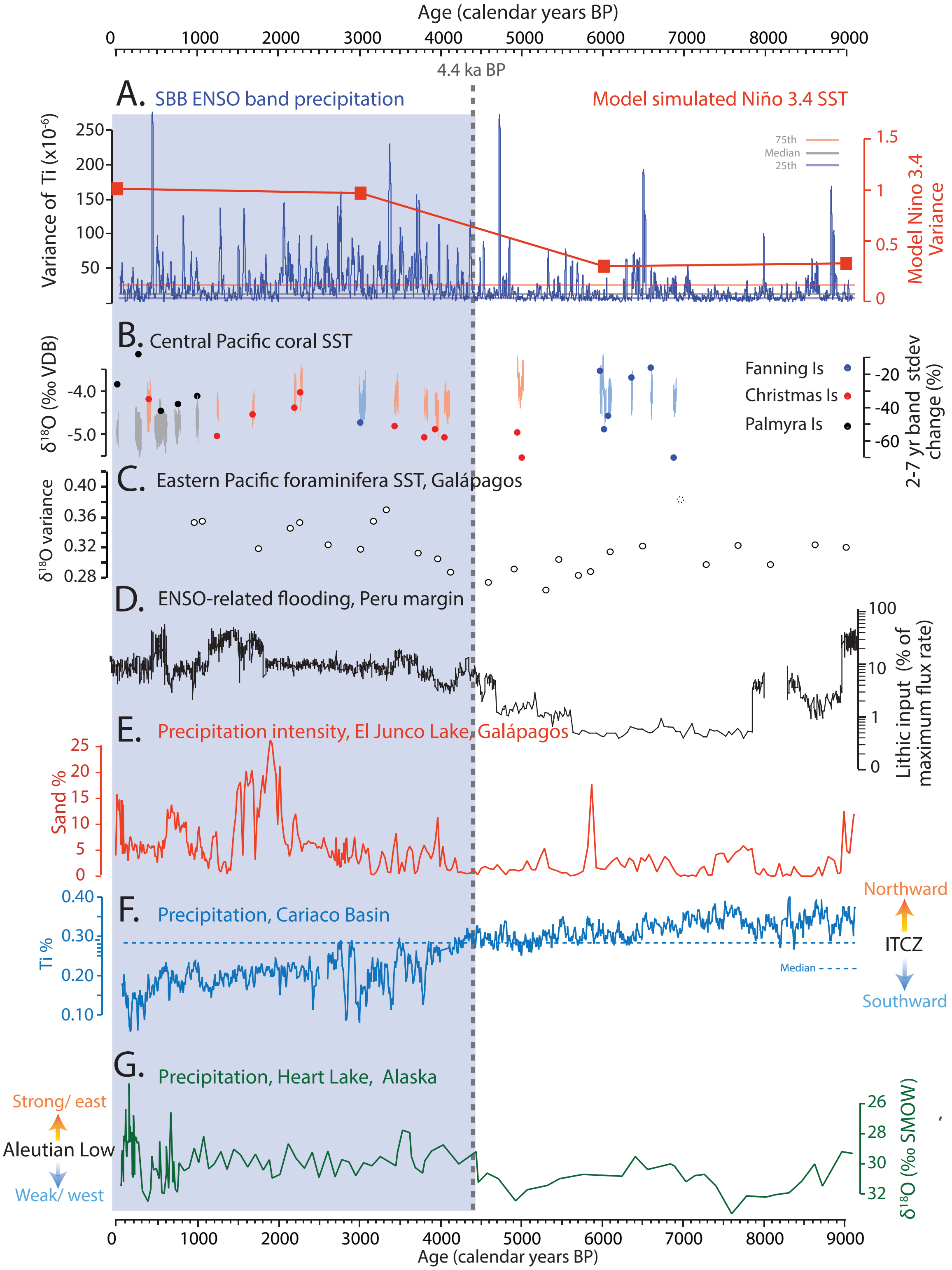

Figure 0-6 Comparison of ENSO-band interannual precipitation variance in Southern California, ENSO reconstructions from the tropical Pacific, ITCZ migration and Aleutian Low reconstruction for the Holocene. (A) 2–7-year variance of the Ti time series in running 100-year windows (blue line), and 2–7-year variance of Niño 3.4 SST (red boxes) from the 4 time-

slice simulations (pre-industrial, 3 ka, 6 ka, and 9 ka) in this study. (B) Central tropical Pacific Northern Line Islands fossil coral δ18O (‰, relative to Vee Dee Belemite) from Fanning Island (blue lines), Christmas Island (red lines), and Palmyra Island (black lines) (Cobb et al., 2013). The standard deviation of the 2–7-year band (dots) is plotted as percent difference from 1968–1998 intervals of a corresponding modern coral δ18O time series from each site (Cobb et al., 2013). (C.) δ18O variance of individual Globigerina ruber from Core V21-30, eastern equatorial Pacific (open circles) (Koutavas and Joanides, 2012). The variance sample (dashed circle) at 7,000 years BP is driven by two outliers (Koutavas and Joanides, 2012). (D.) The lithic flux rate of core 106 KL, off Peru, as a percent relative to the maximum flux (black line) (Koutavas and Joanides, 2012). (E.) Sand (%) from El Junco Lake sediments in the Galápago Islands (red line) (Conroy et al., 2008). (F) ITCZ migration indicated by Ti (%) from Cariaco Basin (light blue line) (Haug et al., 2001). (G.) Aleutian Low reconstruction based on δ18O diatom (‰, relative to Vienna Standard Mean Ocean Water (VSMOW)) from Heart Lake, Aleutian Islands Alaska (Green line) (Bailey et al., 2018).

simulation, with a slightly higher precipitation at ~5°N and lower precipitation along the western coast of US. No evident change in the strength of trade wind was observed, and AL strength was only slightly reduced compared to the pre-industrial simulation.

4.4. Discussion

4.4.1 20th century precipitation in Southern California

The field correlation between Southern California winter precipitation and SSTs (1900–2013) reveals the climatic processes driving precipitation variability in Southern California during the last 113 years (Du et al., in press). The spatial pattern of the correlation coefficient indicates an ENSO-driven teleconnection between tropical Pacific SSTs and Southern California: i.e. regions with positive correlation coefficient (warm color in Fig. 4.2A) have warm SSTA during El Niño years shown in Fig. 4.1A. Thus, abnormal warming of the central and eastern tropical Pacific and eastern north Pacific coincides with greater winter precipitation in Southern California. The close relationship between ENSO and interannual precipitation variability in Southern California can be further demonstrated by applying a 2–7-year bandpass filter to precipitation (Fig. 4.2B). The correlation between precipitation and tropical SST remains strong while that with the North Pacific SST decreases after the band-pass filter, confirming that interannual precipitation in Southern California is mainly driven by tropical SST (Du et al., 2020).

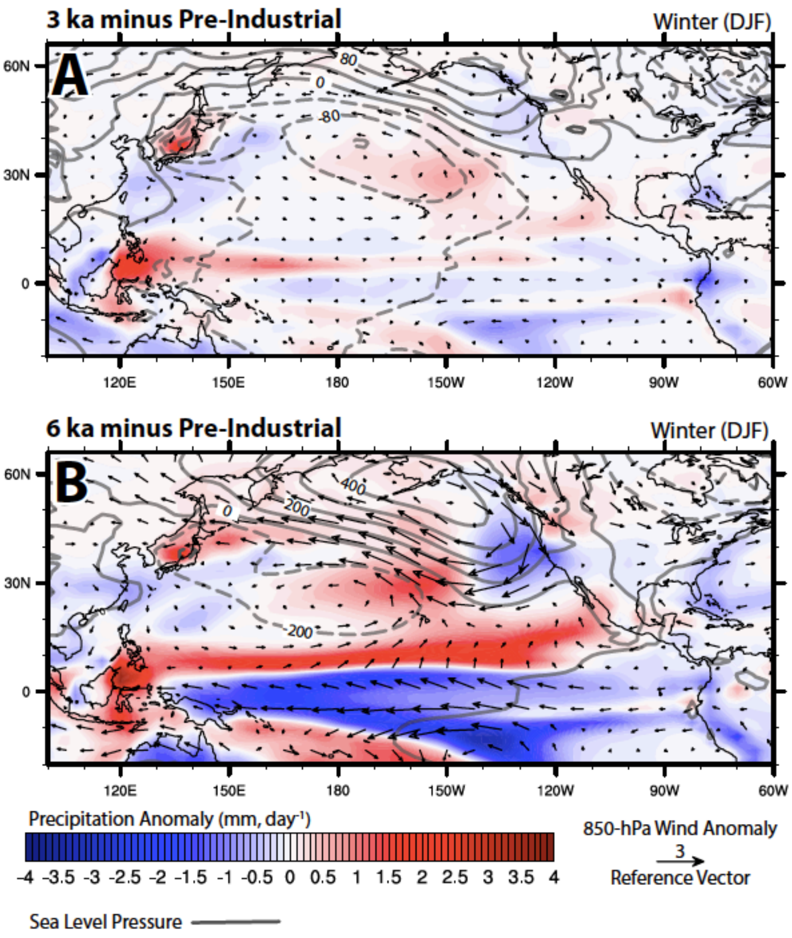

Figure 0-7 Simulated precipitation rate (mm/ day) with dry anomalies indicated by blue shading (>-4 mm/day) and wet anomalies in red shading (<4 mm/day), wind speed vectors at 850 hPa (arrows: m/s), and sea level pressure (Pa) with positive (solid gray line) and negative (dashed gray line) anomalies for the (A) 3 ka and (B) 6 ka time-slices, relative to the pre-industrial control simulation.

Warmer tropical SSTs during El Niño events enhance atmospheric convection in the central Tropical Pacific, producing intensified upper tropospheric tropical divergence and subtropical convergence (Trenberth et al., 1998). The resulting enhanced atmospheric Rossby wave propagation to midlatitude pressure systems produces a deepened AL (Trenberth et al., 1998), that consequently strengthens and shifts the North Pacific Jet (NPJ) southward. This in turn, deflects storm tracks resulting in more precipitation in Southern California. Meanwhile, the correlation between Southern California precipitation and North Pacific SST increases after 30–60-yr band-pass filtering (more positive in the eastern North Pacific and more negative for the Central and Western

Pacific), while no statistically significant correlation (P<0.013) was found with SST of ENSO regions in tropical Pacific. These correlations indicate (Fig. 4.2C) that Southern California precipitation responds to North Pacific SSTs and potentially atmospheric pressure systems on multidecadal timescales.

4.4.2 ENSO variance recorded in SBB during the Holocene

ENSO's impact on Southern California precipitation during the Holocene is demonstrated by SBB Ti variance in the ENSO (2–7 year) band. The 2–7-year scale-averaged wavelet spectrum (as shown in Fig. 4.4C) of the Ti time series is relatively weak before 4.4 ka, except between 6.3–6.6 ka and 8.6–8.9 ka, but increased after ~4.4 ka, especially between 1.2–4.4 and 0.4–1.0 ka. This indicates shifts between strong El Niño and La Niña events and/or extreme El Niño events occurred more frequently, or the ENSO teleconnection between the tropical Pacific and Southern California was enhanced during the late Holocene.

Stronger El Niño events after ~4.4 ka is supported by a greater abundance of El Niño displaced subtropical species in Southern California. During El Niño years, warm tropical-subtropical waters are advected northward along the western coast of North America via a Kelvin wave, contributing to warmer nearshore surface waters and deeper thermocline (Lynn et al., 1998). For example, during the extreme El Niño year 1997-98, the SST in SBB during late summer-early fall of 1997 was nearly 3°C warmer than the same period of 1996 (a non-El Niño year), while during the January-March of 1998, the SST was 1–2 °C warmer than the same period during the two previous years (Wolter and Timlin, 1998).

Tropical, warm water species are associated with the warmer SSTs and deeper thermocline resulting from El Niño events and can be used to identify such conditions in the past. A higher relative abundance of warm-water species planktonic foraminiferal species *Globigerinoides ruber* and *Globoturborotalita rubescens* (previously called *Globigerina rubescens*) found at ODP Site 893 from SBB (Fisler and Hendy, 2008) (Fig. 4.4D) from 1.3 to 4.4 ka. G. *ruber* and G. *rubescens* are subtropical species that prefer warm-water conditions (Parker, 1962). The relative abundance of these two species in both SBB sediments and sediment traps was increased dramatically during extreme 1982-83 and 1997-98 El Niño events (Black et al., 2001; Lange et al., 1987). G. *ruber* and G.

rubescens were likely transported to SBB with the warm tropical-subtropical water advection produced by ENSO-related Kelvin wave, and may be used to reconstruct past El Niño events in SBB (Black et al., 2001). Thus, the increase of G. *ruber* and G. *rubescens* during 1.3– 4.4 ka (Fig. 4.4D), concurrent with higher interannual precipitation variance (Fig. 4.4C), supports the presence of stronger and/or more frequent El Niño events during late Holocene.

4.4.3 Holocene ENSO evolution

The high-resolution Ti record in SBB indicates an increase in ENSO variance in tropical Pacific during the late Holocene (after ~ 4.4 ka, Fig. 4.4C). This result is supported by model simulations that reproduce the long-term trend in ENSO variability observed in SBB sediments (Fig. 4.6A): lower ENSO-band variance of Niño 3.4 SST in the early-mid Holocene (9 ka and 6 ka) simulations, and higher variance in the late Holocene (pre-industrial and 3 ka) simulations. Considering dating uncertainties, a more energetic interannual precipitation variance and more El Niño events during late Holocene recorded in SBB generally agrees with precipitation- and SST-proxy reconstructions of ENSO from the tropical Pacific - the core region of ENSO activity.

Increased El Niño-related rainfall is suggested by a marine sediment record from coastal Peru (Rein et al., 2005) that indicates increased relative lithic sediment flux after ~4.5 ka, associated with more frequent strong flood events, notably during 2–4 ka (Fig. 4.6D). Greater and more variable sand abundance in El Junco Lake sediments, Galápagos (eastern tropical Pacific) after 4.2 ka (Fig. 4.6E) suggests an increased precipitation intensity and more frequent El Niño events (Conroy et al., 2008). The standard deviation (square root of variance) of a 2–7 year bandpass filtered coral δ^{18}O from Northern Line Islands in central tropical Pacific (Cobb et al., 2013) indicates greater ENSO variance during late Holocene (dots, Fig. 4.6B). Increased ENSO variance after ~4 ka is observed in the SST of the equatorial cold tongue, measured from δ^{18}O variance (squared standard deviation) of individual foraminifera retrieved from core V21-30 (Fig. 4.6C), located in the eastern equatorial Pacific (Koutavas and Joanides, 2012). Additionally, Mg/Ca SSTs of *G. ruber* indicates cooler western Pacific warm pool (Stott et al., 2002) and warmer eastern Pacific cold tongue (Koutavas et al., 2006) has been interpreted to be the product of a more El Niño-like mean state after 4 ka, especially between 2–4 ka.

Relatively weak interannual precipitation variance in SBB sediments between 4.4 to 8.3 ka (Fig. 4.4C) indicates either damped ENSO variability and fewer strong El Niño events and/or a weak ENSO teleconnection during mid Holocene. However, the absence of strong El Niño events is supported by precipitation reconstructions based marine and lacustrine sediments in Eastern Equatorial Pacific (EEP): a reduced lithic sediment flux and few El Niño flood events were observed between 4.5–8.5 ka in coastal Peru (Rein et al., 2005) (Fig. 4.6D), while lower sand abundance in the sediments of El Junco lake in Galápagos between 4.2 ka–8.8 ka (Conroy et al., 2008) (Fig. 4.6E). These records of reduced precipitation agree with SST records in eastern equatorial Pacific: theδ^{18}O of individual foraminifera in core V21-30 indicate the SST of eastern Pacific cold tongue (Koutavas and Joanides, 2012) is relatively invariant prior to 4 ka in Holocene, with minimum variance between ~4–6 ka (Fig. 4.6C), attributed to weak ENSO behavior. In addition, SST in Peru-Chile Margin reveals dramatic increase variability after 5 ka, suggesting intensified ENSO variance (Chazen et al., 2009).

4.4.4 Potential drivers of ENSO variance during the Holocene

The change of ENSO variance from the early-mid Holocene to the late Holocene may be associated with the meridional migration of the ITCZ. A southward shift of the ITCZ is accompanied by a strengthened Northern Hemisphere Hadley cell and a weakened Southern Hemisphere cell, reducing cross-equatorial SE trade winds (Chiang and Friedman, 2012). These conditions promote the development of El Niño events, thereby providing a mechanism to increase ENSO variance.

A proxy record of the ITCZ position derived from the Ti concentration of the Cariaco Basin (Venezuela) sediments indicates a general southward shift of the ITCZ since the early Holocene, with more rapid and variable migration beginning at ~4.3 ka (Haug et al., 2001) (Fig. 4.6F). A precipitation reconstruction based on dinosterol-δD biomarker record from Palau, within the West Pacific Warm Pool, also supports a general southward shift of the ITCZ since 8 ka (Sachs et al., 2018). Observed weaker interannual precipitation variance in SBB corresponds to relatively northerly ITCZ positions during the mid-Holocene; while the rapid southward shift of the ITCZ was coincident with increasing late Holocene ENSO variance in SBB. Mg/Ca SSTs of *G. ruber* from the West Pacific Warm Pool (Stott et al., 2002) and Eastern Pacific Cold Tongue (Koutavas et al.,

2006) also record weakened tropical zonal SST gradient between 3.8-1.5 ka (SST was anomalously warm in eastern Pacific and anomalously cold in western Pacific), indicating reduced cross-equatorial trade winds which occur when the ITCZ migrates south. Thus, the Southern California precipitation reconstruction supported by EEP paleoclimate records suggest a link between ENSO variance and the ITCZ migration.

These data observations are consistent with our model simulation, which demonstrates a more northerly position of the ITCZ in the mid-Holocene (6ka, Fig. 4.7B). In the simulation, ITCZ migration is mainly driven by boreal summer insolation via changes in Earth's orbital parameters. In addition, stronger southeasterly cross-equatorial trade winds and diminished variance of Niño 3.4 SST are observed in the simulation (Fig. 4.7B), further supporting a link between northward displacement of the ITCZ and reduced ENSO variance. Our model results are also supported by 20th century simulations and recent observational data that also indicate southward migrations of the ITCZ could lead to greater ENSO variance. Coupled climate simulations indicate a weakening of cross-equatorial winds increases ENSO variance and cause more frequent extreme El Niño events (Hu and Fedorov, 2018). On the other hand, a more northerly ITCZ accompanied by strengthening of these winds leads to suppressed ENSO amplitude and westward shift of the center the tropical SST anomaly, producing a La Niña-like tropical mean state (Hu and Fedorov, 2018). In addition, NOAA twentieth century reanalysis data shows that the ITCZ was positioned northward between 1928–1957 before migrating southward between 1960–70, where it has remained (Green et al., 2017). This observation is consistent with stronger ENSO variance after 1970. Furthermore, an intermediate ocean-atmosphere coupled model used to compare warm (1980–2000) and cold (1950–1970) periods in the tropical Pacific demonstrated that the warm period was characterized by stronger ENSO variance, with longer cycles and an enhanced southward shift of the ITCZ (Fang et al., 2008). Southward migrations of the ITCZ lengthen the season of favorable El Niño development, amplifying and lengthening ENSO events (Fang et al., 2008). The Ti record from SBB also shows that the variance of interannual precipitation with longer periodicity (5–7 years) was stronger during late Holocene (after ~4.4 ka), when the ITCZ moved southward (Fig. 4.5). Therefore, this process may explain the greater variance and longer cycle of the interannual precipitation recorded in SBB during the late Holocene, coincident with the southward migration of the ITCZ (Fig. 4.5).

4.4.5 ENSO teleconnection and precipitation changes in Southern California

In addition to changing ENSO variance through time, the strength of the ENSO teleconnection between the tropical Pacific and Southern California could also vary. Changes in the precipitation variance in Southern California are related to tropical Pacific SST anomalies on interannual time scales (Fig. 4.2B) or extratropical pressure systems on longer time scales (Fig. 4.2C). The location and intensity of extratropical pressure systems, such as the AL, impacts wind speed and direction, trough/ridge patterns and SSTs in North Pacific, which influences the ENSO teleconnection and modulates precipitation variability in Southern California. When AL intensifies, it shifts southeastward and lead to eastward extension and southward shift of the North Pacific Jet (NPJ), which brings warm air and moisture from the subtropical latitudes to the West Coast of North America (Rodionov et al., 2007). Enhanced tropical and North Pacific climate coupling intensifies the ENSO teleconnection and makes the hydroclimate in Southern California more sensitive to ENSO variability. On the other hand, a weak and westward-shifted AL, accompanied by an intensified and more northward NPH, may result in a persistent high-pressure ridge over the central North Pacific, which shifts the NPJ northward and blocks the winter storms from reaching the west coast of US (Rodionov et al., 2007; Wang et al., 2014). As a result, the teleconnection of tropical and Southern California is diminished, and significant precipitation events are less likely to occur in Southern California.

The variability of the AL is not solely related to tropical SST. It is also associated with the Arctic pressure and sea ice variability: higher pressure over the Arctic (e.g. negative phase of Arctic Oscillation) associated with Arctic sea ice loss results in weakening of polar vortex and a less intense AL (Overland et al., 1999). Modeling shows that Arctic sea ice decline in mid-Holocene simulations causes a negative AO-like circulation, weakens the polar vortex and mid-latitude westerlies (Park et al., 2018). The accompanied weakening of storm tracks over North Pacific would lead to fewer precipitation events in Southern California. A $\delta^{18}O_{diatom}$ reconstruction from Heart Lake, Aleutian Islands indicates the AL was relatively weak and positioned westward during early-mid Holocene (9.9-4.5 ka), but strengthened and shifted eastward after ~4.5 ka (Fig. 4.6G) (Bailey et al., 2018). This reconstruction is generally consistent with the North Pacific atmospheric circulation recorded by sediment carbonate $\delta^{18}O$ from Jellybean Lake, southern Yukon Territory, Canada (Anderson et al., 2005). The weak and westerly positioned AL during early-mid Holocene might have produced a weaker ENSO teleconnection between the EEP and North America, reducing the Southern California precipitation response to ENSO variability. The strengthening and eastward-extension of the AL after 4.5 ka coincides with the reconstruction of greater ENSO variance (Fig. 4.6G), as would occur with a southward shift of NPJ that produces a stronger ENSO teleconnection. Our model simulations also support a stronger AL and higher precipitation in Southern California during the late Holocene (3 ka) relative to the mid Holocene (6 ka) (Fig. 4.7A and 4.7B). Thus, both model simulations and paleoclimate reconstructions support the possibility that mid-latitude pressure conditions can modulate the long-term precipitation changes in Southern California through the ENSO teleconnection.

4.5 Conclusion

We reconstruct the magnitude and frequency of interannual precipitation variability in Southern California during the last 9000 years using a sub-annually resolved scanning XRF record from Santa Barbara Basin (SBB). The SBB Ti record demonstrates the Southern California interannual precipitation variance in the 2–7 year ENSO-band was reduced by 48.6% in the mid Holocene (prior to 4.4 ka) compared to that in the late Holocene. In addition, the SBB Ti record reveals that the periodicity of the interannual precipitation variance increased from 2–3 years prior to 4.4 ka to 5–7 years during the late Holocene. We interpret the weakening of ENSO-band variability in our precipitation record from SBB to reflect a decrease in ENSO variability during the early and mid-Holocene. This interpretation is supported by field correlation analysis of the 20th century instrumental records and time-slice simulations of the Holocene using the Community Earth System Model version 1.2. In simulations of the early and mid-Holocene (9 ka and 6 ka), the 2–7 year ENSO-band variance of precipitation in Southern California and Niño 3.4 SST is reduced by 51.8% and 69.4% during early-mid Holocene (6 ka and 9 ka), respectively, compared to the late Holocene (pre-industrial and 3 ka).

Combining proxy and modeling evidence, we suggest that the Intertropical Convergence Zone (ITCZ) migrated south during the Holocene. As southeasterly trade winds weakened and the tropical Pacific zonal SST gradient decreased in response, ENSO variance in the tropical Pacific may have increased. This relationship between ITCZ migration and ENSO variance is supported by our model simulations: the ITCZ is displaced southward in the late Holocene simulation (3 ka time slice), mainly due to decreased boreal summer insolation, and was accompanied by weaker southeasterly trade winds and increased ENSO variance. This southward shift of the ITCZ is concurrent with increased interannual (2–7 year) precipitation variance in Southern California during the late Holocene after 4.4 ka.

Additionally, mid-latitude pressure systems, like the Aleutian Low (AL), may have impacted the multi-decadal precipitation variability in Southern California via an ENSO teleconnection. Potential strengthening and eastward-extension of the AL could have shifted the North Pacific Jet southward resulting in a stronger ENSO teleconnection. Proxy evidence for a stronger AL after 4.5 ka coincides with greater interannual precipitation variance in Southern California. Our model simulations also support a stronger AL during the late Holocene than the mid Holocene. Thus, we suggest that the changing Holocene climate could influence the ENSO variance via the migration of ITCZ and midlatitude pressure systems. A high-resolution AL reconstruction is needed, however, to further explore the impact of mid-latitude pressure systems on ENSO teleconnections and further data-model intercomparison studies are needed to explore the mechanisms driving changes in ENSO variance during the Holocene.

4.6 References

Anderson, L., Abbott, M.B., Finney, B.P., Burns, S.J., 2005. Regional atmospheric circulation change in the North Pacific during the Holocene inferred from lacustrine carbonate oxygen isotopes, Yukon Territory, Canada. Quaternary Research 65, 350-351.

Bailey, H.L., Kaufman, D.S., Sloane, H.J., Hubbard, A.L., Henderson, A.C.C., Leng, M.J., Meyer, H., Welker, J.M., 2018. Holocene atmospheric circulation in the central North Pacific: A new terrestrial diatom and delta O-18 dataset from the Aleutian Islands. Quaternary Science Reviews 194, 27-38.

Blaauw, M., Christen, J.A., 2011. Flexible paleoclimate age-depth models using an autoregressive gamma process. Bayesian Anal 6, 457-474.

Black, D.E., Thunell, R.C., Tappa, E.J., 2001. Planktonic foraminiferal response to the 1997-1998 El Nino: A sediment-trap record from the Santa Barbara Basin. Geology 29, 1075-1078.

Chazen, C.R., Altabet, M.A., Herbert, T.D., 2009. Abrupt mid-Holocene onset of centennial-scale climate variability on the Peru-Chile Margin. Geophysical Research Letters 36.

Chen, S., Hoffmann, S.S., Lund, D.C., Cobb, K.M., Emile-Geay, J., Adkins, J.F., 2016. A high-resolution speleothem record of western equatorial Pacific rainfall: Implications for Holocene ENSO evolution. Earth Planet Sc Lett 442, 61-71.

Chiang, J.C.H., Friedman, A.R., 2012. Extratropical Cooling, Interhemispheric Thermal Gradients, and Tropical Climate Change. Annual Review of Earth and Planetary Sciences, Vol 40 40, 383-412.

Clement, A.C., Seager, R., Cane, M.A., 2000. Suppression of El Nino during the mid-Holocene by changes in the Earth's orbit. Paleoceanography 15, 731-737.

Cobb, K.M., Westphal, N., Sayani, H.R., Watson, J.T., Di Lorenzo, E., Cheng, H., Edwards, R.L., Charles, C.D., 2013. Highly Variable El Nino-Southern Oscillation Throughout the Holocene. Science 339, 67-70.

Conroy, J.L., Overpeck, J.T., Cole, J.E., Shanahan, T.M., Steinitz-Kannan, M., 2008. Holocene changes in eastern tropical Pacific climate inferred from a Galápagos lake sediment record. Quaternary Science Reviews 27, 1166-1180.

Croudace, I.W., Rindby, A., Rothwell, R.G., 2006. ITRAX: description and evaluation of a new multi-function X-ray core scanner. Geol Soc Spec Publ 267, 51-63.

Du, X., Hendy, I.L., Hinnov, L., Brown, E., Schimmelmann, A., Pak, D. (in press), 2020. Interannual Southern California precipitation variability during the Common Era and the ENSO teleconnection. Geophysical Research Letters.

Emile-Geay, J., Seager, R., Cane, M.A., Cook, E.R., Haug, G.H., 2008. Volcanoes and ENSO over the past millennium. Journal of Climate 21, 3134-3148.

Fang, Y., Chiang, J.C.H., Chang, P., 2008. Variation of mean sea surface temperature and modulation of El Nino-Southern Oscillation variance during the past 150 years. Geophysical Research Letters 35.

Fisler, J., Hendy, I.L., 2008. California Current System response to late Holocene climate cooling in southern California. Geophysical Research Letters 35, L09702.

Green, B., Marshall, J., Donohoe, A., 2017. Twentieth century correlations between extratropical SST variability and ITCZ shifts. Geophysical Research Letters 44, 9039-9047.

Haug, G.H., Hughen, K.A., Sigman, D.M., Peterson, L.C., Rohl, U., 2001. Southward migration of the intertropical convergence zone through the Holocene. Science 293, 1304-1308.

Hendy, I.L., Dunn, L., Schimmelmann, A., Pak, D.K., 2013. Resolving varve and radiocarbon chronology differences during the last 2000 years in the Santa Barbara Basin sedimentary record, California. Quaternary International 310, 155-168.

Hendy, I.L., Napier, T.J., Schimmelmann, A., 2015. From extreme rainfall to drought: 250 years of annually resolved sediment deposition in Santa Barbara Basin, California. Quaternary International 387, 3-12.

Hu, S., Fedorov, V.A., 2018. Cross-equatorial winds control El Niño diversity and change. Nat Clim Change.

Hu, Z.Z., Kumar, A., Huang, B.H., Zhu, J.S., Ren, H.L., 2017. Interdecadal Variations of ENSO around 1999/ 2000. J Meteorol Res-Prc 31, 73-81.

Huang, B.Y., Banzon, V.F., Freeman, E., Lawrimore, J., Liu, W., Peterson, T.C., Smith, T.M., Thorne, P.W., Woodruff, S.D., Zhang, H.M., 2015. Extended Reconstructed Sea Surface Temperature Version 4 (ERSST.v4). Part I: Upgrades and Intercomparisons. Journal of Climate 28, 911-930.

Hurrell, J.W., Holland, M.M., Gent, P.R., Ghan, S., Kay, J.E., Kushner, P.J., Lamarque, J.F., Large, W.G., Lawrence, D., Lindsay, K., Lipscomb, W.H., Long, M.C., Mahowald, N., Marsh, D.R., Neale, R.B., Rasch, P., Vavrus, S., Vertenstein, M., Bader, D., Collins, W.D., Hack, J.J., Kiehl, J., Marshall, S., 2013. The

Community Earth System Model A Framework for Collaborative Research. B Am Meteorol Soc 94, 1339-1360.

Koutavas, A., Demenocal, P.B., Olive, G.C., Lynch-Stieglitz, J., 2006. Mid-Holocene El Nino-Southern Oscillation (ENSO) attenuation revealed by individual foraminifera in eastern tropical Pacific sediments. Geology 34, 993-996.

Koutavas, A., Joanides, S., 2012. El Nino-Southern Oscillation extrema in the Holocene and Last Glacial Maximum. Paleoceanography 27.

Lange, C.B., Berger, W.H., Burke, S.K., Casey, R.E., Schimmelmann, A., Soutar, A., Weinheimer, A.L., 1987. El Niño in Santa Barbara Basin: Diatom, radiolarian and foraminiferan responses to the "1983 El Niño" event. Marine Geology 78, 153-160.

Liu, Y., Cobb, K.M., Song, H.M., Li, Q., Li, C.Y., Nakatsuka, T., An, Z.S., Zhou, W.J., Cai, Q.F., Li, J.B., Leavitt, S.W., Sun, C.F., Mei, R.C., Shen, C.C., Chan, M.H., Sun, J.Y., Yan, L.B., Lei, Y., Ma, Y.Y., Li, X.X., Chen, D.L., Linderholm, H.W., 2017. Recent enhancement of central Pacific El Nino variability relative to last eight centuries. Nature Communications 8.

Lynn, R.J., Baumgartner, T., Garcia, J., Collins, C.A., Hayward, T.L., Hyrenbach, K.D., Mantyla, A.W., Murphree, T., Shankle, A., Schwing, F.B., Sakuma, K.M., Tegner, M.J., 1998. The state of the California current, 1997-1998: Transition to El Nino conditions. Cal Coop Ocean Fish 39, 25-49.

Mann, M.E., Cane, M.A., Zebiak, S.E., Clement, A., 2005. Volcanic and solar forcing of the tropical Pacific over the past 1000 years. Journal of Climate 18, 447-456.

Napier, T.J., Hendy, I.L., 2016. The impact of hydroclimate and dam construction on terrigenous detrital sediment composition in a 250-year Santa Barbara Basin record off southern California. Quaternary International.

Overland, J.E., Adams, J.M., Bond, N.A., 1999. Decadal variability of the Aleutian low and its relation to high-latitude circulation. Journal of Climate 12, 1542-1548.

Paillard, D., L. Labeyrie, Yiou, P., 1996. Macintosh Program performs time-series analysis. Eos, Trans. Am. Geophys. Union 77, 379.

Park, H.S., Kim, S.J., Seo, K.H., Stewart, A.L., Kim, S.Y., Son, S.W., 2018. The impact of Arctic sea ice loss on mid-Holocene climate. Nature Communications 9.

Parker, F.L., 1962. Planktonic foraminiferal species in Pacific sediments. Micropaleontology 8, 219-254.

Reimer, P.J., Bard, E., Bayliss, A., Beck, J.W., Blackwell, P.G., Ramsey, C.B., Buck, C.E., Cheng, H., Edwards, R.L., Friedrich, M., Grootes, P.M., Guilderson, T.P., Haflidason, H., Hajdas, I., Hatte, C., Heaton, T.J., Hoffmann, D.L., Hogg, A.G., Hughen, K.A., Kaiser, K.F., Kromer, B., Manning, S.W., Niu, M., Reimer, R.W., Richards, D.A., Scott, E.M., Southon, J.R., Staff, R.A., Turney, C.S.M., van der Plicht, J., 2013. IntCal13 and Marine13 radiocarbon age calibration curves 0–50,000 years cal BP. Radiocarbon 55, 1869-1887.

Rein, B., Luckge, A., Reinhardt, L., Sirocko, F., Wolf, A., Dullo, W.C., 2005. El Nino variability off Peru during the last 20,000 years. Paleoceanography 20.

Rodionov, S.N., 2004. A sequential algorithm for testing climate regime shifts. Geophysical Research Letters 31.

Rodionov, S.N., Bond, N.A., Overland, J.E., 2007. The Aleutian Low, storm tracks, and winter climate variability in the Bering Sea. Deep-Sea Res Pt Ii 54, 2560-2577.

Sachs, J.P., Blois, J.L., McGee, T., Wolhowe, M., Haberle, S., Clark, G., Atahan, P., 2018. Southward Shift of the Pacific ITCZ During the Holocene. Paleoceanogr Paleocl 33, 1383-1395.

Schimmelmann, A., Lange, C.B., Berger, W.H., Simon, A., Burke, S.K., Dunbar, R.B., 1992. Extreme climatic conditions recorded in Santa Barbara Basin laminated sediments: the 1835-1840 Macoma event. Marine Geology 106, 279-299.

Seager, R., Naik, N., Ting, M., Cane, M.A., Harnik, N., Kushnir, Y., 2010. Adjustment of the atmospheric circulation to tropical Pacific SST anomalies: Variability of transient eddy propagation in the Pacific-North America sector. Q J Roy Meteor Soc 136, 277-296.

Stott, L., Poulsen, C., Lund, S., Thunell, R., 2002. Super ENSO and global climate oscillations at millennial time scales. Science 297, 222-226.

Thomson, D.J., 1982. Spectrum estimation and harmonic analysis: Proceedings of the IEEE. 70, 1055-1096.

Thunell, R.C., 1998. Particle fluxes in a coastal upwelling zone: Sediment trap results from Santa Barbara Basin, California. Deep-Sea Research Part II: Topical Studies in Oceanography 45, 1863-1884.

Trenberth, K.E., Branstator, G.W., Karoly, D., Kumar, A., Lau, N.C., Ropelewski, C., 1998. Progress during TOGA in understanding and modeling global teleconnections associated with tropical sea surface temperatures. J Geophys Res-Oceans 103, 14291-14324.

Vecchi, G.A., Wittenberg, A.T., 2010. El Nino and our future climate: where do we stand? Wires Clim Change 1, 260-270.

Wang, S.Y., Hipps, L., Gillies, R.R., Yoon, J.H., 2014. Probable causes of the abnormal ridge accompanying the 2013-2014 California drought: ENSO precursor and anthropogenic warming footprint. Geophysical Research Letters 41, 3220-3226.

Warrick, J.A., Farnsworth, K.L., 2009. Dispersal of river sediment in the Southern California Bight. Geol Soc Am Spec Pap 454, 53-67.

Wolter, K., Timlin, M.S., 1998. Measuring the strength of ENSO events: How does 1997/98 rank? Weather 53, 315-324.

Zhu, J., Liu, Z.Y., Brady, E., Otto-Bliesner, B., Zhang, J.X., Noone, D., Tomas, R., Nusbaumer, J., Wong, T., Jahn, A., Tabor, C., 2017. Reduced ENSO variability at the LGM revealed by an isotope-enabled Earth system model. Geophysical Research Letters 44, 6984-6992.

Chapter 5

Holocene Vegetation Response to Hydroclimate Change in Southern California

Abstract

Southern California has experienced both warming and drying over the past few decades, which could significantly impact regional vegetation distributions. To investigate vegetation responses to hydroclimate change in Southern California over long timescales. We present a new multidecadal pollen record over the past 9,000 years from Kasten core SPR0901-02KC and piston core MV0811-14JC in Santa Barbara Basin (SBB), California. Subtle long-term changes in the pollen assemblage are observed in the sedimentary record, corresponding to an orbitally-forced temperature trend over the Holocene. Arboreal pollen components were 3% higher than the mean value prior ~8 ka, accompanied by less xeric vegetation components (4% lower than the mean value), suggesting slightly cooler and more mesic conditions during the early Holocene. The relative abundance of mesic pollen decreased by 6% from 7.2 ka to 5.0 ka, and 4% increased xeric pollen during this interval, indicating the transition to slightly warmer/more xeric conditions during mid-Holocene. A return to ~10% higher mesic pollen suggests slightly cooler/mesic conditions during the late Holocene. Such subtle changes in pollen record from SBB relative to known climate change during the Holocene indicate that the heat- and drought-adapted vegetation in the coastal Southern California ecosystem is well adapted to hydroclimate and temperature changes. Comparison of the SBB pollen record to other hydroclimate and vegetation reconstructions throughout California reveals that vegetation may respond to different aspects of hydroclimate change: vegetation communities in Southern California coast are insensitive to interannual precipitation variability associated with ENSO, while megadrought events would lead to drop of arboreal pollen and increasing xeric pollen on multidecadal to centennial timescales.

5.1 Introduction

Southern California has a highly variable hydroclimate, characterized by extreme precipitation and prolonged droughts. A long-term drying trend over the past decades (Seager and Hoerling, 2014; Seager and Vecchi, 2010), together with extreme events such as floods and prolonged droughts has been reported in this region. Vegetation dynamics are closely related to climate change through hydroclimate as total precipitation, hydrological variability, and air temperature all impact soil moisture and evapotranspiration (Dong et al., 2019; Fensham et al., 2019). Increasing temperature, continued drying, and changes in precipitation frequency and fire regimes have been predicted in Southern California for the next century (Meehl et al. 2007; Westerlin and Bryant 2008; Krawchuk et al. 2009), and will likely severely impact regional vegetation distributions (IPCC, 2007). Increasing air temperature, together with drier soil condition is predicted to increase evapotranspiration, alongside drought stress, and this combination will reduce oak woodland distribution in Southern California over this century (McLaughlin and Zavaleta, 2012). Understanding climate, hydrology, and vegetation interactions is of fundamental importance for improving predictions of vegetation response to climate change and maintaining the stability of forest ecosystems (USDA Forest Service, 2018). However, instrumental records of hydroclimate and vegetation change (e.g., precipitation, river discharge, lake level, satellite-based Normalized Difference Vegetation Index) are impacted by anthropogenic forcing, such as emissions of greenhouse gases and changes in land use. Additionally, historical observations are of insufficient duration (<200 years) to reflect the hydroclimate variability and vegetation on decadal to centennial timescales, prohibiting a complete understanding of the long-term natural interaction between ecosystems and climate in this region.

Sedimentary records provide an opportunity to reconstruct regional hydroclimate and vegetation changes over centennial to millennial timescales during the Holocene. In Southern California, Holocene hydroclimate variability (Du et al., 2020; Du et al., 2018; Hendy et al., 2015; Hiner et al., 2016; Kirby et al., 2015; Kirby et al., 2010; Kirby et al., 2005; Kirby et al., 2012; Schimmelmann et al., 2003) and changes in vegetation (Glover, 2016; Heusser, 1978; Heusser et al., 2015a; Heusser and Sirocko, 1997) have been reconstructed using both marine and lacustrine sediments. Lithogenic element concentration and flood layers preserved in marine sediments from Santa Barbara Basin (SBB), located in the Southern California Bight (Fig.5.1), provide a reconstruction of the frequency/amplitude of interannual precipitation variability and extreme precipitation events in Southern California (Du et al., 2020; Du et al., 2018). Additionally, multiple proxies from lake sediments, including sedimentological features (Negrini et al., 2006), grain size (Kirby et al., 2010; Kirby et al., 2005), hydrogen (Feakins et al., 2014) and oxygen isotope ratios (Kirby et al., 2019), and elemental geochemistry (Hiner et al., 2016; Kirby et al., 2015; Kirby et al., 2010; Kirby et al., 2005; Kirby et al., 2012), have been employed to reconstruct lake-level variability and through inference, precipitation in this region.

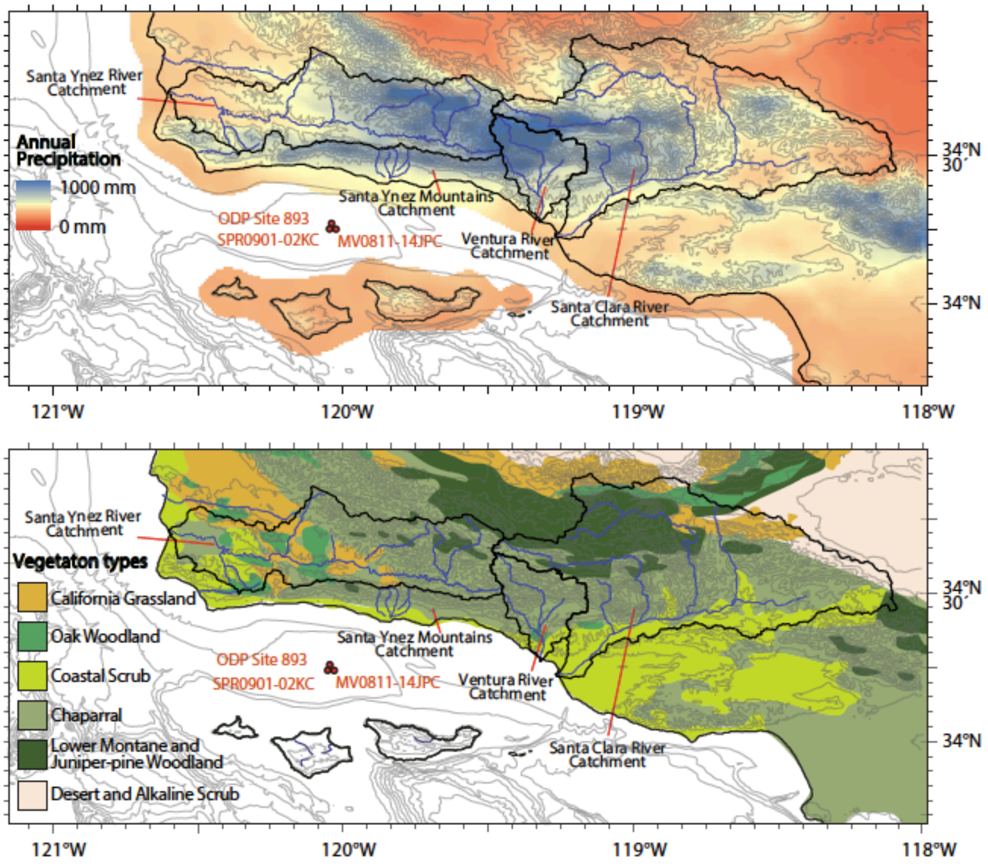

Figure 0-1(A) 30-year (1981-2010) annual precipitation distribution Precipitation data are from PRISM Climate Group, Oregon State University and (B) dominant vegetation types in the coastal region of Southern California (Heusser et al., 2015). The locations of core MV0811-14JC, core SPR0901-02KC, and ODP Site 893 in the Santa Barbara Basin (SBB) are shown. The river catchments draining into SBB are outlined by solid black lines. Elevation is shown at 200 m intervals.

Pollen records reflect vegetation distribution and composition in the catchments draining into sedimentary basins, providing potential information about vegetation response to hydroclimate variability. Such pollen records have been extracted from lake sediments across coastal Southwest America, such as San Bernardino Mountains (Glover, 2016; Glover et al., 2020; Paladino, 2008), San Joaquin Valley (Davis, 1999), Santa Rosa Island (Cole and Liu, 1994), and Mojave Desert (Balmaki and Wigand, 2019; Koehler et al., 2005). However, the diverse topography and local hydroclimate conditions across these regions precludes a direct comparison between pollen and hydroclimate records, complicating the investigation of vegetation response to hydroclimate change. Compared to terrestrial records, pollen records collected from SBB reflect the history of major vegetation changes over a broader catchment (the catchments of the Santa Clara River, Ventura River, and the Santa Ynez River). Together with hydroclimate reconstructions from this basin (Du et al., 2020; Du et al., 2018), pollen records from SBB allow for a more direct vegetation-hydroclimate comparison on the Southern California coast. A pollen record from ODP Hole 893A in SBB with ~1000-yr resolution suggests the vegetation in Southern California shifts between oak woodland and conifer forests corresponding to interstadials and stadials over the past 160 ka (Heusser, 1995). Heusser et al. (1997) resampled the ODP Hole 893A over the past 24 ka to reconstruct a centennial-resolution pollen record. Millennial-scale *Pinus* events, characterized by high pine abundance, low pollen concentration and charcoal maxima, were discovered and interpreted as evidence of rapid hydrologic changes associated with enhanced seasonality (Heusser and Sirocko, 1997). At high resolution, an interannually-resolved (5 year) SBB pollen record spans 800 to 1500 AD, and shows coastal sagebrush and chaparral dominated early and late Medieval Climate Anomaly, while arboreal pollen increased between 1090 to 1200 AD and during Little Ice Age (Heusser et al., 2015a). Therefore, previous studies suggest that pollen records deposited in SBB reflect vegetation response to hydroclimate changes in the Southern California region on orbital to decadal scales. However, a synthesis of hydroclimate and vegetation in Southern California is needed to investigate the vegetation response to different aspects of hydroclimate changes, such as precipitation variability, extreme hydroclimate events, precipitation/evaporation rate, and river run-off intensity in this region.

Here we present a new multidecadal pollen record spanning the last 9,000 years from Kasten core SPR0901-02KC and piston core MV0811-14JC in SBB. Previously published multiproxy hydroclimate records preserved in SBB are compared to this pollen record, using the master stratigraphy with a revised radiocarbon chronology (Du et al., 2018). Using this compilation, we investigate the vegetation response in the SBB catchment to different aspects of hydroclimate change (e.g. interannual precipitation variability, the frequency/amplitude of megadroughts and floods) over the Holocene. Finally, this SBB pollen compilation is compared to lake records across the Southern California, to identify the vegetation response to hydroclimate changes in a broader region.

5.2 Regional setting

5.2.1 Southern California climate

Southern California has a Mediterranean climate, characterized by hot dry summers and cool wet winters. The latitudinal changes in northeast Pacific large-scale atmospheric pressure fields contribute to these highly seasonal precipitation changes. Precipitation typically occurs in winter when the North Pacific High is relatively weak and the Aleutian Low migrates southward, steering storm tracks toward Southern California (Haston and Michaelsen, 1997; Kenyon, 1999; Nezlin and Stein, 2005). Dry atmospheric conditions generally prevail in spring and summer when the North Pacific High strengthens and migrates poleward, blocking storm systems (Haston, 1997). The annual precipitation in Santa Barbara coastal region ranges from 25 to > 75 cm, with a mean of ~38.9 cm. Additionally, this seasonal change in atmospheric circulation produces coastal upwelling during spring-summer, bringing cool ocean water to the surface to interact with air at sea level. In coastal regions, the associated fog that accompanies upwelling moderates air temperatures and increases effective moisture (producing fog drip) during the driest months of the year, and shade from these persistent clouds at the coast reduce annual drought stress by 22-40% (Fischer et al., 2009).

5.2.2 Modern vegetation

The stature, structure, and composition of the natural vegetation of southern coastal California is associated with elevation-related climatic gradients (Fig. 5.1b). Mean air temperatures on the coast range from ~10°C in winter to 20°C in summer; mid-elevations range from 5 ˚C to 22 ˚C. Summer air temperatures average ~10˚C and winters are mild (7˚C) in the higher elevations of the Santa Ynez Mountains. Annual precipitation averages are ≦110 mm in coastal scrub, ~ 550 mm in chaparral, ~650 mm in lower montane oak woodland/forest, and ~1200 mm on montane peaks (~1200-1400 m elevation) (Wahl, 2003) (Fig. 5.1a). Fog drip, which extends inland, can reduce drought stress in summer by 20-36% (Fischer et al., 2009).

Along the Santa Barbara coast, estuarine wetlands marshes are dominated by Chenopodiaceae and Gramineae (Callaway et al., 1990). Marine terraces and the lower, montane slopes (< 600m) support a mosaic of coastal strand coastal sage scrub (drought-deciduous shrubs, which include *Artemisia, Eriogonum, Baccharis* and other Asteraceae) and grasses that interfingers upslope with chaparral (mainly evergreen, woody, thickly branched shrubs of *Adenostoma* (chamise)*, Cercocarpus* (mountain mahogany)*, Ceanothus* (California lilac)*, Rhamnus* (buckthorn)*, Quercus agrifolia* (coast live oak) and patches of valley oak (*Q. lobata,)* and blue oak (*Q. douglasii*) open woodland with grassland. Mesic chaparral that includes scrub oak (*Q. dumosa, Q. durata*) occurs on mid-montane (<900 m) north-facing slopes of the Santa Ynez Mountains. At higher elevations, large, woody oak (*Q. dumosa*) shrubs, and open *Quercus*-dominated woodlands are succeeded upslope by open, park-like conifer woodlands or isolated stands of conifers with pine (*Pinus pondero*sa, *P. muricata*) and *Pseudotsuga macrocarpa* (Big-cone Douglas fir*). Juniperus* (Juniper), *Cupressus* (Cypress), and *Calocedrus* (California incense Cedar) may also be present (Critchfield, 1971) (Harrison et al., 1971; Munz, 1974). Riparian forests in the SBB drainage are dominated by *Quercus, Alnus* (alder)*, Populus* (c), *Platanus* (sycamore)*, Salix* (willow), and *Juglans* (walnut) (Bendix, 1994). A unique coastal floodplain scrub vegetation that includes *Artemisia Eriogonum Rhus Salvia*, and *Baccharis* grows on sandy, rocky alluvium deposited along the main river channels during episodic flood events (Hanes et al., 1989)

5.2.3 Santa Barbara Basin

Santa Barbara Basin (SBB), located in the Southern California Bight, contains continuous, annual-scale marine sediment records (Fig. 5.1) (Hendy et al., 2015; Kennett and Ingram, 1995; Schimmelmann et al., 2006). The high tectonic uplift rates of Santa Ynez Mountains (>5 mm/yr) contribute to unusually high sedimentation rates in SBB

(Duvall et al., 2004; Warrick and Mertes, 2009) with lithogenic sediment dominating the sediment supply (Thunell, 1998). In winter, precipitation events generate episodic sediment-laden discharge from the Santa Clara, Ventura and Santa Ynez River (Fig. 5.1), delivering terrigenous detrital siliciclastic sediments to SBB as plumes (Nezlin et al., 2005; Warrick et al., 2007; Warrick and Farnsworth, 2009; Warrick et al., 2008). Precipitation totals control the lithogenic sediment flux into the basin (Soutar and Crill, 1977; Warrick and Farnsworth, 2009b).

The composition of the major vegetation types of cismontane southern California coast is reflected in pollen assemblages from moss pollsters, humus and soil samples taken in onshore (Wahl, 2003) and in sediment deposited offshore (Heusser, 1978; Heusser et al., 2015a). Heusser et al. (2015a) found close relationship between the concentration of pollen deposited in a SBB sediment trap and the flowering of plant communities in the catchment, illustrating that pollen deposited in SBB can be used to reconstruct vegetation changes in the coast of Southern California. Fluvial dispersal is assumed to carry significant amounts of pollen, while aeolian dispersal is limited (Heusser, 1978, 1995; Heusser et al., 2015a). Terrigenous sediments in SBB are derived from the catchments of the Santa Clara, Ventura, and the southern flanks of the Santa Ynez Mountains (Napier and Hendy, 2016; Napier et al., 2020). Therefore, pollen deposited in SBB is presumed to reflect the vegetation primarily found within the above catchments.

5.3 Methods

5.3.1 Sediment cores and chronology

Kasten core SPR0901-02KC (34˚16.80’ N, 120˚02.30’ W; 588m water depth; 02KC) and piston core MV0811-14JC (34˚16.906’ N, 120˚02.162’ W; 580 m water depth; 14JC) (Fig. 5.1) were spliced together to create a pollen record spanning the last 9000 years. An high-resolution chronology for Holocene sediments in SBB were generated based on AMS ^{14}C dates of mixed planktonic foraminiferal from core kasten core SPR0901-06KC (Hendy et al., 2013) (34˚ 16.914N, 120˚ 02.419W; 591 m water depth; 06KC; 38 ^{14}C dates), core 14JC (44 ^{14}C dates) and ODP Hole 893A (34˚17.25’ N 120˚ 02.2’ W; 588 m water depth; 893A; 7 ^{14}C dates). All the above cores were correlated using instantaneous flood layers and turbidites identified with highly resolved core images. The thickness of the instantaneous layers was then subtracted from the original cores to generate a corrected depth. The ^{14}C dates from 893A and 06KC were then transposed to 14JC with the corrected depth scale, in order to generate a master chronology for Holocene sediment in SBB (Du et al, 2018). In addition, five stratigraphic marker layers (the core top (1905 CE), a gray layer at 1861–62 CE, the *Macoma* layer at 1841 CE, a turbidite at 1811 CE and a gray layer at 1761 CE) with dates generated from varve chronology (Schimmelmann et al., 1992), were used in this age model to avoid the impact of ^{14}C plateaus during the last 300 years. Aside from known turbidites and flood layers, an additional 12 tie points were identified based on reproducible core fabric changes and used to correlate 02KC and 06KC. The depth used in this study is according to corrected depth in a master stratigraphy, which splices core 02KC and 14JC. An age-depth model was then generated in Bacon 2.2, where Bayesian statistics were used to reconstruct coherent accumulation histories (Blaauw and Christen, 2011). Marine 13 calibration curves (Reimer et al., 2013) were applied to convert ^{14}C dates to years BP. Variable reservoir ages estimated by Hendy et al. (2013) were used for the last 2000 years, and a constant reservoir age of 147 ± 70 yrs was employed from 2000 to 9000 yrs BP (Hendy et al., 2013). The age model is described in detail in Du et al. (2018). The high-resolution master chronology was applied to the spliced pollen record from core 02KC and 14JC.

5.3.2 Pollen analysis

Samples from core 14JC was collected at ~10 cm intervals over a total length of 980 cm. Reference collections of modern pollen and published references were used to identify pollen and spores. Identification varied taxonomically from generic to familial levels. Inaperturate pollen grains that are or could have been produced by conifers such as *Juniperus* or *Cupressus* are here referred to as Cupressaceae; plant families Taxodiaceae, Cupressaceae, and Taxaceae are referred as TCT; and pollen produced by chaparral constituents of the Rosaceae, Rhamnaceae, and Anacardiaceae families (*Adenostoma*, *Cercocarpus*, *Ceanothus*, and *Rhamnus*) are grouped as RRA.

5.3.3 Statistical analysis

Pollen assemblage zones were determined using stratigraphically constrained cluster analysis (CONISS) (Grimm, 1987) in the software Tilia 2.1.1. The original pollen percent data were interpolated to an evenly spaced time series (dt = 85 year) prior to the constrained cluster analysis. The Sequential Regime Shift Detection (SRSD) method was used to detect the regime shifts (Rodionov, 2004) in the relative abundance of pollen. Weighed means of the regimes were calculated using the Huber weight function (tuning constant =2). The length of the regimes is 5 data points (~450 years). Target p-value equals 0.20. The SRSD was performed in Excel using the software package Regime shift test-v6.2.xlsm (https://sites.google.com/site/climatelogic/).

5.4 Results

5.4.1 Pollen assemblage zones

Four pollen assemblage zones (zone 1-4) are recognized according to the constrained cluster analysis (CONISS) (Fig. 5.2). Zone 2 and 4 are subdivided into zone 2a-2c, and zone 4a and 4b, respectively.

Zone 1 (823.36–685.78 cm, 9 ka –7.7 ka)

Zone 1 is characterized by the highest relative abundances of *Alnus* (4.55% in average) and *Conifers* (TCT; 3.24% in average). In comparison, the relative abundance of chaparral (RAA) is minimal in zone 1, increasing from ~5% in at base to 11% at the top of zone 1, with average percent of 10.5%. In addition, the relative abundance of Gramineae, *Pinus* and *Quercus* are slightly higher than zone 2.

Zone 2 (685.78 –310.78 cm, 7.7-3.7 ka)

2a (685.78 –509.161 cm, 7.7–5.8 ka), 2b (509.161–364.58 cm, 5.8–4.3 ka), 2c (364.58–310.78 cm, 4.3–3.7 ka)

Compared to zone 1, zone 2 is characterized by lower *Alnus* and *Quercus*, and higher RRA and Chenopodiaceae relative abundance. RRA relative abundance increased gradually throughout zone 2a-2c, from an average of 14.6% in zone 2a to 18% in zone 2c. Chenopodiaceae component is consistently high, and reaches its maximum in zone 2c. The relative abundance of *Alnus* in zone 2 decreased by more than 50% compared to zone 1 (4.6% in zone 1 and 2.2% in zone 2). Notably, the relative abundance of *Alnus* pollen reaches a minimum (1.78% in average) in zone 2b. *Quercus* relative abundance decreased from the base of zone 2a, to a minimum (19%) between zone 2a and 2b (~5.8 ka), and increased to a maximum of ~33% near the top of zone 2b (~4.5 ka), before decreasing again in zone 2c. On average, *Quercus* reached its lowest abundance in upper zone 2a and lower zone 2b relative to other zones within the Holocene.

Zone 3 (310.78–169.50 cm, 3.7–1.9 ka)

A significant increase in Gramineae and *Alnus* relative abundance, distinguishes zone 3 from the other zones. A maximum relative abundance (8.6%, average percentage) of Gramineae, occurred between ~2 ka –3 ka. Both *Quercus* and *Artemisia* abundance are slightly higher than zone 2. RRA pollen is slightly less abundant in this zone, compared to the earlier zone 2c. Asteraceae component decreased throughout zone 3, reaching a

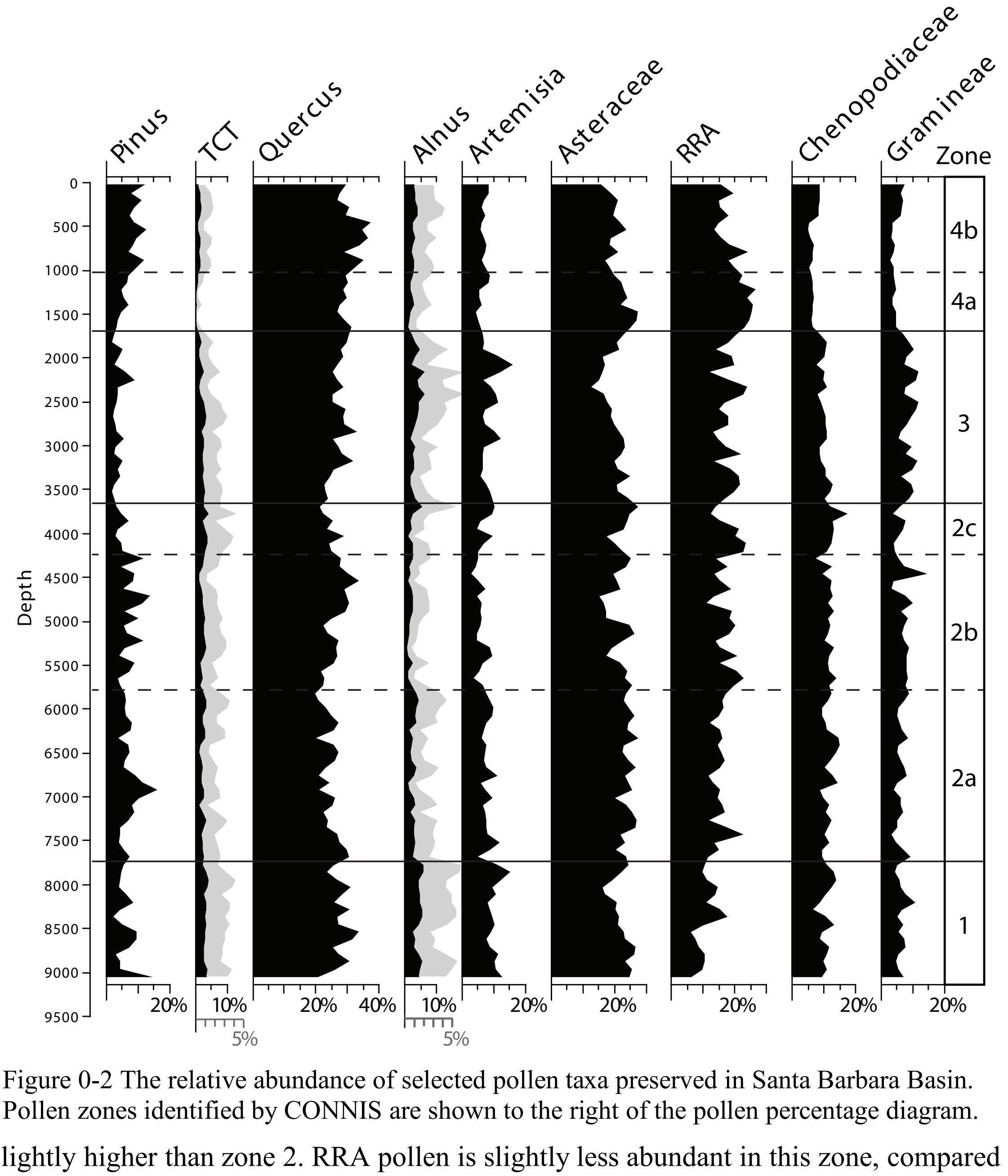

Figure 0-2 The relative abundance of selected pollen taxa preserved in Santa Barbara Basin. Pollen zones identified by CONNIS are shown to the right of the pollen percentage diagram.

minimum around 2.3 ka. In addition, *Pinus* and TCT relative abundance are lower than that in zone 1 and 2. In summary, the arboreal pollen abundance is relatively high, Asteraceae and RRA components slight decreased, and the abundance of Gramineae increased in zone 3.

Zone 4 (169.50–0 cm, 1.7 ka–40 years BP)

Zone 4 is subdivided into zone 4a *(169.50–126.5 cm, 1.7-1.0 ka),* and 4b *(126.5–0 cm, 1.0 ka-40 years BP).* Zone 4a is characterized by abrupt increase of Asteraceae and RRA, whose peak abundance occurred around 1.5 ka. In addition, a minimum average percentage of both Gramineae and *Alnus* pollen is observed in zone 4a. Zone 4b is characterized by a maximum relative abundance of *Pinus* (8.5%, average percentage) and *Quercus* (30.1%, average percentage), and a minimum relative abundance of Asteraceae (19.6%, average percentage) pollen, compared to other zones. In addition, RRA relative abundance decreased rapidly, while *Alnus* abundance is ~50% higher than that in zone 4a.

5.5 Discussion

5.5.1 Vegetation changes in Southern California coast during the Holocene

As the pollen preserved in SBB sediments represents the major plant associations on the Southern California coast (Heusser, 1978, 1995), the record presented here should capture changes in the regional vegetation in response to climate variability. Yet only subtle changes are observed in the Holocene pollen record preserved in SBB compared to previously published last glacial records (Fig. 5.2). The Holocene pollen assemblages in SBB are mainly composed of *Quercus* (~30%), shrub (RRA, 17%), and herb (Asteraceae, 20%) taxa, with low percentage of *Pinus* (~3%) and TCT (less than 1%), representing modern coastal mosaic oak woodland/ chaparral/ sage scrub communities. This oak-dominated vegetation contrasts with the Pinus/TCT (Taxaceae-Cupressaceae-Taxodiaceae)-dominated vegetation of the Last Glacial Maximum (~21 ka ago) (Heusser, 1995), which is currently restricted to the high elevation montane-juniper woodlands of the Transverse Ranges (Wells and Berger, 1967). After the Last Glacial Maximum, Southern California experienced significant drying (Kirby et al., 2018; Oster et al., 2009) and SST on the California Margin warmed by ~7-12 ˚C (Hendy and Kennett, 1999, 2000; Pak et al., 2012). The post-glacial warming and drying trend caused the oak woodland extent to steadily increase in mostly coastal and low-elevation areas of Southern California, reaching a maximum abundance about 8,000-7,000 yrs BP, and remained high throughout the Holocene (Byrne et al., 1991; Davis, 1999; Heusser, 1978; Mensing, 2014). Coast live oak (*Quercus agrifolia*) has since persisted throughout the Holocene as the dominant oak woodland species along the Southern California coast (Barbour and Minnich., 1988; Mensing, 2005).

The modern vegetation distribution in Southern California has a relationship with mean annual precipitation and the mean air temperature of warmest month and coldest month, while annual soil water moisture content is also inferred to be a major limiting factor (Barbour and Major, 1977; Mather and Yoshioka, 1968; Minckley et al., 2008; Minnich et al., 2007). Therefore, simply interpreted, the subtle variability in pollen abundance observed over the last 9,000 years in SBB suggest little change in precipitation and air temperature throughout the Holocene. Indeed, Holocene climate was relatively stable compared to the last glacial period. Warming/ cooling of California surface temperature were on the order of 1–3˚C during the Holocene (Potito et al., 2006). On the other hands, the Northern Hemisphere experienced a long-term changes in surface temperature during the Holocene due to the effects of orbital forcing (precession and obliquity) on summer insolation (Crucifix et al., 2002). The slight long-term change of pollen components observed in our record might be associated with the orbital-forced surface temperature variance over the Holocene (Kutzbach and Guetter, 1986).

Mesic conditions refer to habitat with a moderate or well-balanced supply of moisture. In contrast to mesic conditions, xeric conditions are extremely dry, lacking humidity and water. Here, we used the relative abundance of arboreal pollen as an index of cool-mesic conditions and the percentage of *Artemisia* and Chaparral pollen were employed as a warm-xeric proxy. Arboreal pollen types (e.g., *Pinus*, TCT, *Quercus*, and *Alnus*) represent relatively cooler (mean warmest month temperature ~10–26 ˚C) and wetter (mean annual precipitation ~500-2000 mm) environments, while nonarboreal pollen types (e.g., *Artemisia*, RRA, and Asteraceae) indicate warmer (mean warmest month temperature ~12–28 ˚C) and drier (mean annual precipitation ~150-800 mm) conditions (Minckley et al., 2008). In addition, the relative concentration of *Quercus* and chaparral pollen has been interpreted as a proxy for effective soil moisture (Heuuesser et al., 2015). Coast live oak is more susceptible to drought than other California oaks and is more abundant in cooler, steeper slopes (Barbour and Minnich., 1988). The coastal oak woodland occupied by coast live oak has mean annual precipitation varies from 1000 to 3800 mm, and seasonal temperature ranges from cool air temperature of 2–7 ˚C to a maximum of 24–36 ˚C (Holland, 1988). Shrubs and herbs in the chaparral ecotones tolerate severe drought conditions and occupy warm, xeric shrubland environments. Presently chaparral is found in areas with a mean annual precipitation of 250–750 mm, and seasonal cool air temperatures of 5–15 ˚C and a maximum of 30–40 ˚C (Barbour et al., 2007).

Climate models demonstrate that due to the increased amplitude of seasonal insolation, the summer temperature in the western United States during mid-Holocene (~6.0 ka) was 1-2.5˚C warmer than today (Diffenbaugh and Sloan, 2004). This model output agrees with a chironomid-based summer surface water temperature reconstruction from Hidden Lake in the Sierra Nevada, showing the surface water temperature was relatively low (~17˚C) prior 7.5 ka, and then increased to a maximum of ~20˚C by 6.5 ka (Potito et al., 2006). In SBB, Regime Shift Detection Index (RSDI) demonstrates that arboreal components (*Quercus*, *Alnus*, TCT, *Pinus*) were ~3% higher, and xeric pollen (*Artemisia* and Chaparral) was ~4% higher than mean Holocene values prior ~8 ka (Fig. 5.3a and 5.3b), consistent with Hidden Lake water temperature. Mesic pollen components decreased below mean Holocene values between ~5.2–7.9 ka (Fig. 5.3b), suggesting slightly warmer and drier conditions during the mid-Holocene. This is further supported by persistently high Asteraceae contributions to SBB pollen through this time interval. As Asteraceae is highly tolerant to drought and is associated with environments disturbed by wildfires, higher abundance of this family of flowering plants suggests drought had an impact of regional vegetation (Winter et al., 2011). This assertion is supported by the slightly increase in RRA contributions from 7.7 to 5.8 ka, and maximum abundance at ~5.7 ka. Pollen analysis from core Y71-10-117P (latitude 34˚16'N, longitude 120˚4'W) in SBB demonstrated that coniferous communities dominated prior to 7.8 ka, and then were succeeded by oak woodland communities. The relative abundance of *Quercus* and Asteraceae also peaked at ~5.7 ka (Heusser, 1978). Reconstructed summer surface water temperature from Hidden Lake decreased after ~0.8 ka (Potito et al., 2006), consistent with the increased relative abundance of mesic vegetation (~10%) and decreased xeric vegetation (~6%) after ~1.0 ka in SBB (Fig 5.3). The relative abundance of *Quercus* from Hole 893A in SBB is slightly higher prior 7.4 ka and after 0.8 ka (Heusser, 1995; Heusser and Sirocko, 1997), supporting more mesic conditions during early Holocene and the late Holocene, in line with the new pollen record.

However, the subtle changes in the Holocene pollen record of coastal vegetation preserved in SBB contrasts with significant vegetation composition changes reflected by regional terrestrial pollen records from high elevations (Balmaki and Wigand, 2019; Davis, 1999; Glover, 2016; Koehler et al., 2005; Mensing et al., 2004; Paladino, 2008). In Lower Bear Lake (elevation >2000 m), San Bernardino Mountains, the relative abundance of *Pinus* decreased significantly (>20%) from 8.6 ka to 7.1-4.5 ka, together with increasing herb and shrub pollen abundance (>15%), suggesting a shift to a warm/xeric mid-Holocene environment (Glover, 2016). Further north, the pollen record from Tulare Lake, San Joaquin Valley also suggests a dramatic transition from pine-juniper woodland to oak woodland and chaparral after 8.5 ka, followed by decreasing *Quercus* and increasing Asteraceae relative abundance from 7.0-4.0 ka, suggesting expansion of xeric vegetation during the mid-Holocene (Davis, 1999). In the central Mojave Desert, the absence of *Pinus* combined with the presence of *Agave utahensis* suggests an increase in air temperature during mid-Holocene (Koehler et al., 2005). The more significant vegetation changes observed in these interior pollen records could due to the fact that air temperature response to climate change at high elevation, interior regions is greater than that in low elevation coastal regions. Coastal air temperatures are moderated by the ocean and fog associated with upwells, which also increases effective moisture in summer. Alternatively, the subtle changes of pollen components reflected from SBB could be caused by the fact that endemic heat- and drought-adapted vegetation in coastal Southern California have evolved to be resistant to hydroclimate and temperature changes over the past millions of years. The characteristics of Holocene hydroclimate changes in Southern California and their impact to vegetation is further discussed in the following two sections.

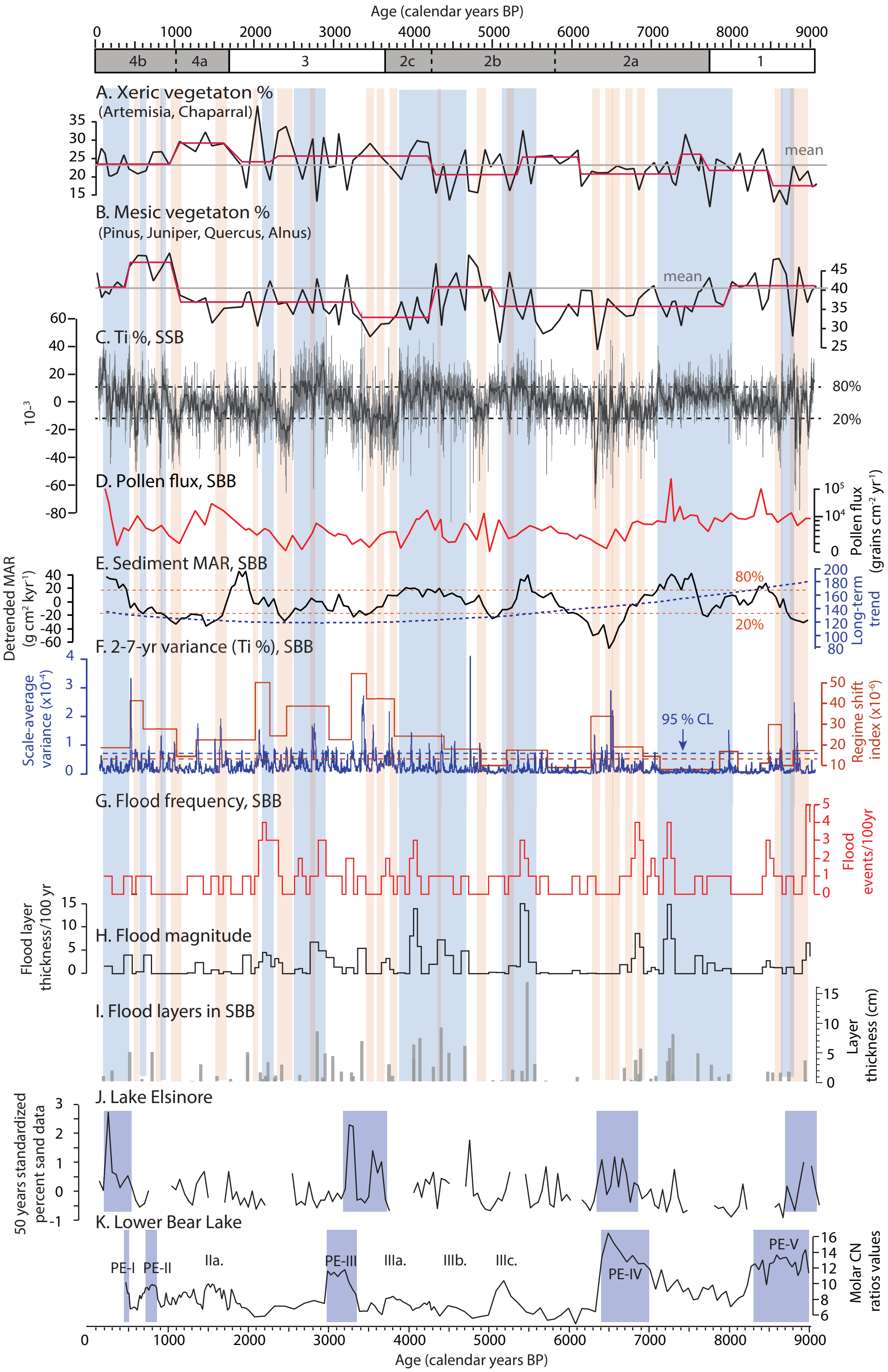
Age (calendar years BP)
0
1000
2000
3000
4000
5000
6000
7000
8000
9000
4b
4a
3
2c
2b
2a
1
A. Xeric vegetaton %
(Artemisia, Chaparral)
35
30
25
20
15
mean
B. Mesic vegetaton %
(Pinus, Juniper, Quercus, Alnus)
mean
45
40
35
30
25
C. Ti %, SSB
60
40
20
0
-20
-40
-60
-80
10^{-3}
80%
20%
D. Pollen flux, SBB
10^5
10^4
0
Pollen flux (grains cm^{-2} yr^{-1})
E. Sediment MAR, SBB
Detrended MAR (g cm^2 kyr^{-1})
40
20
0
-20
-40
-60
80%
20%
200
180
160
140
120
100
80
Long-term trend
F. 2-7-yr variance (Ti %), SBB
Scale-average variance (x10^{-4})
4
3
2
1
0
95 % CL
50
40
30
20
10
Regime shift index (x10^{-6})
G. Flood frequency, SBB
5
4
3
2
1
0
Flood events/100yr
H. Flood magnitude
Flood layer thickness/100 yr
15
10
5
0
I. Flood layers in SBB
15
10
5
0
Layer thickness (cm)
J. Lake Elsinore
50 years standardized percent sand data
3
2
1
0
-1
K. Lower Bear Lake
PE-I
PE-II
IIa.
PE-III
IIIa.
IIIb.
IIIc.
PE-IV
PE-V
16
14
12
10
8
6
Molar CN ratios values
0
1000
2000
3000
4000
5000
6000
7000
8000
9000
Age (calendar years BP)

Figure 0-3 Relative abundance of (A) xeric pollen, Artemisia and RRA (Rosaceae, Rhamnaceae, and Anacardiaceae families) (black line) and (B) mesic pollen, *Pinus*, *Quercus*, *Alnus*, and TCT (Taxodiaceae, Cupressaceae, and Taxaceae) (black line) preserved in Santa Barbara Basin (SBB). Red line represents the weighted mean of relative abundance produced by Sequential Regime Shift Detection (SRSD), and gray line represents the mean value. (C) Standardized Ti concentration from SBB (gray line), smoothed using 100-point moving box (black solid line) (Du et al., under review). Black dashed lines represent the 20th and 80th percentile, respectively. (D) Pollen flux in grains cm^{-2} kyr^{-1}. Pollen flux = Dry bulk density (g/cm^3) × Linear sedimentation rate (cm/yr) × pollen concentration (grains/g). (D) Mass accumulation rate (black line) of SBB (Du et al., 2018). Red dashed lines represent the 20th and 80th percentile, respectively. The long-term trend (black dashed line) was removed by subtracting the LOESS (locally estimated scatterplot smoothing) curve (with window equals the length of the Ti time series) curve. (E) The 2–7-year scale-averaged wavelet spectrum of Ti time series recorded from SBB (blue line) and 95% confidence level (Du et al., under review) (blue dashed line). The red line represents the weighted mean produced by SRSD. (F) Flood frequency (flood layers per 100 years, red line), (G) flood magnitude (flood layer thickness per 100 years, black line), and (H) age and thickness of flood layers (gray bars) preserved in SBB (Du et al., 2018). (I) 50-year binned standardized percent total sand of sediments from Lake Elsinore (Kirby et al., 2010) (black line). (J) C/N ratio of sediments from Lower Bear Lake (Kirby et al., 2012) (black line). Dark blue shading represents pluvial intervals based on lake records. Light blue shading represents wet intervals recorded in SBB, characterized by high Ti% (above the 80th percentile). Orange shading represents megadroughts, defined as intervals with 100-point (~20 years) smoothed Ti% below the 20th percentile.

5.5.2 Hydroclimate changes in Southern California

Holocene multiproxy reconstructions can respond to different aspects of Southern California hydroclimate change including the magnitude and frequency of megadroughts, interannual precipitation variability, flood events, and the intensity of evaporation. A synthesis of these multiple hydroclimate proxies allows us to explore the vegetation response to different aspects of hydroclimate change. Terrestrial sediments in SBB are predictive of regional precipitation (Napier et al., 2020) and correlated with interannual climate change (Du et al, 2019). As SBB sediments are dominated by terrestrial input (Thunell et al., 1995), the mass accumulation rate of sediments in the basin is mainly controlled by precipitation-driven river runoff (Du et al., 2018) Thus an increase in sediment accumulation reflects increased precipitation. The Holocene precipitation changes in Southern California has been reconstructed using an annually-resolved (4-7 samples per year) scanning XRF record from SBB (Du et al., under review). This reconstruction uses the siliciclastic element - Ti - to record terrestrial sediment delivery via river runoff to SBB and reflects interannual precipitation variability. This variability in Southern California is related to El Niño Southern Oscillation (ENSO). The precipitation reconstruction also records megadroughts, which we define as intervals with 20-year averaged Ti% below the 20th percentile (indicated by orange bars in Fig. 5.3), and wet intervals (pluvials) characterized by high Ti% (above the 80th percentile, indicated by blue bars in Fig. 5.3). Additionally, gray layers derived from suspended silt to clay-size particles delivered by large flood plumes are preserved in SBB, representing extreme precipitation events in Southern California, indicated by anomaly high Ti concentration (Du et al., 2018; Schimmelmann et al., 1998).

A synthesis of hydroclimate reconstructions from SBB reveals the connection between interannual precipitation variability and extreme events. Intervals with higher interannual precipitation variability in Southern California are associated with more frequent or large magnitude flood events (2.0–3.0, 3.8–4.3, and 5.1–5.7 ka) (Du et al., 2018), significant drought (Ti% below the 20th percentile) events (6.3–6.9 ka), or alternating flood and drought events (0.4–1.0 and 3.2–3.8 ka) (Fig.5.3). Given that interannual precipitation variability in Southern California is closely related to ENSO (Du et al., 2020), high ENSO variability may increase the occurrence of hydroclimate extreme events in Southern California. Such a relationship is supported by historical records: the 1987-1992 drought, an extended dry period lasting for 6 years, was intensified by a strong La Niña year at 1988, and ended by a strong El Niño event at 1991-1992 winter (Resources, 2015). Extreme precipitation and flood events are closely related to El Niño years: during the 1982-1983 El Niño, large parts of Southern California received over 200% of normal rainfall and were subjected to severe flooding (Santa Barbara County Flood Control and Water Conservation District). Climate model results also suggest ENSO events can increase the possibility of extreme precipitation events occurring in Southern California (Gershunov and Barnett, 1998; Kim et al., 2017).

Lake levels likely reflect precipitation integrated over decadal to multidecadal timescales. Higher frequency precipitation is muted in lakes by the complex delayed interactions among inputs (precipitation and stream inflow), outputs (evaporation and stream outflow) and other factors, such as the lag between precipitation and its accumulation (Brunk, 1959; Kirby et al., 2010; Norton et al., 2019). In Lake Elsinore, increased sand accumulation has been related to higher lake levels, increased river discharge, and greater regional precipitation on decadal timescales, in contrast several consecutive low-precipitation years are required to reduce lake level (Kirby et al., 2010). $C_{organic}$ to N_{total} (CN) ratios are also used as a proxy for precipitation and river run-off. Terrestrial biomass has a higher organic carbon content relative to N than that of aquatic biomass, and high C/N ratio therefore indicates enhanced terrestrial biomass delivery as precipitation and river run-off increase (Kirby et al., 2012). Thus high lake levels indicated by increased C/N ratios from Lower Bear Lake (Kirby et al., 2012), and sand deposits in Lake Elsinore (Kirby et al., 2010), are coincident within age uncertainties with intervals of greater flood frequency/magnitude and increased precipitation (high Ti%) in SBB at ~0.3–0.6, 2.5–3.5, 3.7–4.2, 5.1–5.5, 8.1–8.3 ka (Du et al., 2018) (Fig 5.3. dark blue bars in 3I and 3J) and are indicative of pluvial intervals.

Still, inconsistencies between the high-resolution precipitation record in SBB and lake level reconstructions can be observed during early Holocene. High sediment mass accumulation rates and Ti concentrations observed in SBB indicate wet conditions between 7.1–8.0 ka, but at this time Elsinore and Lower Bear Lake levels were relatively low. One possible explanation for this disagreement is that lake levels would be more sensitive to extreme precipitation events such as the modern reservoir-filling events seen during El Niño events, compared to consistent moderate precipitation. Alternatively, cooler air temperature during early Holocene could increase the snowmelt contribution to lake levels, especially for high-elevation lakes like Lower Bear Lake. Lower Bear Lake receives >1600 mm snowfall per year between November and April. Significant snow accumulation in Sierra Nevada, high precipitation and stream flow in Southern California occurred at ~1600 AD, and led to high lake stands in Mojave River (Enzel et al., 1992). Thus wet years with extreme precipitation events generate larger snow accumulation, producing greater spring runoff, which brings more terrestrial biomass and sediment into high elevation lakes (Minnich et al., 2007).

Similarly, both Lake Elsinore and Lower Bear Lake displayed high lake levels during 6.2-6.8 ka and 8.5-9.0 ka, when megadroughts and low mass accumulation rates are observed in SBB sediments (Fig. 5.3). In this case, such discrepancies between hydroclimate records in regional lake sediments and SBB can be explained by changes in the extended North American Monsoon (NAM) during the early Holocene. The NAM provides significant component of mean annual precipitation to central and northern

Mexico, Arizona, and New Mexico during summer (Mitchell et al., 2002). Previous paleoproxy and modeling studies suggest that NAM was enhanced and extended into Mojave Desert and San Bernardino Mountains during early Holocene, due to the greater North Hemisphere insolation. (Barron et al., 2012; Bird and Kirby, 2006; Liu et al., 2003). The broad region affected by the early-Holocene NAM in the model simulation (Harrison et al., 2003) includes both Lower Bear Lake and Lake Elsinore. Therefore, the high lake levels observed from these two lakes during the earth Holocene could be due to increased summer precipitation delivered by the enhanced NAM. The coastal catchments draining into SBB do not receive precipitation from NAM and therefore this early Holocene wet interval should not be expected in the SBB precipitation reconstruction.

The different aspects to hydroclimate discussed above impact the growth and distribution of vegetation in Southern California mostly through the modulation of effective soil moisture by precipitation. Soil moisture in Southern California mainly depends on recharge by winter precipitation. As evapotranspiration exceeds precipitation in this region during summer, soil moisture deficits affect vegetation growth seasonally during the dry season. Therefore, the summer precipitation brought by NAM in the early Holocene could impact Southern California vegetation distribution away from the coast, explaining the different vegetation responses between SBB and interior pollen records. Alternatively, the different response of vegetation at high altitude sites relative to SBB could be the results of snowpack or air temperatures. Winter snowpack melt in spring and summer also contributes to dry season soil moisture, especially in high mountain watersheds as winter precipitation is released as air temperatures increase (Barbour et al., 2007). In addition, cooler air temperature may decrease evaporation and therefore increase effective soil moisture.

We observe a very muted response in the SBB pollen record (the transition between zones 2b and c, and increase/decrease in Xeric/mesic vegetation) to changes in interannual precipitation variability at 4.4 ka. Precipitation variability is expressed as river runoff in the SBB precipitation reconstruction. River runoff represents surplus water that is either delivered too rapidly to saturate the ground or cannot penetrate an already saturated ground. Thus river runoff may not reflect the amount of soil moisture available to vegetation. The vegetation response to precipitation reflected by runoff therefore would be stronger when water is in deficit, because the vegetation utilizes most precipitation. The changes of vegetation responding to different aspects of hydroclimate changes will be further discussed in the section below.

5.5.3. Vegetation response to hydroclimate change in Southern California over the Holocene

The long-term temperature trend associated with orbital forced seasonal insolation variance, is the main factor controlling vegetation composition and distribution in Southern California (Davis, 1999; Glover, 2016). The slightly high percentage of mesic pollen and low xeric vegetation component prior 8 ka is consistent with higher lake levels recorded in Lower Bear Lake. The cooler air temperature during the early Holocene could decrease evaporate rate and lead to higher lake levels in Lower Bear Lake and Lake Elsinore. The decreased evaporation would also increase the effective soil moisture in coastal Southern California, and therefore contribute to expansion of oak woodland (higher relative abundance of *Quercus* and the reduced RRA contribution to pollen records). In contrast to other Southern Californian pollen records (Glover, 2016; Paladino, 2008), only subtle variability is observed in the SBB pollen record after 9 ka (Heusser, 1978{Heusser, 1995 #485; Heusser and Sirocko, 1997) requiring further explanation.

Hydroclimate changes during the Holocene may have been insufficient to cause large-scale vegetation changes. Oak-dominated vegetation replaced *Pinus/*TCT-dominated vegetation in response to the Pleistocene-Holocene transition (Heusser et al., 2015b; Kirby et al., 2018), when proxy records and climate model simulations indicate moisture availability was substantial decreased during deglaciation (Lora and Ibarra, 2019). Mean annual precipitation on the Southern California coast reduced by ~50% from 21 ka to 10 ka in climate simulations (Transient Climate Evolution of the past 21 kyr; Liu et al., 2009). Additionally, 7-12 ˚C surface ocean warming is observed on the California Margin (Hendy and Kennett, 1999, 2000; Pak et al., 2012). However, small changes in ice cap advances (Clark and Gillespie, 1997) and lake levels (Benson et al., 1990) indicate that Southern California precipitation was relatively stable during the Holocene compared to the rapid hydroclimate change that occurred during the

Pleistocene-Holocene transition and therefore subtle changes in vegetation composition and distribution in this region should be expected.

Alternatively, the drought-adapted endemic vegetation may be resistant to the hydroclimate shifts observed in Southern California during the Holocene, having evolved to withstand similar hydroclimate changes over the millions of years. Van Devender (1990) found xeric scrub composition in southwestern US changed little since the early Holocene and concluded that modern floras in this region have equilibrated to the modern climate. *Quercus* (~30%) pollen dominates the SBB pollen record. Oak woodlands have a low-moderate sensitivity to summer precipitation and soil moisture (Hilberg and Kershner., 2018). Oak species in Southern California are resilient to short-term drought events and feature adaptations to accommodate seasonal summer drought, such as winter growth periods (coast live oak), rapid seedling growth early in the season (blue oak), and drought deciduousness (blue oak and Engelmann oak) (Principe et al., 2013). On the other hand, pine-juniper woodlands, occupying mid- to high-elevation areas of the Mojave Desert, San Jacinto, San Bernardino, and Santa Rosa Mountains, are moderately sensitive to drought, due to low seedling recruitment and slow growth rate, such that drought has been linked to tree mortality and range contraction (Hilberg and Kershner., 2017). The different habitat vulnerability could explain the more significant changes in pollen components observed in high-elevation terrestrial records during the early to the mid Holocene transition (Davis, 1999; Glover, 2016; Paladino, 2008), contrasting to subtle variance in our pollen record from SBB. Finally, long-lived communities need centuries to complete population changes even if climate change is rapid. There could be a strong inertia in vegetation composition and distribution that contributes to the subtle vegetation change throughout the Holocene. Coast live oak stands are typically from 40 to 110 years old, and individual trees may live over 250 years (Plumb and Gomez, 1983). Seedling recruitment is the only mechanism by which oak woodland stands expand, and as such, the establishment of new stands (>40 years) takes longer than the periodicity of interannual hydroclimate variability (2-7 years).

Thus it should be expected, regional vegetation composition reconstructed in this study does not show a significant response to changes in interannual precipitation variability or the amplitude/ frequency of flood events. ENSO-related interannual precipitation variability in Southern California increased after ~4.4 ka, notably between ~2.0–4.0 ka. Xeric vegetation components increased while the relative abundance of arboreal vegetation pollen decreased between 1.0–4.0 ka (Fig. 5.3). As interannual water storage is very limited, especially for shrublands and forests, the effects of interannual precipitation variability on soil moisture and vegetation growth are very small (Minnich et al., 2007). Additionally, interannual precipitation variability is insufficient to impact the growth of coast live oak, because of their long-life span. Therefore, the distribution of coast live oak and hence *Quercus* pollen abundance likely represents the integration of hydroclimate over decadal to centennial timescales. Frequent flood events between 2.0–4.0 ka may uproot vegetation, however, the 1992 AD historical flood had an insignificant impact on riparian vegetation, suggesting the impacts are likely minimal (Bendix, 1998). On the other hand, intense fires could damage conifer forests and oak woodlands severely and rapidly,while chaparral, coastal sage scrub, and grassland habitats are well adapted to fires and will recover within a few years (Lentile et al., 2007). Therefore, wildfires can alter the composition and distribution of vegetation in Southern California on interannual timescales. However, high resolution fires reconstructions, such as large charcoal particle accumulation rates, are needed to further test the effect of wildfire in this region over the Holocene.

On multidecadal to centennial timescales throughout the Holocene, Southern California vegetation does responds to megadroughts. A reduction in the arboreal vegetation (~3%-10%) contribute to the pollen record, coincides with a greater relative abundance of xeric vegetation in SBB when megadroughts occur (orange bars in Fig. 5.3) between 0.9–1.1, 1.5–1.7, 2.0–2.1, 2.3–2.5, 2.7–2.8, 3.4–3.6, 3.7–3.8, 6.25–6.35, 6.5–6.6, 8.75-9.0 ka (Fig. 5.3). Multiyear-decadal droughts or short acute 1-year droughts (e.g., 2002) impact the growth of trees by reducing seedling recruitment (Mahall et al., 2009). Historical records suggest that during the megadrought centered on the 1580 AD (the most severe statewide over the past 1000 years in California), trees (e.g. pine) grew very slowly until sufficient soil moisture became available during a pluvial in the early 1600s AD (Brown and Wu, 2005). Oak woodlands are generally sensitive to prolonged drought periods, however drought sensitivity varies amongst oak species and age classes. Coastal live oak is particularly vulnerable to megadrought (Steinberg 2002) as this species has less adaptive root growth in response to reduced soil moisture in simulated drought conditions (Hilberg and Kershner., 2018).

Although chaparral is a drought-adapted community typical of Mediterranean hydroclimates, severe and/or prolonged drought can lead to significant chaparral dieback and higher mortality (Ehleringer and Sandquist, 2018; Paddock et al., 2013; Reynier et al., 2017). The driest interval (6.3–6.8 ka) in the SBB hydroclimate reconstruction is characterized by dramatic drop in sediment mass accumulation rate, low pollen accumulation rate, more frequent megadroughts and absent of flood layers (Fig. 5.3) and is consistent with the maximum warm mid-Holocene (~6.5 ka) suggested by temperature proxy records (Potito et al., 2006). During this extremely dry interval, both xeric and mesic vegetation abundances were lower than average, consistent with the fact that severe prolonged drought can cause mortality of chaparral and *Quercus*. Additionally, drought conditions can also increase fire risk. The persistent high percentage of Asteraceae during 6.3–6.8 is likely a response to significant drought and more frequent wildfire, as the perennial herbaceous plants are often part of a successional community as the fast-growing plants take advantage of decreased competition for water and light.

5.6 Conclusions

The new multidecadal- to centennial- resolution pollen record from SBB indicates only subtle changes in vegetation composition and distribution occurred during the Holocene, contrast to the dramatic changes observed after the Last Glacial Maximum. Regime shift analysis suggested that relative abundance of arboreal pollen (*Pinus*, TCT, *Quercus*, and *Alnus*) was 3% higher than the mean value prior ~8 ka, while xeric vegetation (Chaparral and *Artemisia*) was less abundant (4% lower than the mean value) suggesting slightly cooler and more mesic condition during the early Holocene. The relatively abundance of mesic pollen decreased by 6% from 7.2 ka to 5.0 ka, consistent with slightly more abundant (by 4%) xeric pollen during this interval, indicating the transition to the warmer/xeric mid-Holocene. Mesic pollen percentage increased again by ~10% after ~1.0 ka, indicating a return to slightly cooler/mesic conditions during the late Holocene. These very subtle long-term trends could be related to orbitally forced temperature changes over the Holocene, characterized by warmer/drier conditions during the mid-Holocene. Holocene pollen records from high-elevation lake sediments, such as

Low Bear Lake in San Bernadino Mountains display more significant changes in vegetation composition and distribution, contrast to the subtle variance observed in the pollen record from SBB. This discrepancy could be related to greater air temperature change at high-elevations compared to that over the catchment of SBB OR orbitally forced changes in NAM, and/or changes in snowpack.

The comparison between SBB hydroclimate reconstructions and new pollen record suggests that coastal vegetation in Southern California is not sensitive to interannual precipitation variability. Only a subtle increase in xeric vegetation abundance is recorded between 4 and 1 ka when interannual precipitation variability increases in the SBB reconstruction. The driest interval between 6.3–6.8 ka recorded in SBB resulted in decreased arboreal and chaparral pollen relative abundance, while the fast-growing plants such as Asteraceae were more abundant. Thus although megadrought events lead to drop of arboreal pollen and increasing xeric pollen on multidecadal to centennial timescales, the heat- and drought-adapted vegetation in Southern California coast appears generally resistant to hydroclimate and temperature changes.

This study suggests that air temperature fluctuations on the order of 1–3 ˚C during the Holocene may be insufficient to drive significant vegetation change in coastal Southern California. Additionally, coastal woodlands communities appear insensitive to either interannual precipitation variability related to ENSO, or extreme precipitation events. Climate model simulations predict that the mean annual temperature in California will increase by ~2.2 ˚C by 2100 (Gordon et al., 2000). Such temperature increases in addition to potential changes in ENSO related extreme precipitation will be insufficient, however, to dramatically change vegetation composition and distribution in Southern California, as the endemic vegetation are heat- and drought-adapted. Additionally, global warming over the next few decades is predicted to increase the probability of co-occurring warm-dry conditions in California in climate model (Diffenbaugh et al., 2015). The consequent extreme or/and prolonged drought events have the potential to cause oak woodland contraction and rise mortality of chaparral.

5.7 References

Balmaki, B., Wigand, P.E., 2019. Reconstruction of the Late Pleistocene to Late Holocene vegetation transition using packrat midden and pollen evidence from the Central Mojave Desert. Acta Bot Bras 33, 539-547.

Barbour, M., Keeler-Wolf, T., Schoenherr, A.A., Keeler-Wolf, T., 2007. Terrestrial Vegetation of California, 3rd Edition. University of California Press, Berkeley, UNITED STATES.

Barbour, M.G., Major, J., 1977. Terrestrial vegetation of California, Univ of California Press.

Barbour, M.G., Minnich., R.A., 1988. Califomian upland forests and woodlands. North American terrestrial vegetation, 131-164.

Barron, J.A., Metcalfe, S.E., Addison, J.A., 2012. Response of the North American monsoon to regional changes in ocean surface temperature. Paleoceanography 27.

Bendix, J., 1994. Scale, Direction, and Pattern in Riparian Vegetation-Environment Relationships. Ann Assoc Am Geogr 84, 652-665.

Bendix, J., 1998. Impact of a flood on southern California riparian vegetation. Phys Geogr 19, 162-174.

Benson, L.V., Currey, D.R., Dorn, R.I., Lajoie, K.R., Oviatt, C.G., Robinson, S.W., Smith, G.I., Stine, S., 1990. Chronology of Expansion and Contraction of 4 Great-Basin Lake Systems during the Past 35,000 Years. Palaeogeogr Palaeocl 78, 241-286.

Bird, B.W., Kirby, M.E., 2006. An alpine lacustrine record of early Holocene North American Monsoon dynamics from Dry Lake, southern California (USA). Journal of Paleolimnology 35, 179-192.

Blaauw, M., Christen, J.A., 2011. Flexible paleoclimate age-depth models using an autoregressive gamma process. Bayesian Anal 6, 457-474.

Brown, P.M., Wu, R., 2005. Climate and disturbance forcing of episodic tree recruitment in a southwestern ponderosa pine landscape. Ecology 86, 3030-3038.

Brunk, I.W., 1959. Precipitation and the Levels of Lakes Michigan and Huron. Journal of Geophysical Research 64, 1591-1595.

Byrne, R., Edlund, E., Mensing, S., 1991. Holocene Changes in the Distribution and Abundance of Oaks in California. Us for Serv T R Psw 126, 182-188.

Callaway, R.M., Jones, S., Ferren, W.R., Parikh, A., 1990. Ecology of a Mediterranean-Climate Estuarine Wetland at Carpinteria, California - Plant-Distributions and Soil-Salinity in the Upper Marsh. Can J Bot 68, 1139-1146.

Clark, D.H., Gillespie, A.R., 1997. Timing and significance of late-glacial and Holocene cirque glaciation in the Sierra Nevada, California. Quaternary International 38-9, 21-38.

Cole, K.L., Liu, G.W., 1994. Holocene Paleoecology of an Estuary on Santa-Rosa-Island, California. Quaternary Research 41, 326-335.

Critchfield, W.B., 1971. Profiles of California vegetation. Pacific Southwest Forest & Range Experiment Station, Forest Service, U.S. Department of Agriculture, Berkeley, CA.

Crucifix, M., Loutre, M.F., Tulkens, P., Fichefet, T., Berger, A., 2002. Climate evolution during the Holocene: a study with an Earth system model of intermediate complexity. Climate Dynamics 19, 43-60.

Davis, O.K., 1999. Pollen analysis of Tulare Lake, California: Great Basin-like vegetation in Central California during the full-glacial and early Holocene. Rev Palaeobot Palyno 107, 249-257.

Diffenbaugh, N.S., Sloan, L.C., 2004. Mid-Holocene orbital forcing of regional-scale climate: A case study of western North America using a high-resolution RCM. Journal of Climate 17, 2927-2937.

Diffenbaugh, N.S., Swain, D.L., Touma, D., 2015. Anthropogenic warming has increased drought risk in California. Proceedings of the National Academy of Sciences of the United States of America 112, 3931-3936.

Dong, C.Y., MacDonald, G.M., Willis, K., Gillespie, T.W., Okin, G.S., Williams, A.P., 2019. Vegetation Responses to 2012-2016 Drought in Northern and Southern California. Geophysical Research Letters 46, 3810-3821.

Du, X., Hendy, I., Hinnov, L., Brown, E., Schimmelmann, A., Pak, D., 2020. Interannual Southern California Precipitation Variability During the Common Era and the ENSO Teleconnection. Geophysical Research Letters 47, e2019GL085891.

Du, X., Hendy, I.L., Schimmelmann, A., 2018. A 9000-year flood history for Southern California: A revised stratigraphy of varved sediments in Santa Barbara Basin. Marine Geology 397, 29-42.

Ehleringer, J.R., Sandquist, D.R., 2018. A tale of ENSO, PDO, and increasing aridity impacts on drought-deciduous shrubs in the Death Valley region. Oecologia 187, 879-895.

Enzel, Y., Brown, W.J., Anderson, R.Y., McFadden, L.D., Wells, S.G., 1992. Short-duration Holocene lakes in the Mojave River drainage basin, southern California. Quaternary Research 38, 60-73.

Feakins, S.J., Kirby, M.E., Cheetham, M.I., Ibarra, Y., Zimmerman, S.R.H., 2014. Fluctuation in leaf wax D/H ratio from a southern California lake records significant variability in isotopes in precipitation during the late Holocene. Organic Geochemistry 66, 48-59.

Fensham, R.J., Laffineur, B., Allen, C.D., 2019. To what extent is drought-induced tree mortality a natural phenomenon? Global Ecol Biogeogr 28, 365-373.

Fischer, D.T., Still, C.J., Williams, A.P., 2009. Significance of summer fog and overcast for drought stress and ecological functioning of coastal California endemic plant species. J Biogeogr 36, 783-799.

Gershunov, A., Barnett, T.P., 1998. ENSO influence on intraseasonal extreme rainfall and temperature frequencies in the contiguous United States: Observations and model results (vol 11, pg 1575, 1998). Journal of Climate 11, 3062-3065.

Glover, K.C., 2016. Southern California Climate and Vegetation Over the Past 125,000 Years from Lake Sequences in the San Bernardino Mountains. University of California, Los Angeles.

Glover, K.C., Chaney, A., Kirby, E.M., Patterson, P.W., MacDonald, M.G., 2020. Southern California Vegetation, Wildfire, and Erosion Had Nonlinear Responses to Climatic Forcing During Marine Isotope Stages 5–2 (120–15 ka). Paleoceanogr Paleocl 35, e2019PA003628.

Gordon, C., Cooper, C., Senior, C.A., Banks, H., Gregory, J.M., Johns, T.C., Mitchell, J.F.B., Wood, R.A., 2000. The simulation of SST, sea ice extents and ocean heat transports in a version of the Hadley Centre coupled model without flux adjustments. Climate Dynamics 16, 147-168.

Grimm, E.C., 1987. Coniss - a Fortran-77 Program for Stratigraphically Constrained Cluster-Analysis by the Method of Incremental Sum of Squares. Comput Geosci 13, 13-35.

Hanes, T.L., Richard D. Friesen, Keane, K., 1989. Alluvial scrub vegetation in coastal southern California. Pacific Southwest Forest and Range Experiment Station, Forest Service, US Department of Agriculture, Berkeley, CA.

Harrison, A.T., Small, E., Mooney, H.A., 1971. Drought Relationships and Distribution of Two Mediterranean-Climate California Plant Communities. Ecology 52, 869-875.

Harrison, S.P., Kutzbach, J.E., Liu, Z., Bartlein, P.J., Otto-Bliesner, B., Muhs, D., Prentice, I.C., Thompson, R.S., 2003. Mid-Holocene climates of the Americas: a dynamical response to changed seasonality. Climate Dynamics 20, 663-688.

Haston, L., Michaelsen, J., 1997. Spatial and temporal variability of southern California precipitation over the last 400 yr and relationships to atmospheric circulation patterns. Journal of Climate 10, 1836-1852.

Hendy, I.L., Dunn, L., Schimmelmann, A., Pak, D.K., 2013. Resolving varve and radiocarbon chronology differences during the last 2000 years in the Santa Barbara Basin sedimentary record, California. Quaternary International 310, 155-168.

Hendy, I.L., Kennett, J.P., 1999. Latest quaternary north Pacific surface-water responses imply atmosphere-driven climate instability. Geology 27, 291-294.

Hendy, I.L., Kennett, J.P., 2000. Dansgaard-Oeschger cycles and the California Current System: Planktonic foraminiferal response to rapid climate change in Santa Barbara Basin, Ocean Drilling Program hole 893A. Paleoceanography 15, 30-42.

Hendy, I.L., Napier, T.J., Schimmelmann, A., 2015. From extreme rainfall to drought: 250 years of annually resolved sediment deposition in Santa Barbara Basin, California. Quaternary International 387, 3-12.

Heusser, L., 1978. Pollen in Santa Barbara Basin, California: A 12,000-yr record Geol Soc Am Bull 89, 673-678.

Heusser, L., 1995. Pollen stratigraphy and paleoecologic interpretation of the 160-k.y. record from Santa Barbara Basin, Hole 893A.

Heusser, L.E., Hendy, I.L., Barron, J.A., 2015a. Vegetation response to southern California drought during the Medieval Climate Anomaly and early Little Ice Age (AD 800-1600). Quaternary International 387, 23-35.

Heusser, L.E., Kirby, M.E., Nichols, J.E., 2015b. Pollen-based evidence of extreme drought during the last Glacial (32.6-9.0 ka) in coastal southern California. Quaternary Science Reviews 126, 242-253.

Heusser, L.E., Sirocko, F., 1997. Millennial pulsing of environmental change in southern California from the past 24 k.y.: A record of Indo-Pacific ENSO events? Geology 25, 243-246.

Hilberg, L., Kershner., J., 2017. Southern California Pinyon-Juniper Woodlands, in: Gregg., R.M. (Ed.), Southern California Climate Adaptation Project.

Hilberg, L., Kershner., J., 2018. Southern California Oak Woodland Habitats, Southern California Climate Adaptation Project.

Hiner, C.A., Kirby, M.E., Bonuso, N., Patterson, W.P., Palermo, J., Silveira, E., 2016. Late Holocene hydroclimatic variability linked to Pacific forcing: evidence from Abbott Lake, coastal central California. Journal of Paleolimnology 56, 299-313.

Kennett, J.P., Ingram, B.L., 1995. A 20,000-year record of ocean circulation and climate change from the Santa Barbara basin. Nature 377, 510-514.

Kenyon, K.E., 1999. North Pacific High: an hypothesis. Atmos Res 51, 15-34.

Kim, H.-M., Zhou, Y., Alexander, M.A., 2017. Changes in atmospheric rivers and moisture transport over the Northeast Pacific and western North America in response to ENSO diversity. Climate Dynamics.

Kirby, M.E., Heusser, L., Scholz, C., Ramezan, R., Anderson, M.A., Markle, B., Rhodes, E., Glover, K.C., Fantozzi, J., Hiner, C., Price, B., Rangel, H., 2018. A late Wisconsin (32-10k cal a BP) history of pluvials, droughts and vegetation in the Pacific south-west United States (Lake Elsinore, CA). Journal of Quaternary Science 33, 238-254.

Kirby, M.E., Knell, E.J., Anderson, W.T., Lachniet, M.S., Palermo, J., Eeg, H., Lucero, R., Murrieta, R., Arevalo, A., Silveira, E., Hiner, C.A., 2015. Evidence for insolation and Pacific forcing of late glacial through Holocene climate in the Central Mojave Desert (Silver Lake, CA). Quaternary Research 84, 174-186.

Kirby, M.E., Lund, S.P., Patterson, W.P., Anderson, M.A., Bird, B.W., Ivanovici, L., Monarrez, P., Nielsen, S., 2010. A Holocene record of Pacific Decadal Oscillation (PDO)-related hydrologic variability in Southern California (Lake Elsinore, CA). Journal of Paleolimnology 44, 819-839.

Kirby, M.E., Lund, S.P., Poulsen, C.J., 2005. Hydrologic variability and the onset of modern El Niño-Southern Oscillation: A 19 250-year record from Lake Elsinore, southern California. Journal of Quaternary Science 20, 239-254.

Kirby, M.E., Zimmerman, S.R.H., Patterson, W.P., Rivera, J.J., 2012. A 9170-year record of decadal-to-multi-centennial scale pluvial episodes from the coastal Southwest United States: A role for atmospheric rivers? Quaternary Science Reviews 46, 57-65.

Kirby, M.E.C., Patterson, W.P., Lachniet, M., Noblet, J.A., Anderson, M.A., Nichols, K., Avila, J., 2019. Pacific Southwest United States Holocene Droughts and Pluvials Inferred From Sediment delta O-18((calcite)) and Grain Size Data (Lake Elsinore, California). Front Earth Sc-Switz 7.

Koehler, P.A., Anderson, R.S., Spaulding, W.G., 2005. Development of vegetation in the Central Mojave Desert of California during the late quaternary. Palaeogeogr Palaeocl 215, 297-311.

Kutzbach, J.E., Guetter, P.J., 1986. The Influence of Changing Orbital Parameters and Surface Boundary Conditions on Climate Simulations for the Past 18 000 Years. J Atmos Sci 43, 1726-1759.

Lentile, L.B., Morgan, P., Hudak, A.T., Bobbitt, M.J., Lewis, S.A., Smith, A.M.S., Robichaud, P.R., 2007. Post-Fire Burn Severity and Vegetation Response Following Eight Large Wildfires Across the Western United States. Fire Ecology 3, 91-108.

Liu, Z., Otto-Bliesner, B., Kutzbach, J., Li, L., Shields, C., 2003. Coupled climate simulation of the evolution of global monsoons in the Holocene. Journal of Climate 16, 2472-2490.

Lora, J.M., Ibarra, D.E., 2019. The North American hydrologic cycle through the last deglaciation. Quaternary Science Reviews 226.

Mahall, B.E., Tyler, C.M., Cole, E.S., Mata, C., 2009. A Comparative Study of Oak (Quercus, Fagaceae) Seedling Physiology during Summer Drought in Southern California. Am J Bot 96, 751-761.

Mather, J.R., Yoshioka, G.A., 1968. THE ROLE OF CLIMATE IN THE DISTRIBUTION OF VEGETATION. Ann Assoc Am Geogr 58, 29-41.

McLaughlin, B.C., Zavaleta, E.S., 2012. Predicting species responses to climate change: demography and climate microrefugia in California valley oak (Quercus lobata). Global Change Biol 18, 2301-2312.

Mensing, S., 2005. The history of oak woodlands in California, Part I: The paleoecologic record. The California Geographer 45, 1–38.

Mensing, S., 2014. The Paleohistory of California Oaks, Seventh California Oak Symposium: Managing Oak Woodlands in a Dynamic World, Visalia, California.

Mensing, S.A., Benson, L.V., Kashgarian, M., Lund, S., 2004. A Holocene pollen record of persistent droughts from Pyramid Lake, Nevada, USA. Quaternary Research 62, 29-38.

Minckley, T.A., Bartlein, P.J., Whitlock, C., Shuman, B.N., Williams, J.W., Davis, O.K., 2008. Associations among modern pollen, vegetation, and climate in western North America. Quaternary Science Reviews 27, 1962-1991.

Minnich, R.A., M. Barbour, T. Keeler-Wolf, Schoenherr, A., 2007. Climate, paleoclimate, and paleovegetation. Terrestrial vegetation of California, 43-70.

Mitchell, D.L., Ivanova, D., Rabin, R., Brown, T.J., Redmond, K., 2002. Gulf of California sea surface temperatures and the North American monsoon: Mechanistic implications from observations. Journal of Climate 15, 2261-2281.

Munz, P.A., 1974. A flora of southern California.

Napier, T.J., Hendy, I.L., 2016. The impact of hydroclimate and dam construction on terrigenous detrital sediment composition in a 250-year Santa Barbara Basin record off southern California. Quaternary International.

Napier, T.J., Hendy, I.L., Fahnestock, M.F., Bryce, J.G., 2020. Provenance of detrital sediments in Santa Barbara Basin, California, USA: Changes in source contributions between the Last Glacial Maximum and Holocene. Geol Soc Am Bull 132, 65-84.

Negrini, R.M., Wigand, P.E., Draucker, S., Gobalet, K., Gardner, J.K., Sutton, M.Q., Yohe, R.M., 2006. The Rambla highstand shoreline and the Holocene lake-level history of Tulare Lake, California, USA. Quaternary Science Reviews 25, 1599-1618.

Nezlin, N.P., Stein, E.D., 2005. Spatial and temporal patterns of remotely-sensed and field-measured rainfall in southern California. Remote Sensing of Environment 96, 228-245.

Norton, P.A., Driscoll, D.G., Carter, J.M., 2019. Climate, streamflow, and lake-level trends in the Great Lakes Basin of the United States and Canada, water years 1960–2015. US Geological Survey.

Oster, J.L., Montanez, I.P., Sharp, W.D., Cooper, K.M., 2009. Late Pleistocene California droughts during deglaciation and Arctic warming. Earth Planet Sc Lett 288, 434-443.

Paddock, W.A.S.I., Davis, S.D., Pratt, R.B.J., Anna L.;, Tobin, M.F., López-Portillo, J., Ewers, F.W., 2013. Factors Determining Mortality of Adult Chaparral Shrubs in an Extreme Drought Year in California. Aliso: A Journal of Systematic and Evolutionary Botany 31, 49-57.

Pak, D.K., Lea, D.W., Kennett, J.P., 2012. Millennial scale changes in sea surface temperature and ocean circulation in the northeast Pacific, 10-60 kyr BP. Paleoceanography 27.

Paladino, L., 2008. A vegetation reconstruction of Big Bear Lake: local changes and inferred regional climatology.

Plumb, T.R., Gomez, A.P., 1983. Five southern California oaks: identification and postfire management. U.S. Department of Agriculture, Forest Service, Pacific Southwest Forest and Range Experiment Station, Berkeley, CA, p. 56.

Potito, A.P., Porinchu, D.F., MacDonald, G.M., Moser, K.A., 2006. A late Quaternary chironomid-inferred temperature record from the Sierra Nevada, Califomia, with connections to northeast Pacific sea surface temperatures. Quaternary Research 66, 356-363.

Principe, Z., J.B. MacKenzie, B. Cohen, J.M. Randall, W. Tippets, T. Smith, Morrison, S.A., 2013. 50-Year Climate Scenarios and Plant Species Distribution Forecasts for Setting Conservation Priorities in Southwestern California, Southwestern California Climate Report. The Nature Conservancy of Californ.

Reimer, P.J., Bard, E., Bayliss, A., Beck, J.W., Blackwell, P.G., Ramsey, C.B., Buck, C.E., Cheng, H., Edwards, R.L., Friedrich, M., Grootes, P.M., Guilderson, T.P., Haflidason, H., Hajdas, I., Hatte, C., Heaton, T.J., Hoffmann, D.L., Hogg, A.G., Hughen, K.A., Kaiser, K.F., Kromer, B., Manning, S.W., Niu, M., Reimer, R.W., Richards, D.A., Scott, E.M., Southon, J.R., Staff, R.A., Turney, C.S.M., van der Plicht, J., 2013. IntCal13 and Marine13 radiocarbon age calibration curves 0–50,000 years cal BP. Radiocarbon 55, 1869-1887.

Resources, C.D.o.W., 2015. California's Most Significant Droughts: Comparing Historical and Recent Conditions.

Reynier, W.A., L.E. Hillberg, Kershner., J.M., 2017. Southern California Chaparral Habitats: Climate Change Vulnerability Assessment Synthesis. Version 1.0. , Bainbridge Island, WA.

Schimmelmann, A., Lange, C.B., Berger, W.H., Simon, A., Burke, S.K., Dunbar, R.B., 1992. Extreme climatic conditions recorded in Santa Barbara Basin laminated sediments: the 1835-1840 Macoma event. Marine Geology 106, 279-299.

Schimmelmann, A., Lange, C.B., Meggers, B.J., 2003. Palaeoclimatic and archaeological evidence for a similar to 200-yr recurrence of floods and droughts linking California, Mesoamerica and South America over the past 2000 years. Holocene 13, 763-778.

Schimmelmann, A., Lange, C.B., Roark, E.B., Ingram, B.L., 2006. Resources for paleoceanographic and paleoclimatic analysis: A 6,700-year stratigraphy and regional radiocarbon reservoir-age (ΔR) record based on varve counting and 14C-AMS dating for the Santa Barbara Basin, offshore California, U.S.A. Journal of Sedimentary Research 76, 74-80.

Schimmelmann, A., Zhao, M., Harvey, C.C., Lange, C.B., 1998. A large California flood and correlative global climatic events 400 years ago. Quaternary Research 49, 51-61.

Seager, R., Hoerling, M., 2014. Atmosphere and Ocean Origins of North American Droughts. Journal of Climate 27, 4581-4606.

Seager, R., Vecchi, G.A., 2010. Greenhouse warming and the 21st century hydroclimate of southwestern North America. Proceedings of the National Academy of Sciences of the United States of America 107, 21277-21282.

Thunell, R.C., 1998. Particle fluxes in a coastal upwelling zone: Sediment trap results from Santa Barbara Basin, California. Deep-Sea Research Part II: Topical Studies in Oceanography 45, 1863-1884.

Thunell, R.C., Tappa, E., Anderson, D.M., 1995. Sediment Fluxes and Varve Formation in Santa-Barbara Basin, Offshore California. Geology 23, 1083-1086.

Van Devender, T.R., 1990. Late Quaternary vegetation and climate of the Sonoran Desert, US and Mexico. University of Arizona Press, Tuscon.

Wahl, E.R., 2003. ASSIGNING CLIMATE VALUES TO MODERN POLLEN SURFACE SAMPLE SITES AND VALIDATING MODERN ANALOG CLIMATE RECONSTRUCTIONS IN THE SOUTHERN CALIFORNIA REGION. Madroño 50, 271-285.

Wells, P.V., Berger, R., 1967. Late Pleistocene History of Coniferous Woodland in the Mohave Desert. Science 155, 3770.

Winter, S.L., Fuhlendorf, S.D., Goad, C.L., Davis, C.A., Hickman, K.R., Leslie, D.M., 2011. Fire tolerance of a resprouting Artemisia (Asteraceae) shrub. Plant Ecology 212, 2085-2094.

Chapter 6

Conclusion

The Southern California hydroclimate has experienced a variety of changes during the Holocene, as evidenced from marine sediment cores in the Santa Barbara Basin (SBB) and regional terrestrial records. My Holocene hydroclimate reconstructions in this region, alongside climate model outputs, provide a new perspective on the mechanisms of hydroclimate change on interannual timescales. The effect of different aspects of hydroclimate changes on vegetation over Southern California coast during the Holocene is also demonstrated.

I focused in particular on how Southern California interannual precipitation responded to climate dynamics changing through the Holocene. I found a significant correlation between Southern California and SST in tropical Pacific through an ENSO teleconnection in the instrumental record of precipitation in Santa Barbara. Furthermore, the high-resolution precipitation reconstruction from SBB demonstrates that the ENSO teleconnection between tropical Pacific and Southern California is nonstationary throughout the Common Era, through a combination of mid-latitude pressure system (Aleutian Low) modulation, and the position of the ITCZ. The linkage I found between Southern California interannual precipitation, ENSO, the ITCZ, and the Aleutian Low via the ENSO teleconnection contained through the Holocene in my reconstruction. This finding indicates the ENSO teleconnection between tropical Pacific and Southern California could be nonstationary on long time scale, and therefore both ENSO variance and the strength/ pattern of Aleutian Low need to be considered when predicting the regional precipitation changes in the future.

The SBB pollen record indicates that heat- and drought-adapted coastal oak woodlands dominated the Southern California coast during the Holocene, but only subtle changes in distribution occurred over the last 9000 years. This finding demonstrates that coastal oak woodlands are resilient to soil moisture changes brought by interannual precipitation variability, but may respond to prolonged droughts on multidecadal timescales or severe droughts. Global warming over the next few decades is predicted to change the ENSO variance in the tropical Pacific and increase the mean annual temperature in Southern California by ~2.2 ˚C. The increase of surface temperature or changes in interannual precipitation associated with ENSO alone may not be sufficient to dramatically change vegetation composition and distribution in Southern California. However, the increased probability of co-occurring warm-dry conditions in this region caused by global warming have the potential to cause contraction of oak woodland.

6.1 Summary of results in each data chapter

In **Chapter 2**, a high-resolution radiocarbon chronology for varved sediments in SBB over the Holocene was generated, providing an improved timescale for the following paleoclimate reconstructions and comparisons. Based on 89 accelerator mass spectrometric ^{14}C dates of mixed planktonic foraminiferal carbonate from three sediment cores collected from three sediment cores collected in SBB (MV0811-14JC, SPR0901-06KC and ODP Hole 893A), I created an age-depth model for 9000 years using the software BACON2.2 (Blaauw and Christen, 2011). In addition, gray flood layers and olive turbidite layers were identified in multiple cores from SBB through visual examination based on color, composition and sediment fabric. Relative to laminated sections, gray layers contain high Ti (average Ti wt. % ~ 0.45 ±0.02) concentrations and low Ca/Ti elemental ratios (average Ca/Ti ~ 4.10 ±0.68) and are interpreted to represent instantaneous flood events. Olive layers are characterized by Ti concentrations (average Ti wt. % ~ 0.38 ±0.01) between laminated sections and gray layers and high Ca/Ti elemental ratios (average Ca/Ti ~ 10.66 ±0.91). Olive layers are interpreted as turbidites produced by downslope flows generated by large earthquakes. The improved radiocarbon chronology together with the identified gray and olive layers provides a valuable well constrained and easily accessible master stratigraphy for the Holocene which allows accurate core-to-core correlations increasing the value of SBB sediments for paleoceanographic and paleoclimatic studies.

In total, the 75 gray flood layers were identified and dated from SBB over the last 9000 years, providing a Holocene flood history for Southern California. The frequency and magnitude of floods generally increased during high precipitation/run-off intervals indicated by lacustrine records from Southern California (Hiner et al., 2016; Kirby et al., 2014; Kirby et al., 2010; Kirby et al., 2005; Kirby et al., 2012) between ~400-800, 3000-5500, 6600-7300 and 8500-9000 yrs BP, accompanied by high mass accumulation rate in SBB, confirming precipitation is the principal process driving sediment accumulation in SBB during the Holocene. The reconstruction of flood events and comparison with regional terrestrial records also provide a framework from hydroclimate changes in Southern California over the Holocene. In addition to climate reconstructions, this work also contributes to our understanding of the regional geology and stratigraphy. Nine turbidite olive layers identified from SBB have been temporally linked to large earthquakes associated with regional tectonics in the Transverse Ranges. A slump (9000 ±200 yrs) related to the Goleta submarine slide complex was identified at the base of MV0811-14JC by folded sediments in high-resolution core images.

Chapter 3 focuses on the reconstruction of Southern California interannual precipitation variability over the Common Era (the last 2,000 years), and its relationship with an ENSO teleconnection is investigated. The field correlation analysis of instrumental Pacific SST and Southern California precipitation (from 1900-2013) demonstrates that Southern California winter precipitation tends to increase when the central and eastern tropical Pacific Ocean warms and the western tropical Pacific cools, consistent with the El Niño sea surface temperature (SST) pattern. This relationship is a result of the ENSO teleconnection between tropical Pacific and Southern California: increased tropical mean zonal SSTs enhances tropical convection during El Niño events, the consequent stronger upper tropospheric tropical divergence and subtropical convergence shifts the mid-latitude jet (North Pacific Jet) toward Southern California, bringing more moisture to the region (Seager et al., 2010; Trenberth et al., 1998). Meanwhile, an eastward shift of a deepened Aleutian Low enhances precipitation in Southern California through the advection of warm, moist air onto North America (Trenberth et al., 1998).

To test whether the ENSO teleconnection between the tropical Pacific and Southern California was stationary during the Common Era, Southern California precipitation over the last 2000 years was reconstructed using sub-annually resolved scanning XRF Ti counts from SBB.

Statistically significant correlation (r=0.30, P<0.01) was found between the Niño 3.4 and annually tuned Ti time series from 1900 to 2008. Together the Multi-taper method (MTM) spectrum analysis and cross-spectral analysis provides evidence that the relationship between Southern California precipitation and ENSO can be reproduced in the sedimentary archive of runoff in SBB. The 2000-year SBB precipitation reconstruction reveals that both tropical and mid-latitude atmospheric circulation influences the interannual precipitation variability in Southern California by modulating the ENSO teleconnection. Strong interannual variability in precipitation with a strengthening of the 5–7 year event periodicity is observed when the ENSO teleconnection is anticipated to be strong (e.g. 1370-1540 CE): That is when greater ENSO variance is observed in the tropical Pacific, a southward shift of ITCZ is reported, and a deepening of the Aleutian Low is recorded in the NE Pacific. On the other hand, precipitation variability is weak, with event periodicities limited to 2-4 years, when either ENSO variance is reduced in the tropical Pacific (700-900 CE) such as when then ITCZ is displaced northward or if the ENSO teleconnection is muted by a weakening of the AL (1540-1680 CE). Thus, although interannual precipitation in Southern California is driven by tropical ENSO variance via the ENSO teleconnection between Southern California and tropical Pacific, this teleconnection is modulated by extratropical pressure systems and therefore is nonstationary during the Common Era.

I extended the subannually-resolved SBB precipitation reconstruction through the Holocene in **Chapter 4** to further explore the climate dynamics responsible for interannual precipitation changes in Southern California over the last 9,000 years. Wavelet analysis of the SBB Ti record demonstrates interannual (2–7 years) precipitation variance was relatively weak, with shorter intervals (2–3 years) between events prior to 4.4 ka. After 4.4 ka precipitation variability increased accompanied by the appearance of longer intervals between events (5–7 years). Synthesizing the Holocene Ti record with previously published proxy records from about the tropical Pacific suggests that a southward shift of ITCZ in the late Holocene may have amplified ENSO variability through a weakening of the zonal SST gradient and southeasterly trade winds across the equatorial Pacific. At the same time, a stronger, westward-shifted Aleutian Low after 4.4 ka may have strengthened the ENSO teleconnection between the tropical Pacific and Southern California, thereby enhancing interannual precipitation variance recorded in SBB. The relationship between ITCZ migration and ENSO variance is supported by model simulations (pre-industrial, 3 ka, 6 ka and 9 ka timeslices performed in CESM 1.2): The ITCZ is displaced southward during the late Holocene simulation (3 ka time slice), mainly due to decreased boreal summer insolation. This shift was accompanied by weaker southeasterly trade winds and increased ENSO variance. Thus, both model simulations and paleoclimate reconstructions support the possibility that mid-latitude pressure conditions can modulate the long-term precipitation changes in Southern California through the ENSO teleconnection.

In **Chapter 5**, the effect of hydroclimate changes on vegetation ecosystem in Southern California is investigated, using a Holocene pollen record from SBB with multidecadal to centennial resolution. In contrast to the dramatic changes in vegetation distribution seen during the Last Glacial Maximum and deglacial warming, only subtle shifts were observed in the Holocene pollen record in SBB. During the Holocene, the Southern California coast was dominated by a mosaic of oak woodland/ chaparral/ sage scrub communities. Regime shift analysis inidicated that the relative abundance of arboreal pollen (*Pinus*, TCT, *Quercus*, and *Alnus*) was only 3% higher than the average values prior ~8 ka, accompanied by fewer xeric vegetation (Chaparral and *Artemisia*) components (4% lower than average), suggesting slightly cooler and wetter condition during the early Holocene. The relatively abundance of meric pollen decreased 6% from 7.2 ka to 5.0 ka, coincident with slightly increased xeric pollen abundance, indicating a transition to a warmer/drier mid-Holocene. The meric pollen percentage increased 10% again after ~1.0 ka, indicating slightly cooler/meric conditions during the late Holocene. Such subtle long-term trends could be related to orbital forced temperature change over the Holocene, which are characterized by warmer/drier condition during the mid-Holocene.

In contrast, Holocene pollen records from high-elevation lacustrine sediments reflect more significant changes, suggesting high-elevation regions may experience great temperature and precipitation changes through the Holocene compared to the coast.

Alternatively, the subtle variance observed in the pollen record from SBB may be caused by the fact that the endemic drought-adapted vegetation in Southern California coast are resistant to hydroclimate and temperature changes over Holocene. The comparison of the SBB pollen record with the precipitation reconstructions presented in **Chapter 4** demonstrates that oak woodland/ chaparral/ sage scrub communities are relatively insensitive to interannual precipitation variability associated with ENSO. Additionally, I found concurrent reduced meric pollen abundance and megadrought events (Ti% below the 20th percentile) in the SBB Holocene sediment record, indicating prolonged or severe drought events would lead to contraction of oak woodlands on multilectal to centennial timescales.

6.2 Future research directions

Following my dissertation results, I would like to pursue the following potential research directions. Two ENSO flavors, Eastern Pacific (EP) and Central Pacific (CP) El Niño events, are identified based on the where the maximum warm anomaly occurring during El Niño events is located in the tropical Pacific (Ashok et al., 2007; Kao and Yu, 2009). Research on the changes of ENSO flavors during the Holocene would contribute to a more complete understanding of the ENSO teleconnection between tropical Pacific and Southern California. In Chapter 3, a discrepancy was observed when comparing the interannual precipitation variability in Southern California and ENSO records from eastern equatorial lake sediments during the last millennium. Such inconsistencies could be caused by distinct teleconnection patterns of EP relative to CP El Niño events. Recent studies (Lee and McPhaden, 2010; Yeh et al., 2009) have suggested that CP El Niño events could occur much more frequently under the projected global warming scenarios. Therefore, a better understanding of the response of the ENSO teleconnection to Southern California to these different flavors of El Niño events are critical for accurate future prediction of Southern California precipitation. However, our understanding of the pattern and stationarity of the teleconnection between CP or EP El Niño and Southern California on long timescales remain unclear. Model simulation results suggest the frequency of the strongest EP events decreases in the mid-Holocene, while the frequency of CP events increases (Karamperidou et al., 2015), providing a potential opportunity to test the teleconnection patterns of EP and CP events in association with Southern

California precipitation. But proxy records of CP El Niño with sufficient resolution and long duration over the Holocene are very rare. A previous study suggests the two ENSO flavors have distinct impacts of on precipitation in Western Pacific Warm Pool (Schollaen et al., 2015), and therefore continuous precipitation reconstructions from lake sediments in the Western Pacific Warm Pool could shed some light on Holocene CP events. Together with published high-resolution ENSO records from the eastern equatorial Pacific, such records may allow for detection of changes in the ENSO teleconnection to Southern California corresponding to the two ENSO flavors.

Results from Chapter 4 demonstrate that the interannual precipitation variability recorded from SBB increased after 4.4 ka, concurrent with a southward shift of the ITCZ such as reflected in precipitation recorded in marine sediments from Cariaco Basin, off the Venezuelan coast. The intensified interannual precipitation variability suggests either more energetic ENSO variance in the tropical Pacific or a stronger ENSO teleconnection to the Southern California. But the latitudinal position, structure and strength across the tropical Pacific remains unclear. Alongside comparison with available eastern equatorial Pacific Holocene precipitation records (Atwood and Sachs, 2014; Sachs et al., 2009; Thompson et al., 2017), continuous, high resolution precipitation reconstructions from Western Pacific Warm Pool would provide insight into ITCZ migration across the tropical Pacific over the Holocene. Such a reconstruction of the latitudinal position, contraction/expansion, and strength of the Pacific ITCZ during the Holocene would allow for a more complete understanding of the linkage between ITCZ migration, ENSO variance, and interannual hydroclimate changes in Southern California, contributing to a better understanding of the teleconnection between tropical Pacific and extratropical regions.

Further study on the interannual precipitation in Southern California will also benefit from Holocene high-resolution Aleutian Low reconstructions, in order to test the role mid-latitude pressure systems play in the ENSO teleconnection between the tropical Pacific and Southern California during the Holocene. Aside from interannual variance, precipitation variability on multidecadal are also observed in my precipitation reconstruction from SBB. Exploring the mechanisms, especially the oceanic forcing (e.g. Pacific Decadal Oscillation, Pacific Meridional Mode, and Multidecadal Atlantic

Oscillation) that could drive multidecadal precipitation variability in Southern California will allow us to understand the long-term hydroclimate changes in this region, and the interaction with precipitation changes on interannual timescales. Additionally, the integration of proxy data with climate model can result in a useful tool to investigate mechanisms of climate changes in the past. Further data-model comparison studies are needed to identify climate dynamics responsible for hydroclimate changes in Southern California on different timescales, and explore mechanisms driving ENSO variance shifts from the mid to late Holocene. A more complete understanding of the climate dynamics responsible hydroclimate variability in Southern California on interannual to multidecadal timescales and mechanisms contributing to changes in ENSO variance is critical for future prediction of precipitation in this region.

6.3 References

Ashok, K., Behera, S.K., Rao, S.A., Weng, H.Y., Yamagata, T., 2007. El Nino Modoki and its possible teleconnection. J Geophys Res-Oceans 112.

Atwood, A.R., Sachs, J.P., 2014. Separating ITCZ- and ENSO-related rainfall changes in the Galapagos over the last 3 kyr using D/H ratios of multiple lipid biomarkers. Earth Planet Sc Lett 404, 408-419.

Blaauw, M., Christen, J.A., 2011. Flexible paleoclimate age-depth models using an autoregressive gamma process. Bayesian Anal 6, 457-474.

Hiner, C.A., Kirby, M.E., Bonuso, N., Patterson, W.P., Palermo, J., Silveira, E., 2016. Late Holocene hydroclimatic variability linked to Pacific forcing: evidence from Abbott Lake, coastal central California. Journal of Paleolimnology 56, 299-313.

Kao, H.Y., Yu, J.Y., 2009. Contrasting Eastern-Pacific and Central-Pacific Types of ENSO. Journal of Climate 22, 615-632.

Karamperidou, C., Di Nezio, P.N., Timmermann, A., Jin, F.F., Cobb, K.M., 2015. The response of ENSO flavors to mid-Holocene climate: Implications for proxy interpretation. Paleoceanography 30, 527-547.

Kirby, M.E., Feakins, S.J., Hiner, C.A., Fantozzi, J., Zimmerman, S.R.H., Dingemans, T., Mensing, S.A., 2014. Tropical Pacific forcing of Late-Holocene hydrologic variability in the coastal southwest United States. Quaternary Science Reviews 102, 27-38.

Kirby, M.E., Lund, S.P., Patterson, W.P., Anderson, M.A., Bird, B.W., Ivanovici, L., Monarrez, P., Nielsen, S., 2010. A Holocene record of Pacific Decadal Oscillation (PDO)-related hydrologic variability in Southern California (Lake Elsinore, CA). Journal of Paleolimnology 44, 819-839.

Kirby, M.E., Lund, S.P., Poulsen, C.J., 2005. Hydrologic variability and the onset of modern El Niño-Southern Oscillation: A 19 250-year record from Lake Elsinore, southern California. Journal of Quaternary Science 20, 239-254.

Kirby, M.E., Zimmerman, S.R.H., Patterson, W.P., Rivera, J.J., 2012. A 9170-year record of decadal-to-multi-centennial scale pluvial episodes from the coastal Southwest United States: A role for atmospheric rivers? Quaternary Science Reviews 46, 57-65.

Lee, T., McPhaden, M.J., 2010. Increasing intensity of El Nino in the central-equatorial Pacific. Geophysical Research Letters 37.

Sachs, J.P., Sachse, D., Smittenberg, R.H., Zhang, Z.H., Battisti, D.S., Golubic, S., 2009. Southward movement of the Pacific intertropical convergence zone AD 1400-1850. Nature Geoscience 2, 519-525.

Schollaen, K., Karamperidou, C., Krusic, P., Cook, E., Helle, G., 2015. ENSO flavors in a tree-ring delta O-18 record of Tectona grandis from Indonesia. Climate of the Past 11, 1325-1333.

Seager, R., Naik, N., Ting, M., Cane, M.A., Harnik, N., Kushnir, Y., 2010. Adjustment of the atmospheric circulation to tropical Pacific SST anomalies: Variability of transient eddy propagation in the Pacific-North America sector. Q J Roy Meteor Soc 136, 277-296.

Thompson, D.M., Conroy, J.L., Collins, A., Hlohowskyj, S.R., Overpeck, J.T., Riedinger-Whitmore, M., Cole, J.E., Bush, M.B., Whitney, H., Corley, T.L., Kannan, M.S., 2017. Tropical Pacific climate variability over the last 6000 years as recorded in Bainbridge Crater Lake, Galapagos. Paleoceanography 32, 903-922.

Trenberth, K.E., Branstator, G.W., Karoly, D., Kumar, A., Lau, N.C., Ropelewski, C., 1998. Progress during TOGA in understanding and modeling global teleconnections associated with tropical sea surface temperatures. J Geophys Res-Oceans 103, 14291-14324.

Yeh, S.W., Kug, J.S., Dewitte, B., Kwon, M.H., Kirtman, B.P., Jin, F.F., 2009. El Niño in a changing climate. Nature 461, 511-U570.

Appendix A

Supporting information for Chapter 2: A 9000-year flood history for Southern California: A revised stratigraphy of varved sediments in Santa Barbara Basin

Table A.1 Values of Ti concentration and Ca/Ti elemental ratio elements analyzed by ICP-MS/AES.

Figure A.1 Photographic images of MV0811-14JC, SPR0901-03KC, ODP Hole 893A and ODP Hole 893B. Prominent gray and olive layers are labeled.

Table A-1 Values of Ti concentration and Ca/Ti elemental ratio elements analyzed by ICP-MS/AES.

Lab ID	Section	Gray/Olive layer	Uncorrected depth	Adjusted depth	Ca (wt.%)	Ti (wt.%)	Ca/Ti
Q646501	Sec 1		0.00	0.00	3.96	0.37	10.62
Q646502	Sec 1		10.00	9.98	4.56	0.35	13.10
Q646503	Sec 1	1A	16.00	15.02	1.86	0.43	4.33
Q646504	Sec 1		20.00	15.06	5.11	0.34	15.03
Q646505	Sec 1		30.00	19.00	5.22	0.33	15.77
Q646506	Sec 1	2A	39.40	29.36	1.71	0.45	3.77
Q646507	Sec 1		48.50	34.98	5.28	0.35	14.92
Q646508	Sec 1	2E	53.00	37.50	1.77	0.46	3.83
Q646509	Sec 1		60.00	41.54	4.47	0.36	12.52
Q646510	Sec 1		68.00	47.64	5.20	0.35	14.81
Q646511	Sec 1	2H	71.50	50.86	1.77	0.42	4.19
Q646512	Sec 1		80.00	56.70	4.85	0.34	14.48
Q646513	Sec 2		96.00	64.80	4.71	0.35	13.61
Q646514	Sec 2	2I	99.50	67.26	1.85	0.45	4.13
Q646515	Sec 2		106.00	73.38	4.49	0.34	13.09
Q646516	Sec 2		116.00	83.38	4.32	0.37	11.80
Q646517	Sec 2	2K	122.00	84.72	1.78	0.45	4.00
Q646518	Sec 2		126.50	85.36	4.17	0.36	11.71
Q646519	Sec 2	2N	136.00	91.36	1.78	0.45	3.94
Q646520	Sec 2	2N	138.00	91.36	2.05	0.42	4.93
Q646521	Sec 2	2O	147.00	98.60	1.79	0.46	3.87
Q646522	Sec 2	2O	149.50	98.60	2.12	0.43	4.99
Q646523	Sec 2	3A	156.00	102.20	3.45	0.38	9.18
Q646524	Sec 2	3B	166.00	106.02	2.14	0.41	5.19
Q646525	Sec 2		167.50	106.64	4.31	0.35	12.21
Q646526	Sec 2		176.00	115.14	4.53	0.36	12.72
Q646527	Sec 2	3C	178.00	116.22	1.64	0.44	3.70
Q646528	Sec 2		186.00	122.46	4.54	0.35	12.86
Q646529	Sec 2	3E	190.00	125.60	1.75	0.46	3.83
Q646530	Sec 2		197.00	126.62	4.14	0.36	11.37
Q646531	Sec 2		206.00	135.62	4.65	0.35	13.44
Q646532	Sec 2		216.00	145.62	4.41	0.37	12.08
Q646533	Sec 2	3F	222.00	150.48	1.53	0.45	3.37
Q646534	Sec 2		226.00	152.60	4.42	0.37	12.04
Q646535	Sec 3		238.00	168.88	4.94	0.34	14.53
Q646536	Sec 3		248.00	177.74	4.37	0.35	12.52
Q646537	Sec 3	4B	252.00	177.76	1.82	0.46	3.97
Q646538	Sec 3	4C	258.00	177.92	1.61	0.46	3.50
Q646539	Sec 3	4D	269.00	185.32	1.45	0.47	3.12
Q646540	Sec 3		278.00	189.88	4.76	0.37	12.83
Q646541	Sec 3		288.00	199.82	4.06	0.36	11.25
Q646542	Sec 3	4E	292.00	200.96	1.86	0.44	4.22
Q646543	Sec 3		298.00	207.26	4.48	0.39	11.52
Q646544	Sec 3	4F	308.00	211.16	1.70	0.45	3.79
Q646545	Sec 3		318.00	218.14	4.40	0.37	11.89
Q646546	Sec 3	4G	324.00	220.18	1.68	0.45	3.75

Q646547	Sec 3		328.00	223.24	4.20	0.35	11.93
Q646548	Sec 3		338.00	233.24	4.59	0.37	12.44
Q646549	Sec 3	4H	348.00	238.68	1.73	0.46	3.76
Q646550	Sec 3		358.00	245.74	4.50	0.36	12.47
Q646551	Sec 3		368.00	255.74	4.98	0.36	13.91
Q646552	Sec 3		377.30	265.04	4.17	0.38	11.00
Q646553	Sec 4		379.00	265.20	4.36	0.38	11.56
Q646554	Sec 4		389.00	274.80	4.55	0.39	11.73
Q646555	Sec 4		399.00	284.50	5.12	0.38	13.44
Q646556	Sec 4		409.00	292.36	5.04	0.38	13.40
Q646557	Sec 4		419.00	299.38	4.14	0.39	10.70
Q646558	Sec 4	5E	421.00	301.26	2.04	0.47	4.39
Q646559	Sec 4		429.00	307.20	3.97	0.39	10.28
Q646560	Sec 4	5G	434.00	308.74	1.57	0.47	3.32
Q646561	Sec 4	5G	439.00	308.74	1.95	0.43	4.51
Q646562	Sec 4	5G	444.00	308.74	2.13	0.45	4.75
Q646563	Sec 4		449.00	310.52	4.93	0.37	13.32
Q646564	Sec 4	5H	458.00	318.68	1.67	0.47	3.58
Q646565	Sec 4		468.00	326.42	5.42	0.37	14.53
Q646566	Sec 4		479.00	337.16	4.79	0.39	12.35
Q646567	Sec 4		489.00	347.16	5.40	0.37	14.52
Q646568	Sec 4		499.00	357.16	5.18	0.38	13.49
Q646569	Sec 4		509.00	367.16	5.19	0.39	13.24
Q646570	Sec 5		525.34	373.74	4.95	0.39	12.63
Q646571	Sec 5		535.34	386.02	5.10	0.39	13.08
Q646572	Sec 6		527.34	386.12	4.94	0.38	13.14
Q646573	Sec 6		537.34	394.88	4.89	0.38	12.73
Q646574	Sec 6		547.34	403.38	4.14	0.38	10.78
Q646575	Sec 6		556.34	412.26	3.65	0.42	8.80
Q646576	Sec 6	6C	559.34	415.26	1.79	0.47	3.85
Q646577	Sec 6		566.34	419.84	4.74	0.40	11.97
Q646578	Sec 6		572.34	425.44	4.77	0.39	12.33
Q646579	Sec 6	6E	576.34	429.08	1.77	0.48	3.66
Q646580	Sec 6		580.34	429.70	4.28	0.38	11.32
Q646581	Sec 6	6G	583.34	433.46	2.49	0.45	5.50
Q646582	Sec 6		585.34	433.52	4.53	0.39	11.62
Q646583	Sec 6	6H	589.34	435.42	1.39	0.48	2.90
Q646584	Sec 6		597.34	435.74	4.91	0.39	12.72
Q646585	Sec 6		607.34	445.74	5.27	0.39	13.65
Q646586	Sec 6		614.34	452.10	4.69	0.38	12.51
Q646587	Sec 6		623.34	460.02	4.25	0.38	11.21
Q646588	Sec 6		631.34	468.02	4.77	0.40	11.84
Q646589	Sec 6	7C	635.34	471.62	1.73	0.49	3.56
Q646590	Sec 6		638.34	471.72	4.36	0.41	10.58
Q646591	Sec 6	7D	643.34	473.40	1.87	0.47	3.97
Q646592	Sec 6		648.34	475.68	4.79	0.39	12.38
Q646593	Sec 6	7E	658.34	479.04	2.11	0.43	4.91
Q646594	Sec 6		662.34	480.26	3.96	0.39	10.26
Q646595	Sec 6	7G	672.34	487.60	3.88	0.38	10.10
Q646596	Sec 7		674.54	490.00	4.31	0.39	11.08
Q646597	Sec 7		684.54	500.00	4.20	0.38	11.05

Q646598	Sec 7		694.54	510.00	4.96	0.39	12.69
Q646599	Sec 7	7J	702.54	515.22	1.64	0.46	3.57
Q646600	Sec 7		712.54	520.58	4.74	0.38	12.51
Q646601	Sec 7	7K	721.54	530.24	1.57	0.46	3.38
Q646602	Sec 7		730.54	535.68	4.20	0.39	10.77
Q646603	Sec 7	7L	732.54	539.38	1.98	0.48	4.17
Q646604	Sec 7		741.54	545.84	4.44	0.39	11.50
Q646605	Sec 7	7M	746.54	551.32	1.80	0.44	4.09
Q646606	Sec 7		751.54	554.44	4.71	0.39	12.11
Q646607	Sec 7		758.54	561.44	4.65	0.37	12.57
Q646608	Sec 7		765.54	568.44	4.72	0.39	12.23
Q646609	Sec 7		775.54	578.44	4.06	0.38	10.83
Q646610	Sec 7		785.54	588.44	5.15	0.36	14.15
Q646611	Sec 7	8A	792.04	594.50	4.21	0.37	11.29
Q646612	Sec 7		795.54	596.78	5.20	0.36	14.44
Q646613	Sec 7	8B	802.54	603.78	1.90	0.46	4.16
Q646614	Sec 7		805.54	604.40	4.35	0.39	11.10
Q646615	Sec 7	8D	811.54	611.24	1.55	0.48	3.26
Q646616	Sec 7		818.54	615.62	5.13	0.36	14.21
Q646617	Sec 8	8F	825.54	622.98	1.93	0.44	4.36
Q646618	Sec 8		827.54	623.04	4.59	0.37	12.44
Q646619	Sec 8		835.54	630.94	4.55	0.38	11.88
Q646620	Sec 8	8G	839.54	634.60	2.74	0.43	6.33
Q646621	Sec 8		845.54	638.44	4.90	0.37	13.10
Q646622	Sec 8		856.54	649.36	4.80	0.38	12.60
Q646623	Sec 8	8I	860.54	652.96	1.74	0.43	4.07
Q646624	Sec 8		866.54	655.86	5.45	0.35	15.75
Q646625	Sec 8	9A	871.54	659.20	2.26	0.43	5.21
Q646626	Sec 8	9A	874.04	659.20	2.09	0.45	4.68
Q646627	Sec 8		878.54	663.26	4.53	0.37	12.21
Q646628	Sec 8	9E	891.54	664.14	3.72	0.39	9.61

ODP 893A

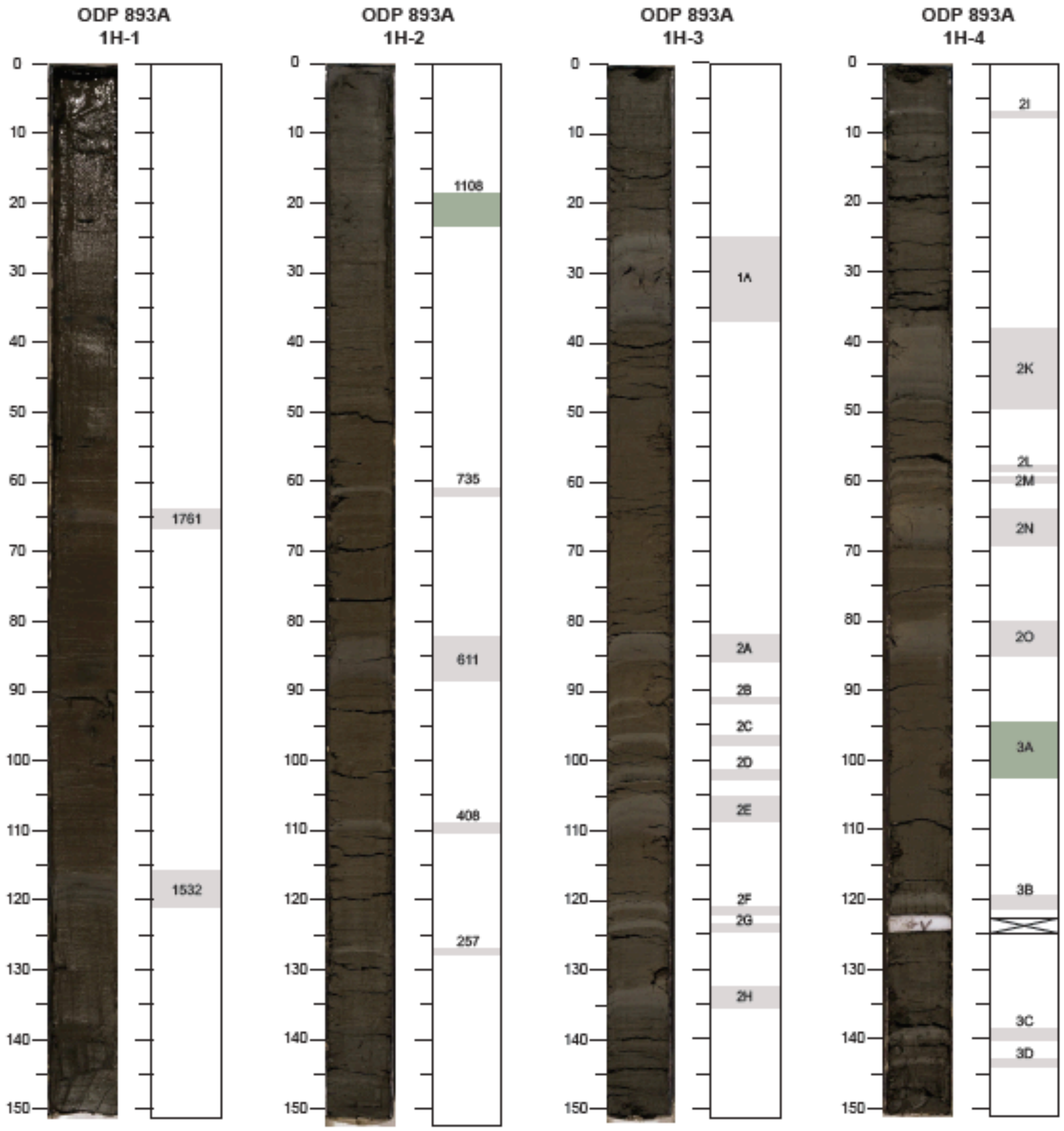
ODP 893A 1H-1
ODP 893A 1H-2
ODP 893A 1H-3
ODP 893A 1H-4
0
10
20
30
40
50
60
70
80
90
100
110
120
130
140
150
1761
1532
1108
735
611
408
257
1A
2A
2B
2C
2D
2E
2F
2G
2H
2I
2K
2L
2M
2N
2O
3A
3B
3C
3D

ODP 893A
1H-5

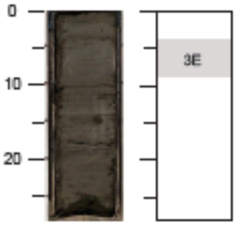

ODP 893A
1H-CC

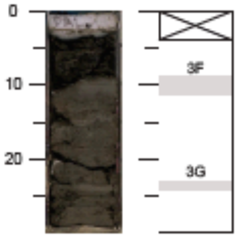

ODP 893A
2H-1

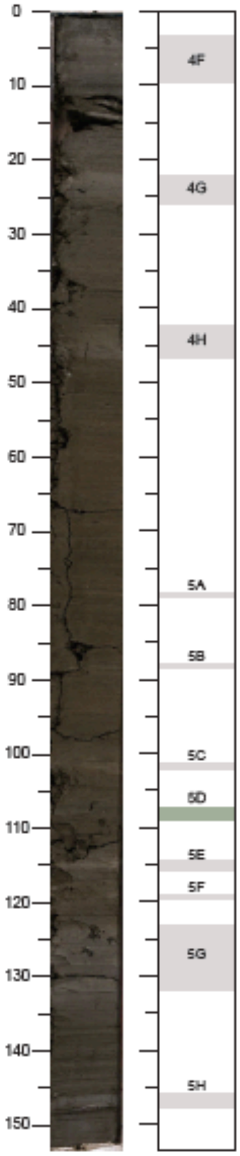

ODP 893A
2H-2

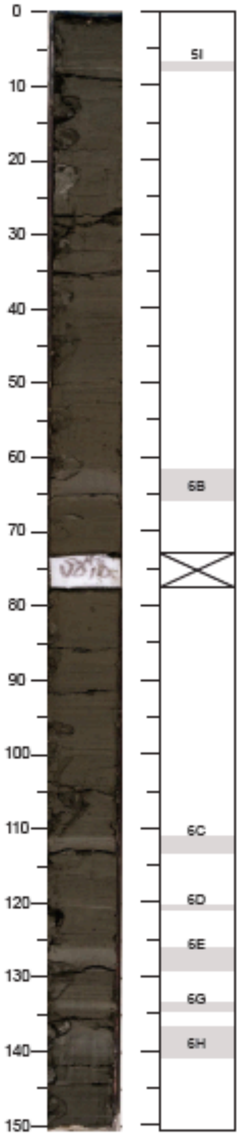

ODP 893A
2H-3

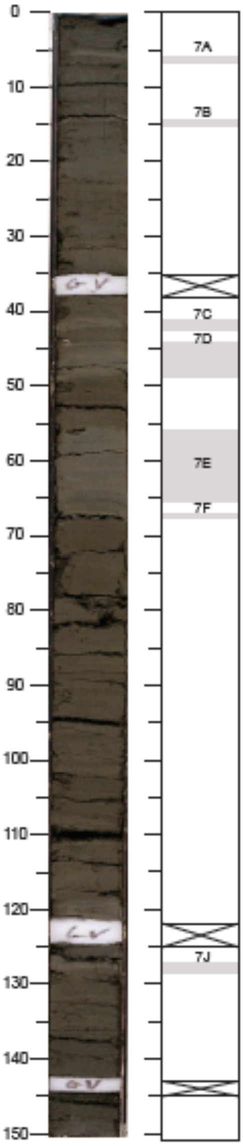

ODP 893A
2H-4

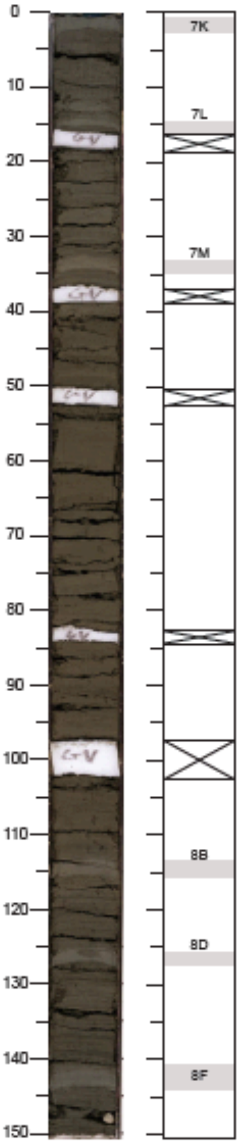

ODP 893A
2H-5

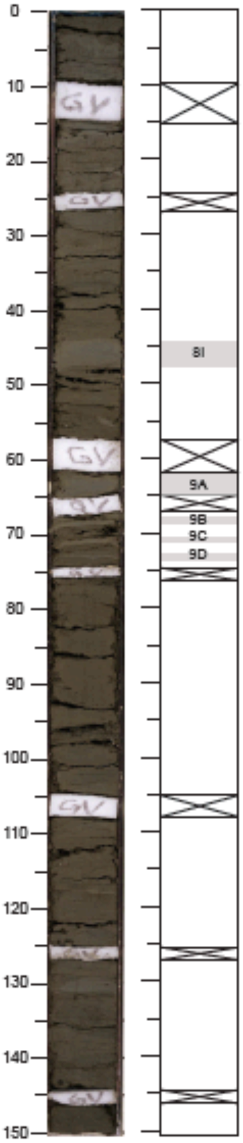

ODP 893B

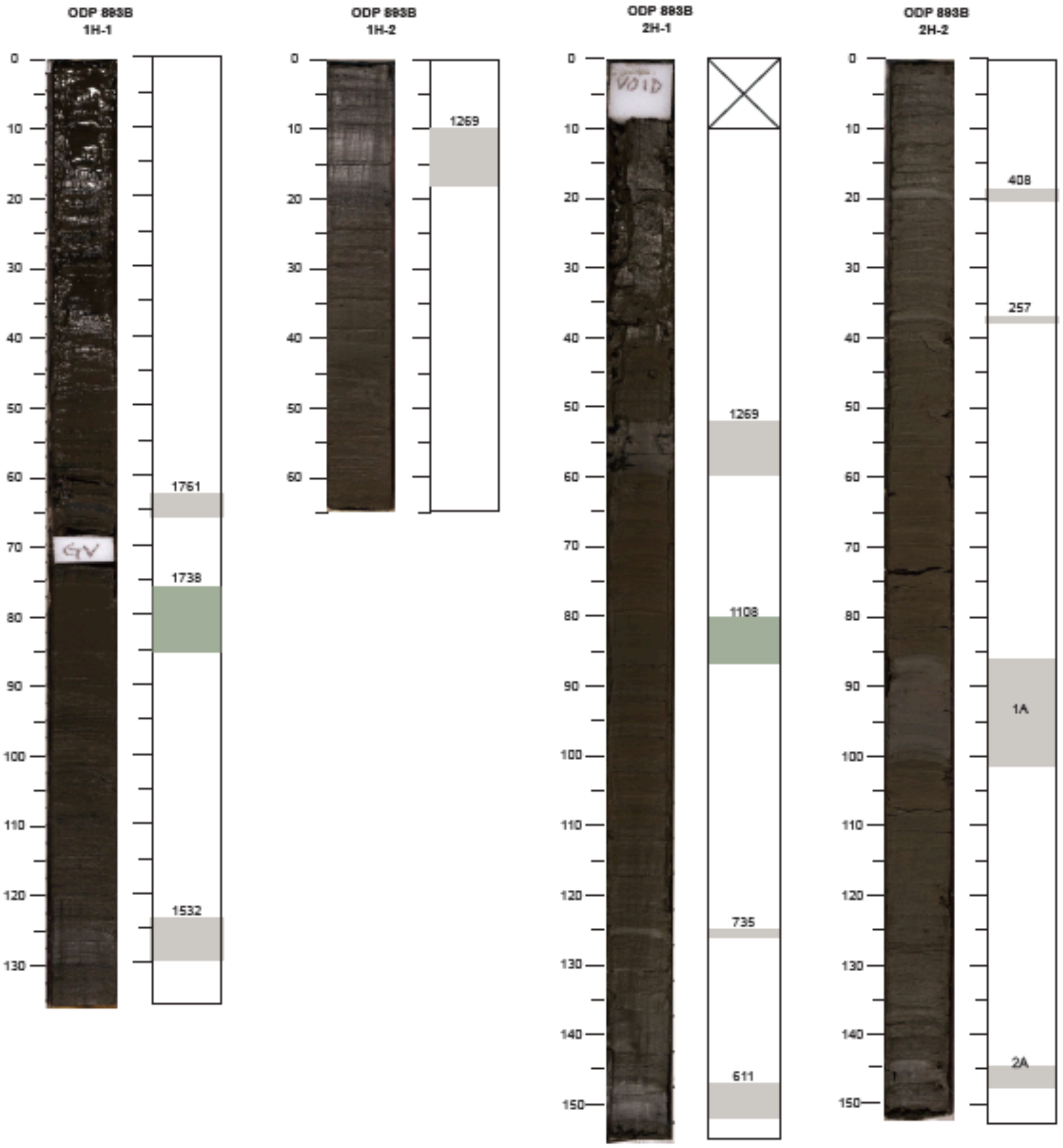
ODP 893B 1H-1
0
10
20
30
40
50
60
70
80
90
100
110
120
130
GV
1761
1738
1532
ODP 893B 1H-2
0
10
20
30
40
50
60
1269
ODP 893B 2H-1
0
10
20
30
40
50
60
70
80
90
100
110
120
130
140
150
VOID
1269
1108
735
611
ODP 893B 2H-2
0
10
20
30
40
50
60
70
80
90
100
110
120
130
140
150
408
257
1A
2A

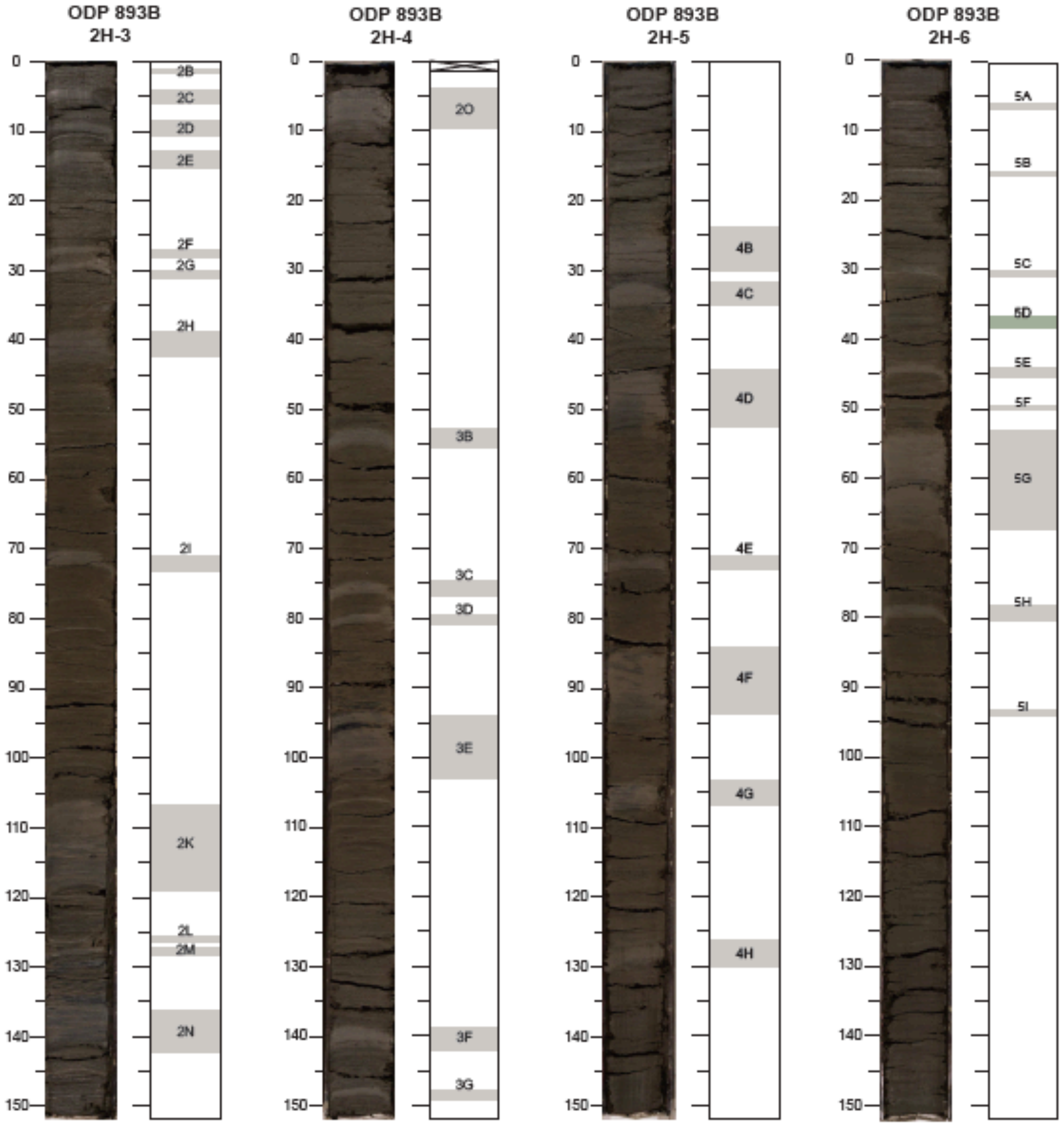
ODP 893B
2H-3
2B
2C
2D
2E
2F
2G
2H
2I
2K
2L
2M
2N
ODP 893B
2H-4
2O
3B
3C
3D
3E
3F
3G
ODP 893B
2H-5
4B
4C
4D
4E
4F
4G
4H
ODP 893B
2H-6
5A
5B
5C
5D
5E
5F
5G
5H
5I
0
10
20
30
40
50
60
70
80
90
100
110
120
130
140
150

ODP 893B
2H-7

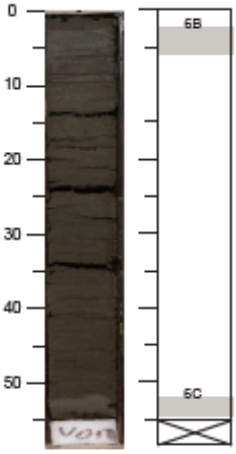

ODP 893B
2H-CC

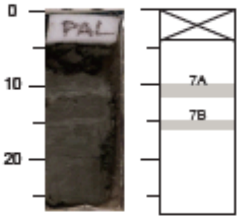

ODP 893B
3H-1

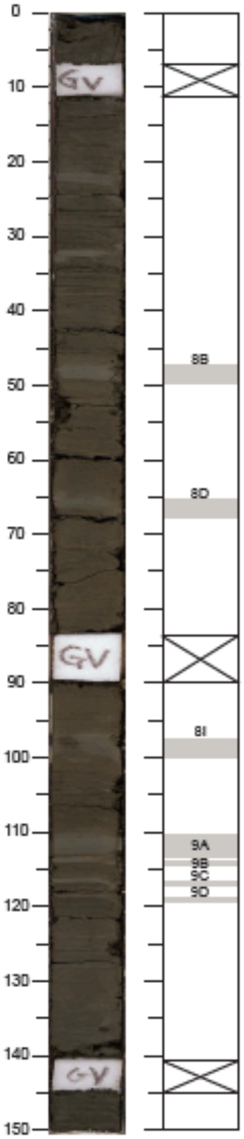

SPR0901-3KC

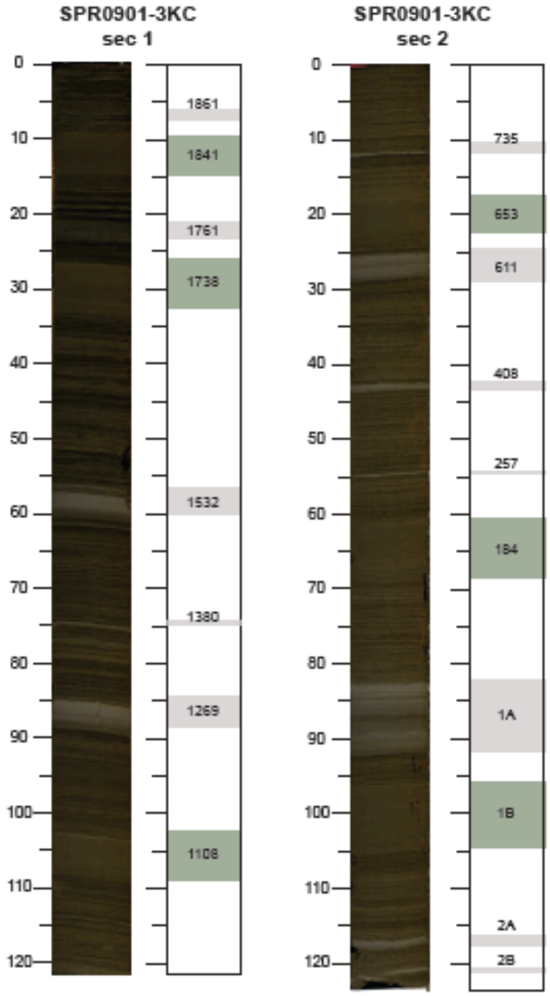
SPR0901-3KC
sec 1
0
10
20
30
40
50
60
70
80
90
100
110
120
1861
1841
1761
1738
1532
1380
1269
1108
SPR0901-3KC
sec 2
0
10
20
30
40
50
60
70
80
90
100
110
120
735
653
611
408
257
184
1A
1B
2A
2B

MV0811-14JC

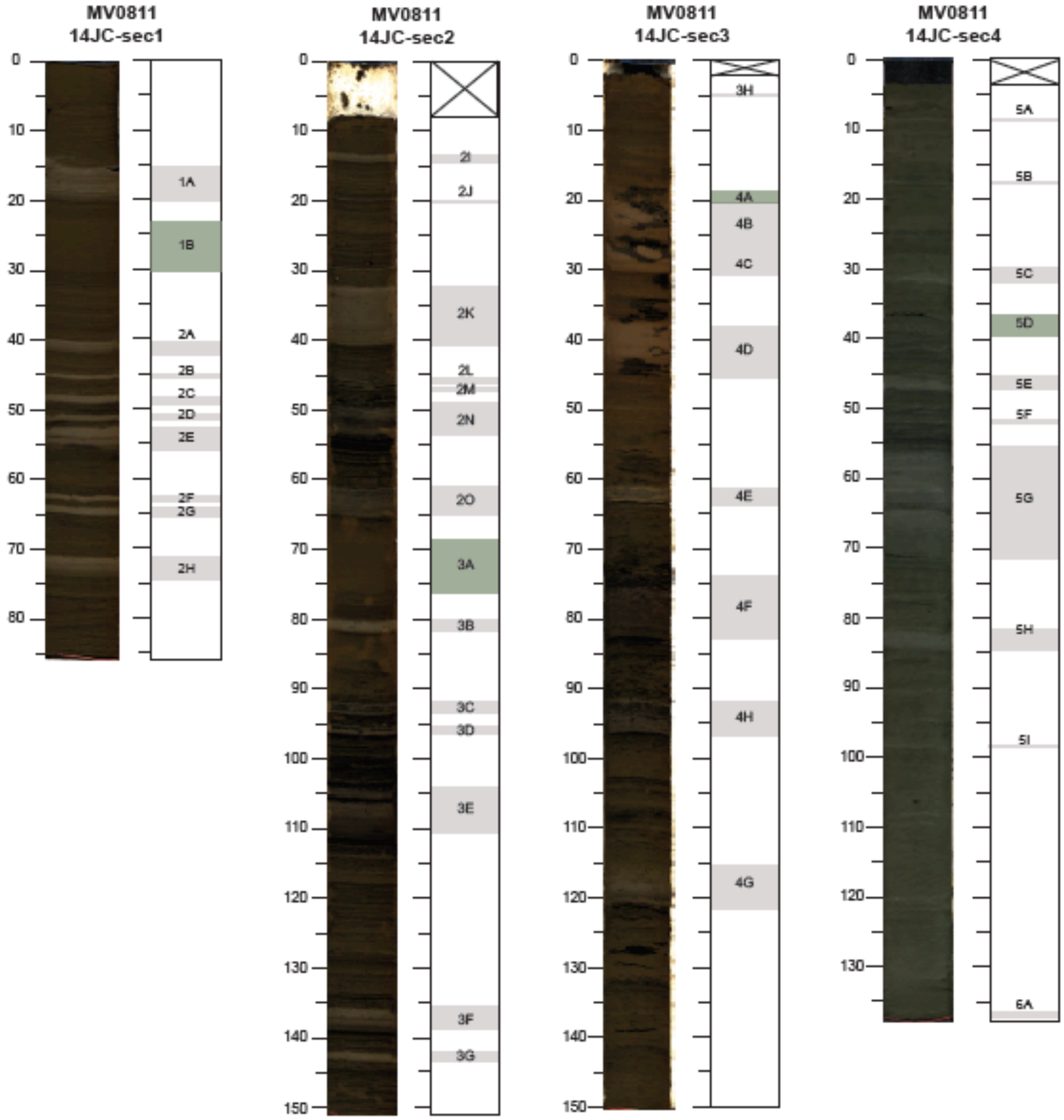

MV0811 14JC-sec1
MV0811 14JC-sec2
MV0811 14JC-sec3
MV0811 14JC-sec4
0
10
20
30
40
50
60
70
80
90
100
110
120
130
140
150
1A
1B
2A
2B
2C
2D
2E
2F
2G
2H
2I
2J
2K
2L
2M
2N
2O
3A
3B
3C
3D
3E
3F
3G
3H
4A
4B
4C
4D
4E
4F
4H
4G
5A
5B
5C
5D
5E
5F
5G
5H
5I
6A

MV0811
14JC-sec5

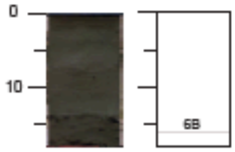

MV0811
14JC-sec6

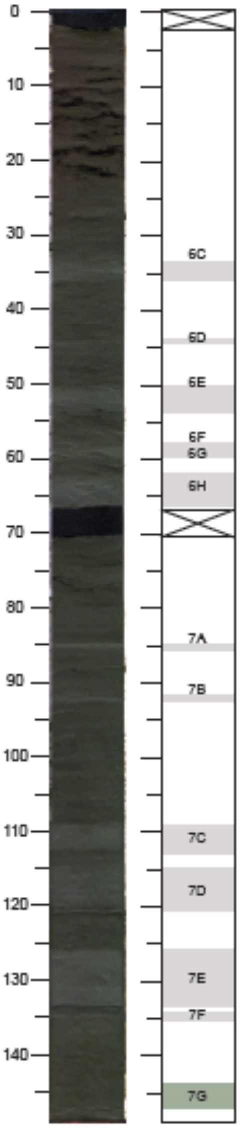

MV0811
14JC-sec7

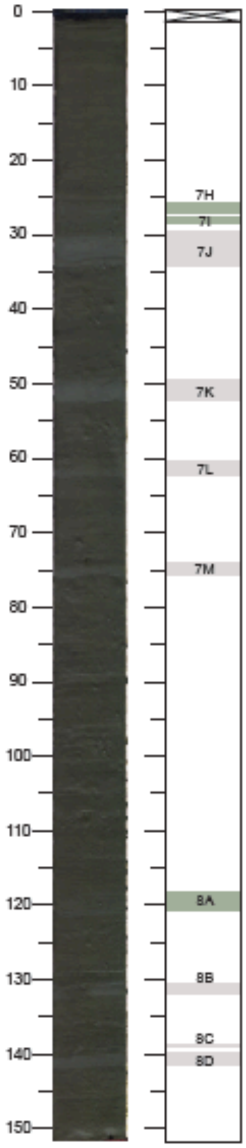

MV0811
14JC-sec8

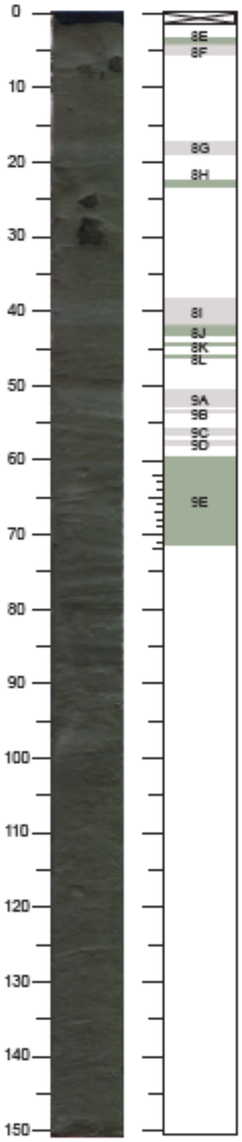

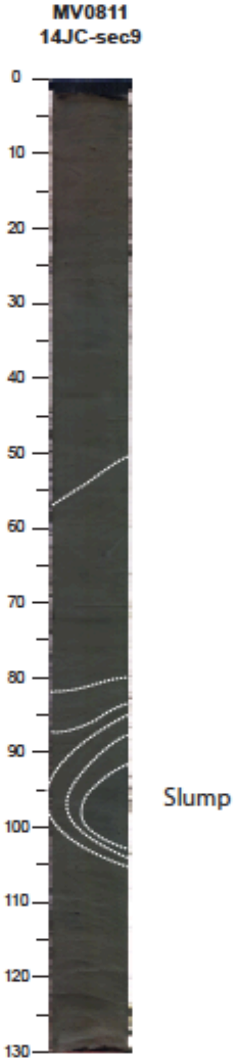

Figure A-1 Photographic images of MV0811-14JC, SPR0901-03KC, ODP Hole 893A and ODP Hole 893B. Prominent gray and olive layers are labeled.

Appendix B

Supporting information for Chapter 3: Interannual Southern California precipitation variability during the Common Era and the ENSO teleconnection

Materials and Methods
Figures B. 1 to B. 6

Materials and Methods

Bulk elemental analysis

The elemental composition of the sediment cores was measured using a second-generation ITRAX core scanner using a Cr tube at 200 mm intervals with data output in courts per second. Raw XRF data were reprocessed with Q-Spec 8.6.0 software to optimize peak fitting. The Ti counts used in this research were standardized (subtract mean and divide by standard deviation).

Age models

Peaks of Ti counts represent the maximum siliciclastic delivery occurs in winter season rainfall. We can therefore generate an annual tuned chronology by counting the Ti maxima associated with siliciclastic laminae downcore (with a resolution of 4-7 data points per year). The 1812 earthquake turbidite and bioturbation associated with the Macoma shell layer (~1840 ±2 years) destroyed deposited laminations, therefore we only use the annual tuned chronology before 1800 in kasten core SPR0901-03KC and after 1870 in box core SPR0901-04BC (588 m; 34° 16.895' N, 120° 02.489' W). The Ti timeseries was assigned an annually tuned chronology in Matlab with the script depthtotime.m. When winter siliciclastic laminae are not deposited in SBB, missing years occur in this annual tuned chronology. For this reason, the radiocarbon chronology is used to provide absolute ages for comparison with other paleoclimate records.

A radiocarbon chronology (from ~140 BCE to 1905 CE) for kasten core SPR0901-03KC (591 m; 34° 16.914' N, 120° 02.419' W) was generated using 38 14C dates of mixed planktonic foraminifera (with sampling intervals of ~ 4- 5 cm) from Kasten core SPR0901-06KC (591 m; 34° 16.914' N, 120° 02.419' W) [Du et al., 2018; Hendy et al., 2013] and 5 varve-chronology dates via the Bayesian statistical R program, Bacon 2.2 [Blaauw and Christen, 2011] (Fig S1, Table S1). Kasten cores SPR0901-06KC and SPR0901-03KC are proximal cores with almost identical sedimentology. Gray and olive massive layers [Hendy et al., 2013; Schimmelmann et al., 2013], together with 12 additional marker layers with distinctive sedimentary fabric changes were identified in SPR0901-06KC and SPR0901-03KC and work as stratigraphic tie points to correlate them. As instantaneous sedimentary events, the gray and olive massive layers were subtracted from the original depth, to generate corrected depth scale for both cores. The corrected core depth of 14C dates from SPR0901-06KC were mapped onto the corrected core depth of SPR0901-03KC. Five stratigraphic marker layers previously identified in SBB with dates generated from varve chronology [Hendy et al., 2015] also appear in SPR0901-03KC identified by high resolution imaging. The dates of these 5 marker layers (the coretop at 1905, a gray layer at 1861–62, the Macoma layer at 1841, a turbidite at 1811 and a gray layer at 1761 [Hendy et al., 2015; Hendy et al., 2013; Schimmelmann et al., 1992]) were employed in the age model for core SPR0901-03KC to avoid the global 14C plateaus of the past ~300 years. Variable reservoir ages generated using radiocarbon dates of paired planktonic foraminifera and terrestrial organic carbon [Hendy et al., 2013] were applied to the 14C dates. Radiocarbon dates were calibrated to calendar years with Marine 13 calibration curve [Reimer et al., 2013]. The minimum age error was 4.1 yr at 7.7 cm and maximum age error of 243.9 was at 180.92 cm.

Time series analysis

Several different time series analysis methods were employed using the annual tuned Ti time series. To remove the long-term trend, the annual tuned Ti time series was pre-whitened by subtracting the LOESS-smoothing curve with a half-length sliding window using smooth.m. The detrended Ti time series was linearly interpolated with mean time step (0.21 year). We analyzed the time series with Multi-taper method (MTM) [Thomson, 1982] using pmtm.m and annual frequency was removed with deharm.m before the estimated spectra were compared with red noise models at the 95% and 99% confidence levels using Rednoise.m [Kodama and Hinnov, 2015]. Evolutionary fast Fourier transform (FFT) power spectrogram was calculated using evofft.m [Kodama and Hinnov, 2015] with sliding windows. Tanerfilter.m [Kodama and Hinnov, 2015] was used to isolate ENSO band (2–7 yrs) from the Ti time series. Wavelet analysis was used to analyze the localized variations of power within the Ti time series. Wavelet power spectrum was calculated using the Morlet wavelet. Average ENSO variance is defined as the weighted sum of the wavelet power spectrum over all scales between 2-7 year. 95% confidence level of the wavelet power spectrum was estimated by deriving theoretical wavelet spectra for red noise processes. The wavelet analysis was performed in MATLAB using the software package wavelets [Torrence and Compo, 1998] (http://paos.colorado.edu/research/wavelets//).

Regime shift analysis

Regime shifts are defined as rapid reorganizations of the climate system from one relatively stable state to another [Rodionov, 2004]. Here, Sequential Regime Shift Detection (SRSD) method is used to detect the regime shifts in mean of Aleutian Low and ITCZ migration reconstructions (Fig 3d and e). The SRSD was performed in Excel using the software package Regime shift test-v6.2.xlsm (https://sites.google.com/site/climatelogic/).

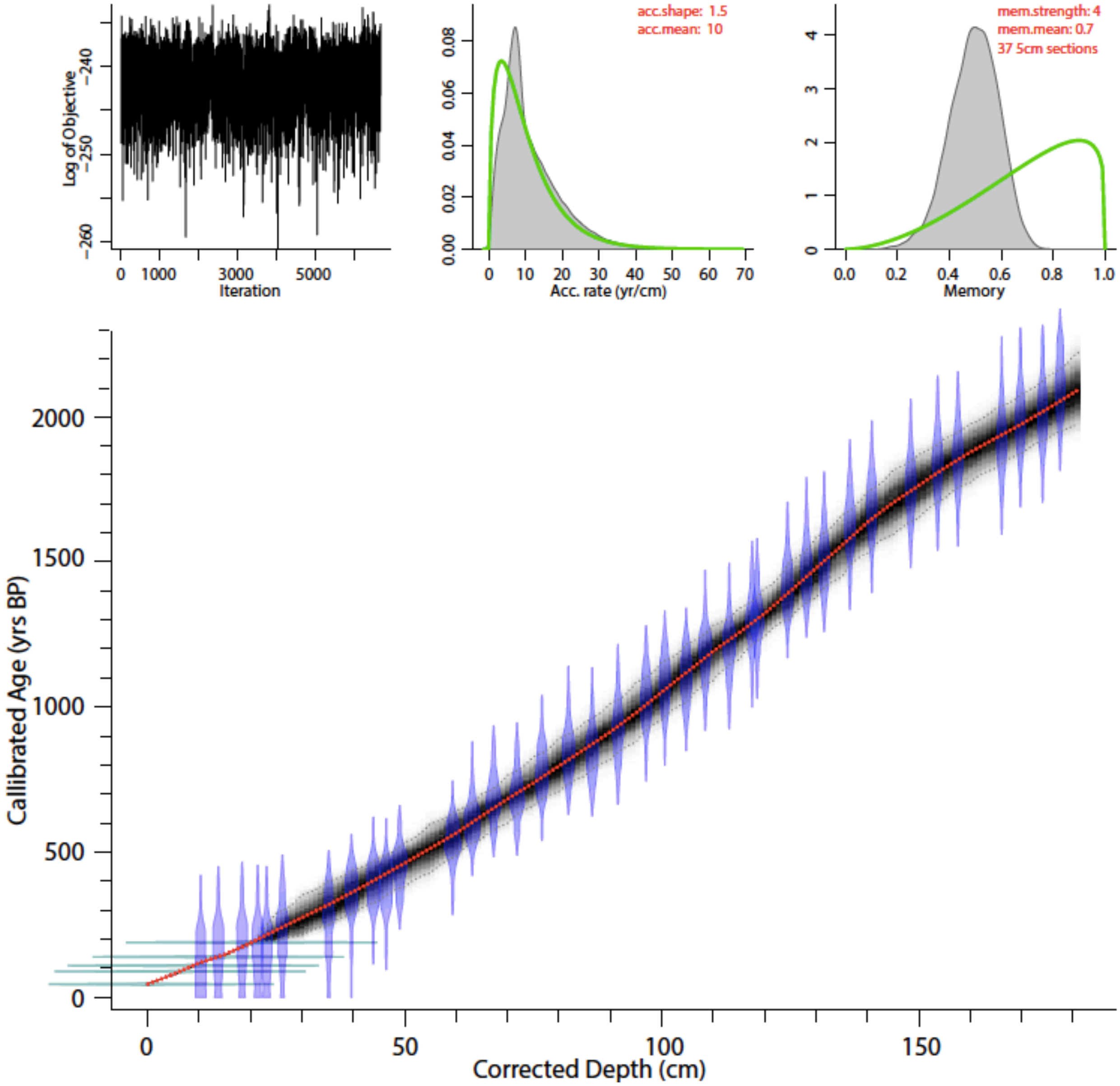

Figure B-1 BACON 2.2 output graph showing calibrated 14C dates from SPR0901-06KC and the age-depth model. Gray shading indicates probability within the 95% confidence interval with darkness indicating greater probability. The red curve shows single 'best' model based on the weighted mean age for each depth. Green horizontal lines indicate 5 varve-chronology dates.

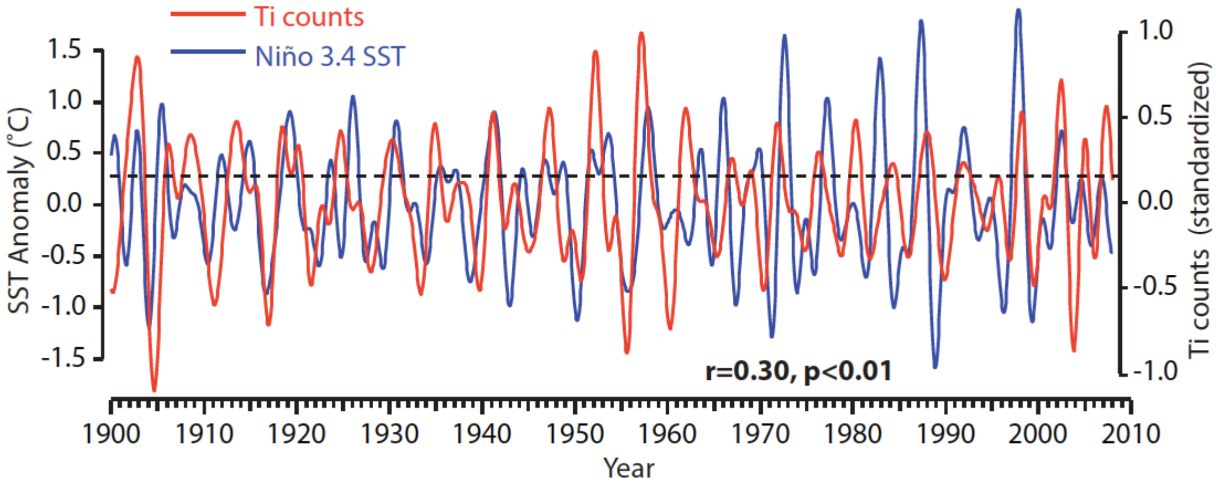

Figure B-2 Comparison of Ti time sires from SPR0901-04BC (red line) and Niño 3.4 SST (blue line) from 1900 to 2008. 2–7-year bandpass filter was applied.

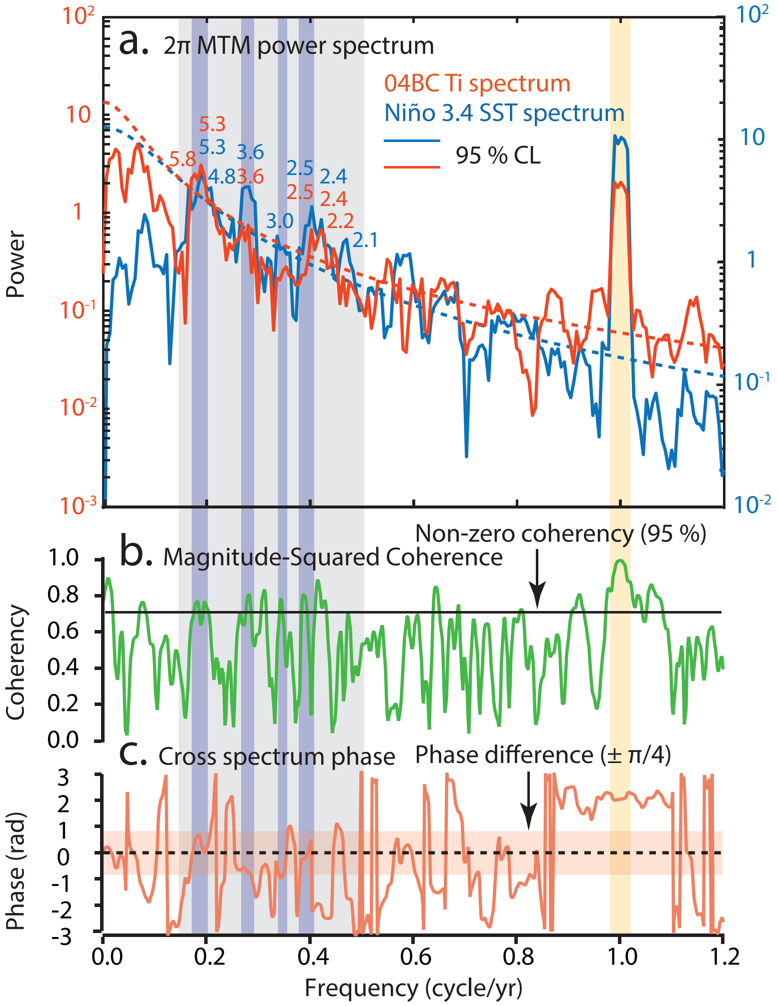

Figure B-3 (a) 2π prolate multitaper power spectrum of the annually tuned SPR0901-04BC Ti time series compared to the Niño 3.4 SST monthly time series from 1900 to 2008 [Rayner et al., 2003] (data source: http://www.esrl.noaa.gov/psd/gcos_wgsp/Timeseries/Nino34/). Periods exceeding 95 % confidence level of classical red noise modeling are labeled. (b) The coherence spectrum of the Niño 3.4 SST and Ti time series (green line), with the 95 % confidence level indicated and (c) Cross-phase spectrum of the Niño 3.4 SST and Ti time series (orange line). Orange shading represents a π/4 phase lead/lag and the dashed line indicates no phase difference. All the significant signals (⩾95% confidence level) produced by multitaper power spectrum (Fig. B3a), with coherency above 95% confidence level (Fig. B3b) and phase lag (Fig. B3c) within π/4 (equals 1.5 year for annual cycle) are marked with purple bars. The annual signal is indicated by a yellow bar. Niño 3.4 SST data (5˚ S-5˚ N and 170˚-120˚ W average area) were calculated from the HadISST1 (Hadley Centre Sea Ice and Sea Surface Temperature data set). Cross-phase spectrum was calculated using AnalySeries 2.0.8 [Paillard, 1996].

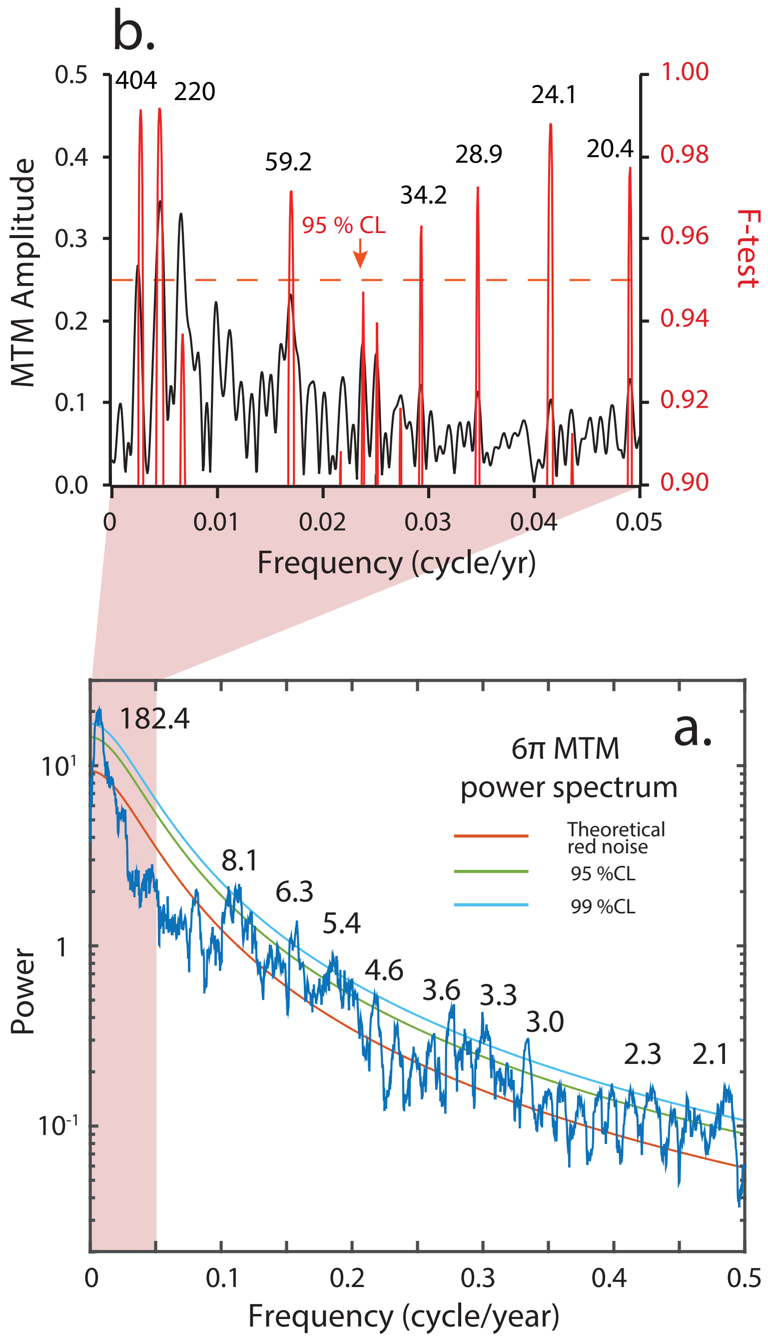

Figure B-4 (a) 6π MTM power spectrum of annually tuned, pre-whitened Ti time series from SPR0901-03KC. The Ti time series are pre-whitened by removing a LOESS-smoothed curve. Red noise was calculated after removing the annual signal. Confidence levels shown in legend with significant periodicities labeled. (b) MTM amplitude and F-test for low frequency power (lower than 0.05 cycle/yr) of the Ti time series.

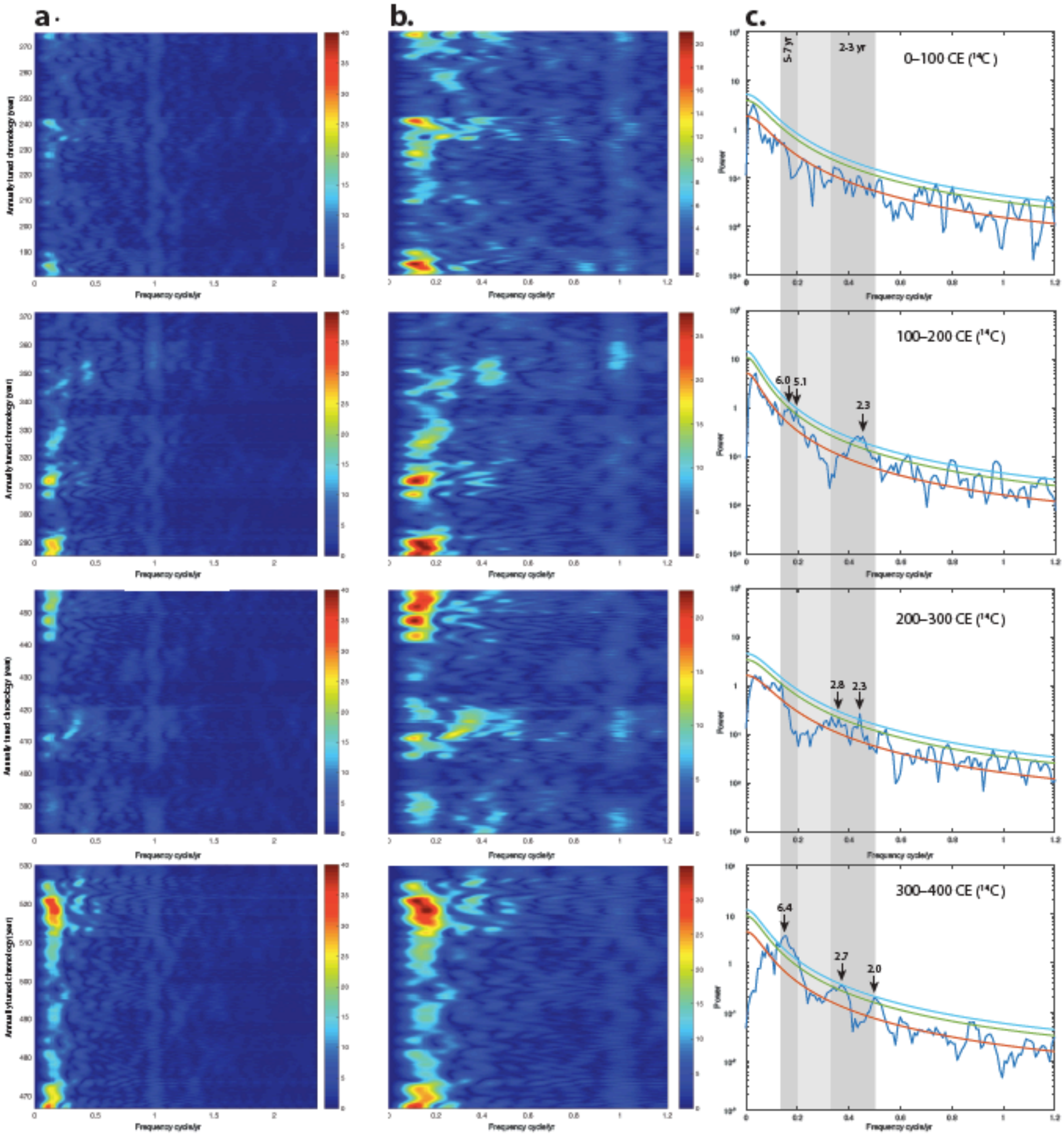
a.
b.
c.
Annually tuned chronology (year)
Frequency cycle/yr
Power
5-7 yr
2-3 yr
0–100 CE (^{14}C)
100–200 CE (^{14}C)
6.0
5.1
2.3
200–300 CE (^{14}C)
2.8
2.3
300–400 CE (^{14}C)
6.4
2.7
2.0

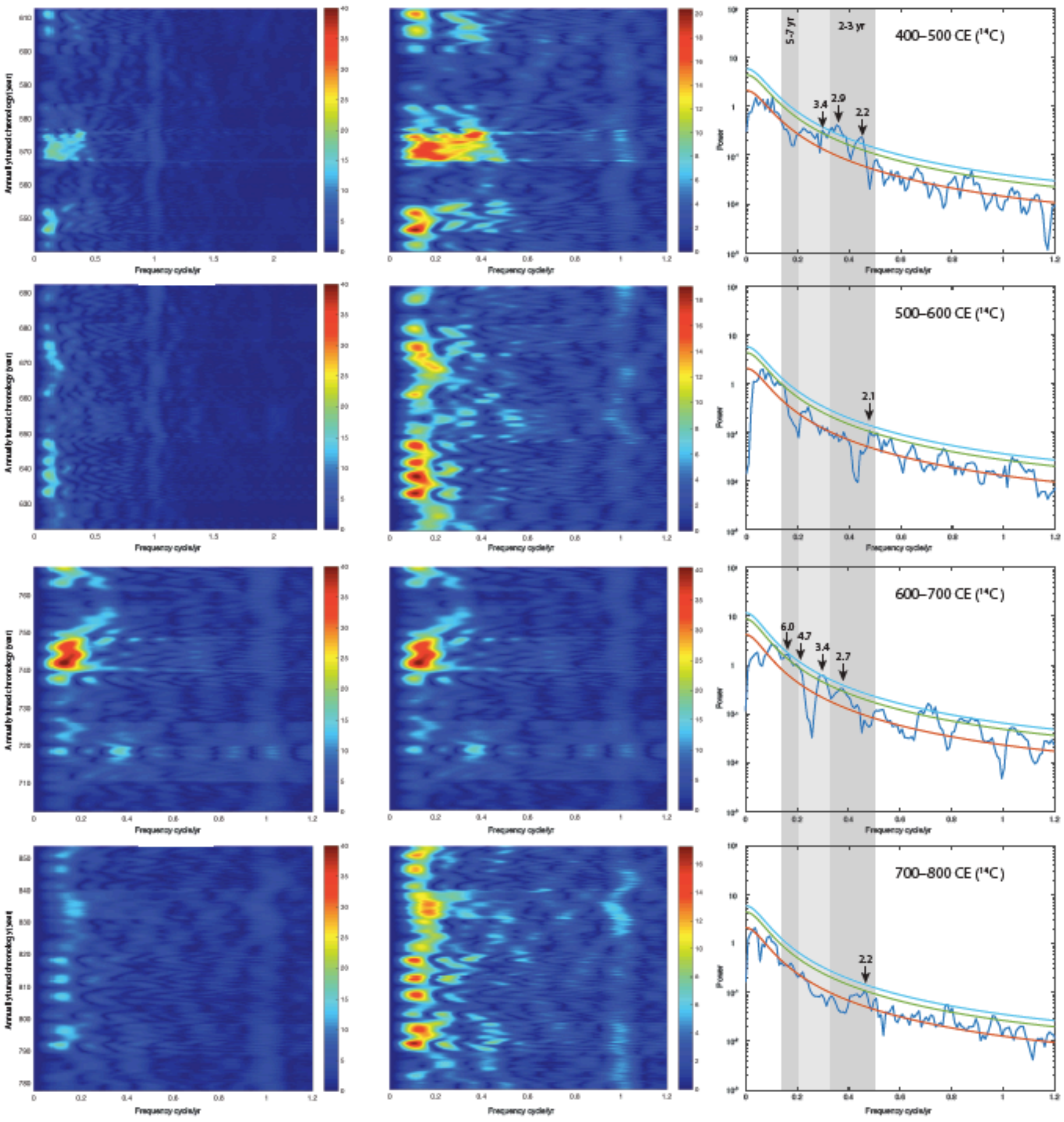
Annually tuned chronology (year)
Frequency cycle/yr
Power
5-7 yr
2-3 yr
400–500 CE (¹⁴C)
3.4
2.9
2.2
500–600 CE (¹⁴C)
2.1
600–700 CE (¹⁴C)
6.0
4.7
3.4
2.7
700–800 CE (¹⁴C)
2.2

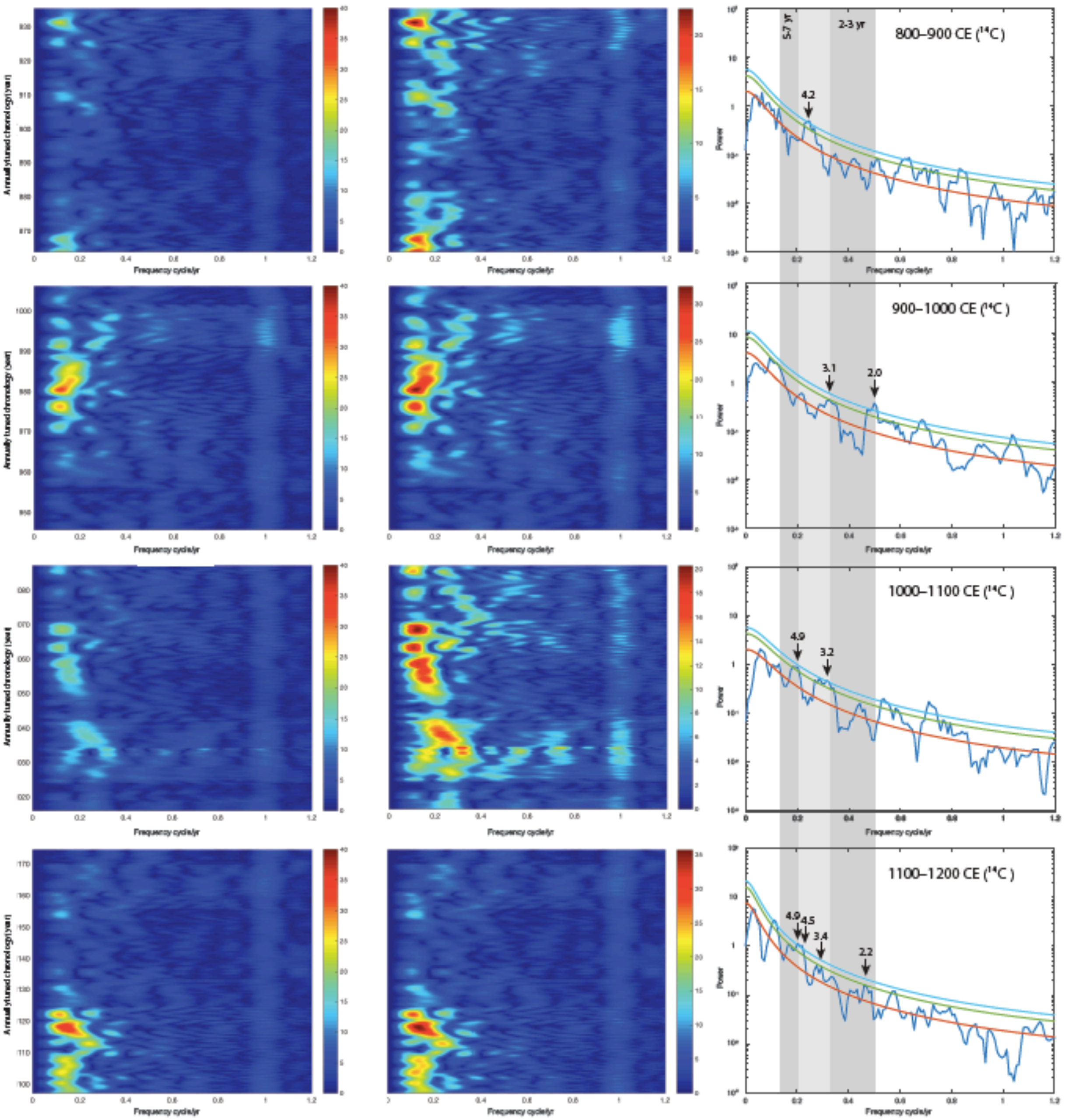
5-7 yr
2-3 yr
800–900 CE (14C)
4.2
900–1000 CE (14C)
3.1
2.0
1000–1100 CE (14C)
4.9
3.2
1100–1200 CE (14C)
4.9
4.5
3.4
2.2
Annually tuned chronology (year)
Frequency cycle/yr
Power

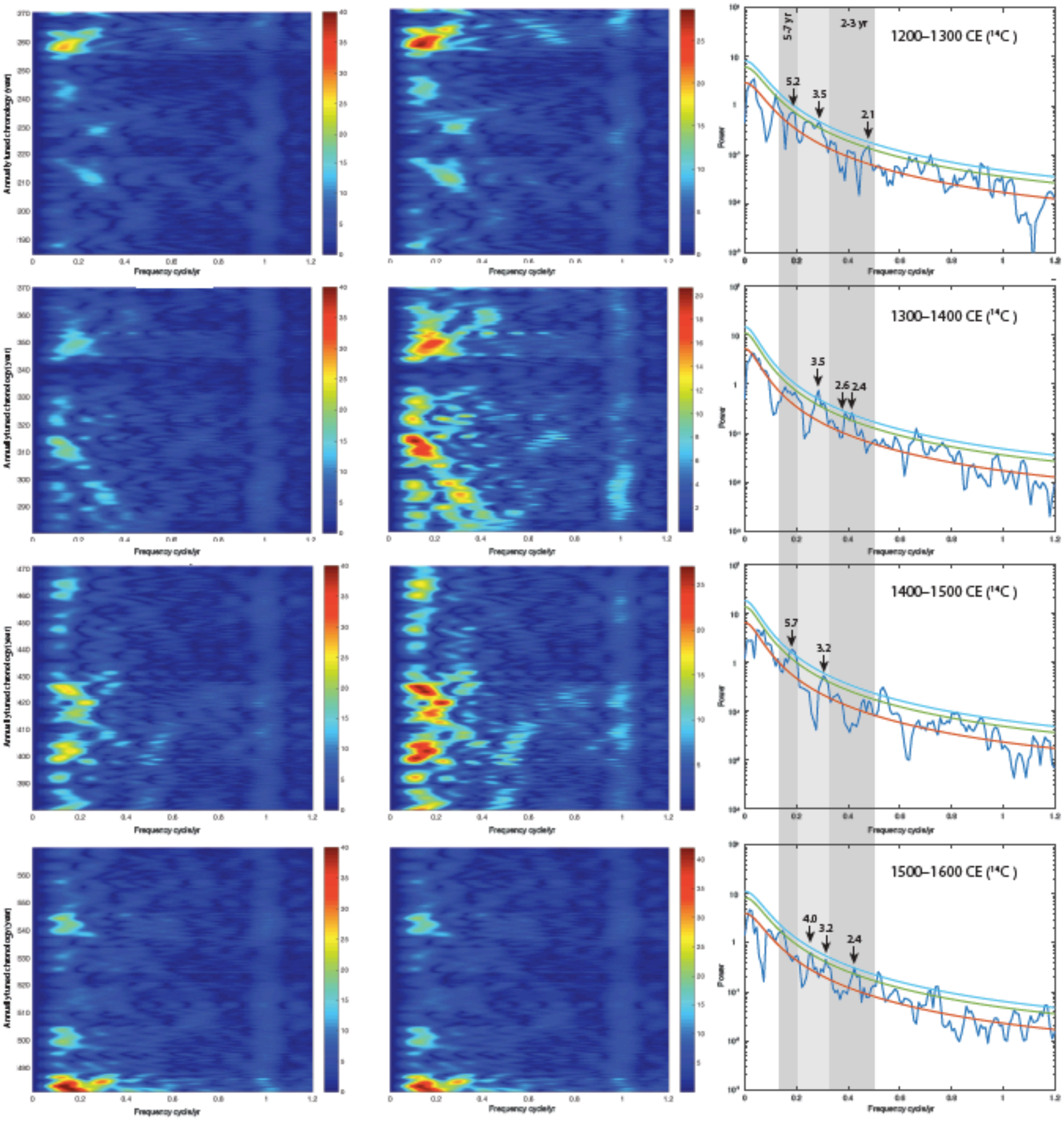
Annually tuned chronology (year)
Frequency cycle/yr
0
0.2
0.4
0.6
0.8
1
1.2
Power
5-7 yr
2-3 yr
1200–1300 CE (^{14}C)
5.2
3.5
2.1
1300–1400 CE (^{14}C)
3.5
2.6
2.4
1400–1500 CE (^{14}C)
5.7
3.2
1500–1600 CE (^{14}C)
4.0
3.2
2.4

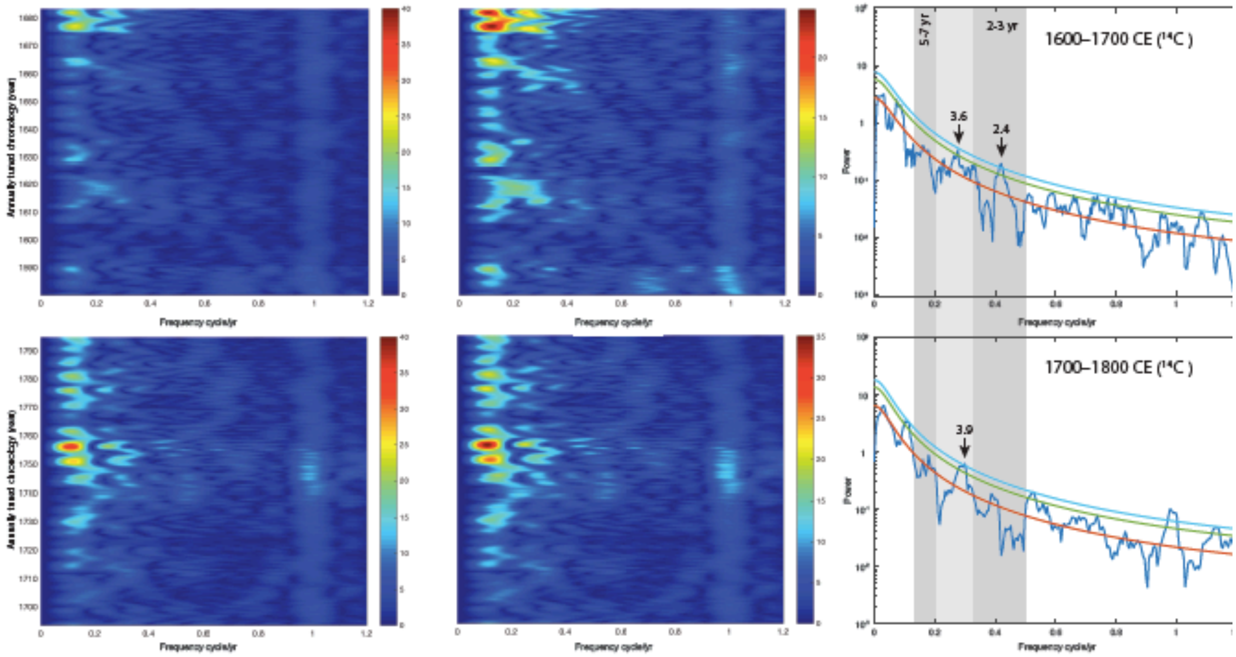

Figure B-5 Time series analysis of annually tuned, pre-whitened 100-year Ti series. The start and end date of each 100-year window are based on radiocarbon chronology. Column (a): Evolutionary FFT power spectrogram of 100-year Ti time series with a 10-year sliding window. Power is not normalized per spectrum for each series, with the highest power in dark red and the lowest in dark blue (in the same color scale, from 0 to 40). Column (b): Evolutionary FFT power spectrogram again, except that different color scales are applied (dark red and dark blue represent the highest nad lowest power in each 100-year window, respectively). Column (c): 2π prolate multitaper power spectrum of each 100-year Ti time series with the annual frequency removed to allow for red noise hypothesis testing. 95% and 99% confidence levels shown with significant (⩾95% confidence level) periodicities labeled.

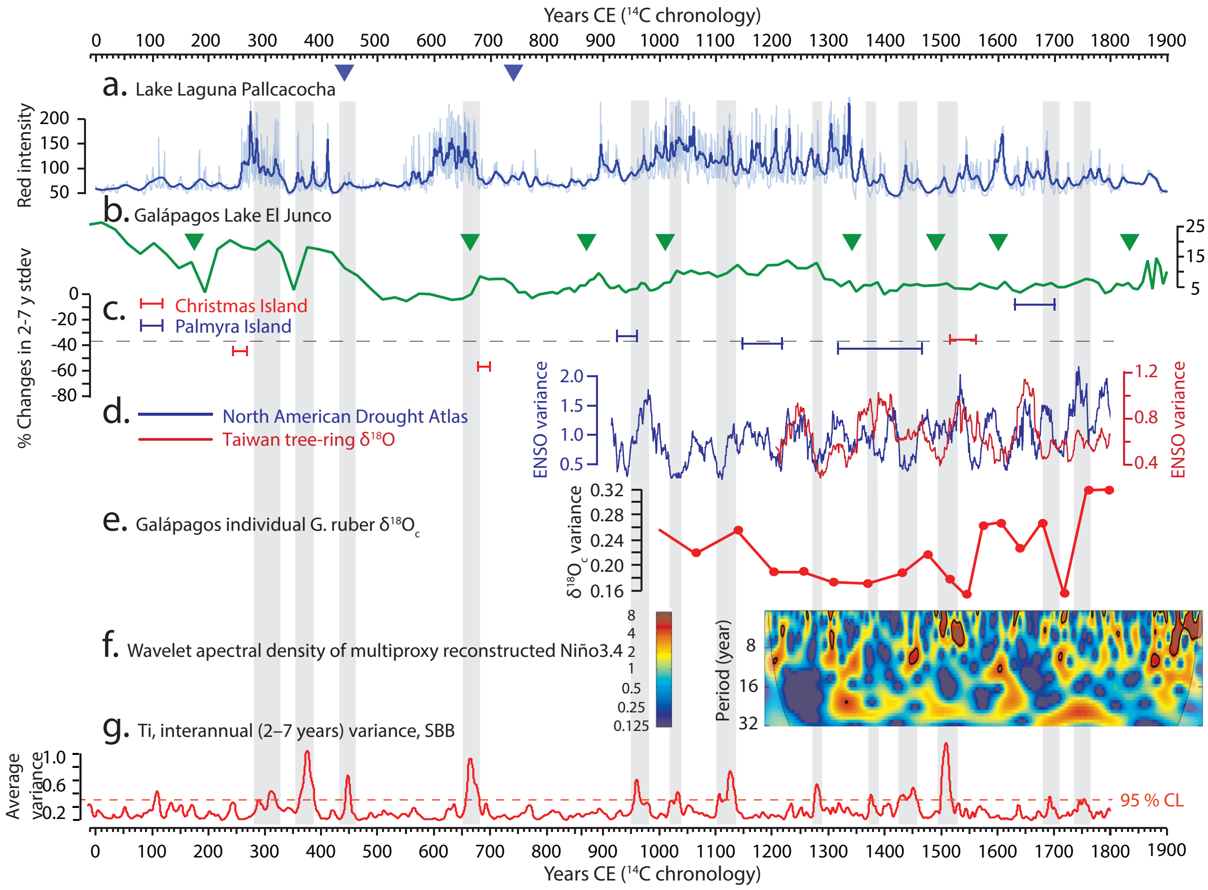

Figure B-6 Overview of ENSO reconstructions over the last two millennia. (a) The time series of red color intensity from lake Laguna Pallcacocha (light blue line), smoothed using a 80-yr running average (dark blue line) [Moy et al., 2002]. Blue triangles indicate the 14C dates constraining the record. (b) Sand record from Galápagos lake El Junco (green line; plotted as percent sand fraction) Green triangles indicate 14C dates constraining the record [Conroy et al., 2008]. (c) Relative ENSO variance (SD of the 2- to 7-year band, plotted as percent differences from 1968–1998) of fossil coral □18O time series from Palmyra (blue) and Christmas (red). [Cobb et al., 2003; Cobb et al., 2013]. (d) Time series of North America North American Drought Atlas (NADA)-derived ENSO variance (blue, 21-year running variance of 9-year high-pass filtered variability) and ENSO-band variability of Taiwan tree-ring δ18O-based Niño 4 SST reconstruction (red, 31-year running variance of 2-7-year band-pass filtered variability). (e) East equatorial Pacific δ18O variance from individual G. ruber [Rustic et al., 2015] (f) Wavelet spectral density reconstructed Niño 3.4. (g) Average ENSO variance (2–7-year band). The 95 % confidence level is shown with red dashed lines. Intervals with strong interannual precipitation variance are indicated by grey bars.

References

Blaauw, M., and J. A. Christen (2011), Flexible paleoclimate age-depth models using an autoregressive gamma process, Bayesian Anal, 6(3), 457-474, doi: 10.1214/11-Ba618.

Cobb, K. M., C. D. Charles, H. Cheng, and R. L. Edwards (2003), El Niño/Southern Oscillation and tropical Pacific climate during the last millennium, Nature, 424(6946), 271-276, doi: 10.1038/nature01779.

Cobb, K. M., N. Westphal, H. R. Sayani, J. T. Watson, E. Di Lorenzo, H. Cheng, R. L. Edwards, and C. D. Charles (2013), Highly variable El Niño-Southern Oscillation throughout the Holocene, Science, 339(6115), 67-70, doi: 10.1126/science.1228246.

Conroy, J. L., J. T. Overpeck, J. E. Cole, T. M. Shanahan, and M. Steinitz-Kannan (2008), Holocene changes in eastern tropical Pacific climate inferred from a Galápagos lake sediment record, Quaternary Science Reviews, 27(11-12), 1166-1180, doi: 10.1016/j.quascirev.2008.02.015.

Du, X., I. L. Hendy, and A. Schimmelmann (2018), A 9000-year flood history for Southern California: A revised stratigraphy of varved sediments in Santa Barbara Basin, Marine Geology, 397, 29-42.

Hendy, I. L., T. J. Napier, and A. Schimmelmann (2015), From extreme rainfall to drought: 250 years of annually resolved sediment deposition in Santa Barbara Basin, California, Quaternary International, 387, 3-12, doi: 10.1016/j.quaint.2015.01.026.

Hendy, I. L., L. Dunn, A. Schimmelmann, and D. K. Pak (2013), Resolving varve and radiocarbon chronology differences during the last 2000 years in the Santa Barbara Basin sedimentary record, California, Quaternary International, 310, 155-168, doi: 10.1016/j.quaint.2012.09.006.

Huang, B. Y., V. F. Banzon, E. Freeman, J. Lawrimore, W. Liu, T. C. Peterson, T. M. Smith, P. W. Thorne, S. D. Woodruff, and H. M. Zhang (2015), Extended Reconstructed Sea Surface Temperature Version 4 (ERSST.v4). Part I: Upgrades and Intercomparisons, Journal of Climate, 28(3), 911-930, doi: 10.1175/Jcli-D-14-00006.1.

Kodama, K. P., and L. A. Hinnov (2015), Rock Magnetic Cyclostratigraphy, Rock Magnetic Cyclostratigraphy, 145-156.

Moy, C. M., G. O. Seltzer, D. T. Rodbell, and D. M. Anderson (2002), Variability of El Niño/Southern Oscillation activity at millennial timescales during the Holocene epoch, Nature, 420(6912), 162-165, doi: 10.1038/nature01194.

Paillard, D., L. Labeyrie, and P. Yiou (1996), Macintosh Program performs time-series analysis, Eos, Trans. Am. Geophys. Union, 77(39), 379, doi: 10.1029/96EO00259.

Rayner, N. A., D. E. Parker, E. B. Horton, C. K. Folland, L. V. Alexander, D. P. Rowell, E. C. Kent, and A. Kaplan (2003), Global analyses of sea surface temperature, sea ice, and night marine air temperature since the late nineteenth century, J Geophys Res-Atmos, 108(D14), doi: 10.1029/2002JD002670.

Reimer, P. J., et al. (2013), IntCal13 and Marine13 radiocarbon age calibration curves 0–50,000 years cal BP, Radiocarbon, 55(4), 1869-1887.

Rodionov, S. N. (2004), A sequential algorithm for testing climate regime shifts, Geophysical Research Letters, 31(9), doi: 10.1029/2004gl019448.

Schimmelmann, A., I. L. Hendy, L. Dunn, D. K. Pak, and C. B. Lange (2013), Revised ~2000-year chronostratigraphy of partially varved marine sediment in Santa Barbara Basin, California, Geologiska Föreningen i Stockholm Förhandlingar (GFF), 135(3-4), 258-264, doi: 10.1080/11035897.2013.773066.

Schimmelmann, A., C. B. Lange, W. H. Berger, A. Simon, S. K. Burke, and R. B. Dunbar (1992), Extreme climatic conditions recorded in Santa Barbara Basin laminated sediments: the 1835-1840 Macoma event, Marine Geology, 106(3-4), 279-299, doi: 10.1016/0025-3227(92)90134-4.

Schneider, U., A. Becker, P. Finger, A. Meyer-Christoffer, M. Ziese, and B. Rudolf (2014), GPCC's new land surface precipitation climatology based on quality-controlled in situ data and its role in quantifying the global water cycle, Theoretical and Applied Climatology, 115(1-2), 15-40, doi: 10.1007/s00704-013-0860-x.

Thomson, D. J. (1982), Spectrum estimation and harmonic analysis: Proceedings of the IEEE, 70(9), 1055-1096.

Torrence, C., and G. P. Compo (1998), A practical guide to wavelet analysis, B Am Meteorol Soc, 79(1), 61-78, doi: 10.1175/1520-0477(1998)079<0061:Apgtwa>2.0.Co;2.